Elliptic Flow Measurements of Inclusive Photons and Neutral Pion Reconstructions

Ahmed M. Hamed

Submitted in partial fulfillment of the
requirements for the degree of

Doctor of Philosophy

in the Graduate School of Arts and Sciences
Wayne State University
July 2006

Wayne State University

The Graduate School

Ahmed M. Hamed

Major: Nuclear Physics

We, the dissertation committee for the above candidate for the Doctor of Philosophy degree, hereby recommend acceptance of this dissertation.

Thomas M. Cormier
Relativistic Heavy Ion Group, Wayne State University
Chairman of Dissertation

Sergei A. Voloshin
Relativistic Heavy Ion Group, Wayne State University
Chairman of Dissertation

Rene Bellwied
Relativistic Heavy Ion Group, Wayne State University

Claude Pruneau
Relativistic Heavy Ion Group, Wayne State University

Jay Burmeister
School of Medicine, Wayne State University
External Member

This dissertation is accepted by the Graduate School.

Dean of the Graduate School

Dedication

To Dear

Mom, Dad,

Sister, Brothers,

Wife, Son, and

Daughter.

TABLE OF CONTENTS

List of Tables

List of Figures

Chapter 1

The Road to Asymptotic Freedom

"The primary lesson of physics
in this century is that the secret of nature is
symmetry."

David J. Gross (1992)

This chapter is a grab bag of special topics having to do with the elementary particles, specifically partons (quarks and gluons). The current understanding for the answer of the most fundamental questions in physics, "What is matter made of?" on the most fundamental level and "How do matter constituents interact with one another?", is disscused through the victorious history. The effect of the nuclear environment on the behaviour of quarks inside the nucleon is briefly introduced. The basic concepts of the gauge theories and the renormalization theory are presented in this chapter. The running coupling of the QCD is discussed quantitatively and qualitatively. The connection of the asymptotic freedom phenomena to the heavy-ion program is introduced to pave the way for the next chapter.

1.1 Degrees of Freedom

From atoms to quarks: In the early nineteenth century John Dalton used the idea of atoms to establish quantitative rules for chemical reactions. Nevertheless, it took till the beginning of the twentieth century until the atomic theory was firmly

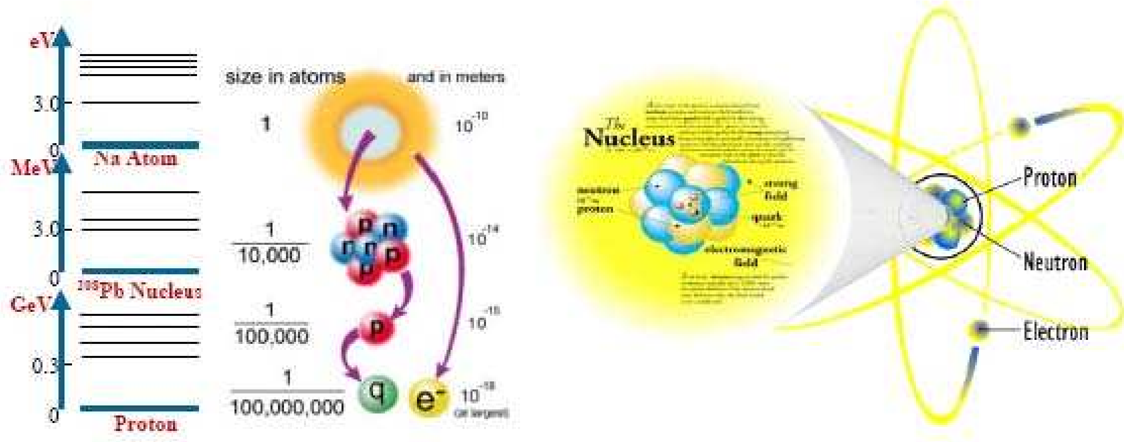

Figure 1.1: Length scales and structural hierarchy in atomic structure. To the left, typical excitation energies and spectra are shown. Smaller bound systems possess larger excitation energies.

established by Einstein's paper on Brownian motion in 1905.

The development of the atomism idea has led to matter consists of molecules and molecules are built up from atoms, which are the basic units of any chemical element. The independence of the cathode ray in the discharge tubes on the kind of cathode and the used gas has resulted in the discovery of the first sub-atomic particle, "the electron", in 1897 by J.J.Thomson. The hydrogen nuclei were identified as protons in the famous Rutherford scattering experiment in his study of elements conversions. After Chadwick discovery of neutrons in 1932 the atom was understood to consist of a central nucleus-containing protons and, except for ordinary hydrogen, neutrons-surrounded by orbiting electrons.

In the late sixties, it turned out that protons and neutrons are made of varieties of still smaller particle called the quarks (partons) supporting the quark model which was developed by Murray Gell-Mann and Kazuhiko Nishijima in order to set a classification scheme for the hadrons in terms of their valence quarks. After around one century from the discovery of the electron, the most massive quark (top quark) was discovered in 1995 by the CDF and D0 experiments at Fermilab [1].

Figure 1.1 shows the energy and the size scales from the atomic level to the sub-atomic level. It is clear that the partonic degrees of freedom are largely *frozen* in nuclear physics, just as the nucleonic ones are frozen in atomic physics. Also, whereas the various energy levels in the atomic system are relatively close together (the spacings are typically several electron volts in an atom whose rest energy is nearly 10^9 electron volts), so that we naturally think of them all as exited states of the same atom, the energy spacings for different states of a bound quark system are very large, and we normally regard them as distinct particles.

In contrast to the nucleus, almost all the volume of the atom is empty. The nucleus radius is smaller than the atomic radius by four orders of magnitude; however, the nucleon radius is just one order of magnitude smaller than the nucleus radius. The density of the normal nuclear matter is $\rho_0 \sim 0.15$ nucleon/fm^3 and therefore the specific volume is ~ 6 fm^3 which is only a factor of two greater than the typical nucleonic volume.

One must expect in case of nuclear density greater than $3\rho_0$ (neutron star for example) the nucleons to overlap, and their individuality to be lost [2]. It is predicted that the matter undergoes a phase transition from hadronic matter to quark gluon plasma under such high density. This prediction has initiated the high-energy program of the heavy-ion collisions. However, the mechanism of the phase transition from hadronic matter to quark soup phase depends on the dynamics of quarks inside the nucleus.

1.2 Structure Functions

Extensive studies of nucleon structure through the Deep Inelastic Scattering (DIS) in the late sixties showed that the nucleon is not an elementary particle but is in fact a composite entity comprising quarks and gluons. The probability for a quark or gluon to carry a fraction x of the proton's momentum (structure function) multiplied by the fraction x is defined as the quark distribution function. Explaining the DIS results,

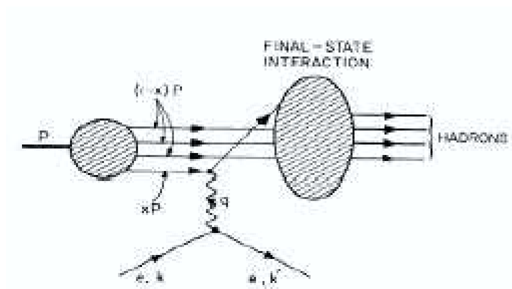

Figure 1.2: Schematic representation of deep inelastic electron-proton scattering according to the parton model in the laboratory system.The arrows indicate the directions of the momenta.

Bjorken suggested that the structure function doesn't depend on the resolution [3] and it dependes only on the value of x. The Bjorken scaling has led to the concept of a proton composed of point like "partons" [4]. It also suggests that the strong interactions must have the property of *asymptotic freedom*.

According to the parton model, (Figure 1.2) the interaction of the electron with the proton can be viewed as the incoherent sum of its interactions with the individual partons. These interactions in turn can be regarded as elastic scattering. This approximation is valid as long as the duration of the photon-parton interaction is so short that the interaction between the partons themselves can be safely neglected (Impulse approximation). In DIS this approximation is valid because the interaction between partons at short distances is weak.

In deep inelastic scattering, however, a new phenomenon is observed. With increasing resolution, quarks and gluons turn out to be composed of quarks and gluons; which themselves, at even higher resolutions, turn out to be composite as well (Figures 1.3 and 1.4). The quantum numbers (spin, flavour, colour,...) of these particles remain the same; only the mass, size, and the color charge change. Hence, there appears to be in some sense a self-similarity in the internal structure of strongly interacting particles. Although the values of momentum transfer Q^2 in the DIS are of orders of magnitude greater than the typical energies and momenta in nuclear physics, further complication arises in the structure function in the presence of nuclear environment.

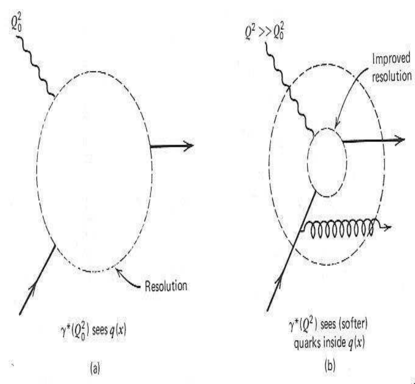

Figure 1.3: At small $Q^2 = Q_0^2$, the quark and the gluon are seen as a unit. At larger $Q^2 \gg Q_0^2$, the resolution increases and the momentum fraction of the quark alone is measured, i.e., without that of gluon; hence, a smaller value is obtained.

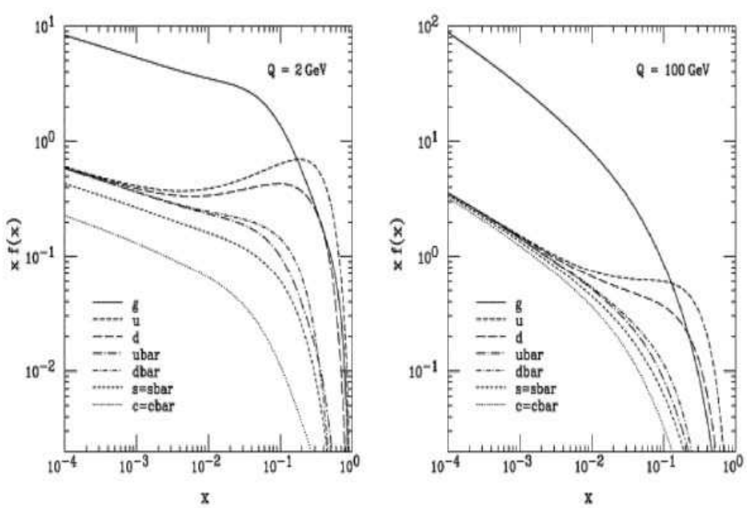

Figure 1.4: CTEQ6M partons shown as a function of x at Q=2GeV and Q=100GeV.

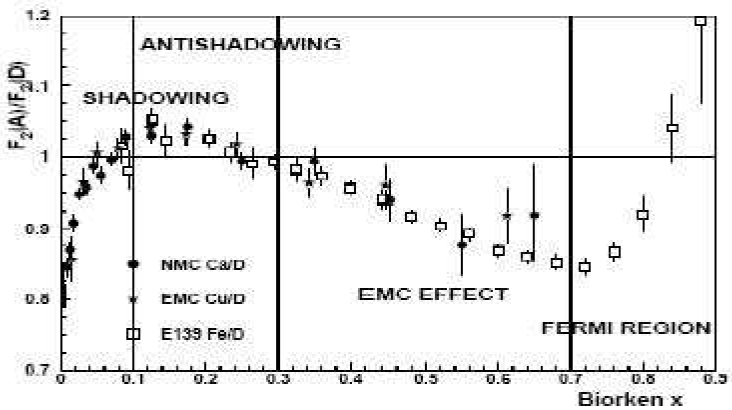

Figure 1.5: The ratio of quark structure functions as a function of Bjorken x.

When several nucleons are in close proximity (as in a nucleus, for example) a parton from one nucleon could leak into a neighbor and fuse with one of the latter's parton. While this leakage can occur for all partons, the most important contributions arise from partons with the largest spatial uncertainty, i.e., those significant as x→0. The effect of gluon fusion is expected to be appreciable at small x where the gluon density is dramatically suppressed. At the same time the small-x behavior of the quarks is largely governed by gluon density and so the shadowing of the gluons is translated into a shadowing of the nuclear structure function.

The influence of the surrounding nuclear medium on the momentum distribution of the quarks is shown in Figure (1.5). Despite the great theoretical efforts, there is no single commonly accepted picture of the physics underlying the dependence of the structure functions on the nuclear environment[1].

1.3 Strong Force

Physicists have known since the 1960s that the proton is not a fundamental particle but is instead made up of building blocks called quarks. These are bound together by the strong force, just as electrons are bound to the nuclei of atoms by the electromagnetic force. Although the electromagnetic force is more familiar to us in everyday

[1]See chapter 3 for more detail of the nuclear environment effect.

life, the strong force is just as important a component of the world in which we live. It not only keeps quarks together in protons but also keeps protons together in the nuclei of the atoms. Without it all matter around us would fall apart.

The strong force is unique among the four fundamental forces of nature “gravitional, electromagnetic, weak, and strong force” in that the particles which feel it directly-quarks and gluons-are completely hidden from us. We can only infer their existence from the experimental observations, and we will never, we believe, be able to isolate these particles. It is impossible, for example to weight them as we can electrons. Indeed, the only strongly interacting particles that we can “see” in particle detectors are the bound states of quarks and gluons, called hadrons. The property of the strong force that prevents quarks and gluons from ever being free is known as “*confinement*”. It is the source of the enormous richness structure of particle and nuclear physics, and is of fundamental importance to the world around us. However, it makes the strong force much harder to handle theoretically than the weak and electromagnetic forces.

Another impetus for theorists to enhance their knowledge of the strong force is to measure the way in which quarks interact through the weak force. These interactions could help us to understand why there is so much more matter than anti-matter in the universe even though equal amounts are thought to have been produced during the Big Bang. Unfortunately, the experimental signature of weak interactions between quarks is always obscured by the strong force interactions that confine them in hadrons. It will require an enormous theoretical effort -which is already underway- to separate the strong and weak force components of the quark interactions to help us to interpret the experimental results.

The strong force interaction between quarks and gluons inside the hadrons are so powerful that they make the quarks and gluons behave in a highly complex way. Indeed, it is impossible to study this behavior analytically. Physicists have therefore turned to numerical simulations performed on the world's fast supercomputers. Recent progress in computing technology, together with the development of new computational and theoretical techniques, means that these numerical simulations becomes more reliable opening up a whole new era of accurate predictions of the properties of hadrons. And by combining these predictions with experimental results, it will become possible to test our understanding of the physics of the strong force in a way that has previously been impossible. The quantitative information that we can extract about the weak interactions will also pave the way to new physics.

In terms of forces[2], the phenomenological potential between two quarks can be expressed as

$$V(r) = -\frac{4\alpha_s}{3r} + kr \tag{1.1}$$

where α_s is the strong coupling constant, k is a constant ($\sim$ 1GeV/fm), and r is the separation between two quarks [5]. The potential between quarks is subject to the density of the force-carrying gluons shared among them.

With increasing distance, the quarks exhibit increasing pull towards each other; the intermediary gluons form a color flux tube such the potential increases linearly with distance while the energy density k remains constant. The stored energy kT eventually reaches a point where it is energetically favorable to create a $q\overline{q}$ pair, hence this linear term is associated with confinement at large r. Decreasing the distance between the quarks gives rise to a coulomb like $1/r$ potential which comes from single gluon exchange, in analogous to the second order process of coulomb scattering between two electrons, Rutherford scattering. Equation (1.1) implies two color-charged quarks cannot be separated. However, by pushing the quarks closer to each other, it should be possible to achieve deconfinement if α_s tends to 0 faster than r.

[2]This is a bit of an oversimplification. Typically, the forces go like $e^{-(r/a)}/r^2$, where a is the (range.) For coulomb's law and Newton's law of universal gravitation, $a = \infty$; for the strong force a is about $10^{-13}cm$.

1.4 QFT and Four Nobel Prizes

The contradiction between Newtonian mechanics and Maxwell's equations inspired Einstein to establish his Special Relativity theory in 1905. The time independence of the universal gravitational law motivated Einstein for gravitational theory, which obeys the special relativity. In 1915 Einstein succeeded in his endeavor and established the General Relativity theory.

The ultraviolet catastrophe initiated the quantum physics. The idea of the outcome is not uniquely determined by the initial conditions has resolved many puzzles in physics. By 1926 the quantum theory with the ad hoc hypothesis "Pauli exclusion principles" were enough to describe almost all the physics on the atomic level assuming the existence of electrons and nuclei. But the nucleus itself was still not understood.

Although quantum mechanics and special relativity are two great theories of twentieth-century physics, both are very successful. But these two theories are based on entirely different ideas, which are not easy to reconcile. In particular, special relativity puts space and time on the same footing, but quantum mechanics treats them very differently. This leads to a creative tension, whose resolution has led to four Nobel Prizes.

The first of these prizes went to P.A.M. Dirac (1933). According to the Special Relativity the laws of physics must be formulated in a form, which is Lorentz-invariant. The search for quantum mechanics equations, which obeys the special relativity principles, has resulted in the existence of the antiparticles. Depending on the nature of the particle under study "fermions or bosons" some of the equations need to be formulated in a representation for which the wave functions $\psi(\overrightarrow{r}, t)$ are vectors of dimension larger one, the components representing the spin attribute of particles and also representing together with a particle its anti-particle.

It is not possible to uncouple the equations to describe only a single type particle without affecting negatively the Lorentz invariance of the equations. Furthermore, the equations need to be interpreted as actually describing many-particle-systems: the equivalence of mass and energy in relativistic formulations of physics allows that energy converts into particles such that any particle described will have ‘companions’ which assume at least a virtual existence. It turned out that the second quantization formalism is more adequate for treating many-particle problems hence in the first quantization formalism the wave function has fixed number of the particles. Finally, the union of relativity and quantum mechanics brings certain extra dividends that neither one by itself can offer: in addition to the existence of antiparticles, a proof of the Pauli exclusion principle, and the so-called TCP theorem.

The need for light theory to reconcile the quantum theory “QED” was the reason for the second Nobel Prize, which went to R. Feynman, J. Schwinger, and S. Tomonaga in 1965. Prior to World War II, Dirac, Heisenberg, and Pauli all made significant contributions to the mathematical foundations related to the quantum light theory. Even for these experienced physicists, however, working with the QED theory posed formidable obstacles because of the presence of “infinities” (infinite values) in the mathematical calculations. The calculation used to define QED were made more accessible and reliable by a process termed *renormalization*, independently developed by the second Nobel Prize winners.

The QED was the first Quantum field theory (QFT) to appear. Quantum field theory is the application of quantum mechanics to fields. It provides a theoretical framework, widely used in particle physics and condensed matter physics, in which to formulate consistent quantum theories of many-particle systems, especially in situations where particles may be created and destroyed. Non-relativistic quantum field theories are needed in condensed matter physics for example in the BCS theory of superconductivity. Relativistic quantum field theories are indispensable in particle physics, although they are known to arise as effective field theories in condensed matter physics.

1.4.1 Gauge Theories

Gauge field theory first appeared in Maxwell formulation of electro-dynamics in 1864. Maxwell theory was the first field theory to appear in physics in addition to being the original gauge theory. However the symmetries of this theory were not truly appreciated for many decades. Electromagnetism contained two important symmetries, Lorentz invariance and gauge invariance. Both went unrecognized. The full understanding of Lorentz invariance required the theory of relativity, a conceptual revolution. It was necessary both to recognize that the symmetry was present in the equations and to realize that this was a symmetry of nature. The full understanding of gauge invariance required the insights of both quantum mechanics and general relativity. Symmetry itself was not appreciated until the end of the nineteenth century. The prominent role that symmetry plays today was only established after the development of quantum mechanics, toward the middle of the twentieth century. The history of gauge invariance (Figure 1.6), its origin and development has been brilliantly reviewed by Yang.

In 1915 Einstein succeeded in his endeavor and established the General Relativity theory. It is important, however, to notice the basic difference between the electromagnetic field and gravitational field. In the electromagnetic field, the field created by a source charge doesn't itself carry charge to become another source. But the fundamental requirement of Einstein's theory of gravity is energy equals mass, which means that all forms of energy become the sources of the gravitational field. Due to this basic difference the electromagnetic filed belongs to "Abelian" fields and the gravitational field belongs to "non-Abelian" fields "Yang-Mills field". Herman Weyl invented the gauge concept in 1918. His motivation was to unify gravity and electromagnetism, to find a geometrical origin for electrodynamics. By 1928 he had reformulated and restated the idea in the way it is still understood today: "gauge invariance corresponds to the conservation of charge as a coordinate invariance corresponds to the conservation of energy-and-momentum".

Gauge symmetry, however, played almost no role in QED. It was largely regarded as a complication and a technical difficulty had to be carefully handled, especially as people were struggling with the quantization of quantum electrodynamics. This is partly due to the difference between local gauge symmetry and ordinary global symmetries of nature[3].

At the nucleus level, in an attempt to generalize the local gauge invariance of electrodynamics to the non-Abelian symmetry of isotopic-spin, Yang and Mills introduced the non-Abelian gauge theories in 1954. Isotopic spin was the first symmetry that was evident in the strong interactions. Introduced by Heisenberg and Wigner, isospin was a good global symmetry of the strong interactions-presumably exact as long as the electromagnetic interaction could be ignored[4].

It took decades until physicists understood that all known fundamental interactions can be described in terms of gauge theories. Nowadays It is known that the gauge symmetries of the Standard Model are very hidden and it is, therefore, not astonishing that progress was very slow indeed. The application of gauge theories to particle physics was a long tricky process. In the case of of the electroweak interactions the issue was how to break the gauge invariance. If unbroken the gauge bosons are necessarily massless. The fact that such particles, aside from photon, do not exist in nature was the major stumbling block for Yang-Mills theory. Glashow, Abdus

[3]There is an essential difference between gauge invariance and global symmetry such as translation or rotational invariance. Global symmetries are symmetries of the laws of nature. They imply that if an observer rotates or translates her experimental apparatus then she will record the same results. Not so for gauge transformations. They do not lead to any new transformations that leave physical measurements unchanged.

[4]Ironically, we now understand that isotopic-spin symmetry, as well as SU(3)×SU(3) symmetry, is an accidental symmetry of the strong interactions. It arises because the light quark (up and down quarks) masses are so small, compared to the mass scale of the strong interaction and appears to have no deep significance.

Salam, and Weinberg have succeeded in breaking the gauge symmetry spontaneously through the Higss mechanism in their electroweak theory. Mathematically, the unification is accomplished under an $SU(2) \times U(1)$ gauge group. The corresponding gauge bosons are the photon of the electromagnetism and the W and Z bosons of the weak force. In the standard model, the weak gauge bosons get their mass from the spontaneous symmetry breaking of the electroweak symmetry from $SU(2) \times U(1)_Y$ to $U(1)_{em}$, caused by the Higgs mechanism. The subscripts are used to indicate that these are different copies of $U(1)$; the generator of $U(1)_{em}$ is given by $Q = Y/2 + I_3$, where Y is the generator of $U(1)_Y$ (called the hypercharge), and I_3 is one of the $SU(2)$ generators (a component of isospin).

Getting rid of infinities in the electroweak theory, a new method called dimensional regularization was inveneted to tame the integrals by carrying them into a space with a fictitious fractional number of dimensions. The third Nobel Prize is awarded to G. 'tHooft, and M. Veltman in 1999 due to their success in showing that all the gauge theories including the broken symmetry ones "spontaneous symmetry breaking" are renormalizable.

The fourth Nobel Prize was awarded due to the renormalization of the QCD which is the QFT of the strong interaction.

1.4.2 **Standard Model**

Standard Model is the current theory of fundamental particles and how they interact. The Standard Model of quarks and leptons is based on some basic principles: special relativity, locality, quantum mechanics, local symmetries and renormalizability. To date, almost all experimental tests of the three forces described by the Standard Model have agreed with its predictions. However, the Standard Model is not a complete theory of the fundamental interactions (Figure 1.7), primarily because it doesn't describe the gravitational force.

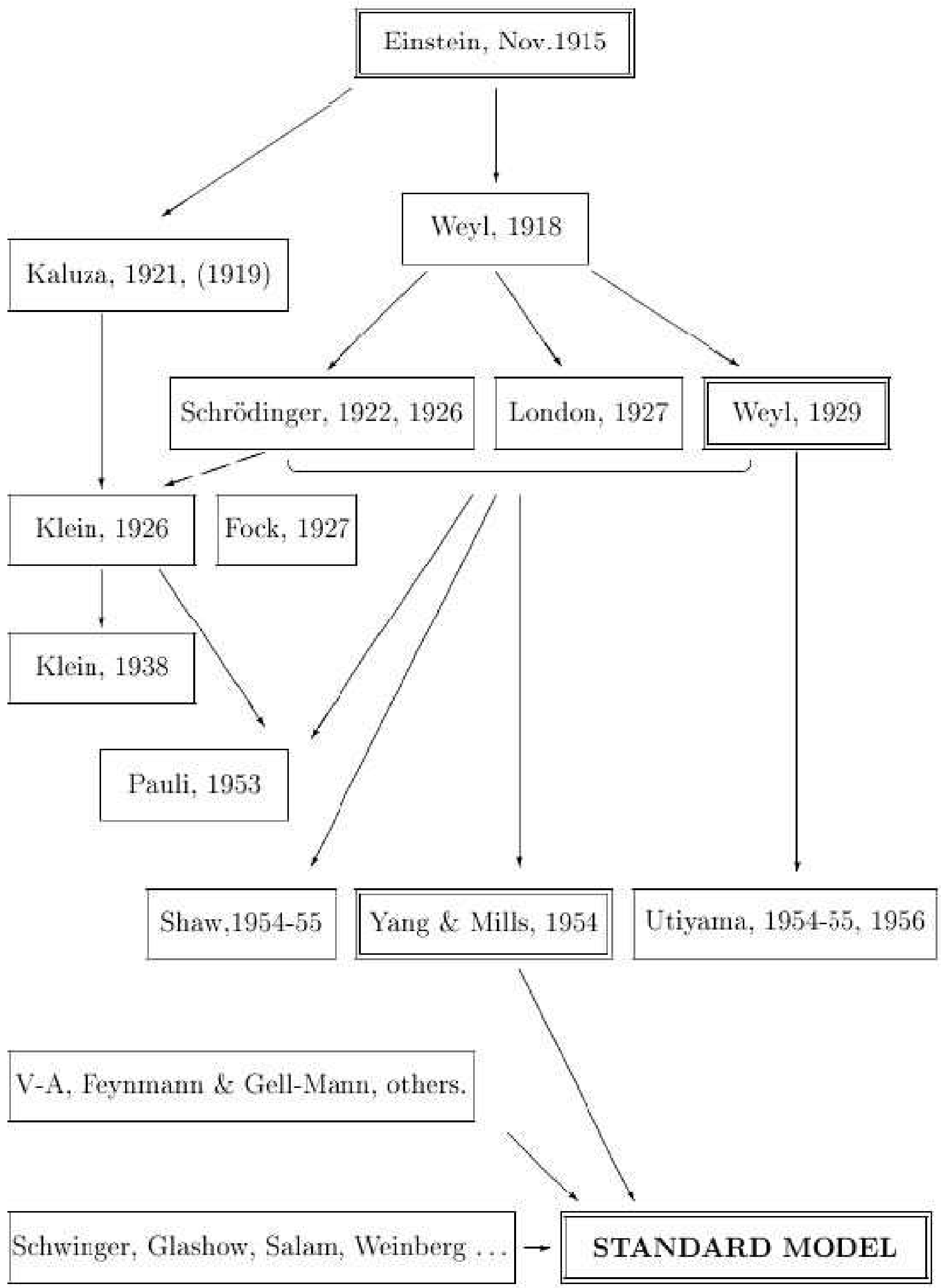

Figure 1.6: Key papers in the development of gauge theories.

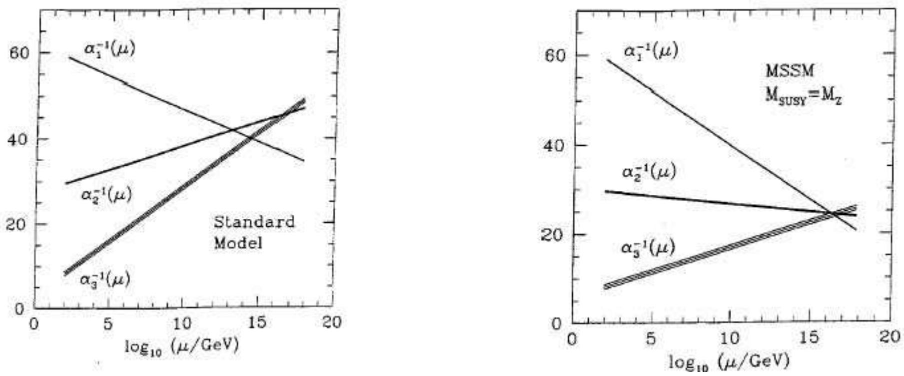

Figure 1.7: Left:Running of the couplings extrapolated toward very high scales, using just the fields of the standard model. The coupling do not quite meet. Experimental uncertainties in the extrapolation are indicated by the width of the lines.Right: Running of the couplings extrapolated to high scales, including thje effects of supersymmetric particles starting at 1 TeV. Within experimental and theoretical uncertainties, the couplings do meet.

The Standard Model (Figure 1.8) contains both fermionic and bosonic fundamental particles. Informally speaking, fermions are particles of matter and bosons are particles that transmit forces. In the Standard Model, the theory of the electroweak interaction is combined with the theory of quantum chromodynamics $SU(3)\times SU(2)\times U(1)$. All of these theories are gauge theories, meaning that they model the forces between fermions by coupling them to bosons which mediate (or "carry") the forces. The Lagrangian of each set of mediating bosons is invariant under a transformation called a gauge transformation, so these mediating bosons are referred to as gauge bosons.

1.4.3 **QCD Lagrangian**

In classical particle mechanics the Lagrangian is derived, but in relativistic field theory the Lagrangian density is usually taken as axiomatic. The Lagangian for a particular system is by no means unique; one can always multiply L by a constant, or add a divergence-such terms cancel out when one apply the Euler-Lagrange equations, so they do not affect the field equations.

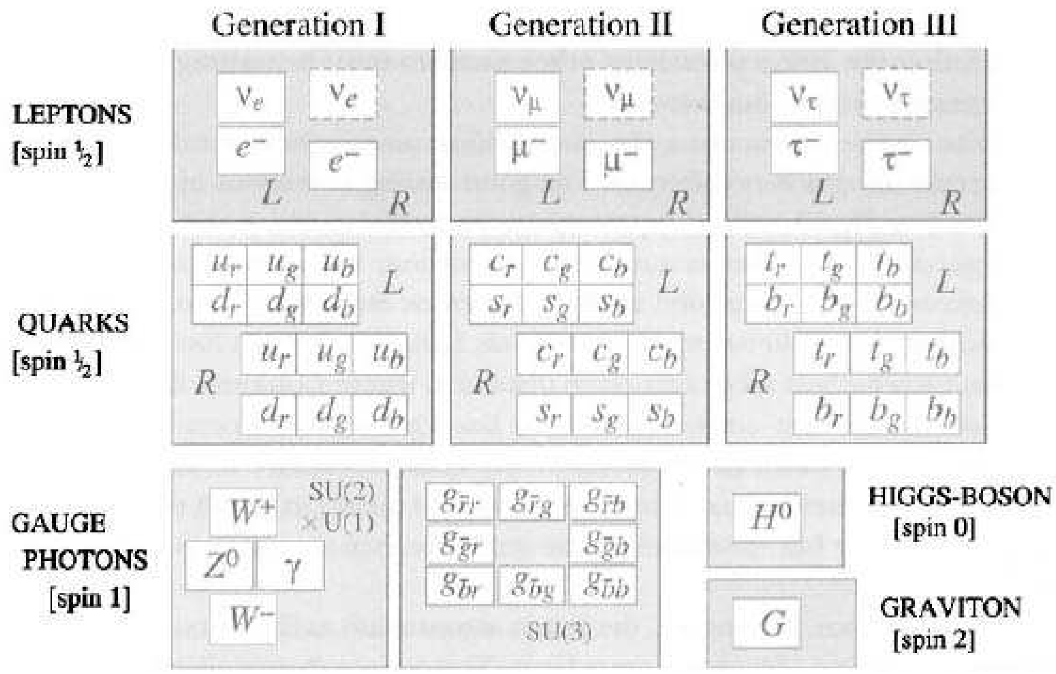

Figure 1.8: The Standard Model, schematically. The leptons and the quarks form three nearly identical generations(only the masses of the entries in these three generations are different). Here, L stands for left-rotating, and R for right-rotating(with respect to the direction of motion). Forces are mainly generated by the gauge photons, $SU(2)(1)$ for the electr-weak force, SU(3) for the strong force. The SU(2) forces act only on the left-rotating fermions.

These are, first of all, the general principles of quantum mechanics, special relativity, and locality, that lead one to relativistic quantum field theory [6]. In addition, one requires invariance under the nonabelian gauge symmetry SU(3), the specific matter content of quarks - six spin 1/2 Dirac fermions which are color triplets - and renormalizability. These requirements determine the theory completely, up to a very small number of continuous parameters.

According to the colored quark model, each flavor of quark comes in three colors red,blue, and green. Although the various flavors carry different masses, the three colors of a given flavor are all supposed to weigh the same.

Let us denote q_f^α a quark field of colour α and flavour f. To simplify the equations, let us adopt a vector notation in colour space: $q_f \equiv$ column (q_f^1, q_f^2, q_f^3). The free Lagrangian

$$\mathcal{L}_0 = \sum_f \overline{q}_f (i\gamma^\mu \partial_\mu - m_f) q_f \tag{1.2}$$

is invariant under arbitrary global $SU(3)_c$ transformations in colour space,

$$q_f^\alpha \to (q_f^\alpha)' = U_\beta^\alpha q_f^\beta; \quad UU^\dagger = U^\dagger U = 1; \quad detU = 1 \tag{1.3}$$

The $SU(3)_c$ matrices can be written in the form

$$U = exp\{-ig_s \frac{\lambda^a}{2} \theta_a\} \tag{1.4}$$

where λ^a (a=1,2,...,8) denote the generators of the fundamental representation of the $SU(3)_c$ algebra, and θ_a are arbitrary parameters. The matrices λ^a are traceless and satisfy the commutation relations

$$[\lambda^a, \lambda^b] = 2if^{abc}\lambda^c, \tag{1.5}$$

with f^{abc} the $SU(3)_c$ structure constants, which are real and totally antisymmetric. As in the QED, we can require the Lagrangian to be also invariant under *local* $SU(3)_c$ transformations, $\theta_a = \theta_a(x)$. To satisfy this requirement, we need to change the quark derivatives by constant objects. Since we have now 8 independents gauge parameters, 8 different gauge bosons $G^\mu_a(x)$, the so-called *gluons*, are needed:

$$D^\mu q_f \equiv [\partial^\mu - ig_s \frac{\lambda^a}{2} G^\mu_a(x)] q_f \equiv [\partial^\mu - ig_s G^\mu(x)] q_f. \tag{1.6}$$

Notice that we have introduced the complex matrix notation

$$[G^\mu(x)]_{\alpha\beta} \equiv (\frac{\lambda^a}{2})_{\alpha\beta} G^\mu_a(x). \tag{1.7}$$

One wants $D^\mu q_f$ to transform in exactly the same way as the colour-vector q_f; this fixes the transformation properties of the gauge fields:

$$D^\mu \to (D^\mu)' = U D^\mu D^\dagger; \quad G^\mu \to (G^\mu)' = U G^\mu U^\dagger - \frac{i}{g_s}(\partial^\mu U)U^\dagger. \tag{1.8}$$

Under an infinitesimal $SU(3)_c$ transformation,

$$q^\alpha_f \to (q^\alpha_f)' = q^\alpha_f - ig_s(\lambda^a/2)_{\alpha\beta}\delta\theta_a q^\beta_f, \quad G^\mu_a \to (G^\mu_a)' = G^\mu_a - \partial^\mu(\delta\theta_a) + g_s f^{abc}\delta\theta_b G^\mu_c. \tag{1.9}$$

The gauge transformation of the gluon filed is more complicated than the one obtained in QED for the photon. The non-commutativity of the $SU(3)_c$ matrices gives rise to an additional term involving the gluon fields themselves. For constant $\delta\theta_a$, the transformation rule for the gauge field is expressed in terms of the structure constants f^{abc} only; thus, the gluon fields belong to the adjoint representation of the colour group. Note also that there is a unique $SU(3)_c$ coupling g_s. In QED it was possible to assign arbitrary electromagnetic charges to different fermions. Since the commutation relation is non-linear, these freedom doesn't exist for $SU(3)_c$. To build a gauge-invariant kinetic term for the gluon fields, the corresponding field strengths are introduced:

$$G^{\mu\nu}(x) \equiv \frac{i}{g_s}[D^\mu, D^\nu] = \partial^\mu G^\nu - \partial^\nu G^\mu - ig_s[G^\mu, G^\nu] \equiv \frac{\lambda^a}{2} G_a^{\mu\nu}(x),$$

$$\mathrm{G}_a^{\mu\nu}(x) = \partial^\mu G_a^\nu - \partial^\nu G_a^\mu + g_s f^{abc} G_b^\mu G_c^\nu \tag{1.10}$$

Under a gauge transformation,

$$G^{\mu\nu} \to (G^{\mu\nu})' = U G^{\mu\nu} U^\dagger, \tag{1.11}$$

And the colour trace $\mathrm{Tr}(G^{\mu\nu}G_{\mu\nu}) = (1/2)G_a^{\mu\nu}G_{\mu\nu}^a$ remains invariant. Taking the proper normalization for the gluon kinetic term, one gets the $SU(3)_c$ invariant QCD Lagrangian:

$$\mathcal{L}_{QCD} \equiv -1/4 G_a^{\mu\nu} G_{\mu\nu}^a + \sum_f \overline{q}_f (i\gamma^\mu D_\mu - m_f) q_f \tag{1.12}$$

It is worth to decompose the Lagrangian into its different pieces:

$$\mathcal{L}_{QCD} = -\frac{1}{4}(\partial^\mu G_a^\nu - \partial^\nu G_a^\mu)(\partial_\mu G_\nu^a - \partial_\nu G_\mu^a) + \sum_f \overline{q}_f^\alpha (i\gamma^\mu \partial_\mu - m_f) q_f$$

$$+\mathrm{g}_s G_a^\mu \textstyle\sum_f \overline{q}_f^\alpha \gamma_\mu (\frac{\lambda^a}{2})_{\alpha\beta} q_f^\beta$$

$$\text{-}(\mathrm{g}_s/2) f^{abc} (\partial^\mu G_a^\nu - \partial^\nu G_a^\mu) G_\mu^b G_\nu^c - \tfrac{g_s^2}{4} f^{abc} f_{ade} G_b^\mu G_c^\nu G_\mu^d G \nu^e. \tag{1.13}$$

The first line contains the correct kinetic terms for different fields, which give rise to the corresponding propagators. The colour interaction between quarks and gluons is given by the second line; it involves the $SU(3)_c$ matrices λ^a. Finally, owing to the non-abelian character of the colour group, the $G_a^{\mu\nu} G_{\mu\nu}^a$term generates the cubic and quartic gluon self-interactions shown in the last line; the strength of these interactions is given by the same coupling g_s which appears in the fermionic piece of the Lagrangian. In spite of the rich physics contained in it, the Lagrangian looks very simple, because of its colour-symmetry properties. All interactions are given in terms of a single universal coupling g_s, which is called the strong coupling constant. The existence of self-interactions among the gauge fields is a new feature that was not present in QED case; it seems reasonable to expect that these gauge self-interactions could explain properties like asymptotic freedom and confinement, which do not appear in QED.

1.4.4 Pros and Cons of QFT

In 1948, Feynman invented the path integral formulation extending the principle of least action to quantum mechanics for electrons and photons. In this formulation, particles travel every possible path between the initial and final states; the probability of a specific final state is obtained by summing over all possible trajectories leading to it. In the classical regime, the path integral formulation cleanly reproduces Hamilton's principle, and Fermat's principle in optics.

This formulation has proved crucial to the subsequent development of theoretical physics, since it provided the basis for the grand synthesis of the 1970's called the renormalization group which unified quantum field theory with statistical mechanics. Feynman showed how to calculate diagram amplitudes using so-called Feynman rules, which can be derived from the system's underlying Lagrangian. The Lagrangian is very useful in relativistic theories since it is a locally defined, Lorentz scalar field. Although Lagrange sought to describe classical mechanics, the action principle that is used to derive the Lagrange equation is now recognized to be deeply tied to quantum mechanics: physical action and quantum-mechanical phase (waves) are related via Planck's constant, and the principle of stationary action can be understood in terms of constructive interference of wave functions. The same principle, and the Lagrange formalism, are tied closely to Noether's Theorem, which relates physical conserved quantities to continuous symmetries of a physical system.

In Feynman diagrams, each internal line corresponds to a factor of the corresponding virtual particle's propagator; each vertex where lines meet gives a factor derived from an interaction term in the Lagrangian, and incoming and outgoing lines provide constraints on energy, momentum and spin. A Feynman diagram is therefore a symbolic notation for the factors appearing in each term of the Dyson series. However, being a perturbative expansion, nonperturbative effects do not show up in Feynman diagrams.

In addition to their value as a mathematical technology, Feynman diagrams provide deep physical insight to the nature of particle interactions. Particles interact in every way available; in fact, intermediate virtual particles are allowed to propagate faster than light. (This is due to the Heisenberg Uncertainty Principle and does not violate relativity for deep reasons; in fact, it helps preserve causality in a relativistic spacetime.)

The naive application of such calculations often produces diagrams whose amplitudes are infinite, which is undesirable in a physical theory. The problem is that particle self-interactions are erroneously ignored. The technique of renormalization, pioneered by Feynman, Schwinger, and Tomonaga compensates for this effect and eliminates the troublesome infinite terms. After such renormalization, calculations using Feynman diagrams often match experimental results with very good accuracy.

However, a very profound problem was identified by Landau [7]. Landau argued that virtual particles would tend to accumulate around a real particle as long as there was any uncancelled influence. This is called screening. The only way for this screening process to terminate is for the source plus its cloud of virtual particles to cease to be of interest to additional virtual particles. But then, in the end, no uncancelled influence would remain - and no interaction! Thus all the brilliant work in QED and more general field theories represented, according to Landau, no more than a temporary fix. You could get finite results for the effect of any particular number of virtual particles, but when you tried to sum the whole thing up, to allow for the possibility of an arbitrary number of virtual particles, you would get nonsense - either infinite answers, or no interaction at all. This problem can be swept under the rug in QED or in electroweak theory, because the answers including only a small finite number of virtual particles provide an excellent fit to experiment. But for the strong interaction that pragmatic approach seemed highly questionable, because there is no reason to expect that lots of virtual particles won't come into play, when they interact strongly.

Acoording to Landau argument quantum field theory is not a valid theory as a way of reconciling quantum mechanics and special relativity. Something would have to give. Either quantum mechanics or special relativity might ultimately fail, or else essentially new methods would have to be invented, beyond quantum field theory, to reconcile them.

Landau pole is defined as the energy scale (or the precise value of the energy) where a coupling constant (the strength of an interaction) of a quantum field theory becomes infinite.

Now it is known that the dependence of coupling constants on the energy scale is one of the basic ideas behind the renormalization group. Nominally empty space is full of virtual particle-antiparticle pairs of all types, and these have dynamical effects. Put another way, nominally empty space is a dynamical medium, and we can expect it to exhibit medium effects including dielectric and paramagnetic behavior, which amount (in a relativistic theory) to charge screening. In other words, the strength of the fields produced by a test charge will be modified by vacuum polarization, so that the effective value of its charge depends on the distance at which it is measured. Theories with asymptotic freedom have Landau poles at very low energies. However, the phrase "Landau pole" is usually used in the context of the theories that are not asymptotically free, such as quantum electrodynamics (QED) or a scalar field with a quartic interaction. The coupling constant grows with energy, and at some energy scale the growth becomes infinite and the coupling constant itself diverges.

Landau poles at high energy are viewed as problems; more precisely, they are evidence that the theory (e.g. QED) is not well-defined nonperturbatively. The Landau pole of QED is removed if QED is embedded into a Grand Unified Theory or an even more powerful framework such as superstring theory.

1.4.5 Renormalization

In quantum field theory and the statistical mechanics of fields, renormalization refers to a collection of techniques used to construct mathematical relationships or approximate relationships between observable quantities, when the standard assumption that the parameters of the theory are finite breaks down (giving the result that many observables are infinite). In the renormalization of quantum field theories, to extract finite physical results from higher order perturbative calculations, a certain subtraction scheme is necessary to be used so as to remove the divergences occurring in the calculations. However, there exists a serious ambiguity problem that different subtraction schemes in general give different physical predictions, conflicting the fact that the physical observables are independent of the subtraction schemes.

The problem arises when special relativity is taken into account. In this case quantum theory must allow for fluctuation in energy over brief intervals of time. This is a generalization of the complementarity between momentum and position that is fundamental for ordinary, non-relativistic quantum mechanics. It means that energy can be borrowed to make evanescent virtual particles, including particle-antiparticle pairs. Each pair passes away soon after it comes into bring, but new pairs are constantly boiling up, to establish an equilibrium distribution. In this way the wave function of empty space becomes densely populated with virtual particles, and empty space comes to behave as a dynamical medium. The virtual particles with very high energy create special problems. If you calculate how much the properties of real particles and their interactions are changed by their interaction with virtual particles, you tend to get divergent answers, due to the contributions from virtual particles of very high energy. This problem is a direct descendant of the problem that triggered the introduction of quantum theory in the first place, i.e. the "ultraviolet catastrophe" of black body radiation theory, addressed by Plank. There the problem was that high-energy modes of the electromagnetic field are predicted, classically, to occur as thermal fluctuations, to such an extent that equilibrium at any finite temperature requires that there is an infinite amount of energy in those modes. The difficulty came from the possibility of small-amplitude fluctuations with rapid variations in space and time. The element of discreteness introduced by quantum theory eliminates the possibility of very small-amplitude fluctuations, because it imposes a lower bound on their size. The (relatively) large-amplitude fluctuations that remain are predicted to occur very rarely in thermal equilibrium, and cause no problem. But quantum fluctuations are much more efficient than are thermal fluctuations at exciting the high-energy modes, in the form of virtual particles, and so those modes come back to haunt us. For example, they give a divergent contribution to the energy of empty space, the so-called zero-point energy.

Renormalization theory was developed to deal with this sort of difficulty. The central observation that is exploited in renormalization theory is that although interactions with high-energy virtual particles appear to produce divergent corrections, they do so in a very structured way. That is, the same corrections appear over and over again in the calculations of many different physical processes. For example in quantum electrodynamics (QED) exactly two independent divergent expressions appear, one of which occurs when we calculate the correction to the mass of the electron, the other of which occurs when we calculate the correction to its charge. To make the calculation mathematically well-defined, we must artificially exclude the highest energy modes, or dampen their interactions, a procedure called applying a cut-off, or regularization. In the end we want to remove the cutoff, but at intermediate stages we need to leave it in, so as to have well-defined (finite) mathematical expressions. If we are willing to take the mass and charge of the electron from experiment, we can identify the formal expressions for these quantities, including the potentially divergent corrections, with their measured values. Having made this identification, we can remove the cutoff. We thereby obtain well-defined answers, in terms of the measured mass and charge, for everything else of interest in QED.

However, finding very special quantum field theories actually have anti-screening "asymptotic freedom" turns Landaus problem on its head. In the case of screening, a source of influence -let us call it charge, understanding that it can represent something quite different from electric charge- induces a canceling cloud of virtual particles. From a large charge, at the center, you get a small observable influence far away. Antiscreening, or asymptotic freedom, implies instead that a charge of intrinsically small magnitude catalyzes a cloud of virtual particles that enhances its power. Since the virtual particles themselves carry charge, this growth is a self-reinforcing, runaway process. The situation appears to be out of control. If that is the case, then the source could never be produced in the first place.

According to the anti-screening picture the confinement of quarks, makes a virtue of theoretical necessity. For it suggests that there are in fact sources specifically, quarks that cannot exist on their own.

The theories that display asymptotic freedom are called nonabelian gauge theories, or Yang-Mills theories. They form a vast generalization of electrodynamics. They postulate the existence of several different kinds of charge, with complete symmetry among them. So instead of one entity, charge, we have several colors. Also, instead of one photon, we have a family of color gluons.

1.4.6 The QCD Running Coupling

The renormalization of the QCD coupling proceeds in a similar way to QED. Owing to the non-abelian character of $SU(3)_c$, there are additional contributions involving gluon selfinteractions. From the calculation of the relevant one-loop diagrams, shown in Figure(1.9) one gets the value of the first β-function coefficient [8,9]:

$$\beta_1 = \frac{2}{3} T_F N_f - \frac{11}{6} C_A = \frac{2N_f - 11N_C}{6} \tag{1.14}$$

The positive contribution proportional to N_f is generated by the $q\overline{q}$ loops and corresponds to the QED result (except for the T_F factor). The gluonic self-interactions introduce the additional negative contribution proportional to N_C. This second term is responsible for the completely different behaviour of QCD: $\beta_1 < 0$ if $N_f \leq 16$. The corresponding QCD running coupling,

$$\alpha_s(Q^2) = \frac{\alpha_s(Q_0^2)}{1 - \frac{\beta_1 \alpha_s(Q_0^2)}{2\pi} ln(Q^2/Q_0^2)} \tag{1.15}$$

decreases at short distances (Figure 1.10), i.e.

$$\lim_{Q^2 \to \infty} \alpha_s(Q^2) = 0. \tag{1.16}$$

Thus, for $N_f \leq 16$, QCD has indeed the required property of asymptotic freedom. The gauge self-interactions of the gluons *spread out* the QCD charge, generating an *antiscreening* effect. This could not happen in QED, because photons do not carry electric charge. Only non-abelian gauge theories, where the intermediate gauge bosons are self-interacting particles, have this antiscreening property. Although quantum effects have introduced a dependence with the energy, we still need a reference scale

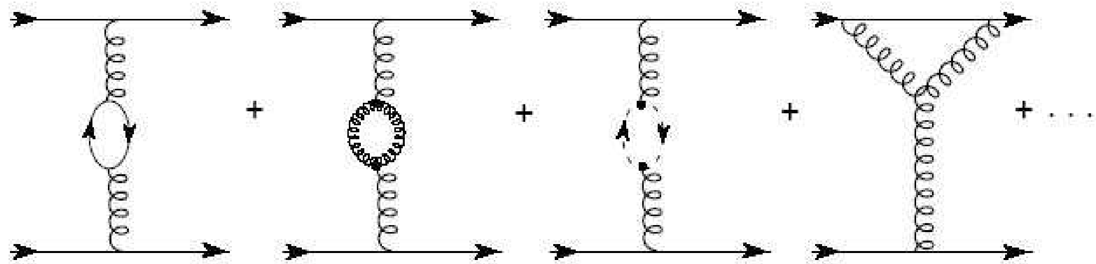

Figure 1.9: Feynman diagrams contributing to the renormalization of the strong coupling.The dashed loop indicates the *ghost* correction.

to decide when a given Q^2 can be considered large or small. An obvious possibility is to choose the scale at which α_s enters into a strong-coupling regime (i.e. $\alpha_s \sim 1$), where perturbation theory is no longer valid. A more precise definition can be obtained from the solution of the β-function differential equation $\mu\frac{d\alpha}{d\mu} \equiv \alpha\beta(\alpha)$; $\beta(\alpha) = \beta_1\frac{\alpha}{\pi} + \beta_2(\frac{\alpha}{\pi})^2 + ...$ At one loop, one gets

$$ln\mu + \frac{\pi}{\beta_1\alpha_s(\mu^2)} = ln\Lambda, \tag{1.17}$$

where ln Λ is just an integration constant. Thus,

$$\alpha_s(\mu^2) = \frac{2\pi}{-\beta_1 ln(\mu^2/\Lambda^2)} \tag{1.18}$$

In this way, the dimensionless parameter g_s is traded by the dimensionful scale Λ. The number of QCD free parameters is the same (1 for massless quarks), but quantum effects have generated an energy scale. Although, Equation (1.15) gives the impression that the scale-dependence of $\alpha_s(\mu^2)$ involves two parameters,μ_0^2 and $\alpha_s(\mu_0^2)$, only the combination (1.17) is actually relevant, as explicitly shown in (1.18). When $\mu \gg \Lambda$, $\alpha_s(\mu_0^2) \to 0$ so that we recover asymptotic freedom. At lower energies the running coupling gets bigger; for $\mu\to$ Λ,$\alpha_s(\mu^2) \to \infty$ and perturbation theory breaks down. The scale indicates when the strong coupling blows up. Equation (1.18) suggests that confinement at low energies is quite plausible in QCD; however,

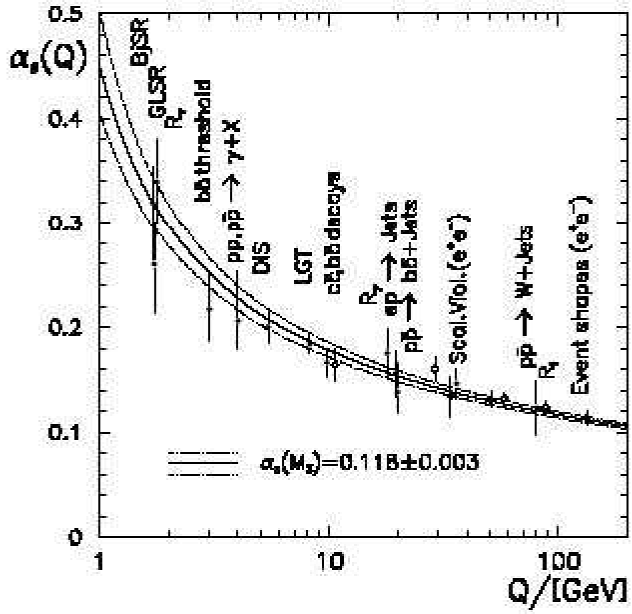

Figure 1.10: Running of the couplings from[10]

it does not provide a proof because perturbation theory is no longer valid when $\mu \rightarrow \Lambda$.

1.4.7 Asymptotic Freedom

Quantum chromodynamics theory (QCD) describes the strong force at high-energy physics. QCD was constructed in analogy to quantum electrodynamics (QED), the theory that describes the electromagnetic force. In both theories there is a fundamental particle (a massless bosons) that "carries" the force: a photon in QED and a gluon in QCD. In both cases there are fundamental particles (massive fermions) that "feel" the force because they have an appropriate charge. In QED, An electron constantly emits and reabsorbs virtual photons, which can produce virtual e^+e^- pairs. This cloud of virtual electrons and positrons produces a shielding effect called vacuum polarization. The QED coupling constant can be approximated by

$$\alpha(Q^2) = \frac{\alpha_{em}}{1 - \frac{\alpha_{em}}{3\pi} ln(Q^2/m_e^2)} \tag{1.19}$$

Where Q is the momentum transfer being examined, m_e is the electron mass, and

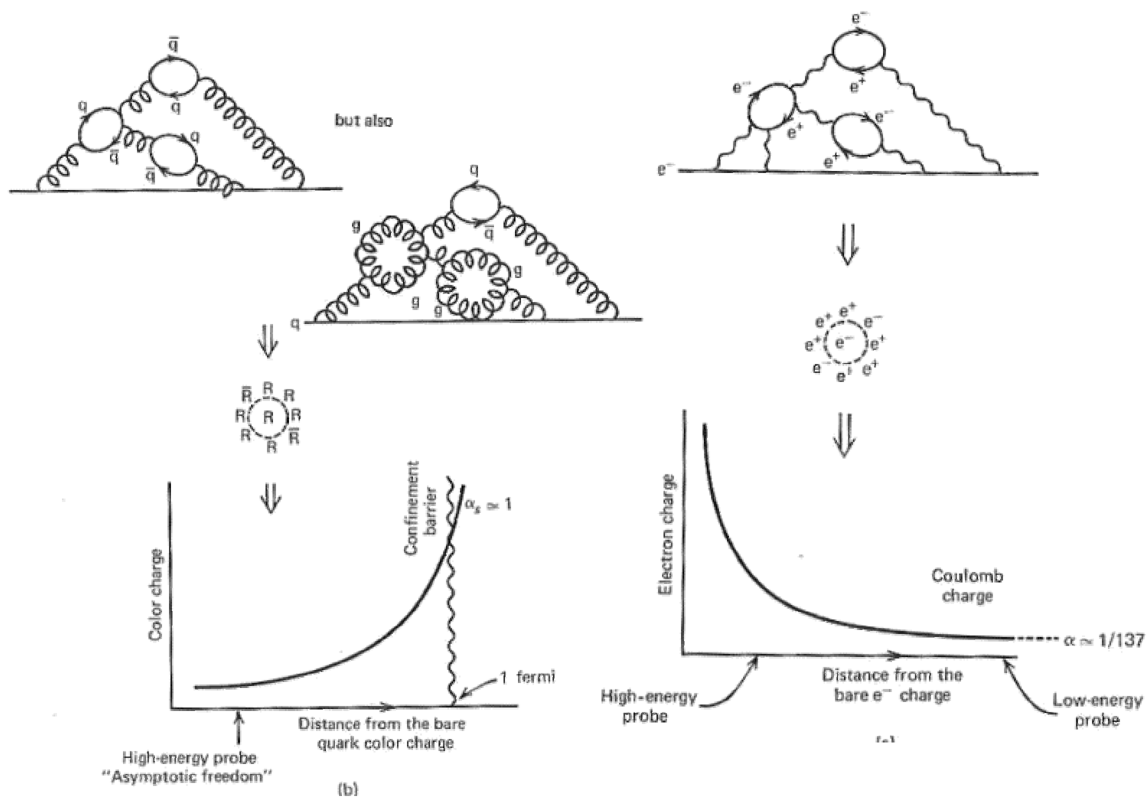

Figure 1.11: Screening and Anti-screening effect for the electrons and quarks.

$\alpha_{em} = e^2/4\pi\epsilon_0\hbar c$ is the fine structure constant, e being the charge of the electron. As Q decreases, or the typical distance $r \approx 1/Q$ increases, the effective coupling α_{em} gets smaller.

In other words, the bare charge is shielded to some extent. Conversely, the shielding effect becomes small at extremely short distances, or very high Q, and one can obtain the potential due to the bare charge. The form of α_{em} in Equation (1.19) is that of a running coupling constant, which depends on the masses or momentum transfers involved in any particular case. In QCD, meanwhile, the quarks have a "color charge" of magnitude g. The quark interactions can also be represented by a running coupling constant, $\alpha_s(Q^2)$. Similar to the QED case, $q\overline{q}$ pairs produce a shielding effect on the value of a test quark. However, gluons also possess color charges and can produce gluon loops, which leads to an anti-shielding effect (Figure 1.11). The effective coupling is approximated by Equation (1.15). As long as $N_f \leq 16$

$\alpha_s(Q2)$ will decrease as Q^2 increases. Thus, at asymptotically large Q^2, or very small distances, $\alpha_s(Q^2) \to 0$. In this regime, the quarks act as if free which is referred to as asymptotic freedom. The similarities between the two theories become evident when we consider the force between two charged particles as a function of the distance between them.

If just one photon is exchanged, QED leads to the familiar coulomb law of classical electromagnetism, which describes the attractive force between an electron and a positron as k/r^2, where k is a constant, which is proportional to e^2. In fact, in QED k is called the "fine structure constant", α_{em} =1/137, the small value of which indicates that the interactions in QED are rather feeble.

Similarly, if we use QCD to calculate the strong force generated when a quark and antiquark exchange just a single gluon we again obtain an expression for the attractive force that is similar to Coulomb's Law. The constant of proportionality is then known as the "strong coupling constant", α_s, and is proportional to g^2. However, α_s is much larger than α_{em} in practical situations and can have a value close to 1. The main difference between QED and QCD is that while photons and electrons can exist on their own-as light waves and static charge, for example-free quarks or gluons have never been seen. Unlike electrons, quarks are forced to play beach ball with each other forever, and the ball (the gluon) can never escape either. In QED the single-photon exchange calculation (giving Coulomb's Law) is an accurate picture because α_{em} is small. Taking into account exchanges of more than one photon makes only a tiny difference to the calculation of the electromagnetic force, because these additional terms are proportional to α_{em}^n, where n is the number of photons exchanged. The result is that an electron and positron, which interact via a force, that decreases as they move further apart, can escape from each other, given enough energy. In QCD, however, the result from a single-gluon exchange is not, in general, a realistic picture. In fact, it only holds when the quark and antiquark are very close together, and it becomes more and more inaccurate as they move apart. The reason is that α_s itself depends on r and grows as r increases. Once α_s is large, a quark and antiquark are as likely to exchange many gluons as they are to exchange just one. Their interaction becomes highly complex and, at present, impossible to calculate analytically. What happens is that instead of being spread out in space, the color field between the quark and antiquark becomes concentrated into a linear "string" between them. This gives a force that no longer weakens as r increases, and however much energy they are given, the quark and antiquark cannot escape from other's clutches. The increase of α_s with r can be traced to a key difference between QCD and QED. In QED, photons have no electric charge, but in QCD gluons carry both a color charge and an anti-color charge. This means that a QCD interaction in which a gluon emits and absorbs other gluons is possible. A gluon being exchanged between a quark and an antiquark can then turn into a shower of gluons, and this is an important factor in the creation of a string and the confinement process. The only free particles that QCD allows are "colorless" ones, where the net colour charge is zero. These particles- protons, neutrons and other hadrons- can be made of groups of quarks, anti-quarks and gluons. More than 100 hadrons of different masses are possible, given all the combinations of quark types and the fact that each combination can have a number of different internal configurations of properties such an angular momentum. Although hadrons can escape from long distance QCD interactions with other particles, their components are always bound together by strong and very complicated internal interactions. When hadrons are smashed together in high-energy experiments at laboratories such as BNL, CERN, quarks and anti-quarks can be created out of the energy of the collisions. But, since a free object with color charge is not allowed; they quickly become clothed in other quarks and gluons, also created in the collision. The particles that eventually reach the detectors are colorless hadrons. Some of these hadrons only live for a short time before decaying into other hadrons, but from the tracks of their decay products in the detector we can reconstruct their brief appearance and subsequently measure their mass and other properties. In this way the "particle zoo" of sub-atomic particles was discovered in the 1950s and 1960s, and new hadrons are still being found today.

Summary

The discovery of asymptotic freedom has explained the SLAC results "parton model". The α_s in equation (1.1) tends to zero faster than the inter-distance between the quarks which make deconfinement possible. Soon, after the discovery of the asymptotic freedom, It is predicted that the superdense matter consists of quarks rather than of hadrons. The heavy-ion collisions program discussed in the next chapter aims to reach that deconfined phase.

Chapter 2

QCD in Extreme Conditions

"The special peculiarity of QCD, that its fundamental entities and abundant symmetries are well hidden in ordinary matter, lends elegance and focus to the discussion of its behavior in extreme conditions."

Frank Wilczek (2000)

The goal of this chapter is to introduce the different phases of nuclear matter and to locate the Quark Gluon Plasma in the phase diagram of the QCD matter. The Lattice Quantum Chromodynamics is presented, in addition to its prediction for the phase transition from the hadronic phase to QGP phase. The Chiral Symmetry Restoration which may accompany the phase transition is introduced. General description of the Ultra-Relativistic Heavy Ion Collisions is discussed and the different proposed siganatures of QGP are presented.

Anomalous Nuclear Matter

The nuclear matter under high temperature and/or high baryon number density the quarks, gluons, and the various symmetries will come into their own. By tracing symmetries lost and found we will be able to distinguish sharply among different phases of hadronic matter, and to make some remarkably precise predictions about the transitions between them.

The behavior of QCD at high temperature and low baryon number density is central to cosmology. Indeed, during the first few seconds of the Big Bang the matter content of the Universe was almost surely dominated by quark-gluon plasma. There are ambitious, extensive programs “Heavy-Ion Collisions” are running to probe this regime experimentally.

The behavior of QCD at high baryon number density and (relatively) low temperature is central to extreme astrophysics - the description of neutron star interiors, neutron star collisions, and conditions near the core of collapsing stars (supernovae, hypernovae). Also, we might hope to find insight into nuclear physics, coming down from the high-density side.

2.1 **Quark Gluon Plasma**

A quark-gluon plasma (QGP) is a phase of quantum chromodynamics which exists at extremely high temperature and density. It is believed to have existed during the first 20 or 30 μs after the universe came into existence in the Big Bang. According to the standard cosmological model [10], the temperature of the cosmic background radiation exceeded 200 MeV during the first 10 μs after the Big Bang. The early universe was hence filled with a quark-gluon plasma rather than with hadrons. Thus, physical processes occurring during this very early period can be described in terms of quark and gluon transition amplitudes rather than hadronic amplitudes.

The high temperature phase of QCD is of interest from many points of view. First of all, it is the answer to a fundamental question of obvious intrinsic interest: What happens to empty space, if you keep adding heat? Moreover, it is a state of matter one can hope to approximate, and study systematically, in heavy ion collisions.

The fundamental theoretical result regarding the asymptotic high temperature phase is that it becomes quasi-free. That is, one can describe major features of this phase quantitatively by modeling it as a plasma of weakly interacting quarks and gluons. In this sense the fundamental degrees of freedom of the microscopic Lagrangian, ordinarily only indirectly and very fleetingly visible, become manifest (or at least, somewhat less fleetingly visible). Likewise the naive symmetry of the classical theory which, is vastly reduced in the familiar, low-temperature hadronic phase, gets restored asymptotically.

The goal of relativistic heavy ion physics is the experimental study of the nature of QCD matter under conditions of extreme temperature. A great emphasis has been placed on "the discovery of the quark-gluon plasma", where the terminology "quark-gluon plasma" is used as a generic descriptor for a system in which the degrees of freedom are no longer the color neutral hadron states observed as isolated particles and resonances. This definition is limited since high-energy proton-proton reactions cannot be described purely in terms of color-neutral hadrons, but rather require analysis of the underlying partonic interactions. The hoped-for essential difference in heavy ion collisions is the dominance of the partonic-level description for essentially all momentum scales and over nuclear size distances.

Beyond this simple criterion, in order to characterize the produced system as a state of matter it is necessary to establish that these non-hadronic degrees of freedom form a statistical ensemble, so that concepts such as temperature, chemical potential and flow velocity apply and the system can be characterized by an experimentally determined equation of state. Additionally, experiments eventually should be able to determine the physical characteristics of the transition, for example the critical temperature, the order of the phase transition, and the speed of sound along with the nature of the underlying quasi-particles. While at (currently unobtainable) very high temperatures $T \gg T_c$ the quark-gluon plasma may act as a weakly interacting gas of quarks and gluons, in the transition region near T_c the fundamental degrees of freedom may be considerably more complex. It is therefore appropriate to argue that the quark-gluon plasma must be defined in terms of its unique properties at a given temperature. To date the definition is provided by lattice QCD calculations. Ultimately we would expect to validate this by characterizing the quark-gluon plasma in terms of its experimentally observed properties. However, the real discoveries will be of the fascinating properties of high temperature nuclear matter, and not the naming of that matter.

Since there are dramatic qualitative differences between the zero-temperature and the high-temperature phases, the question naturally arises whether there are sharp phase transitions separating them, and if so what is their nature. This turns out to be a rich and intricate story, whose answer depends in detail on the number of colors and light flavors.

2.2 Lattice Gauge Theory Basics

When quantum chromodynamics was developed in the 1970s it was meant to do much more than simply classify the "particle zoo". It was hoped that QCD would also predict the masses of hadrons and give details of their internal structure. However, QCD has caused immense problems for theorists. Calculations of the strong force in which it is assumed that just one or two gluons are exchanged only make sense if the quark and antiquark are close together and the value of α_s is small. Such a situation occurs in the instant after the quarks and antiquarks have been produced in high-energy collisions, and using the perturbation theory theorists have succeeded in calculating quantities that do not depend on the fact that the quarks must eventually turn into bound hadrons.

However, when the quarks are further apart-particularly at those distances over which QCD could shed light on the internal structure of the hadrons(q$\leq$1GeV) α_s is much larger and analytic or perturbative solutions are impossible due to the highly nonlinear nature of the strong force. In this case there is no alternative but to include all possible QCD interactions right from the start. The only way to do this is through computer simulations. This approach is called "Lattice QCD", because the space-time is divided into a lattice of points. Lattice QCD was proposed by the US physicist Ken Wilson in the early 1970s, but it is recently that the computational power to perform the calculations fully is becoming available.

Lattice QCD is the theory of quarks and gluons formulated on a space-time lattice. The formulation of QCD on a discrete rather than continuous space-time naturally introduces a momentum cut off at the order of 1/a (a is the lattice size), which regularize the theory. As the result lattice QCD is mathematically well-defined. Most importantly, lattice QCD provides the framework for investigation of non-perturbative phenomena such as confinement and quark-gluon plasma formation, which are intractable by means of analytic field theories.

The great virtue of the lattice version of QCD are that it provides an ultraviolet cutoff and that it allows a convenient strong-coupling expansion, while preserving a very large local gauge symmetry. Its drawbacks are that it destroys translation and rotation symmetry, that it has an awkward weak-coupling expansion, and that it mutilates the ultraviolet behavior of the continuum theory. Using the techniques of lattice gauge theory one can simulate many aspects of the behavior with great flexibility and control. So there is a nice interplay among physical experiments, numerical experiments, and theory.

The space-time lattice which is used for lattice QCD is a four -dimensional box of points, which approximates a portion of the space-time continuum. In QCD, quarks and gluons are represented by "quantum field" in space-time; in lattice QCD these fields take values only at the lattice sites and all the derivatives in the QCD equations become finite differences. A numerical solution is then possible. "Discretising" a problem in this way is a common trick in computational science.

The first step in a lattice QCD calculation is to simulate the vacuum or "nothingness", which is space-time without any hadrons. But the vacuum is not just an empty box. It teems with gluons, quarks and antiquarks that are continually being created and destroyed. This is simulated by randomly generating typical snapshots of the vacuum-i.e. configurations of quantum fields-using "Monte Carlo" techniques. Using the vacuum configurations, one can then do all sorts of calculations. One of the easiest is to calculate the mass of a meson, which is the bound state of a quark and antiquark with no overall color charge.

What one can do in a lattice QCD calculation is to introduce a quark and an anti-quark onto the lattice and numerically solve the equations to obtain their quantum fields on each vacuum configuration. These fields then include the effect of all the QCD interactions between them. The quantum field of a meson is a product of the quark and anti-quark fields, and one can extract the meson's energy or mass from the way the field varies with time. However, to get a precise time variation-and therefore a precise mass- one must average over many possible snapshots of the vacuum. The statistical errors in the value obtained for the mass falls as the inverse square root of the number of the vacuum configurations, and will generally be reduced to a few percent if we average over several hundred configurations.

The value obtained for the meson mass will depend on the free parameters of QCD, which are the quark masses and the value of α_s. These parameters come from some deeper physical theory than QCD and their values can only be determined by comparing the theoretical predictions with experiment. In a lattice calculation this is done by adjusting these parameters in the lattice QCD equation until a certain numbers of calculated hadron masses agree with their experimental values. The number of hadron masses are needed to use in this process is equal to the number of parameters are needed to determine. All other hadron masses and calculated results are then predictions of QCD.

Lattice QCD calculations require a huge amount of computation, the size of the calculation depends on the number of points in the space-time lattice. This in turn depends on the overall size of the box of space-time that one is simulating, and on the fineness of the grid one is using to represent it. The box must obviously be larger than the hadron it contains, which means it must be at least 2 fm in length, since this is a typical hadronic size. However, the box cannot be too big or the calculation will take far too long.

In the past, theorists have used vacuum configurations that included only gluons- and not quarks- in what is known as the "quenched approximation". The reason for taking this short cut is that quarks are fermions and obey the Pauli Exclusion Principle, which means that their quantum fields cannot be represented by simple numbers on a computer. Although it is possible to represent them fully by matrices, the problem is that these matrices are huge- typically 2 million raw by 2 million columns- and inverting them, as is required, takes a huge amount of computing time. In fact, to make vacuum configurations that include quark/antiquark pairs- or"dynamical quarks" as they are known-requires hundreds of matrix inversions for every vacuum configuration obtained. This means that including dynamical quarks takes at least a thousand times longer than a calculation based on the quenched approximation. However, results from a number of different groups have shown (Figure 2.1) that the quenched approximation is wrong, it is now clear that errors of up to 10% exists in the masses that have been calculated for some mesons and baryons. Since one is certainly aiming for an error below 10% for quantitative test of QCD, the calculations must include dynamical quarks.

However, the cost of including dynamical quarks in the calculations depends not only on the size of the lattice (and therefore of the qurak matrix) but also on the quark mass itself. As one moves to lighter and lighter quarks, it takes more and more computer time to invert the matrix. Unfortunately the dynamical quarks that appears most often in the vacuum of the real world will be the lightest-the "up" and "down" quarks-since these cost the least energy to create. The lightest dynamical

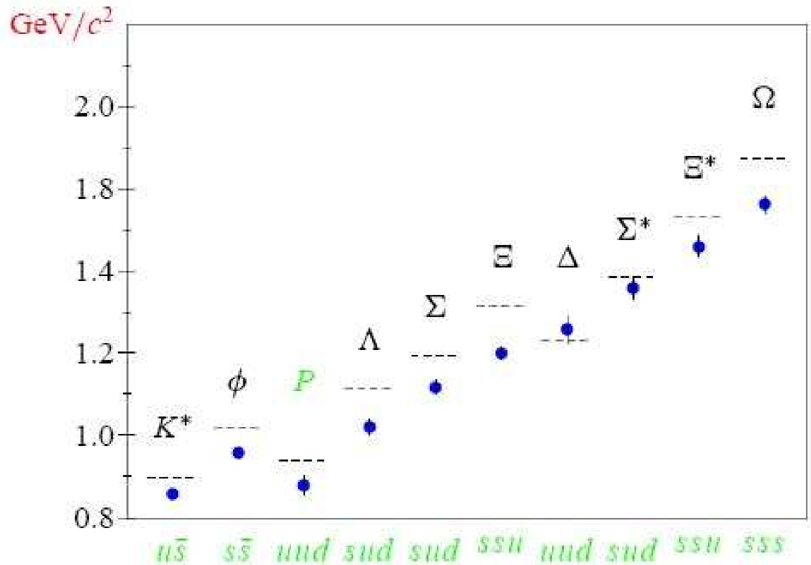

Figure 2.1: The masses of hadrons containing up (u), down (d) and strange (s) quarks and anti-quarks (denoted with a bar above), as calculated by the Japanese CP-PACS collaboration in 1998 using the quenched approximation (filled circles with error bars). Experimental results are given by dashed lines. The K* and f hadrons are mesons, while the other hadrons are baryons. Three meson masses (that of the p, the ρ and the K) are not given since they have been used to fix the parameters of QCD, here as and two quark masses (that of the strange quark and the up and down quarks which are taken to have the same mass). The masses are given in units of GeV/c2 in which the experimental mass of the proton (P) is 0.938 The calculated masses based on the quenched approximation are in error by as much as 10% compared with the experimental results. If we want to test more rigorously the hadron masses that QCD predicts, the calculations must include dynamical quarks.

quarks that the theorists have so far been able to study with lattice calculations are strange quarks, which are much heavier than up and down quarks.However, it becomes possible to include lighter dynamical quarks in the vacuum configurations. Once these vacuum configurations are obtained, the rest of calculation is essentially the same as in the quenched approximation.

Because gluons carry colour charge, QCD also predict the existence of rather weird hadrons called “glueballs”, which are simply bags of gluons. Many different glueballs can exist, each with different internal configurations of the component gluons. Lattice QCD can also help us to calculate the probability that one hadron will decay onto another through radioactive βdecay.

The most straightforward calculation that one can do with lattice QCD is to work out the masses of the many different hadrons that make up the “particle zoo”. This includes everyday particles, such as the proton. However, lattice QCD can be also used to work out the masses of hadrons containing more exotic quarks as “strange”, “charm”and“bottom”.

The spectrum of hadron masses obtained with lattice QCD can be used to determine the fundamental parameters of QCD that are hidden from direct measurement, such as the masses of the quarks and the value of the strong coupling constant, α_s (Figure 2.2), at some specific distance. Determinations of these parameters using lattice calculations are now among the most precise results. One surprise is that the up, down and strange quarks are lighter than was previously thought. This has implications for theorists working on the origin of the mass. A value for α_s is important as an input to those QCD calculations that can be done analytically-for example high-energy collisions when α_s is relatively small and few-gluon exchange is a good approximation. Because quarks are trapped inside hadrons, one cannot isolate their weak interactions from their QCD interactions. The experimental information from hadrons decays must therefore be compared with theoretical calculations from lattice

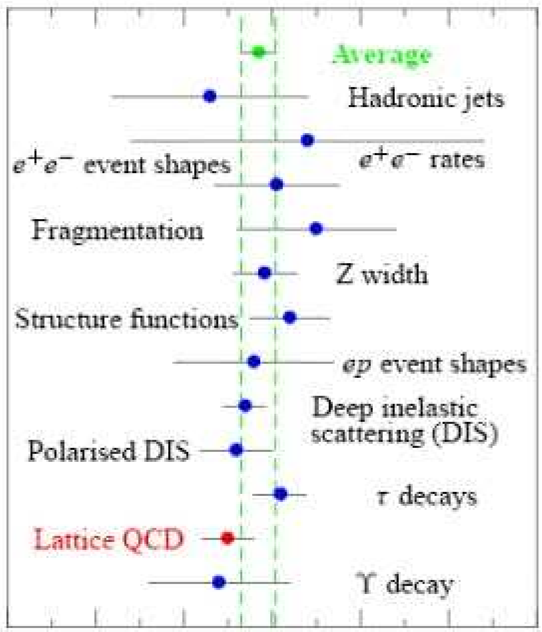

Figure 2.2: The strong coupling constant, as , gives an indication of the strength of the strong force between a quark and an antiquark. The figure shows a compilation of values for as produced by the International Particle Data Group. The results, which are based on a variety of theoretical techniques and experimental processes, were all obtained by comparing theory with experiment to give a value of as at a particular separation. But since as depends on the distance between the two particles, the values of as obtained have been converted to the value that they would have if the quark and antiquark were 10-18 m apart. This reference distance is relatively short and appropriate to high-energy collisions rather than the physics of hadrons, which are about 10-15 m in size. This is why as given here is quite small. The value obtained from lattice QCD using experimental hadron masses (red dot) is one of the most precise. The average over all the results is given by the green dot and the dashed lines gives it error.

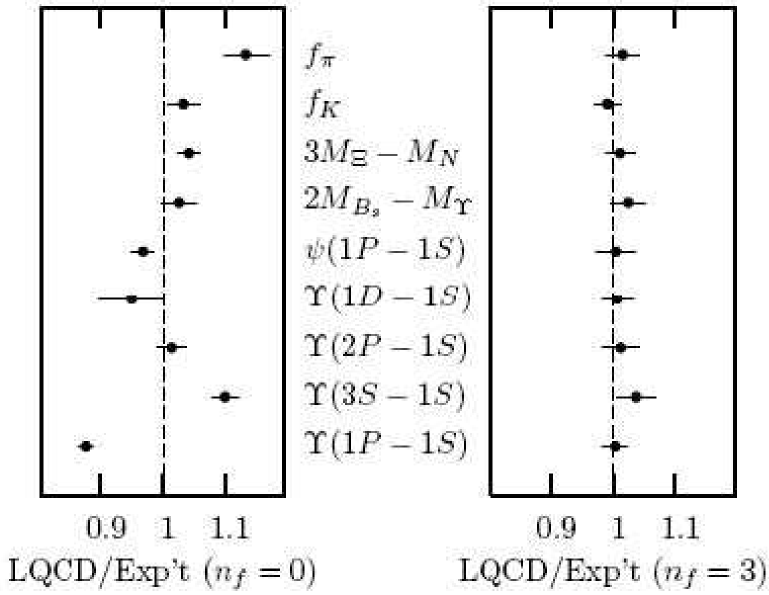

Figure 2.3: LQCD results divided by experimental results for nine different quantities, without and with vacuum polarization(left and right panels, respectively).

QCD. From the comparison one can hope to extract parameters that either give an internally consistent picture of symmetry breaking of the weak interactions within the Standard Model, or pointers to new physics. Until recently, however, the calculations were marred by a crude approximation. A big improvement came only in 2003, when uncertainties in mass predictions went from the 10% level to the 2% level (Figure 2.3) [11]. The mass of the proton, for example, could be calculated within a few percent of the actual value. Progress has come from a better treatment of the light quarks and from greater computer power.

2.3 Phase Transition

Progress in understanding QCD in the extremely non-perturbative domain near the critical temperature has relied on an essential contribution by Creutz [12], who showed that numerical implementations of Wilson's lattice formulation [13] could be used to study phase transition phenomena. This work, together with the continued exponential increases in computing power, stimulated the development of lattice

QCD, which in turn has led to detailed investigations of the thermodynamic properties of quarks and gluons [14]. Lattice QCD has been the best and most reliable tool to extract non-perturbative physics of the strongly interacting theory over a decade now.

Lattice QCD is used to simulate the behavior of quarks and gluons at high temperature in the kind of regime that existed in the early universe a few millionths of a second after the Big Bang. Results show that at temperature above 2×10^{12} Kelvin- a hundred thousand times as hot as the center of the sun.

Hadrons “melt”, and quarks and gluons are freed in a phase of matter called the quark-gluon plasma. Experimentalists are trying to recreate this phase by smashing large nuclei together at high energies in the hope of creating, for a fraction of a second, a hot plasma fireball. Subsequent cooling means that only hadrons are obtained from the collision, and it is difficult to demonstrate the existence of this unusual form of matter.

While simple dimensional arguments suffice to identify both the critical energy density $\epsilon_c \sim$1GeV/fm^3 and the associated critical temperature $T_c \sim 170$ MeV, these values also imply that the transition occurs in a regime where the coupling constant is of order unity, thereby making perturbative descriptions highly questionable. Lattice QCD predicts a phase transformation to a quark-gluon plasma at a temperature of approximately $T_c \sim 170$ MeV as shown in Figure (2.4). This transition temperature corresponds to an energy density $\epsilon_c \sim$1GeV/fm^3 , nearly an order of magnitude larger than that of normal nuclear matter. As noted above, this value is plausible based on dimensional grounds, since such densities correspond to the total overlap of several (light) hadrons within a typical hadron volume of 1-3 fm^3.

Because of asymptotic freedom, the high temperature and high baryon density phases of QCD are more simply and more appropriately described in terms of quarks and gluons as degrees of freedom, rather than hadrons. The chiral symmetry breaking

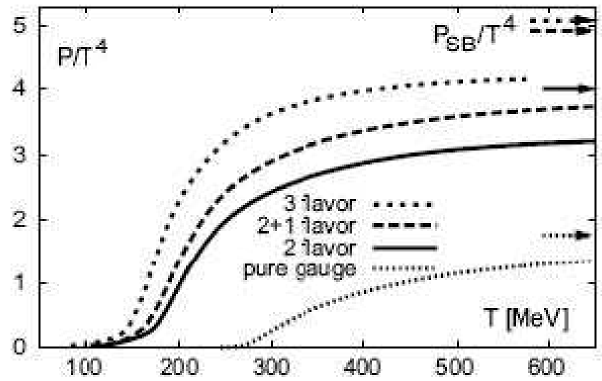

Figure 2.4: LQCD calculation results from Ref.[15] for the pressure divided by T^4 of strongly interacting matter as a function of temperature, for the case of gluons, 2- or 3-flavor light quarks and the one with 2-flavor light quarks plus 1-flavor heavy quark. Arrows show the ideal gas limit ϵ_{SB}

[1] condensate which characterizes the vacuum phase melts away due to greatly reduced or vanishing quark constituent masses.

Lattice calculations also indicate that this significant change in the behavior of the system occurs over a small range in temperature (∼20 MeV). In the limit of massless noninteracting particles, each bosonic degree of freedom contributes $\frac{\pi^2}{30}T^4$ to the energy density; each fermionic degree of freedom contributes $\frac{7}{8}$ this value. The corresponding "Stefan-Boltzmann" limits of the energy density ϵ_{SB} for the case of 2(3) active flavor quark-gluon plasma is then

$$\epsilon_{SB} = (2_f.2_s.2_q.3_c\frac{7}{8} + 2_s.8_c)\frac{\pi^2}{30}T^4 = 37\frac{\pi^2}{30}T^4 \tag{2.1}$$

$$\epsilon_{SB} = (3_f.2_s.2_q.3_c\frac{7}{8} + 2_s.8_c)\frac{\pi^2}{30}T^4 = 47.5\frac{\pi^2}{30}T^4 \tag{2.2}$$

after summing over the appropriate flavor, spin, quark/antiquark and color factors for quarks and spin times color factors for gluons. The large numerical coefficients (37 and 47.5) stand in stark contrast to the value of ∼3 expected for a hadron gas with temperature $T < T_c$, in which case the degrees of freedom are dominated by the

[1] See section 2.4

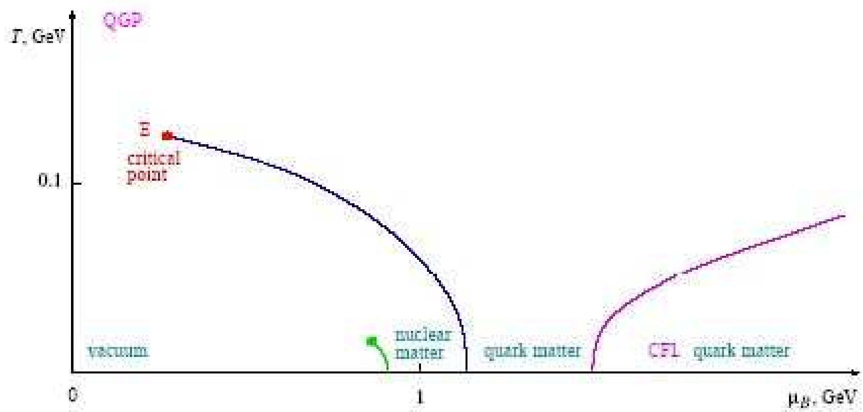

Figure 2.5: QCD phase diagram

three pion species π^-, π^0, π^+.

The exact order of this phase transition is not known. In a pure gauge theory containing only gluons the transition appears to be first order. However, inclusion of two light quarks (up and down) or three light quarks (adding the strange quark) can change the transition from first order to second order to a smooth crossover. These results are obtained at zero net baryon density; dramatic changes in the nature of the transition and in the medium itself are expected when the net baryon density becomes significant.

Figure (2.5) shows a sketch of the QCD phase diagram. By a phase diagram we shall mean the information about the location of the phase boundaries (phase transitions) as well as the physics of the phases that these transitions delineate. The phase transitions are the thermodynamic singularities of the system. The system under consideration is a region (in theory, infinite) occupied by strongly interacting matter, described by QCD, in thermal and chemical equilibrium, characterized by the given values of temperature T and baryo-chemical potential μ_B. In practice, it can be a region in the interior of a neutron star, or inside the hot and dense fireball created by a heavy ion collision.

On the phase diagram, the regime of small T and large μ_B is of relevance to neutron star physics. Because of low temperature, a very rich spectrum of possibilities of ordering can be envisaged. The line separating the Color-Flavor-Locked (CFL) phase, predicted in Ref. [16], from the higher temperature disordered phase (quark-gluon plasma, or QGP) is the most simplified representation of the possible phase structure in this region. This regime is also of particular theoretical interest because analytical controllable calculations are possible, due to asymptotic freedom of QCD. The reader is referred to the reviews[17-21] which cover the recent developments in the study of this domain of the phase diagram. The region of the phase diagram more readily probed by the heavy ion collision experiments is that of rather large T$\sim$100 MeV, commensurate with the inherent dynamical scale in QCD, and small to medium chemical potential $\mu_B \sim$0 - 600 MeV. Theorists expect that this region has an interesting feature -the end point of the first order phase transition line, the critical point marked E on Figure (2.5). The argument (which is not a proof) that the point E must exist is short, and is based on a small number of reasonable assumptions. The two basic facts that it relies on are as follows: (1) The temperature driven transition at zero μ_B is not a thermodynamic singularity. Rather, it is a rapid, but smooth, crossover from the regime describable as a gas of hadrons, to the one dominated by internal degrees of freedom of QCD quarks and gluons. This is the result of finite T lattice calculations. (2) The μ_B driven transition at zero T is a first order phase transition. This conclusion is less robust, since the first principle lattice calculations are not controllable in this regime (naive Euclidean formulation of the theory suffers from the notorious sign problem at any finite μ_B). Nevertheless a number of different model approaches indicate that the transition in this region is strongly first order. (3) The last step of the argument is a logical product of (1) and (2). Since the first order line originating at zero T cannot end at the vertical axis μ_B= 0 (by virtue of (1)), the line must end somewhere in the midst of the phase diagram. The end point of a first order line is a critical point of the second order.

This is by far the most common critical phenomenon in condensed matter physics.

Most liquids possess such a singularity, including water. The line which we know as the water boiling transition ends at pressure $p = 218$ atm and $T = 374^0$C. Along this line the two coexisting phases (water and vapor) become less and less distinct as one approaches the end point (the density of water decreases and of vapor increases), resulting in a single phase at this point and beyond. In QCD the two coexisting phases are hadron gas (lower T), and quark-gluon plasma (higher T). What distinguishes the two phases? As in the case of water and vapor, the distinction is only quantitative, and more obviously so as we approach the critical point. Rigorously, there is no good order parameter which could distinguish the two phases *qualitatively*. The chiral condensate,$< \overline{\psi}\psi >$, which comes closest to being an order parameter, is non-zero in both phases because of the finite bare quark mass. Deconfinement, although a useful concept to discuss the transition from hadron to quark-gluon plasma, strictly speaking, does not provide a good order parameter. Even in vacuum ($T = 0$) the confining potential cannot rise infinitely a quark-antiquark pair inserted into the color flux tube breaks it. The energy required to separate two test color charges from each other is finite if there are light quarks.

Then, for sufficiently large values of the baryon chemical potential μ this system exhibits a first order phase transition between hadronic matter and QGP, along with a tricritical point below which the transition becomes second order. However, non-zero values of the light quark masses dramatically alter this simple picture: The second order phase transition becomes a smooth crossover, and the tricritical point correspondingly becomes a critical point designating the end of the first order transition found at higher values of μ.

Recent calculations [22,23] indicate that the transition is a crossover for values of $\mu \lesssim 400$ MeV. Given that both theoretical arguments and experimental data suggest that nucleus-nucleus collisions at RHIC (at least near mid-rapidity) are characterized by low net baryon density, while noting that the predicted smooth nature of

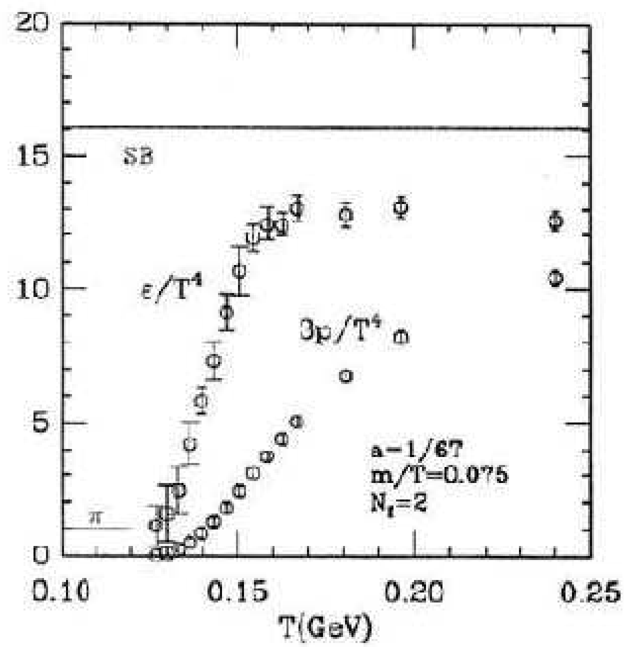

Figure 2.6: Energy density ϵ (upper curve) and pressure p(lower curve) obtained from a numerical evaluation of QCD "on the lattice" with two light flavors of quarks. ϵ and p are divided by T^4 to exhibit the sudden rise in the number of thermally excited degrees of freedom at the critical temperature $T_c \approx$150 MeV due to liberation of color and chiral symmetry restoration.

the transition in this region increases the experimental challenges of unambiguously establishing that such a transition has occurred.

While the lattice results plotted in Figure (2.4) show that the energy density reaches a significant fraction (~ 0.8) of the Stefan-Boltzmann values in the deconfined phase, the deviation from ϵ_{SB}, and the reason for the persistence of that deviation to the highest studied values of T/T_c, are of great interest. For instance, Greiner has noted [24] that "in order to allow for simple calculations the QGP is usually described as a free gas consisting of quarks and gluons. This is theoretically not well founded at T$\approx T_c$". In fact, analysis of the gluon propagator in a thermal system [25,26] has demonstrated that effective masses of order g(T)T are generated, suggesting that the relevant degrees of freedom are in fact massive near T$_c$. mg$\approx T_c$ could be generated by gluons.

Especially interesting is recent work which indicates that both heavy [27,28,29] and light [30] flavor states may remain bound above T$_c$, calling into question the naive interpretation of $\epsilon(T)$ as an indicator of the explicit appearance of quark and gluon degrees of freedom. This is supported by explicit calculations of the spectrum of bound states above T$_c$ [31] which predict a rich structure of states that belies a description as a weakly interacting parton gas.

On general principles, it is clear that the QGP near T$_c$ should not be regarded as an ideal gas of quarks and gluons. How high a temperature is needed not just to form a quark-gluon plasma, but to approach this "weakly" interacting plasma? A calculation of the pressure of hot matter within perturbative QCD [32] shows that temperatures approaching 1000 times of T$_c$ there is converging toward the Stefan-Boltzmann limit (asymptotically free partons). It is interesting that, unlike the case of single parton-parton scattering at zero temperature, the infrared problems of finite-temperature field theory prevent further analytic progress even for very small values of the coupling constant [32,33,34].

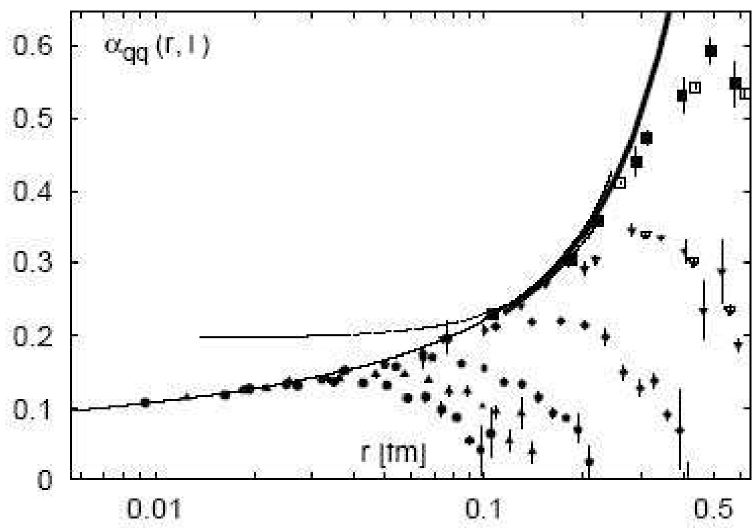

Figure 2.7: The running coupling in the qq-scheme determined on lattices of size $32^3 \times N_\tau$ with $N_\tau = 4$ (open symbols) and 8 (filled symbols) from derivatives the short distance part of the singlet free energy (T = 0: from the force) at different temperatures. The relation of different symbols to the values of the temperature (T/T_c)are from 1.05 to 12 .For the various lines see the reference.

Representative results for the temperature dependence of the energy density and pressure in the two flavor theory are shown in Figure (2.6) A notable feature of the numerical results is that while the energy density(divided by T^4) ascends rapidly to something close to its asymptotic value, the pressure appears much more sluggish. Thus the behaviour of the plasma, even in regard to this bulk property, differs significantly from a free gas of massless particles. It is a worthy challeng to compute the corrections to free behavior analytically in weak coupling. This is not entirely straightforward, due to the absence of magnetic screening in perturbation theory. For recent progress see [35].

Recent study of the running coupling at finite temperature, Figure (2.7), indicates that it is more appropriate to characterize the non-perturbative properties of the QCD plasma phase close to T_c in terms remnants of the confinement part of the QCD force rather than a strong Coulombic force.

2.4 Chiral Symmetry Restoration

Chiral symmetry relates to the helicity of quarks. Quarks that have their spin vectors aligned parallel or anti-parallel to their momentum vectors are said to be right or left handed, respectively. The helicity of particles is conserved exactly in an interaction with massless particles and so chiral symmetry is preserved. However, quarks in hadronic interactions have nonzero masses and so spontaneously break chiral symmetry. In other words, it is possible to transform to a frame of reference where the momentum and spin vectors are aligned opposite from that of a different frame. This means that chiral symmetry is broken since a quark can appear to be left or right handed, depending on the frame of reference.

At temperatures below the QCD phase transition to a QGP, α_s is greater than zero and so interactions between quarks effectively increase their masses to values greater than the bare masses. A quark's constituent mass is approximated from the hadron it makes up, as this mass includes the zero-point energy of the quark in the confining potential. As nucleons have masses of about 1 GeV, the constituent u and d quarks are assigned masses of approximately 300 MeV. Similarly, s quarks are assigned a mass of approximately 500 MeV. Chiral symmetry is broken in this situation.

At low energies, the QCD vacuum is characterized by nonvanishing expectation values of certain operators, usually called vacuum condensates, which encode the nonperturbative physical properties of the QCD vacuum. Most important for this discussion are the quark condensate $< \overline{\psi}\psi > \approx (235 MeV)^3$, and the gluon condensate $< \alpha_s G_{\mu\nu} G^{\mu\nu} > (500 MeV)^4$ [36]. The quark condensate describes the density of quark-antiquark pairs found in the QCD vacuum, which is the source of chiral symmetry breaking. The gluon condensate measures the density of gluon pairs in the QCD vacuum and is a manifestation of the breaking of scale invariance of QCD by quantum effects. It is not uncommon in nature that spontaneously broken symmetries are restored at high temperature through phase transitions. Well-known examples are ferromagnetism, superconductivity, and the transition from solid to liquid. More closely connected to our subject is nuclear matter at low temperatures, which has a dense liquid phase that transforms into a dilute gaseous phase at $T > 5MeV$. Evidence for this phase transition has recently been observed in nuclear collisions at intermediate energies [37].

At high temperatures where α_s tends to zero, the quarks obtain their bare, or current, masses. These current masses are still non-zero, implying chiral symmetry is not completely restored. However, a partial restoration of chiral symmetry is expected. In terms of relativistic heavy ion collisions, this conclusion leads to the possibility of an increase in the production of heavier quarks. Strange quarks, being the lightest of these heavier quarks, will be produced in great amounts compared to normal hadronic channels as the temperature of the system approaches the mass of the $s\overline{s}$ pair. As the temperature increases in QCD, the interactions among quanta occur at ever shorter distances, governed by weak coupling, whereas the long-range interactions become dynamically screened. This picture is supported by finite temperature perturbation theory, which shows that the effective coupling constant $\alpha_s(T)$ falls logarithmically with increasing temperature, and also by more general arguments [38].

Chiral symmetry is also expected to be restored at high baryon density even at zero temperature. Many model studies of this phenomenon have been performed, yielding critical densities $4\rho_0 < \rho_c < 10\rho_0$, where ρ_0 denotes the ground state density of nuclear matter. Because ab initio calculations based on lattice QCD are not yet feasible, the uncertainty of ρ_c remains large. One expects a smooth connection between the high-T and high-ρ phase transitions, giving rise to a continuous phase boundary $T_c(\rho)$. For $T < T_c(\rho)$, the effective description of strongly interacting matter at low momenta is in terms of hadronic degrees of freedom (baryons and mesons), whereas for $T > T_c(\rho)$ the effective degrees of freedom at low momenta carry the quantum numbers of quarks and gluons.

2.5 Ultra-Relativistic Heavy Ion Collisions

Ultra-relativistic heavy ion collisions reactions with center of mass energies for each nucleon-nucleon pair $\sqrt{s_{NN}} \geq$10GeV, provide the opportunity to study strongly interacting matter at high temperatures and densities in the laboratory and to reach energy densities which might be sufficient to create a quark-gluon plasma. However, a single indisputable signature for the creation of a quark-gluon plasma in such collisions is not known. This is partially due to the lack of an exact definition of the new phase. Nevertheless, a number of observables has been proposed which should show a behavior distinctly different from usual nuclear matter. The detection of QGP phase is additionally complicated by the fact that it has only a fleeting existence, which is followed by return to a phase of hot hadronic matter. It is an experimental challenge to find observable that reflect the hot and dense quark-gluon plasma phase, not entirely diluted by the later stages of the reaction, in the detected products of the nuclear collision.

2.5.1 Space-Time Evolution

In ultra-relativistic heavy ion collisions the de-Broglie wavelength of the individual nucleons is so small that the nuclei can be seen as independent accumulation of nucleons. This simplistic view implies that the Lorentz-contracted nuclei interact only in the region of geometrical overlap, determined by the impact parameter b as shown in Figure (2.8). The corresponding nucleons are called participants, while the nucleons outside the geometrical overlap, the spectators, are basically unaffected by the collision. The participants interact with each other in the reaction zone, leading to the formation of a hot and dense region, the fireball. There are two basic scenarios for the formation of the fireball depending on the nuclear stopping in the reaction. For large stopping, described in the Landau model, the complete kinetic energy of the nucleons is converted into thermal energy and a baryon-rich fireball is formed.

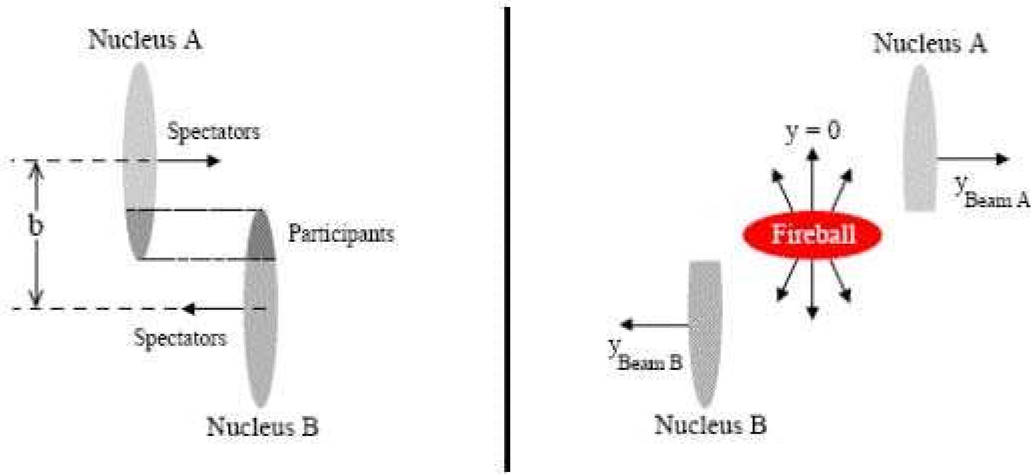

Figure 2.8: Schematic view of two colliding nuclei in the geometrical participant-spectator model. The distance between the centers of the two Lorentz contracted nuclei is the impact parameter b.

The characteristic rapidity distribution of produced particles in such a reaction has a maximum at mid-rapidity. In the Bjorken-McLerran scenario the stopping is limited and the nucleons penetrate each other, they exhibit transparency. This leads to a fireball with low baryo-chemical potential as the baryon number remains concentrated near the beam rapidity. The rapidity distribution in this case should be essentially flat in the rapidity region between the two beams.

The space-time evolution of two colliding nuclei is illustrated in Figure (2.9). The two nuclei approach each other with a velocity close to the speed of light. After the first initial interactions between the nucleons the reaction zone contains highly excited matter, far from thermal equilibrium. After thermalization of the system, provided that the temperature and lifetime is sufficient, a quark-gluon plasma is formed. Due to the rapid expansion into the surrounding vacuum the system cools and the quarks recombine into hadrons. The formation of the hot hadron gas possibly occurs via a mixed phase with domains of co-existing QGP. The final step of the reaction is the complete decoupling (freeze-out) of the hadrons after further expansion of the system.

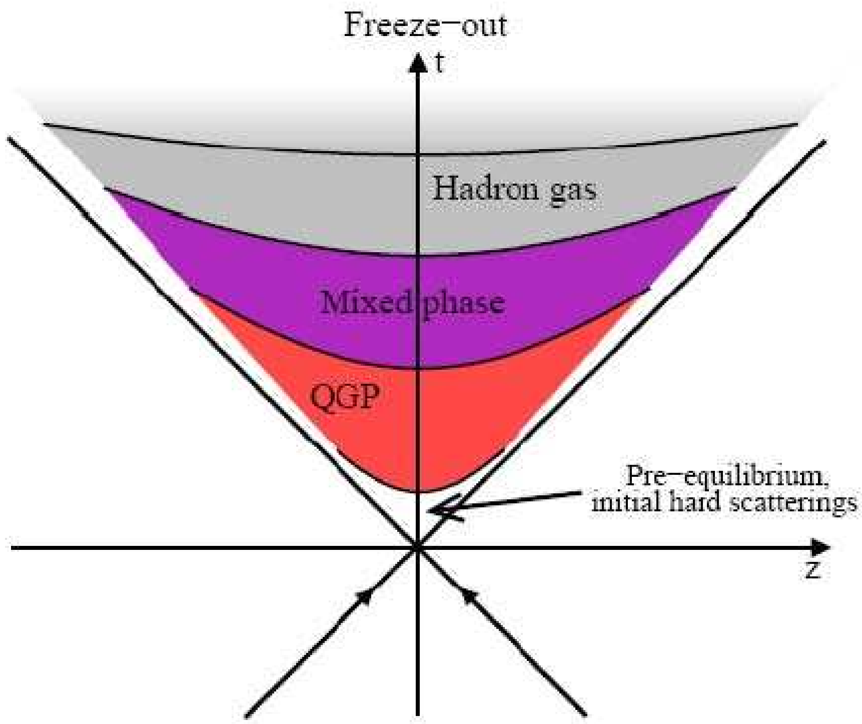

Figure 2.9: The schematic space-time picture of a nucleus-nucleus collision.

2.5.2 Model Descriptions

The models used to describe an ultra-relativistic heavy ion collision can be divided into two classes: microscopic models, which try to incorporate the individual interactions between all particles in a reaction, and macroscopic models, which try to describe the complete system in a hydrodynamical approach treating the fireball as ideal fluid, under presumption of local thermal equilibrium. Most microscopic models start with the description of the elementary process of a nucleon-nucleon collision and extend it to large nuclei by an incoherent superposition of the elementary reaction with additional effects of nuclear matter. One disadvantage of microscopic models is that they do not consider the phase transition to a quark-gluon plasma, only particular properties of the plasma phase can be incorporated as free parameters. For example, the HIJING model combines the model description of hard parton-parton processes, inspired by perturbative QCD, with a string model for soft processes and additional effects of cold and hot nuclear matter, such as shadowing and jet quenching discussed in section 3.1.

Hydrodynamical models describe the hadronic or partonic matter as an ideal fluid, with thermal equilibrium assumed. The conservation of energy-momentum and baryon number governs the space-time evolution of this fluid via the equation of state (EOS), where pressure, energy density, and chemical potential are related. The advantage of such macroscopic models is that the different scenarios with and without formation of a QGP can be tested with different equations of state and compared to experimental data. However, the results of hydrodynamical models depend strongly on the choice of the initial conditions.

Parton Cascades Model

QCD predicts that the energy density at midrapidity grows like $A^{2/3}$, where A is the nuclear mass [40,41], but at most logarithmically with the center-of-mass energy. To reach temperatures far above T_c, the initial kinetic energy of the nuclei must be rapidly thermalized on a time scale on the order of 1 fm/c. Early ideas about the mechanism of energy deposition were based either on the inside-outside cascade model of parton scattering [42] or on the breaking of color flux tubes [43,44]. More recently, detailed microscopic models have been constructed [45-47] that permit the study of the energy deposition process, in space-time as well as in momentum space, within the framework of perturbative QCD. These models are based on the concept that the colliding nuclei can be decomposed into their parton substructure. The perturbative interactions among these partons can then be followed until thermalization. One finds that partonic cascades account for at least half the expected energy deposition at RHIC and for an even larger fraction in the energy range of the LHC [48]. Parton cascade models predict a very rapid thermalization of the deposited energy. This is caused by a combination of radiative energy degradation and kinematic separation of partons with different rapidities. The transverse momentum distribution of initially scattered partons is already to a high degree exponential if radiative processes are taken into account. The subsequent expansion causes the local longitudinal momentum distribution of partons to coincide with the transverse distribution after a time approximately equal to the mean time between parton interactions. The models predict that thermalization occurs on a proper time scale of 0.3-0.5 fm/c at RHIC energies [48]. Due to the large cross sections and higher branching probabilities of gluons, the thermalized parton plasma is initially gluon rich and rather depleted of quarks [49]. Chemical equilibration of the parton plasma proceeds over a time of several fm/c in most scenarios [50,51], but may be faster if higher-order QCD processes are important [52]. Another interesting issue concerns the inhomogeneity of initial conditions. Partonic cascades can lead to a rather uneven energy deposition, because of cross-section fluctuations. Hot spots caused by strongly inelastic parton scatterings could lead to observable, nonstatistical fluctuations in the final hadron distribution.

Hydrodynamics Models

After (local) momentum equilibration, further evolution of the quark-gluon plasma to its final dissolution can be described in the framework of relativistic hydrodynamics. According to the results of parton cascade models, the initial conditions for this evolution in the central rapidity region are boost invariant to a large degree, as anticipated by Bjorken [53]. Assuming purely longitudinal expansion, the temperature then falls as $\tau^{-1/3}$, where τ is the local proper time. Cooling is substantially enhanced by the transverse expansion generated by the high internal pressure of the plasma when the initial temperature is significantly above T_c. Typical estimates of the plasma lifetime are 4 fm/c, after which a mixed quark-hadron phase is formed in a first-order phase transition [54]. Because of transverse expansion, however, even the mixed phase decays on a time scale of 10 fm/c. Where the pressure is minimal, the lifetime of the mixed phase could be longer if the plasma were formed at the critical temperature without initial collective flow [55,56]. A long-lived ($\gg$10 fm/c) mixed phase could be detected by its effect on two-particle correlations [57,58]. The hydrodynamic approach becomes invalid when the typical distance between particles exceeds the mean free path. This happens shortly after the quark-hadron phase transition, when the temperature falls below 120-130 MeV [59,60]. Because various hadrons have different mean free paths, the freezeout for baryon-rich matter is differential with K^+-mesons freezing out first, followed by nucleons, K^-, and finally pions.

2.5.3 Hydrodynamics of QGP

Assuming that nuclear matter behaves as a perfect fluid, its evolution is determined by the equations of relativistic hydrodynamics until the mean free path of the particles is of the order of the dimensions of the system. The complete dynamics of a hydrodynamical system can be described by the energy density field ϵ, the pressure field p, the temperature field T, and the 4-velocity field $u^\mu = dx^\mu/d\tau$, where x^μ is the 4-vector coordinates and τ is the proper time. The first three quantities above are related by the equation of state $\epsilon = \epsilon(p, T)$. When a fluid element is at rest, the energy momentum tensor describes the energy density and the pressure. For example, $T^{00} = \epsilon$, T^{11} = pressure in (2,3) direction. In a frame in which the fluid element is moving with a 4-velocity u^μ, the energy-momentum tensor is carrying out the transformation:

$$T^{\mu\nu} = (\epsilon + p)u^\mu u^\nu - g^{\mu\nu}p. \tag{2.3}$$

From energy and momentum conservation, and neglecting viscosity and thermal conductivity, we have

$$\frac{\partial T_{\mu\nu}}{\partial x_\mu} = 0. \tag{2.4}$$

The Equation 2.4 can be solved with certain simplifications assuming an equation of state (EOS). For example, if we consider only the longitudinal coordinate (beam direction in head-on heavy ion collisions) and the time coordinate, we can end up with (see Bjorken's hydrodynamic model [53])

$$\frac{\partial\epsilon}{\partial\tau} + \frac{(\epsilon + p)}{\tau} = 0. \tag{2.5}$$

In the case of an ideal gas of massless quarks and gluons, the energy density and the pressure are related by $p = \epsilon/3$, thus Equation 2.5 becomes

$$\frac{d\epsilon}{d\tau} = -\frac{4\epsilon}{3\tau}. \tag{2.6}$$

which has the solution

$$\frac{\epsilon(\tau)}{\epsilon(\tau_0)} = \frac{\epsilon(\tau)}{\epsilon_0} = (\frac{\tau_0}{\tau})^{4/3} \tag{2.7}$$

in which τ_0 and ϵ_0 are the proper time and energy density when the local equilibrium begins.

For the pressure we have

$$\frac{p(\tau)}{p(\tau_0)} = (\frac{\tau_0}{\tau})^{4/3} \tag{2.8}$$

For an ideal relativistic gas, the energy density and the pressure are proportional to T^4, where T now signifies temperature [61]. Then

$$\frac{T(\tau)}{T(\tau_0)} = (\frac{\tau_0}{\tau})^{1/3} \tag{2.9}$$

Other thermodynamic quantities such as entropy, S, can be obtained by [61]

$$dE = -pdV + TdS \tag{2.10}$$

thus the entropy density is

$$s \equiv \frac{dS}{dV} = \frac{\epsilon + p}{T}. \tag{2.11}$$

From Equations 2.7, 2.8 and 2.9, it follows that signifies temperature [51]. Then

$$\frac{s(\tau)}{s(\tau_0)} = (\frac{\tau_0}{\tau}) \tag{2.12}$$

which means $s(\tau)\tau$ is constant as a function of proper time. As the volume element dV is given by $dx_{\perp}^2 \tau dy$, the last argument implies that

$$\frac{dS}{dx_{\perp}^2 dy} = \quad constant \;\; as \;\; a \;\; function \;\; of \;\; proper \;\; time, \tag{2.13}$$

and it follows that

$$\frac{d}{d\tau}(\frac{dS}{dy}) = 0. \tag{2.14}$$

For a relativistic system in which local equilibrium is reached at τ_0 with initial energy density ϵ_0 and initial temperature $T(\tau_0) \propto \epsilon_0^{1/4}$, the energy density and the pressure decrease with proper time as $\tau^{-4/3}$, while the temperature drops as $\tau^{-1/3}$. The hydrodynamic motion of the fluid is characterized by a constant entropy per unit of rapidity.

2.5.4 **Signature of a Quark-Gluon Plasma Phase**

Experimental investigations of the quark-gluon plasma require the identification of appropriate experimental tools for observing its formation and for studying its properties. The experimental search for the QGP is complicated by the facts that it has only a fleeting existence 5-10 fm/c in duration, small size which is a few fermi in diameter at most, and that any signal from the QGP phase has to compete with the background from the hadronic gas following the hadronization of the plasma. In spite of this, a wealth of ideas has been proposed to how the identification and investigation of the short-lived quark-gluon plasma phase could be accomplished. It is beyond the scope of this work to present a comprehensive survey of quark-gluon plasma signatures. We therefore concentrate on the most promising ones. More details can be found elsewhere [62-65]. The convincing evidence for the creation of a quark-gluon plasma needs to take into account a variety of signatures. They can be divided further into: change of thermodynamical and hydrodynamical properties characterizing a phase transition, signals from a deconfined phase, and observables influenced by the restoration of chiral symmetry. Most of the single signatures mentioned below can be described in different models without a phase transition. But a simultaneous description of all signatures without assuming a phase transition is not available. It shall also be noted that for the interpretation of many of the promising signatures discussed below. The comparison to more elementary p+p reactions and to p+A collisions, the control experiment for medium effects in cold nuclear matter, at the same energy is crucial.

Kinematical and hydrodynamical probes

Thermodynamical properties such as the temperature, the pressure, the energy density, and the entropy of a system as well as their mutual dependence are directly influenced by a phase transition. For example, a change in the number of degrees of freedom, when going from a quark-gluon plasma back to a hadron gas, can have a direct impact on the dependence of the energy density on the temperature. Also, If a rapid change in the effective number of degrees of freedom occurs, one expects an S-shaped curve, whose essential characteristic feature is the saturation of $< p_T >$ during the persistence of a mixed phase, continuing into a second rise when the structural change from color singlet to colored constituents has been completed. However, most thermodynamical properties show a distinct behavior only in the case of a first order phase transition. The average transverse momentum of particles $< p_T >$ in the QGP phase is in principle related to the temperature of the system. However, hadrons do interact after the chemical freeze-out from the QGP in the hadron gas so that the direct connection to the temperature is distorted. A better probe may be provided by thermally produced dileptons and photons, which do not suffer from strong final state interactions, as discussed below. The entropy and the energy density of the system is usually related to the measured particle multiplicity dN/dy and the transverse energy dE_T/dy at mid-rapidity. The hydrodynamical properties and the equation of state of the system can be studied through collective flow effects arising from pressure gradients in the asymmetric reaction zone[2], while the system size and the life time of the reaction zone can be inferred from interferometry of identical particles, known as Hanbury-Brown-Twiss or HBT interferometry. Because interferometric size determinations will be possible on an event-by-event basis for collisions of heavy nuclei at the RHIC, and LHC, the correlation of global parameters like $< p_T >$ and dN/dy with the fireball geometry can be performed on individual collision events.

Electromagnetic Probes

The main advantage of electromagnetic probes, i.e. direct photons and lepton pairs, is that they are not influenced by the strongly interacting medium. They are created basically throughout all stages of the reaction, in initial hard scattering as well as by thermal production in the QGP and the hadron gas, and can provide a direct measure of the evolution of the fireball. Unfortunately, these probes have rather small yields and must compete with relatively large backgrounds from hadronic processes, especially electromagnetic hadron decays.

Dileptons are produced in a QGP by quark-antiquark annihilation $q\overline{q} \rightarrow l^+l^-$,which is governed by the thermal distribution of the quarks and antiquarks in the plasma. This production channel has to be disentangled from the Drell-Yann production,

[2]See chapter 3 for more detail about the concept of collective flow in the heavy-ion collision systems

which is the annihilation process of a valance quark with a sea quark, already present in nucleus-nucleus collisions, and the production in a hadron gas via the process $\pi^+\pi^- \rightarrow l^+l^-$. With an improved understanding of the collision dynamics and the hadronic backgrounds [66, 67], it has since become clear [68] that lepton pairs from the quark-gluon plasma can probably only be identified for invariant masses above 1-1.5 GeV. At the high-mass end, the yield of Drell-Yan pairs from first nucleon-nucleon collisions exceeds the thermal dilepton yield, for a more detailed description see e.g. [69].

Besides the analysis of the continuum mass spectrum, the study of dilpetons allows the measurement of the ρ, ω and Φ mesons via their dilepton decay branch. Measurement of the mesons also provides an interesting probe for the QGP phase, as their mass might be influenced by chiral symmetry restoration and especially the $\Phi(s\bar{s})$ is sensitive to stangeness enhancement(see below). Another strategy for using the leptonic ρ-meson decay as a probe of the hadronic phase of the fireball is based on the idea that the ρ peak is expected to grow strongly relative to the ω-peak in the lepton pair mass spectrum, if the fireball lives substantially longer than 2 fm/c. Because of the short average lifetime of the ρ-meson, the ρ/ω ratio can, therefore, serve as a fast "clock" for the fireball lifetime [70].

Signatures from the Deconfined Phase

The creation of the deconfined QGP phase should enhance the production of strange quarks because for the creation of a $s\bar{s}$ pair only the current quark mass of approximately 300MeV/c^2 is needed. By contrast, in the associated production of strange particles in a hadron gas the larger constituent quark mass of the strange quark becomes important and a higher energy is needed. For example, for the simplest reaction $pp \rightarrow \lambda K^+ p$ the threshold is 700MeV/c^2. This should be directly visible in the enhanced production rate of strange particles compared to proton-proton collisions.

In addition, the relative abundances of the various strange particle species (mesons, strange and multistrange baryons, and their antiparticles) allow the determination of relative strangeness equilibrium, saturation in the overall strangeness content γ_s , and strangeness neutrality in a thermochemical approach [71]. These ratios can be calculated assuming either a hadron gas scenario or a quark-gluon plasma scenario, and a comparison can be made of the values extracted from the models in the two scenarios in conjunction with other thermodynamic variables of the system, such as the temperature T , the baryo-chemical potential μ_B, and the entropy [72, 73]. Because strange hadrons interact strongly, their final-state interactions must be modeled in considerable detail before firm predictions about strange-hadron yields are possible.

Another promising signature for deconfinement is the J/ψ suppression. The J/ψ, a bound $c\bar{c}$ state, is primarily produced in hard parton-parton scatterings due to its large mass($m_{J/\psi}$=3097MeV/c^2). In a QGP the attractive potential between a $c\bar{c}$ is screened by the large density of free color charges in the medium. At hadronization time the disassociated charm quarks couple with a larger probability to the abundant lighter quarks than recombining to a J/ψ. Owing to the finite size of J/ψ, the formation of a $c\bar{c}$ bound state requires a time on the order of 1 fm/c (74-76). The J/ψ may still survive, if it escapes from the region of high density and temperature before the $c\bar{c}$ pair has been spatially separated by more than the size of the bound state (77). This will happen either if the quark-gluon plasma cools very fast, or if the J/ψ has sufficiently high transverse momentum (78-81).

The deconfined phase of a QGP, with its large color charge density, should also induce an energy loss of quarks and gluons produced in initial hard scatterings. This is discussed separately in section 3.1.

Indications of Chiral Symmetry Restoration

As discussed in Section 2.4 the deconfined phase of the QGP can prelude the restoration of chiral symmetry. A possible signal for the chiral symmetry restoration is the creation of the so-called disoriented chiral condensate (DCC). This term describes a coherent excitation of the pion field corresponding to a local misalignment of the chiral order parameter $< \overline{\psi}\psi >$. When the transition occurs very rapidly from a phase with restored chiral symmetry back into the chirally broken ground state, the chiral condensate may populate an energetically less favorable state than usual nuclear matter, the disoriented chiral condensate. One possible signature for the creation of a DCC is random fluctuations between the production amplitudes of the pion isospin triplet (π^+, π^0, π^-), different from the usual value of $N_{\pi X}/(N_{\pi^+} + N_{\pi^0} + N_{\pi^-}) \approx 1/3$. An additional signal for the chiral symmetry restoration is a modification of the mass and decay width of the light vector ρ, ω, and Φ mesons , which are usually detected via their e^+e^- decay channel. It is predicted that the widths and positions of the ρ, ω, and Φ peaks in the lepton-pair spectrum can sense the medium induced changes of the hadronic mass spectrum, especially to the possible drop of vector meson masses preceding the chiral symmetry restoration transition [82-91].

Hard QCD Probes

The color structure of QCD matter can be probed by its effects on the propagation of a fast parton [92,93]. The mechanisms are similar to those responsible for the electromagnetic energy loss of a fast charged particle in matter: Energy may be lost either by excitation of the penetrated medium or by radiation. The connection between energy loss of a quark and the color-dielectric polarizability of the medium can be established in a way analogous to the theory of electromagnetic energy loss [94-96]. Although radiation is an efficient energy-loss mechanism for relativistic particles, it is strongly suppressed in a dense medium, because the charged particle often rescatters before the radiation has been emitted [97]. The QCD analog of this effect has been analyzed comprehensively [98,99]. By adding the two contributions, the stopping power of a fully established quark-gluon plasma is predicted to be higher than that of hadronic matter. It was suggested first by Bjorken[100] that partons traversing bulk partonic matter undergo signifcant energy loss, with observable consequences on the parton's subsequent fragmentation into hadrons. A quark or gluon jet propagating through a dense medium will not only lose energy, it will also be deflected. This effect destroys the coplanarity of the two jets from a hard parton-parton scattering with the incident beam axis [101-103]. The angular deflection of the jets also results in an azimuthal asymmetry. The presence of a quark-gluon plasma is also predicted to enhance the emission of jet pairs with small azimuthal opening angles [104]. The jet and jet quenching are discussed in more detail in chapter 3.

2.5.5 Does RHIC Achieve The Required Energy Density?

The condition for creating a quark-gluon plasma is producing a system with high energy density. Both elementary estimates [105] and from extensive numerical studies in lattice QCD [106,107], indicate that the required density is on the order of 1 GeV/fm^3. Two important ingredients energy density and thermalization are basic in establishing the creation of a QGP at RHIC.

In this short section we explore what can be deduced about the energy densities achieved in RHIC A+A collisions from measurements of the global transverse energy and multiplicity. In chapter 3 these estimates will be compared to densities inferred from hydrodynamics-based models and from jet quenching evidence (chapter 3).

Under simplifying assumptions (longitudinal boost-invariance, free- streaming expansion in which the matter does no work) first suggested by Bjorken [108] (Figure 2.10), one can extract a crude estimate of the initial spatial energy density of the bulk

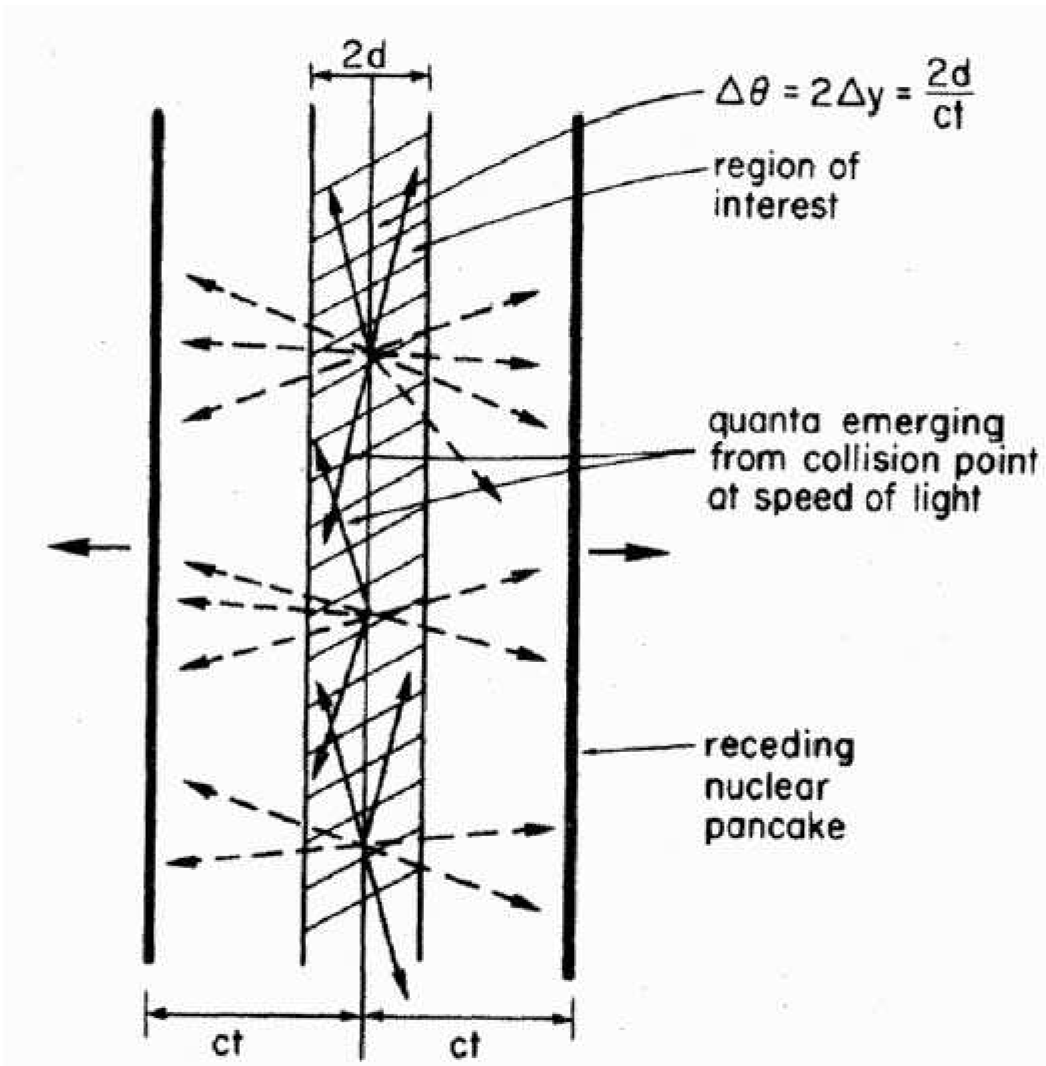

Figure 2.10: Figure from Bjorken[108] illustrating the geometry of initially produced particles at a time t after the overlap of the incoming nuclei in some frame. The picture is valid in any frame in which the incoming nuclei have very high energies and so are highly Lorentz contracted.

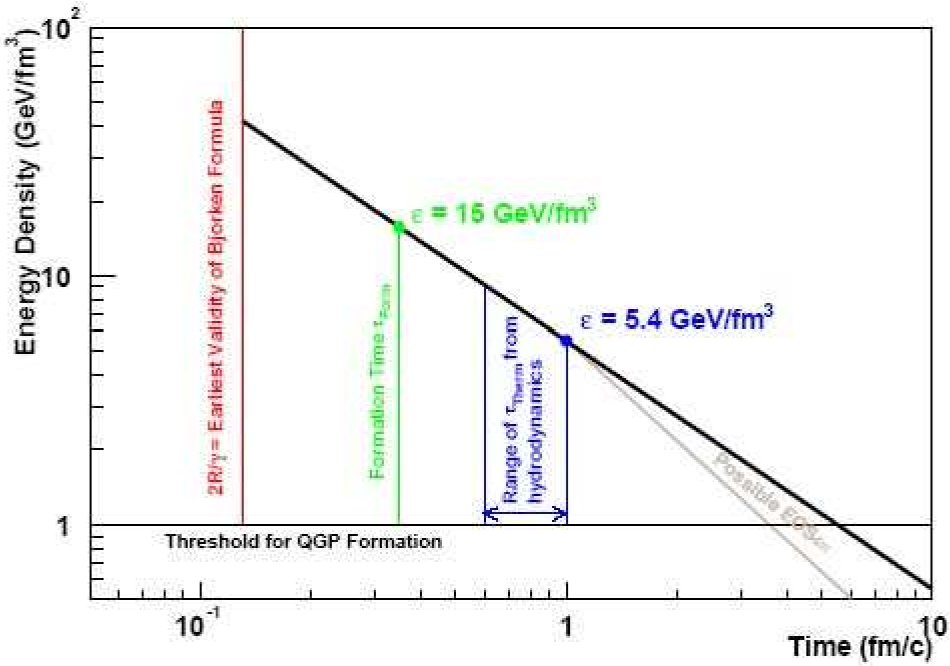

Figure 2.11: Schematic drawing of the time and energy density scales derived through the Bjorken picture.

matter at the start of its transverse expansion:

$$\epsilon_{Bj} = \frac{dE_T}{dy}\frac{1}{\tau_0 \pi R^2} \tag{2.15}$$

where τ_0 is the formation time and R the initial radius of the expanding system.

With reasonable guesses for these parameter values (τ_0 ≈0.35fm/c, R ≈ 1.2A$^{1/3}$ fm), the PHENIX $dE_T/d\eta$ measurements suggest an initial energy density ∼15 GeV/fm^3 for central Au+Au collisions at RHIC, and ∼15 GeV/fm^3 for the thermalized energy density ($\tau_{Therm} \approx$ 1fm/c) (Figure 2.11). Both of these values are well above the critical energy density ∼1 GeV/fm^3 expected from LQCD for the transition to the QGP phase. More results which support the high energy density of the formed medium at RHIC in addition to the justification for the thermalization time using the elliptic flow signal are discussed in chapter 3.

Chapter 3

Highlights of Super-Dense Matter at RHIC

"Interpretation of these complex collisions poses a major problem.
What are the clean experimental signatures and how can one deduce what is going on?
Is there information which unambiguously teaches us about the state of
the matter formed during and immediately after the
collision?"

J. D. Bjorken (1982)

This chapter is aimed to discuss the physics of the super-dense matter. The characteristics of the relativistic heavy ion collisions and comparisons to the nucleon-nucleon reactions are presented. The effect of the cold nuclear matter is discussed. We review the physics of the High p_t, direct photons, and elliptic flow with the theoretical predictions compared to the relevant experimental results.

3.1 Jets and Jet Quenching

Particles with large transverse momenta are predominantly produced in *hard* parton-parton collisions as discussed below. In $p + p$ collisions the scattered partons fragment directly in the QCD vacuum and are visible as jets of particles along the direction of motion of the primordial parton. In heavy ion collisions the hard scattering processes occur in the initial stage of the reaction, as shown in Figure (2.9). The scattered partons now have to traverse the hot and dense medium before they fragment into hadrons. Thus they can probe matter produced in the later stages of the reaction. A largely energy loss in a colored medium was predicted in [109,110]. It should distort the back-to-back correlation of particle jets and lead to a suppression of particle production at high p_T compared to $p+p$ reactions, the jet quenching.

3.1.1 Nucleon-Nucleon Reactions

For the interpretation of results from heavy ion collisions a basic understanding of the more elementary nucleon-nucleon reactions is crucial. Above a center of mass energy of $\sqrt{s}\approx$10GeV the total cross section for $p+p$ collisions is roughly constant at σ_{tot}=40mb [111]. The cross section at these energies is dominated by inelastic reactions, where the colliding particles loose energy, with the deposited energy resulting in the production of new particles. The mean number of produced particles (mostly pions) increases only slowly with the center of mass energy and is dominated by particles with small transverse momenta.

Soft Processes

The total number of produced particles is dominated by the particles with low transverse momenta ($p_T <$2GeV/c), as the mean transverse momentum e.g. for pions produced in $p+p$ collisions is $< p_T >\approx$0.3 GeV/c. As seen in Figure (3.1) the spectral shape in this region is well described by an exponential $e^{-\alpha p_T}$, with $\alpha\approx$6/(GeV/c). The so-called soft processes dominate the particle production at such low momenta, where the momentum transfer Q^2 is on the order of the QCD scales. Soft processes cannot be treated in perturbative QCD; the quarks inside the hadrons cannot be considered as asymptotically free. Instead the description of the bulk of particles produced e.g. in $p+p$ collisions by soft processes is described by phenomenological models, such as the different types of string models [112]. In such models an excited $q\overline{q}$ pair is described as an elastic band, the string, with tension k already introduced

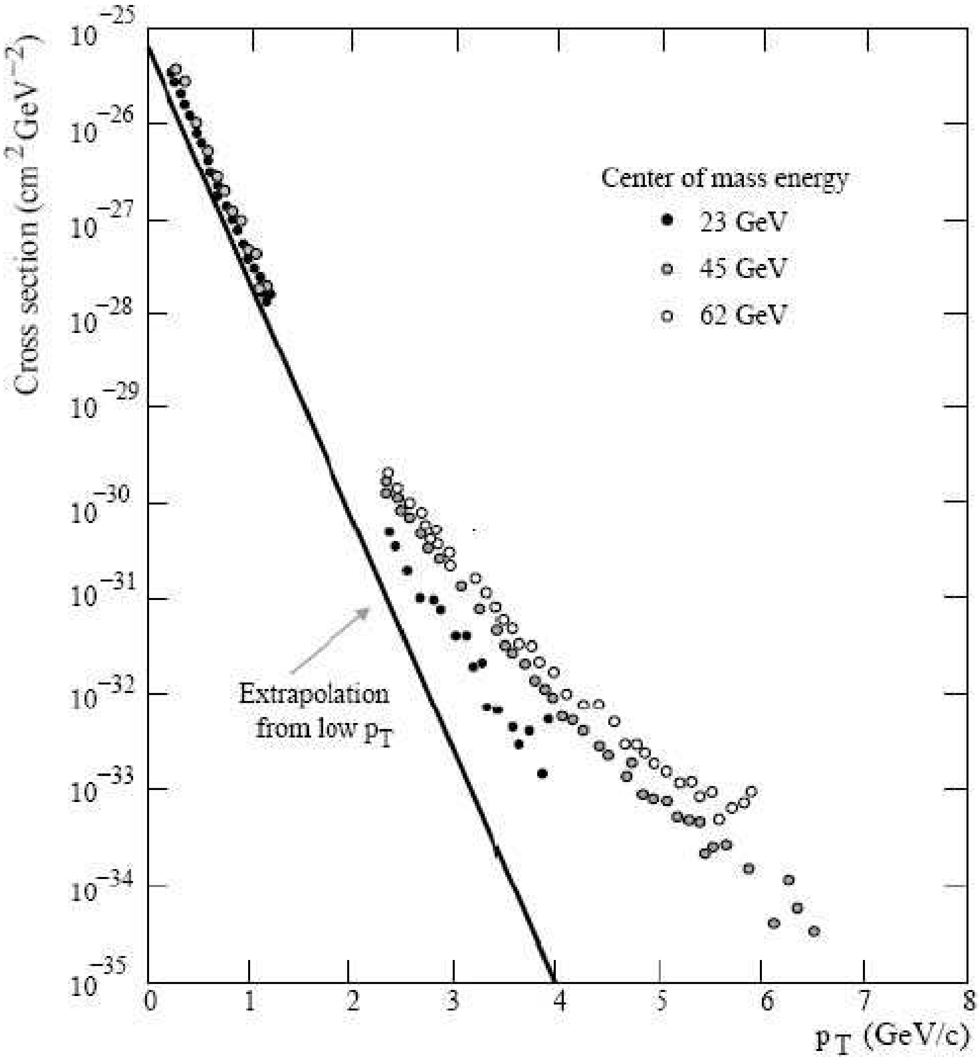

Figure 3.1: Particle production at different energies measured in $p+p$ collisions at the CERN ISR [113].

in Equation (1.1). If the quarks are separated the potential energy stored in the string increases until it breaks and fragments into smaller strings. Hence new $q\overline{q}$ pairs are produced which can fragment further, until their potential energy is too small and the strings can be considered as real hadrons.

String models can be tested against the process $e^+e^- \rightarrow q\overline{q}$ at high energies. This allows to study string fragmentation without the uncertainties introduced from a hadronic initial state. Nucleon-nucleon collisions are then described by fragmentation of strings, i.e. nucleons excited in the inelastic collisions. The mechanisms for excitation are different in the various modesl but involve usually momentum or color exchange between the quarks of the colliding nucleons.

Hard processes

The extrapolation of the exponential shape from low transverse momenta of the production fails for large p_T, as seen in Figure 3.1, and a power law better describes the distribution. In this kinematical region the particle production is governed by *hard* processes with large Q^2 and the quarks can be treated to be asymptotically free. The inelastic hard scattering of the nucleons can be described in the framework of perturbative QCD in terms of the scattering of the pointlike partons (quarks or gluons) inside the nucleons. This leads to the characteristic jets of particles produced along the direction of the scattered partons. The characteristic time and length scale of the parton-parton interaction is short compared to the soft interactions between the bound partons in the initial state and to those of the fragmentation process of the scattered partons in the final state. Therefore the hard inelastic cross section for the production of a given hadron h can be factorized [114]:

$$E\frac{d^3\sigma^{hard}_{NN\to h}}{dp^3} = \sum_{a,b,c} f_a(x,Q^2) \otimes f_b(x,Q^2) \otimes \frac{d^3\sigma^{hard}_{ab\to c}}{dp^3} \otimes D_{c/h}(z,Q^2). \tag{3.1}$$

The different factors are: • The non-perturbative distribution functions $f_{q,g}(x,Q^2)$ of partons in the colliding nucleons, which depend only on the momentum transfer and the parton fractional momentum x. they can be determined e.g. in deep-inelastic electron-nucleus reactions. • The short-distance, perturbatively computable parton-parton scattering $ab \to c$, • The universal but non-perturbative fragmentation function $D_{c/h}(z,Q^2)$ of the scattered parton c into the hadron h carrying a fraction $z = p^h/p^c$ of the parton momentum. It also needs to be determined experimentally. If a photon is produced in the hard scattering the fragmentation function reduces to

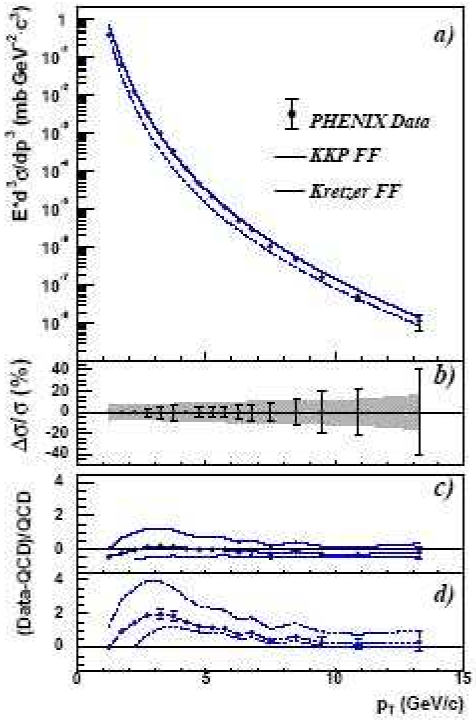

Figure 3.2: PHENIX π^0 invariant cross section at mid-rapidity from $p+p$ collisions at $\sqrt{s}$ = 200 GeV, together with NLO pQCD predictions from Vogelsang [151,152]. a) The invariant differential cross section for inclusive π^0 production (points) and the results from NLO pQCD calculations with equal renormalization and factorization scales of p_T using the "Kniehl-Kramer-Potter" (solid line) and "Kretzer" (dashed line) sets of fragmentation functions. b) The relative statistical (points) and point-to-point systematic (band) errors. c,d) The relative difference between the data and the theory using KKP (c) and Kretzer (d) fragmentation functions with scales of p_T /2 (lower curve), p_T , and $2p_T$ (upper curve). In all figures, the normalization error of 9.6% is not shown [115].

a $\delta(1-z)$ function. It should be noted that the calculation of total cross sections via Equation (3.1) suffers from uncertainties due to the arbitrary choice of factorization, renormalization, and fragmentation scales. The different scales are usually chosen identical and on the order of the transverse momentum.

The PHENIX measurement of the invariant cross section for π^0 production in $p+p$ collisions at $\sqrt{s}$=200GeV [115] agrees with NLO pQCD predictions over the range $2.0 \leqslant p_T \leqslant 15$GeV/c (Figure 3.2).

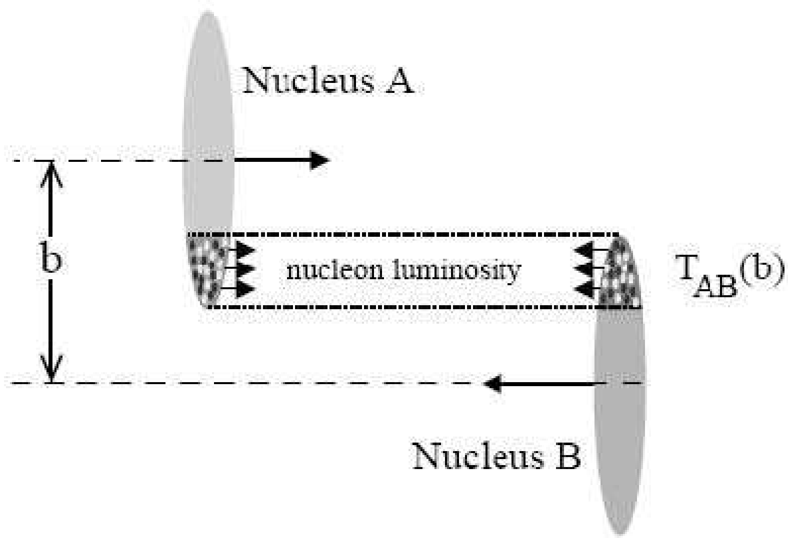

Figure 3.3: The concept of binary scaling: a heavy ion collision as incoherent superposition of nucleon-nucleon collisions.

3.1.2 The Nuclear Modification Factor

For the large momentum transfer in initial hard scatterings the partons can be considered as asymptotically free, as for $p + p$ collisions, and the cross section in a collision of two nuclei $A+B$ should be connected to the $p+p$ cross section by a scaling factor, the number of inelastic, binary nucleon-nucleon collisions N_{coll} in the reaction. For $A + B$ collisions at a fixed impact parameter N_{coll} is proportional to the nuclear thickness function $T_{AB}(b)$, which is analogous to an integrated "nucleon luminosity" for the two overlapping nuclei, as illustrated in Fugure (3.3). Since each centrality selection by experiment samples a different distribution of impact parameters the cross section for a high-p_T particle h produced in an $A + B$ collision with centrality f is linearly connected to the $p + p$ cross section via the average nuclear thickness $< T_{AB} >_f$:

$$\frac{1}{N_{AB}^{evt}} \frac{d^2 N_{AB}^h}{dp_T dy} |_f = < T_{AB} >_f \frac{d^2 \sigma_{pp}^h}{dp_T dy}, \tag{3.2}$$

with:

$$< T_{AB} >_f = \frac{\int_f T_{AB}(b) d^2 b}{\int_f (1 - e^{-\sigma_{NN} T_{AB}(b)}) d^2 b} = \frac{< N_{coll} >_f}{\sigma_{NN}} \tag{3.3}$$

Where $< N_{coll} >_f$ is the average number of inelastic, binary nucleon-nucleon collisions with an inelastic cross section. σ_{NN}The average nuclear thickness function and $< N_{coll} >$ for a given centrality can be calculated via a Glauber Monte Carlo calculation taking into account the experimental centrality selection.

As a factorization of the cross section given in Equation (3.1) implies, the scaling with the number of binary collisions described by Equation (3.2) can be modified when the initial parton distribution is changed in the nuclear environment or the fragmentation process of the hard-scattered partons is modified, e.g. when the partons lose energy prior to fragmentation. Such medium effects are usually studied by means of the *nuclear modification factor* R_{AB}:

$$R_{AB} = \frac{dN^h_{AB}}{< T_{AB} >_f \, d\sigma^h_{NN}} = \frac{dN^h_{AB}}{< N_{coll} >_f \, dN^h_{NN}} \tag{3.4}$$

Which is expected to be unity above a certain p_T, where hard scattering is the dominant source of particle production, and in the absence of any medium effects.

Sometimes, the central to peripheral ratio, R_{CP} , is used as an alternative to R_{AB}. The central to peripheral ratio is defined as:

$$R_{CP} = \frac{dN^{Central} / < N^{Central}_{coll} >}{dN^{Peripheral} / < N^{Peripheral}_{coll} >} \tag{3.5}$$

where $dN^{Central}$ and $dN^{Peripheral}$ are the differential yield per event of the studied process in a central and peripheral collision, respectively. If the yield of the process scales with the number of binary collisions, $R_{CP} = 1$.

3.1.3 **Effects of Cold Nuclear Matter**

In order to identify parton energy loss or jet quenching, which should lead to R_{AB} <1, it is crucial to know all other medium effects leading to a modification of the particle production compared to nucleon-nucleon reactions. Possible medium effects

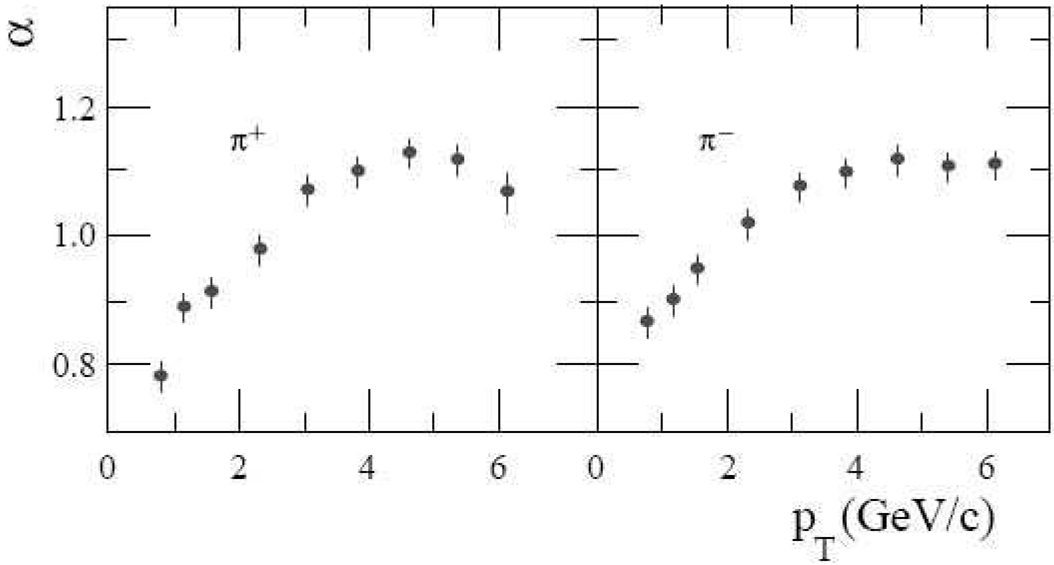

Figure 3.4: Dependence of the exponent α defined in Equation(3.) on the transverse momentum, the nuclear enhancement for charged pion production as reported in [116].

are particle absorption or energy loss already for the passage through cold nuclear matter, enhanced particle production by multiple soft scattering, or a modification of the parton distribution function in the initial state.

Cronin Effect

One experimental observation, when comparing elementary $p+p$ collisions to $p+A$ reactions, is that the cross section does not simply scale with the number of target nucleons A in a $p+A$ collision. This was first shown by Cronin et al. in 1974 [116] with a proton beam on beryllium, titanium, and tungsten targets. They found that the cross section for a given p_T scales like:

$$E\frac{d^3\sigma}{dp^3}(p_T, A) = E\frac{d^3\sigma}{dp^3}(p_T, 1)A^{\alpha(p_T)} \tag{3.6}$$

With α >1 for transverse momenta larger than approximately 2 GeV/c as shown in Figure (3.4). Hence there was observed an enhancement of particle production compared to the expectation from $p+p$ reactions. This effect is usually referred to as *Cronin effect* and is attributed to multiple soft scattering of the incoming nucleons, leading to an additional broadening of their transverse momentum.

Nuclear Shadowing

For the modification of particle production going from protons to heavy ions not only final state effects such as the Cronin effect can be responsible. *Initial state* effects, such as a modification of the nuclear wave function in nuclei, can also have an effect on particle production.

A highly energetic hadron has contributions to its wavefunction from gluons, quarks, and antiquarks each with a probability to carry some fraction of the momentum of the hadron, up to its full momentum. A convienet variable to describe the contribution of a parton to the total hadron momentum is the fractional momentum x, already introduced above. Results on the nuclear structure fuction $F2^{lN}(x, Q^2)$ in various deep-inelastic lepton-nucleon scattering experiments [117,118] can then be used to derive the indivdual parton distribution functions for quarks and antiquarks. Any change in the nuclear structure function implies also a change in the underlying parton distributions, hence a changed number of scattering centers, which has a direct impact on the particle production. For the comaprion of nuclear structure function the deep-inelastic off deuterium is often used as the refernce, as it represents an isospin-averaged nuclear structure function. A collection of data for different nuclei is shown in Figure (3.5) where the nuclear effects are clearly seen: For x <0.2 one observes a reduction of $R^A_{F_2} = F^A_2/F^d_2$, the so-called *nuclear shadowing*. A small enchancement is seen between 0.1< x <0.2, sometimes referred to as *anti-shadowing*. The dip for 0.2< x <0.8 has been first reported by the EMC collaboration [119] and is usually called the *EMC effect*, while the rise for larger x can be associated with Fermi motion of the nucleons inside the nucleus [120]. Similar effects are also expected

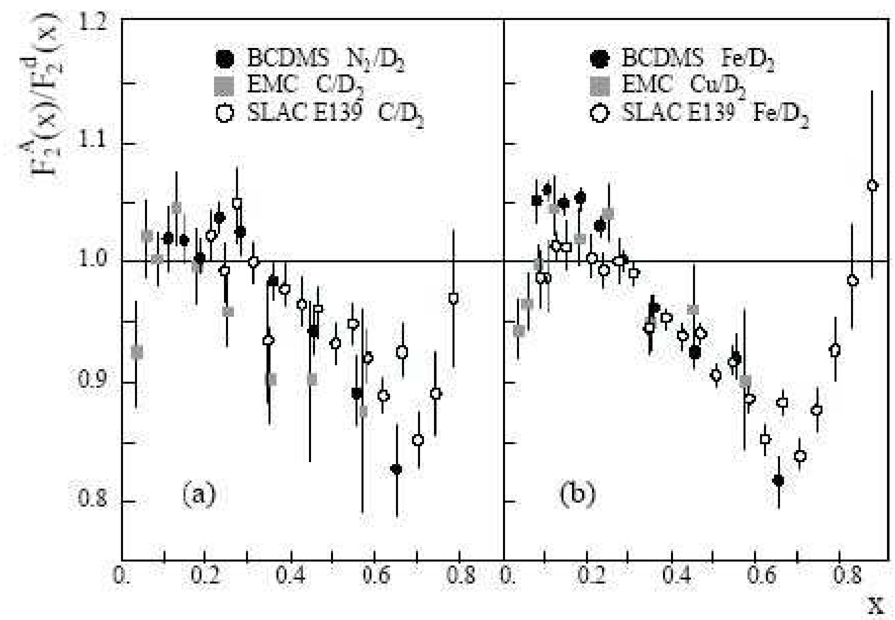

Figure 3.5: The ratio of structure functions F_2^A/F_2^d for nuclear targets A compared to deuterium d, measured in deep-inelastic electron(SLAC-139) and muon(BCDMS,EMC)scattering:(a)medium-weight targets,(b)heavier-weight targets[117]

for the gluon distributions, which are not directly accessible with leptonic probes. The relevant x-region of the scattered parton can be estimated by the transvers momentum of the *leading hadron*, which is the hadron carrying the largest momentum fraction of the original scattered parton:

$$x \approx \frac{2p_T}{\sqrt{s_{NN}}} \tag{3.7}$$

So that for RHIC energies and for transverse momenta up to 10GeV/c the shadowing region x <0.1 is the most relevant. Early predictions for jet quenching at RHIC energies already considered this effect which can reduce the nuclear modification factor by approximately 30%, though with a large uncertainty due to the poorly known gluon contribution [121].

The Color Glass Condensate

In addition to the nuclear shadowing effects discussed above, saturation effects may influence the parton density in a nucleus. The gluon density for different momentum transfers inferred by the ZEUS experiment at HERA from deep-inelastic scattering via a QCD fit [122] is shown in Figure 3.6. It is seen that for a given x the gluon density rises with the resolution, the momentum transfer of the exchanged virtual photon Q^2, and that for low x the gluon density rises rapidly without leveling off. This experimental observation has been accompanied by theoretical calculations that predicted a rise of the gluon density which would lead to a violation of the *Froissart* unitarity bound for the total cross section [1]. This is known as the *small-x problem.*

The model of the *color glass condensate* (CGC) provides a solution for this problem which also has implications for particle production in heavy ion collisions. The basic idea of the color glass condensate is that at sufficiently high gluon densities, when the separation between the gluons becomes small, not only the coupling α_s becomes weak, but the gluons can also start to fuse (gg$\rightarrow$ g), which basically limits the gluon density at small x. As discussed e.g. in [124] these effects become important starting at the saturation scale Q_s which depends on the size of the nucleus, basically the "gluon thickness" or the number of gluons as seen by a hadronic probe when traversing the nucleus A, which is proportional to $A^{1/3}$. Q_s depends also on the rapidity region since the probed x region decreases with $x \sim e^{-y}$. In the case that the saturation scale is reached in RHIC collisions at large transverse momenta the depletion of the gluon density implies a reduction of the nuclear modification factor already in d+Au collisions.

[1] On the basis of very general arguments invoking unitarity Froissart has shown that the total cross section for strong interactions grows at most as fast as ln^2 as $s \rightarrow \infty$ [123]

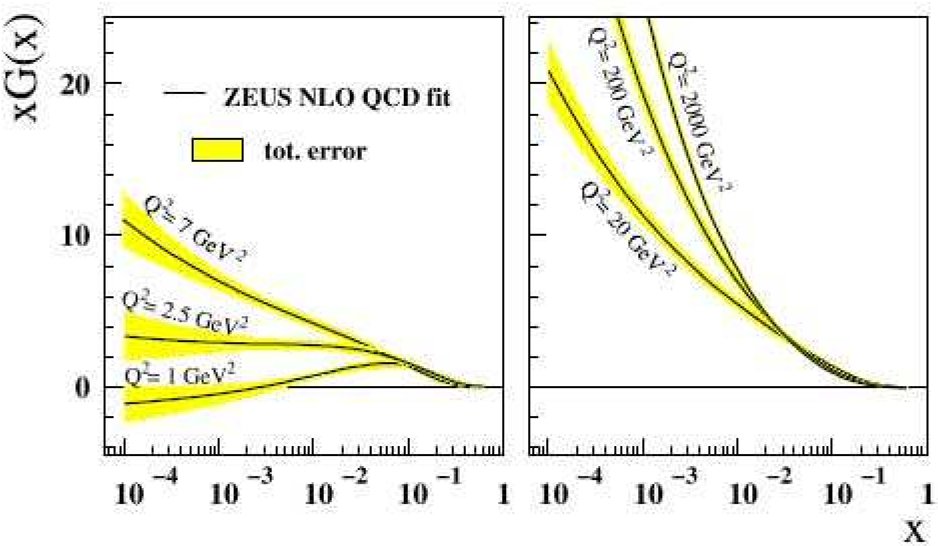

Figure 3.6: The gluon density xG(x) determined by a NLO QCD fit to the ZEUS data from deep-inelastic scattering [122]

3.1.4 Parton Energy Loss

When a parton traverses a colored medium it loses energy predominantly by radiating soft gluons, similar to electromagnetic Bremsstrahlung of an electron passing through matter [125]. The theoretical treatment of the energy loss is complicated by the fact that one has to consider destructive interference effects of the emitted gluons if the formation time of the gluon $\tau \approx \hbar/E_g$ is large compared to its mean free path λ/c in the medium [126]. This effect was first studied for the passage of highly energetic electrons or photons through matter and is known as the Landau-Pomeranchuk-Migdal (LPM) effect [127].

This quantum interference can produce an energy loss $\Delta E/\Delta x$ that grows faster than linearly with the path length L of the parton in the medium [128]:

$$\frac{\Delta E}{\Delta x} \sim \frac{L}{\Lambda} \ln \frac{L}{\Lambda} \tag{3.8}$$

However, this growth of the energy loss is only valid for a static medium. In a heavy ion collision the rapid decrease of energy density and color charge density in the expanding fireball has to be taken into account.

The most commonly used description of the parton energy loss is the GLV formalism [129], which is the perturbative treatment of the energy loss by an expansion in the *opacity* L/Λ. In this formalism the fractional energy loss varies for large jet energies E as lnE/E. However, the numerical calculation of the fractional energy loss at RHIC energies produces a nearly constant $\Delta E/\Delta x$ below $E = 20\text{GeV}$ [130].

The energy loss can also be implemented in an effective way in the factorized cross section, given by Equation (3.1), via a changed fragmentation process. This is done by shifting the fractional parton energy prior to hadronization:

$$z = p_h/p_c \quad \rightarrow \quad Z^* = z/(1-\epsilon), \;\; with \;\; \epsilon \in [0,1]. \tag{3.9}$$

The shift can be directly related to the parton energy loss as discussed in [131,132].This procedure facilitates the calculation of particle production in the energy loss scenario,employing well known techniques.

The expansion of the system in a heavy ion collision leads to a rapid decrease of the color charge density. This is usually taken into account by considering a longitudinally expanding fireball, any transverse expansion is neglected. The color charge density ρ then decreases as a function of proper time τ [132]:

$$\rho(\tau) = \frac{\rho_0 \tau_0}{\tau} \tag{3.10}$$

where τ_0 is the formation time of the partons from which the fireball is composed and ρ_0 is their initial number density.

3.1.5 Binary Scaling in ℓ + A, p + A, and Low-Energy A + A

In deeply inelastic lepton scattering, where hard scattering was discovered [133,134,135], the cross section for μ-A collisions is indeed proportional to $A^{1.00}$ (Figure 3.7). This

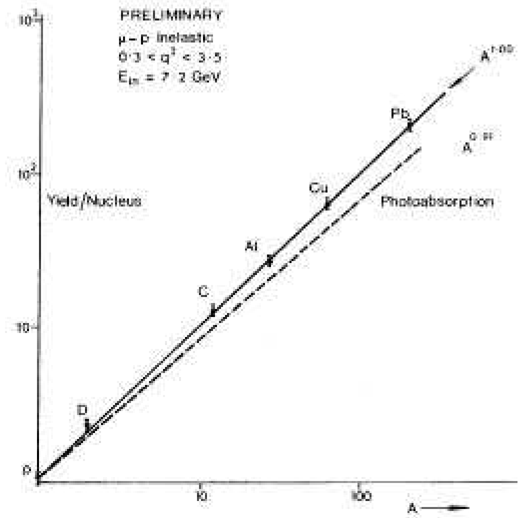

Figure 3.7: μ-A cross section vs. A [136]

indicates that the structure function of a nucleus of mass A is simply A times the structure function of a nucleon (with only minor deviations, $\leq 10\%$ for $0.02 \leq x \leq 0.50$ [137]), which means that the nucleus acts like an incoherent superposition of nucleons for hard scattering of leptons.

The situation is rather different in $p+A$ collisions: the cross section at a given p_T also scales as a power law, $A^{\alpha(p_T)}$ but the power $\alpha(p_T)$ is greater than 1. This is due to the Cronin Effect. At low $p_T < 1$ GeV/c, the cross-section is no longer point like, so the scattering is shadowed ($\alpha A^{2/3}$), thus $R_A < 1$. At larger $p_T > 2$ GeV/c, as the hard-scattering, power-law p_T spectrum begins to dominate, the multiple scattering smears the spectrum to larger p_T leading to an enhancement relative to binary-scaling which dissipates with increasing p_T as the influence of the multiple scattering diminishes.

Previous measurements of high-p_T particle production in $A + A$ collisions at $\sqrt{s_{NN}} \leq 31$ GeV (Figure 3.8) and in p+A (or d+A) collisions (Figure 3.9) including measurements at RHIC [138] at mid-rapidity all show binary scaling or a Cronin effect. This establishes that the initial condition for hard scattering at RHIC at mid-rapidity is an incoherent superposition of nucleon structure functions, including gluons, where multiple scattering before the hard collision smears the p_T spectrum of

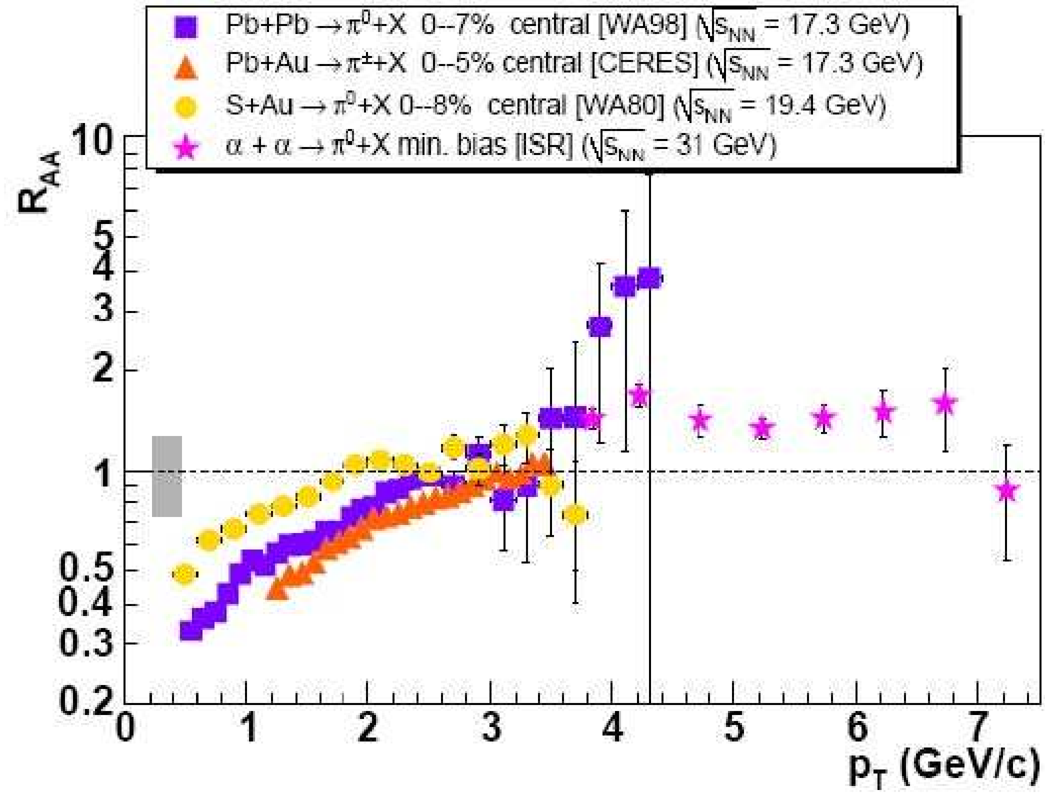

Figure 3.8: Nuclear modification factors for π^0 production at the CERN-ISR in minimum- bias $\alpha + \alpha$ reactions at $\sqrt{sNN} = 31$ GeV [139] and for pion production at the CERN-SPS in central $Pb + Pb$ [140], $Pb + Au$ [141], and $S + Au$ [142] reactions at $\sqrt{s_{NN}} \approx$ 20 GeV. The R_{AA} from SPS are obtained using the $p + p$ parametrization proposed in ref. [143]. The shaded band around $R_{AA} = 1$ represents the overall fractional uncertainty of the SPS data (including in quadrature the 25% uncertainty of the $p + p$ reference and the 10% error of the Glauber calculation of Ncoll). There is an additional overall uncertainty of ±15% for the $CERES$ data not shown in the plot [141].

scattered particles to be somewhat above the simple point like binary (N_{coll}) scaling. An alternative view of the initial state of a nucleus at RHIC is provided by the color glass condensate (CGC). A Cronin effect in d+A collisions, as shown in Figure (3.9), can be reproduced in the CGC with a suitable choice of initial state parameters, which must also reproduce quantitatively the observed binary scaling of the direct photon production in Au+Au collisions (Figure 3.20). However, as of this writing, no detailed quantitative description of the CGC initial state which satisfies these three conditions has been published.

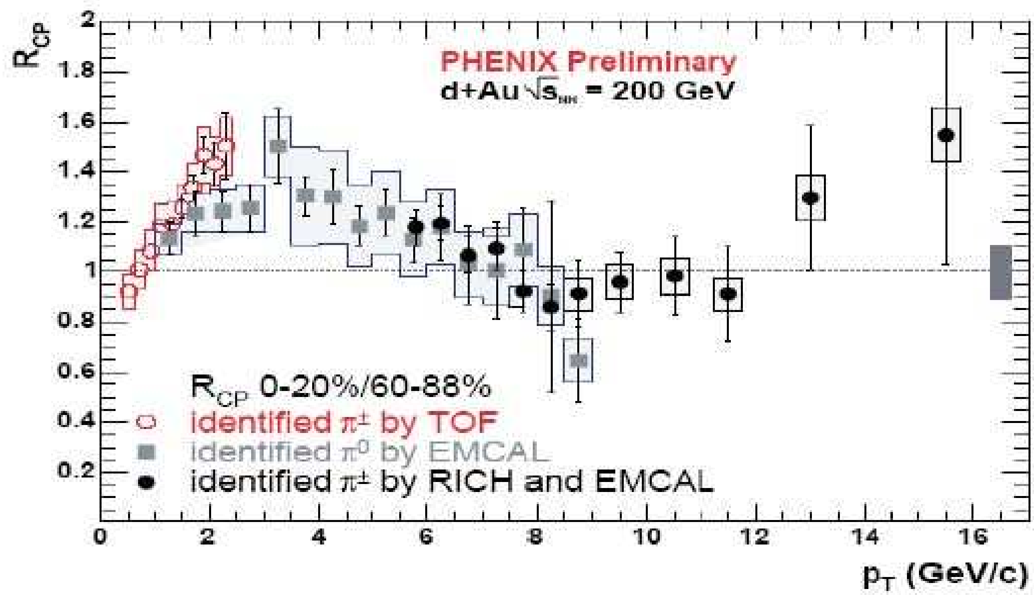

Figure 3.9: Cronin effect in R_{CP} , the ratio of point-like scaled central to peripheral collisions for pions in $d + Au$ at $\sqrt{s_{NN}} = 200$ GeV[144]. Data points for low p_T are $\pi^{\pm}$ identified by Time of Flight (TOF). Data at medium p_T are for π^0 identified by reconstruction in the Electromagnetic Calorimeter (EMCAL). Highest p_T data are for $\pi^{\pm}$ identified by a count in the Ring Imaging Cerenkov Counter (RICH) and a deposited energy/momentum and shower shape in the EMCAL inconsistent with those of a photon or electron. The shaded band on the right represents the overall fractional systematic uncertainty due to N_{coll}.

3.1.6 High p_T Suppression of Hadrons at RHIC

There are several results to date from RHIC exhibiting large and striking effects of the traversed matter on hard probes in central collisions. Figure (3.10) shows the most significant high p_T measurements made at RHIC thus far. The figure incorporate measurements of $\sqrt{s_{NN}}$=200 GeV $p+p$, $d+Au$ and centrality-selected $Au+Au$ collisions at RHIC, with the simpler $p+p$ and $d+Au$ systems providing benchmarks for phenomena seen in the more complex $Au+Au$ collisions. Figure 3.10 shows $R_{AB}(p_T)$, the ratio of inclusive charged hadron yields in $A+B$ (either $Au+Au$ or $d+Au$) collisions to $p+p$, corrected for trivial geometric effects via scaling by $< N_{bin} >$, the calculated mean number of binary nucleon-nucleon collisions contributing to each $A+B$ centrality bin. The large p_T hadrons in central $Au+Au$ collisions are suppressed by a factor $\approx$5 relative to naive (binary scaling) expectations. Conventional nuclear effects, such as nuclear shadowing of the parton distribution functions and initial state multiple scattering, cannot account for the suppression. Further more, the suppression is not seen in $d+Au$ but is unique to $Au+Au$ collisions, proving experimentally that it results not from nuclear effects in the initial state (such as gluon saturation), but rather from the final state interaction (FSI) of hard scattered partons or their fragmentation products in the dense medium generated in Au+Au collisions [145-148].

Figure (3.11) shows seminal STAR measurements of correlations between high p_T hadrons. The left panel shows the azimuthal distribution of hadrons with p_T >2 GeV/c relative to a trigger hadron with p_{Ttrig} >4 GeV/c. A hadron pair drawn from a single jet will generate an enhanced correlation at $\Delta\phi$=0, as observed for $p+p$, $d+Au$ and $Au+Au$, with similar correlation strengths, widths and (not shown) charge-sign ordering (the correlation is stronger for oppositely charged hadron pairs [149]). A hadron pair drawn from back-to-back dijets will generate an enhanced correlation at $\Delta\phi=\pi$, as observed for $p+p$ and for $d+Au$ with somewhat broader width than

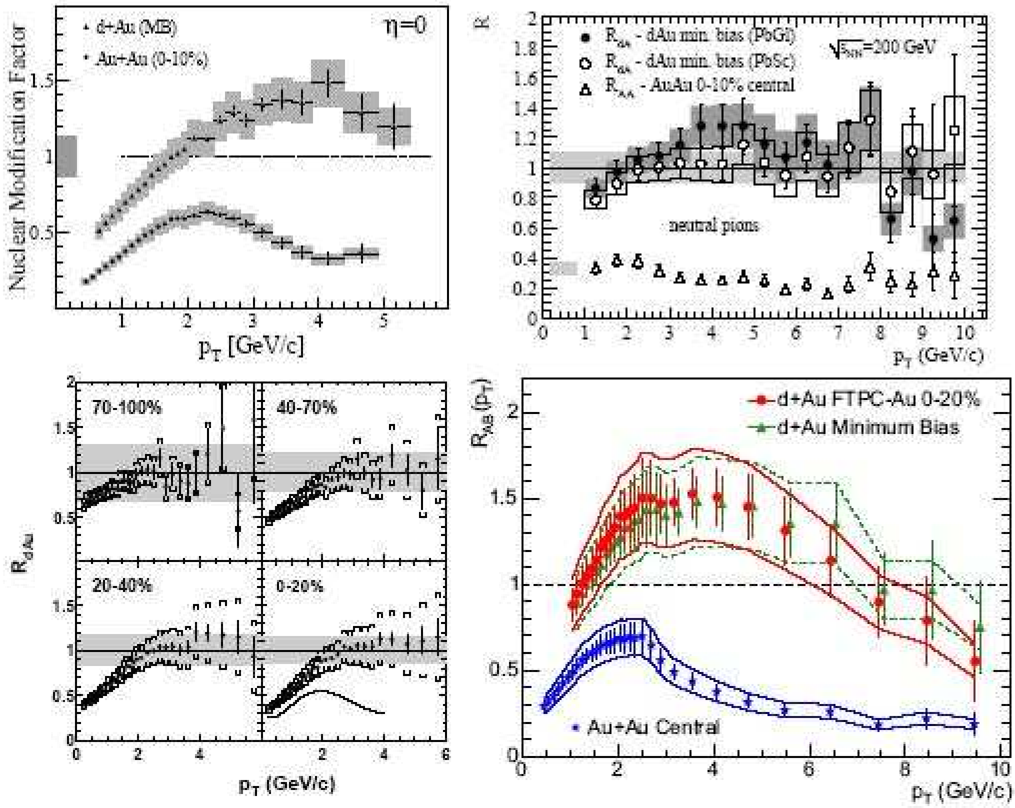

Figure 3.10: Binary-scaled ratio $R_{AB}(p_T)$ of charged hadron and π^0 inclusive yields from 200 GeV $Au+Au$ and $d+Au$ relative to that from $p+p$ collisions, from BRAHMS [145] (upper left), PHENIX [146] (upper right), PHOBOS [147] (lower left) and STAR [148] (lower right). The PHOBOS data points in the lower left frame are for $d+Au$, while the solid curve represents PHOBOS central (0-6%) $Au+Au$ data. The shaded horizontal bands around unity represent the systematic uncertainties in the binary scaling corrections.

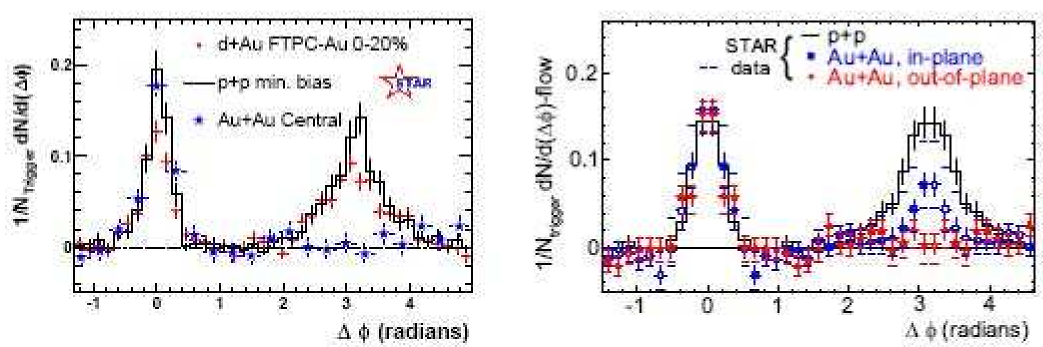

Figure 3.11: Dihadron azimuthal correlations at high p_T . Left panel shows correlations for $p+p$, central $d+Au$ and central $Au+Au$ collisions (background subtracted) from STAR [148,149]. Right panel shows the background-subtracted high pT dihadron correlation for different orientations of the trigger hadron relative to the $Au+Au$ reaction plane [150].

the near-side correlation peak. However, the back-to-back dihadron correlation is strikingly, and uniquely, absent in central $Au + Au$ collisions, while for peripheral $Au + Au$ collisions the correlation appears quite similar to that seen in $p + p$ and $d + Au$. If the correlation is indeed the result of jet fragmentation, the suppression is again due to the FSI of hard-scattered partons or their fragmentation products in the dense medium generated in $Au + Au$ collisions [148]. In this environment, the hard hadrons we do see (and hence, the near-side correlation peak) would arise preferentially from partons scattered outward from the surface region of the collision zone, while the away-side partons must burrow through significant lengths of dense matter.

3.2 Direct Photons

Similar to the analysis of virtual photons via dileptons, the examination of direct photons provides a tool to study the different stages of a heavy ion collision, especially the formation of a quark-gluon plasma, without being influenced by the strong interaction and hadronization processes. *Direct* photons are all photons not originating from hadronic decays, e.g. $\pi^0, \eta \to \gamma\gamma$. They are usually further classified into *prompt* photons produced in early hard scatterings, and *thermal* photons emitted from a thermally equilibrated phase.

Prompt and thermal photons cannot be separated experimentally, but it is expected that at intermediate transverse momenta p_T = 1-3GeV/c the thermal signal is the largest contribution to the total direct photon yield, while prompt photons dominate at large transverse momenta. As the interpretation of the direct photon results relies on the understanding of the different sources of photons during all stages of a heavy ion collision, a short theoretical survey is given in the following. For more details see e.g [151-154].

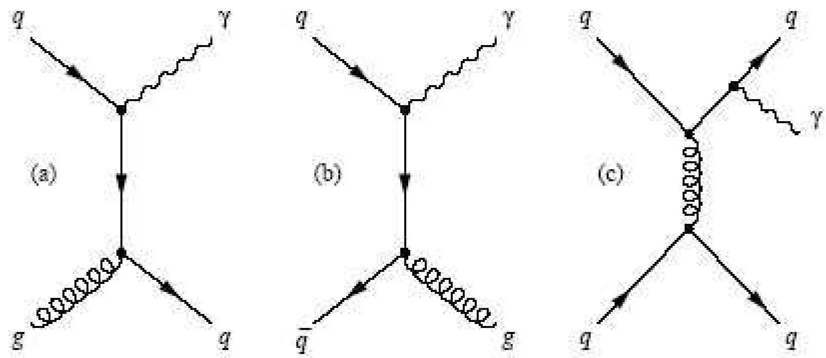

Figure 3.12: Feynman graphs of the main production processes for direct photons in initial hard scatterings as well as in a thermalized quark-gluon plasma phase: (a) quark-gluon Compton scattering of order $\alpha_s\alpha$, (b) quark-antiquark annihilation of order $\alpha_s\alpha$, (c) Bremsstrahlung of order $\alpha_s^2\alpha$

3.2.1 **Thermal Photons From a QGP**

A QGP emits photons, as does every thermal source, but while e.g. in stars the photons themselves are thermalized, the mean free path of photons in the QGP phase is large and so the photons are not likely to interact, although the quarks and gluons should be thermalized. In leading order (LO) perturbation theory real photons are produced via quark-antiquark annihilation ($q\overline{q} \rightarrow g\gamma$) and by quark-gluon Compton scattering ($qg \rightarrow q\gamma$). The corresponding Feynman graphs are shown in Figure 3.12 together with an example of a higher order Bremsstrahlung process, in which a quark radiates a photon. For the calculation of the corresponding emission rates the transition matrix elements for the two LO contributions can be determined analogous to the equivalent QED processes $e^+e^- \rightarrow \gamma\gamma$ and $e\gamma \rightarrow e\gamma$. Together with the introduction of the Mandelstam variables s, u and t this leads to the differential cross section for the two processes [151]:[2]

$$\frac{d\sigma}{dt}(q\overline{q} \rightarrow g\gamma) = (\frac{e_q}{e})^2 \frac{8\pi\alpha_s\alpha}{s(s-4m_q^2)}\{(\frac{m_q^2}{t-m_q^2}+\frac{m_q^2}{u-m_q^2})^2+(\frac{m_q^2}{t-m_q^2}+\frac{m_q^2}{u-m_q^2})-\frac{1}{4}(\frac{t-m_q^2}{u-m_q^2}+\frac{u-m_q^2}{t-m_q^2})\} \tag{3.11}$$

[2]The Mandelstam for the process $1,2 \rightarrow 3,4$ are determined by the corresponding four momenta $P_{1\ldots4}$:$s = (P_1+P_2)^2, t = (P_1-P_3)^2$,and $u = (P_1-P_4)^2 = (P_2-P_3)^2$. We will refer to such processes also as $2 \rightarrow 2$ processes in the following

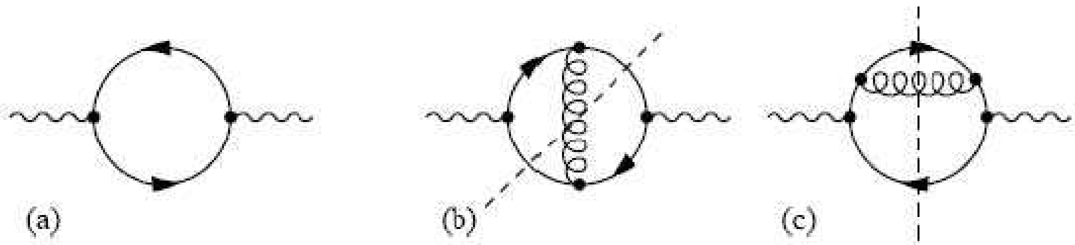

Figure 3.13: Feynman graphs of the photon self-energy: (a) 1-loop polarization tensor, (b) and (c) 2-loop polarization tensor. The dashed lines indicate cuts through the diagram corresponding to the processes in Figure 3.12.

$$\frac{d\sigma}{dt}(qg \to q\gamma) = (\frac{e_q}{e})^2 \frac{8\pi\alpha_s\alpha}{(s-m_q^2)^2}\{(\frac{m_q^2}{s-m_q^2}+\frac{m_q^2}{u-m_q^2})^2+(\frac{m_q^2}{s-m_q^2}+\frac{m_q^2}{u-m_q^2})-\frac{1}{4}(\frac{s-m_q^2}{u-m_q^2}+\frac{u-m_q^2}{s-m_q^2})\} \tag{3.12}$$

where m_q is the quark mass and e_q is the quark charge.

It is very instructive to consider the case where m_q becomes negligible or the quarks are massless. Then only the last term in each sum remains. In this limit the cross section for the annihilation process, Equation (3.12), is maximal when either u or t are minimal. This corresponds to the case where $P_\gamma = P_q$ or $P_\gamma = P_{\overline{q}}$. Hence the annihilation process can be visualized as a conversion of one of the annihilating quarks into a photon, and the momentum distribution of the photon is directly related to the (thermal) distribution of quarks and antiquarks in the QGP. For the Compton process a similar argumentation holds. The dominant contribution comes from the region of small u where$P_\gamma = P_q$.

For the calculation of the total emission rate for each process the initial distributions of quarks $f_{q,\overline{q}}(E)$ and gluons $f_g(E)$ in thermal equilibrium at temperature T are needed. They obey the Fermi-Dirac and the Bose-Einstein statistics, respectively. For vanishing baryo-chemical potential holds:

$$f_{q,\overline{q}}(E) = \frac{1}{e^{E/T}+1} \tag{3.13}$$

$$f_g(E) = \frac{1}{e^{E/T}-1} \tag{3.14}$$

After phase-space integration of the elementary photon production processes with these thermal distributions the total production rate for a quark-gluon plasma with u and d quarks ($N_f = 2$) in the QGP is given by [151]:

$$E_\gamma \frac{dN_\gamma}{d^3pd^4x} = \frac{5\alpha\alpha_s}{18\pi^2} f_q(\overrightarrow{p}_\gamma) T^2 \{\ln(\frac{4E_\gamma T}{m_q^2}) + \frac{C_{ann} + C_{Comp}}{2}\} \tag{3.15}$$

where C_{ann} and C_{Comp} are numerical integration constants. The close relation between the photon production in the plasma and the quark distribution $f_q(\overrightarrow{p}_\gamma)$ is directly seen. However, Equation (3.15) contains the quark mass as a parameter which basically defines a cutoff when the momentum transfer goes to zero. A similar calculation in [155] uses massless quarks and explicitly introduces a cutoff parameter k_c to account for the infrared divergence of Equation (3.12) in the phase-space integration.

To calculate the infrared contribution not considered in Equation (3.15) one can make use of the fact that the thermal emission rate of photons is also given by the imaginary part of the photon self-energy at finite temperature [156,155].

The photon self-energy is determined via loop diagrams as shown in Figure (3.13). The imaginary part is obtained by cuts through the loops: A cut through Figure 3.13(a) gives no contribution because the process $q\overline{q} \rightarrow \gamma$ has no phase space. The familiar Feynman graphs for the Compton and the annihilation process as in Figure 3.13 correspond to certain cuts through the two loop diagrams as shown in Figure 3.13(b) and (c).

The infrared contribution can be calculated by using a technique proposed by Braaten and Pisarski [157]. The bare vertices and propagators as in Figure 3.12 or Figure 3.13 can be replaced by so-called *effective* vertices and propagators. The effective propagators and vertices are the bare ones plus one-loop corrections. The introduction of such effective vertices and propagators basically represents a reorder-

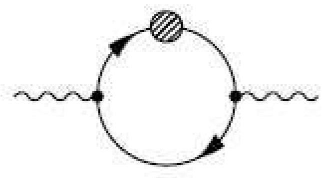

Figure 3.14: Photon self-energy containing a HTL-resummed propagator indicated by the circle. Cuts through the diagram lead to the processes in Figure 3.13(a) and (b) with an effective propagator.

ing of perturbation theory to take into account higher order diagrams, containing an infinite number of loops (screening effects), which can contribute to the same order in the coupling constant (see also [158,152]). The LO diagrams with effective propagators are again obtained by the imaginary part of the self-energy or cuts through the diagram, respectively. Such diagrams are also called hard thermal loops (HTLs), as they are used where the momentum of the propagator is soft (thermal) and the corrections are evaluated for hard loop momentum.

With this technique the infrared contribution has been determined in [155]. Together with the photon production rate corresponding to Equation (3.15) this leads to a photon production rate that does not depend on cutoff parameter or quark mass [155][3]:

$$E_\gamma \frac{dN_\gamma}{d^3p d^4x} \Big|_{2\to 2} = \frac{5\alpha\alpha_s}{18\pi^2} e^{-E_\gamma/T} T^2 \ln\left(\frac{2.912 E_\gamma}{4\pi\alpha_s T}\right) \tag{3.16}$$

One would expect that higher order diagrams, such as Bremsstrahlung shown in Figure 3.12(c) and $q\overline{q}$ annihilation with additional scattering (AWS), contribute only to higher order compared to the leading order diagrams. However, it has been shown in [159] that the contribution of 2-loop HTL corrections, corresponding e.g. to Bremsstrahlung, is of order $\alpha\alpha_s$. Although the rate was initially overestimated by a factor of four, it is still found that the 2-loop contribution enhances the photon

[3]In[155] a Boltzmann distribution has been used instead of Equation(3.13) and (3.14) to make an analytic solution possible.

spectrum from the QGP by a factor of two. It can be parameterized as [160]:

$$E_\gamma \frac{dN_\gamma}{d^3pd^4x}\mid_{Brems}= 0.0219\alpha\alpha_s T^2 e^{-E_\gamma/T} \tag{3.17}$$

$$E_\gamma \frac{dN_\gamma}{d^3pd^4x}\mid_{AWS}= 0.0105\alpha\alpha_s T e^{-E_\gamma/T} \tag{3.18}$$

for the contribution from Bremsstrahlung and annihilation with rescattering, respectively. The contribution to the total photon rate is shown in Figure 3.15(a). It is seen that the photon production via Bremsstrahlung surpasses the $2 \rightarrow 2$ processes of the 1-loop calculation by a factor of two. Investigations on 3-loop corrections in [161] showed that they also can contribute to order $\alpha\alpha_s$indicating that the thermal photon production may not be calculable via perturbative techniques [160].

When calculating the thermal photon production from a QGP an additional complication is introduced by the consideration of the Landau-Pomeranchuk-Migdal effect already discussed for the parton energy loss. A calculation considering all processes contributing to the order $\alpha\alpha_s$, including Bremsstrahlung, inelastic pair annihilation, as well as the LPM effect, has been performed for the first time in [162]. The photon rates in [162] are given in a slightly different notation compared to Equation (3.16) - (3.18). They can be rewritten to the same notation for two quark flavors ($N_f = 2$) and are given by:

$$E_\gamma \frac{dN_\gamma}{d^3pd^4x}\mid_{2\rightarrow 2}= \frac{5\alpha\alpha_s}{18\pi^2} T^2 e^{-E_\gamma/T}\{log(\frac{3E_\gamma/T}{2\pi\alpha_s}E_\gamma/T) + 2.02e^{-1.35E_\gamma/T} - 0.6328 + \frac{0.082}{E_\gamma/T}\} \tag{3.19}$$

$$E_\gamma \frac{dN_\gamma}{d^3pd^4x}\mid_{Brems}= \alpha\alpha_s T^2 e^{-E_\gamma/T}\{\frac{0.0411log(12.28+\frac{1}{E_\gamma/T}}{(E_\gamma/T)^{3/2}}\} \tag{3.20}$$

$$E_\gamma \frac{dN_\gamma}{d^3pd^4x}\mid_{aws}= \alpha\alpha_s T E_\gamma e^{-E_\gamma/T}\{\frac{7.49\times 10^{-3}}{\sqrt{1+\frac{E_\gamma/T}{16.27}}}\} \tag{3.21}$$

where Equation (3.19) is a more general expression for Equation (3.16) with im-

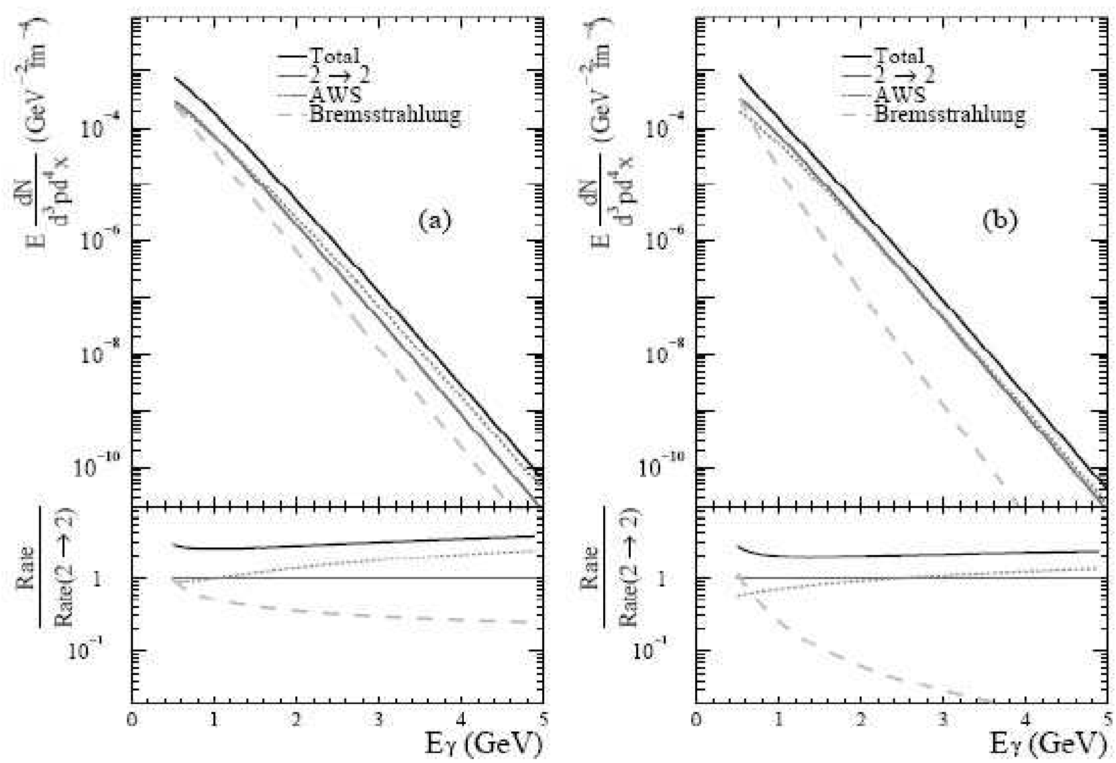

Figure 3.15: The static photon emission rates for a QGP with T =250MeV, N_f =2, and T_c =170MeV. The strong coupling constant is given by the parameterization as $\alpha_s(T) = \frac{6\pi}{(32-2N_f)log(gT/T_c}$ [163] The different contributions are calculated with: (a) Equation (3.16)-(3.18) considering contributions up to 2-loop order [155,160], (b) Equation (3.19)-(3.21) considering the LPM effect for Bremsstrahlung and inelastic pair annihilation, and 2→2 processes [162].

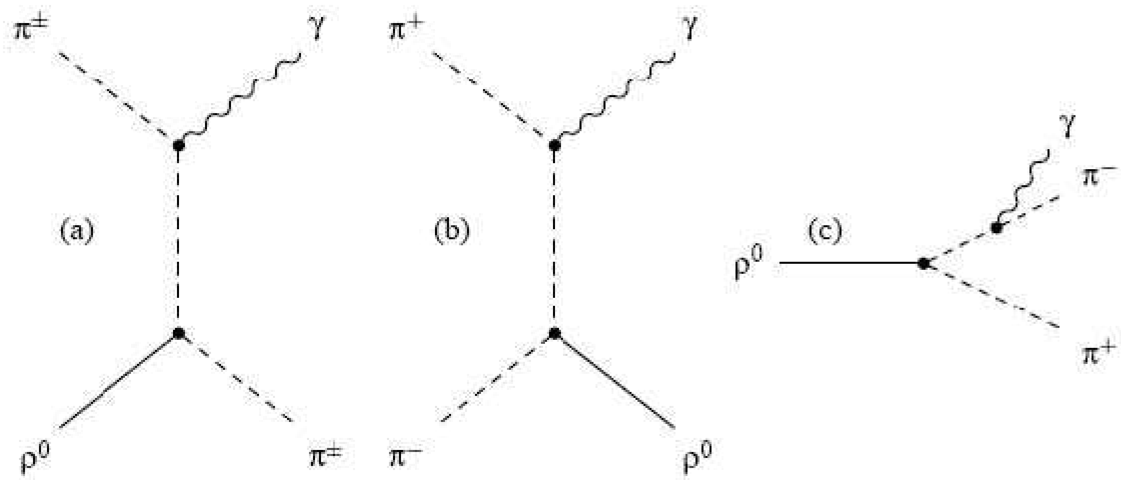

Figure 3.16: Examples of processes for the production of photons in a hadron gas: (a) $\pi\rho$ Compton scattering, (b) $\pi^+\pi^-$ annihilation, (c)ρ decay.

proved accuracy at low photon energies. The contribution from $2 \rightarrow 2$ processes (the 1-loop HTL rates), can serve as a reference when comparing the different contributions to the rate. As seen in Figure 3.15(b), the inclusion of the LPM effect as in [162] leads to a contribution from inelastic annihilation to the total photon rate that is reduced by a factor of two. It is of the same order of magnitude as the rate from $2 \rightarrow 2$ processes. The photon rate from Bremsstrahlung decreases strongly with the photon energy, in contrast to the 2-loop calculation. In the future one hopes to get more definitive answers on the static photon emission rates in a thermalized QGP from non-perturbative methods such as lattice QCD.

3.2.2 **Thermal Photons From a Hadron Gas**

The calculation of the thermal photon spectrum from the fireball produced in heavy ion collisions involves also the contribution from the hot hadron gas (HHG) phase following the QGP. It is also needed as reference for a scenario without a phase transition, to see if the thermal photon spectrum can be used as a signature for the QGP. The emission rate of thermal photons from the HHG can be treated very similar to the QGP case, discussed above. Again the rate is proportional to the imaginary part of the photon self-energy, with the difference that pions, ηs, and the ρ mesons constitute the loop corrections instead of quarks and gluons [155]. The coupling between the different vertices of the loop is determined by experimental observations, such as the decay rate for $\rho \rightarrow \pi\pi$. This *effective* coupling already considers higher-order effects, e.g. vertex corrections. The cuts through the loop diagrams can be identified with the relevant hadronic processes, e.g.: $\pi^{\pm}\rho^0 \rightarrow \pi^{\pm}\gamma$, Compton scattering shown in Figure 3.16(a), $\pi^+\pi^- \rightarrow \rho^0\gamma$ the annihilation process shown in Figure 3.16(b), $\rho^0 \rightarrow \pi{+}\pi^-\gamma, \rho^0$decay shown in Figure 3.16(c), $\omega \rightarrow \pi^0\gamma, \omega$ decay.

The first estimate of the emission rate from a hot hadronic gas has been presented in [155] together with the already discussed emission rate from a QGP phase. The comparison of the rates at T = 200MeV lead to the surprising result that "The hadron gas shines as brightly as the quark-gluon plasma" [155]. This would make direct photons a good thermometer of the fireball but not a signature for a phase transition. However, apart from the fact that the space-time evolution of a hadron gas and a QGP can be different, it has been already discussed that the QGP rates need to incorporate higher-order processes and the LPM effect. It was also found that the inclusion of the production of photons via the $a_1(1260)$ resonance in the hadron gas ($\pi\rho \rightarrow a_1 \rightarrow \pi\gamma$) strongly enhances the rate from the hadron gas [160].

A recent parameterization of the rate for thermal photon production in the hot hadron gas is given in [160]. It considers the exact expression for the decay $\omega \rightarrow \pi\gamma$ from [155] and parameterizations for the processes $\pi\pi \rightarrow \rho\gamma, \pi\rho \rightarrow \pi\gamma$, and $\rho \rightarrow \pi\pi\gamma$ from [164,165], where the a_1 meson is taken into account:

$$E_\gamma \frac{dN_{gamma}}{d^3pd^4x} \mid_{HHG} = 4.6T^{2.15} e^{-1/(1.35TE_\gamma)^{0.77}} e^{-E_{\gamma/T}} \tag{3.22}$$

This can be compared to the rates obtained for the QGP, considering the Bremsstrahlung

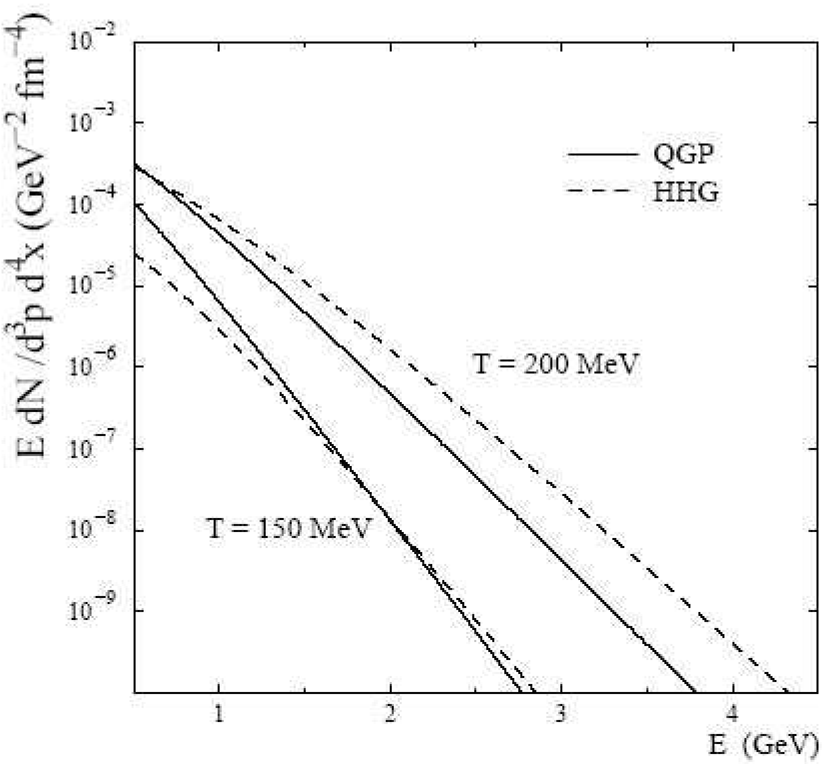

Figure 3.17: Comparison of the photon production rate from the quark-gluon plasma and the hadron gas at two different temperatures and for two quark flavors [160].

and inelastic annihilation contribution from [159], for different temperatures. As seen in Figure (3.17), the agreement between the rates of QGP and HHG may be a coincidence at a certain temperature, but it cannot be ruled out especially given the current uncertainties of the calculations.

3.2.3 Non-Thermal Photons

The main source of non-thermal direct photons are the prompt photons. They are produced in early hard scatterings, similar to hadrons with large transverse momenta and are calculable via perturbative QCD invoking the factorization theorem Equation (3.1). The basic underlying processes are the same as in the QGP (see Figure 3.12), with the main difference that the initial parton distribution is not given by the thermal distributions in the QGP, but by the parton distributions in the incoming nuclei. The photon production in hard scattering is in principle not influenced by the uncertainty in the fragmentation function as in the case of hadron production, since it is a δ-function for photons. However, photons can also be produced during the fragmentation process of scattered partons. For the production of photons in p+A collisions the same effects become important as for the hadron production: the nuclear p_T-broadening, the Cronin effect, the shadowing of the parton distribution function, and possible saturation effects. Especially the Cronin effect can be a rather significant contribution to the total yield in the intermediate p_T range, where the largest thermal signal is expected. This has been demonstrated for the measurement of direct photons at SPS energies and for RHIC energies in [166].

An additional source of non-thermal direct photons arises from the pre-equilibrium phase, where the theoretical description is rather difficult due to the uncertainties in the formation time of the thermalized phase. It is often treated in parton cascade models (chapter 2) for photon production, which combine perturbative QCD with relativistic transport models (see e.g. [167,168]). The passage of high energy quark jets through the QGP leads to Compton scattering with the thermal gluons and annihilation with thermal antiquarks. This has also been considered as a source for direct photons, which may dominate in the region below $p_T = 6$GeV/c for Au+Au collisions at RHIC [169].

3.2.4 **Photon Spectra**

In the experiment, only photons from the entire space-time evolution of the heavy ion collision can be observed. Therefore thermal and non-thermal production rates have to be convoluted with the entire evolution of the reaction.

The elementary thermal photon rate depends basically on the temperature at a given space-time point $T(x)$, hence the observed photon spectrum is given by:

$$E_\gamma \frac{dN_\gamma}{d^3p_\gamma} = \int d^4x \frac{dN_\gamma}{d^3p_\gamma d^4x}(T(c)) \tag{3.23}$$

The evolution of the fireball is usually described as an ideal fluid in terms of relativistic hydrodynamics (for a more detailed description on this topic see e.g. [170]). The hydrodynamic equations of motions are basic conservation laws, e.g. the local conservation of energy-momentum(chapter 2).

$$\frac{d\epsilon}{d\tau} + \frac{\epsilon + P}{\tau} = 0 \tag{3.24}$$

The equation of state depends on model assumptions. Usually the QGP phase and the hot hadron gas are treated separately, with the EOSs matched at the phase transition according to the order of the phase transition. The EOS for the QGP in most hydrodynamic models is from simple bag models with quarks and gluons described as an ideal gas. One obtains e.g. for a QGP with baryo-chemical potential $\mu_B = 0$ [171]:

$$P_{QGP} = g_{QGP}\frac{\pi^2}{90}T^4 - B, \tag{3.25}$$

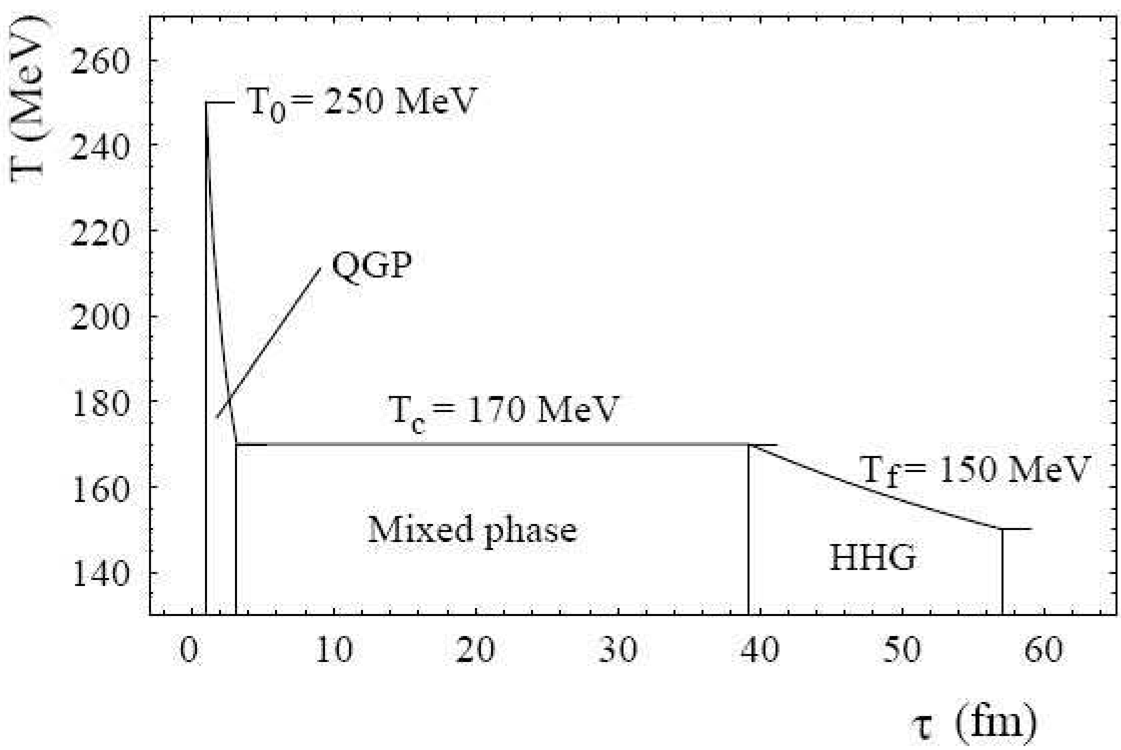

Figure 3.18: Sketch of the temperature evolution for Bjorken expansion in the phase transition scenario from an ideal gas of massless quarks and gluons in the QGP to an ideal hadron gas of massless pions.

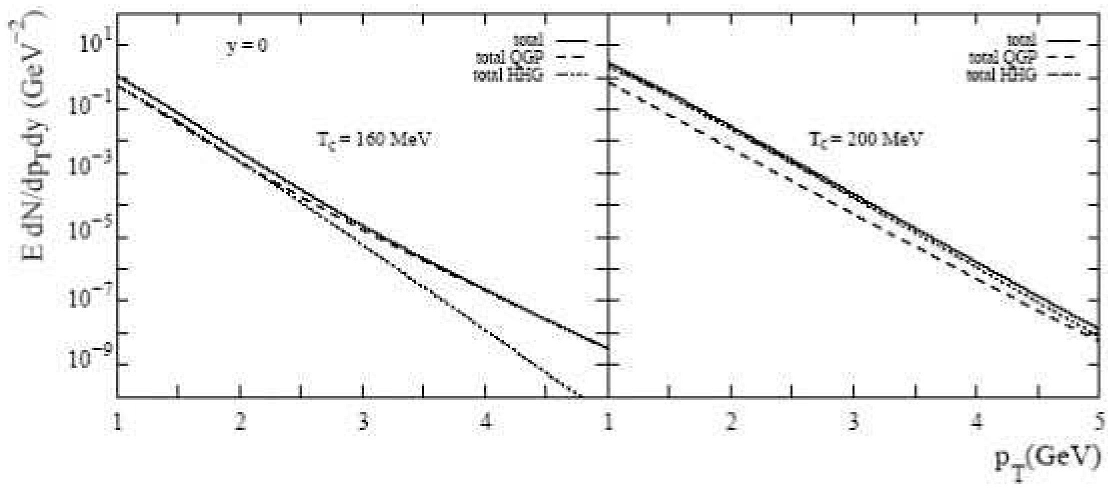

Figure 3.19: Total thermal photon emission from a QGP phase and a hot hadron gas for different critical temperatures [152].

$$\epsilon_{QGP} = g_{QGP}\frac{\pi^2}{30}T^4 - B, \tag{3.26}$$

where g_{QGP} is the effective number of degrees of freedom of gluons (8 color-anticolor combinations and 2 spin states) and quarks (3 colors, 2 spin states, e.g. 2 flavors, $q$and $\overline{q}$):

$$g_{QGP} = 8 \times 2 + \frac{7}{8} \times 3 \times 2 \times 2 \times 2 = 37 \tag{3.27}$$

and B is the bag constant. It determines the energy density of the QCD vacuum necessary for the confinement of quarks and gluons in the hadron bag. It is typically of the order of $B^{1/4} \approx$200MeV. The EOS of a QGP in the bag model is given by:

$$\epsilon_{QGP} = 3P_{QGP} + 4B \tag{3.28}$$

Similarly, the pressure and the energy density of a hadron gas can be determined for an ideal gas of massless pions [171]:

$$P_{HG} = g_{HG}\frac{\pi^2}{90}T^4 \tag{3.29}$$

$$\epsilon_{HG} = g_{HG}\frac{\pi^2}{30}T^4 \tag{3.30}$$

where g_{HG} is the number of degrees of freedom in the hadron gas, which is $g_{HG} = 3$ for a pion gas. The EOS is given by:

$$\epsilon_{HG} = 3P_{HG} \tag{3.31}$$

The critical temperature T_c for the phase transition from a QGP into a hadron gas, in this simple model with first order phase transition, is determined by the Gibbs Criteria ($T_{QGP} = T_c = T_{HG}$ and $P_{QGP} = P_c = P_{HG}$) and the two EOS:

$$T_c = \{(\frac{90B}{(g_{QGP} - g_{HG})\pi^2})^{1/4}\} \tag{3.32}$$

The initial conditions of the QGP are given by the formation time τ_0 and the initial temperature T_0. The phase transition is characterized by the critical temperature, which is $T_c \approx$150MeV for $B^{1/4} \approx$ 200MeV. The kinetic decoupling of the hadrons is where the thermodynamic treatment of the fireball is no longer valid. It is characterized by the *freeze-out* temperature T_f.

For the first order phase transition, which is implied by this simple model but probably not realistic [172], a mixed phase of QGP and hadron gas exists during which the temperature stays constant at the critical temperature. The lifetimes of the three different phases in this simple model are determined by the evolution given by the Bjorken scenario together with the different EOS, as discussed in [173]:

$$\Delta\tau_{QGP} = \tau_0\{(\frac{T_0}{T_c})^3 - 1\} \tag{3.33}$$

$$\Delta\tau_{mixed} = \tau_0(\frac{T_0}{T_c})^3\{\frac{g_{QGP}}{g_{HG}} - 1\} \tag{3.34}$$

$$\Delta\tau_{HG} = \tau_0(\frac{T_0}{T_c})^3\{\frac{T_c}{T_f} - 1\} \tag{3.35}$$

The lifetimes of the different phases for an initial temperature of $T_0 = 250$MeV, critical temperature $T_c = 170$MeV, and freeze-out temperature $T_f = 150$MeV are shown in Figure (3.18). The emission of thermal photons is now given by the convolution of this temperature evolution with the corresponding static emission rates following Equation (3.23)[4]. The resulting (thermal) photon spectra are shown in Figure (3.19) for two different assumptions for the critical temperature. An increase of the critical temperature obviously leads to a larger contribution from the hadron gas, as this leads to a decrease in the lifetime of the QGP.

The simple one-dimensional hydrodynamic expansion used in this section should only serve as an example, more complex scenarios are given in the literature (see e.g. [174] and references therein). The uncertainty from the description of the space-time evolution, together with the unknown initial condition, is another source of uncertainty for the theoretical description of the direct photon production in heavy ion collisions, in addition to the uncertainties in the static rates.

3.2.5 Binary Scaling in Direct Photons

The first measurement of direct photons in heavy ion collisions has been reported by the WA98 experiment at the CERN SPS in central $Pb + Pb$ collisions at $\sqrt{s_{NN}}$ = 17.2 GeV [175,176]. It is shown in Figure (3.20) together with scaled results from $p + A$ collisions.

The comparison with proton induced reactions suggests a modification of the direct photon production in heavy ion collisions. Whether this is due to quark-gluon plasma formation or other nuclear effects is still debated. A recent review of different theoretical models, which describe the WA98 data, partially without a phase

[4] In the mixed phase the contributions from the QGP and the hadron gas have to be weighted accordingly.

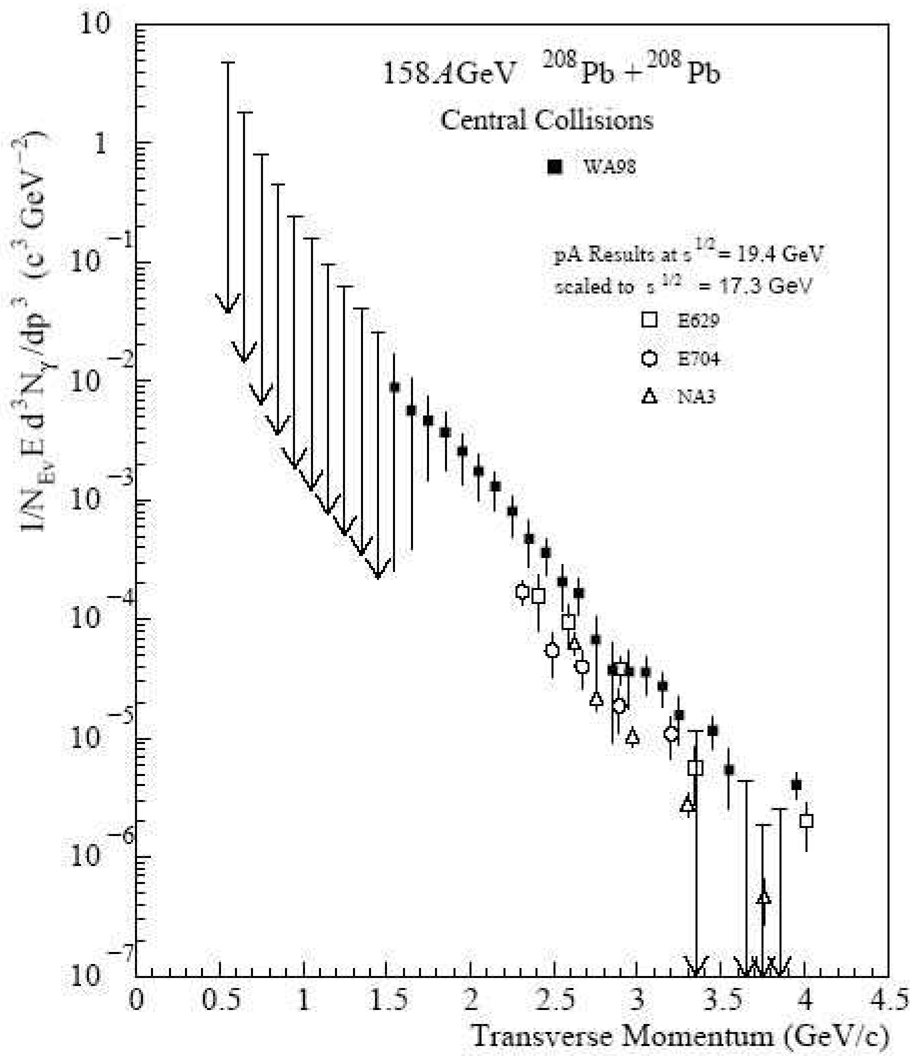

Figure 3.20: First measurement of direct photons in heavy ion collisions reported by the WA98 experiment together with scaled results from p+A collisions [175].

transition scenario, is given in [152].

At RHIC, it has been observed that the matter is very opaque and dense. It is so dense that even a 20 GeV/c pion is stopped. In Figure (3.21) the preliminary result for the nuclear modification factor is shown, R_{AA}, of π^0 in central $Au + Au$ collisions in the p_T range up to 20 GeV/c [177]. The suppression is very strong, and it is flat at R_{AA} ≈0.2 up to 20 GeV/c . There is no hint that it returns to unity. The figure also shows that the suppression of π^0's and η's is very similar, which supports the conclusion that the suppression occurs at the parton level, not the hadron level. This strong suppression of mesons is in stark contrast to the behavior of direct photons [178], also shown in the Figure (3.21). The direct photons follow binary scaling (i.e. R_{AA} ∼1). This is strong evidence that the suppression is not an inital state effect, but a final state effect caused by the high density medium created in the collision. The curve in the plot shows a theoretical prediction [179] using the GLV parton energy loss model. The model assumes an inital parton density $dN/dy = 1100$, which corresponds to an energy density of approximately 15 GeV/fm^3. The data show that the suppression is somewhat stronger than the prediction, suggesting that the matter density may be even higher than these estimates.

3.3 Collective Flow

Two heavy nuclei can be compressed to more than ground-state saturation density and heated in head-on collisions at high energy. A flow pattern will develop as the system subsequently expands. In macroscopic classical physics flow can be described in the language and with the tools of hydrodynamics, where one links in a conceptually simple way conservation laws (mass, momentum, energy) with fundamental properties of the fluid: the equation of state and transport coefficients, such as viscosity and heat conductivity.

The equation of state (EoS) of nuclear matter, i.e. the relationship specifying

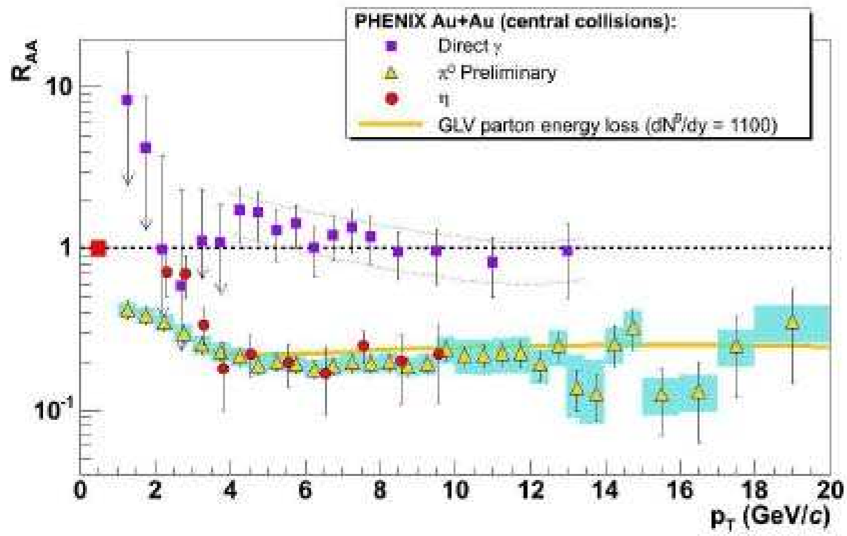

Figure 3.21: Nuclear modification factor, R_{AA} of π^0 (triangles), η(circles), and direct photon (squares).

how the pressure, or alternatively the energy per particle, depends on density and temperature, is of fundamental interest. One of the properties characterizing the EoS is the incompressibility K, which measures the resistance against compression (stiffness) and is expected to directly influence flow phenomena.

In 1955 Belenkij and Landau first used a fluid-dynamics model to describe collisions of nucleons and nuclei. In 1959 Glassgold, Heckrotte, and Watson [180] considered the shock waves that could be formed when a high-energy proton or pion exceeding the nuclear speed of sound passes through a nucleus. They proposed a way to determine the nuclear compressibility coefficient. In the mid-1970s a number of theoretical papers assumed that hydrodynamics was governed by the formation of a shock wave [181-186] that most of the studies found propagating in the longitudinal direction.

The importance of transverse expansion was first shown by Scheid, Muller, and Greiner [182] in an ideal-fluid hydrodynamics calculation. For beam energies as low as 12.5A MeV, it was predicted that in the first 15 fm/c after penetration the transverse border of the stopped and shocked matter was expanding faster than the longitudinal border. The authors concluded matter is pushed outwards perpendicular to the relative motion of the two nuclei [182].

Experimentally, the first convincing evidence for the occurrence of sideward flow [187,188] was obtained by so-called 4π detectors, the Streamer Chamber [189] and the Plastic-Ball/Wall [190] at the Bevalac in Berkeley. These detectors could fully characterize events by identifying and measuring the momenta of most of the emitted charged particles. The data [187] could be reproduced in a theoretical analysis [191] confirming a long series of predictions based on fluid dynamics [192].

The collective component arises from the matter density gradient from the center to the boundary of the fireball created in high-energy nuclear collisions. Interactions among constituents push matter outwards; frequent interactions lead to a common constituent velocity distribution. This so-called collective flow is therefore sensitive to the strength of the interactions. The collective flow is additive and thus accumulated over the whole system evolution, making it potentially sensitive to the Equation of State of the expanding matter. At lower energies the collective flow reflects the properties of dense hadronic matter, while at RHIC energies a contribution from a pre-hadronic phase is anticipated.

Although all forms of flow are interrelated and represent only different parts of one global picture, one can classify the collective flow as longitudinal expansion, radial transverse flow, and anisotropic transverse flow. At high energies the longitudinal flow is well decoupled from transverse flow. This makes it possible to discuss the anisotropic transverse flow from the particle azimuthal distributions at fixed pseudo-rapidity.

3.3.1 Anisotropic Transverse Flow

Anisotropic transverse flow is defined as the correlations with respect to the reaction plane. Since the observation of anisotropic flow at AGS [193] and at the SPS

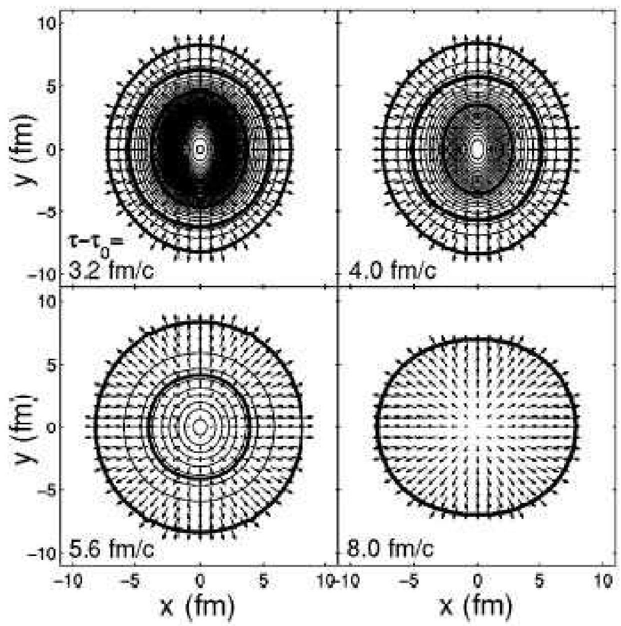

Figure 3.22: The evolution of the source shape is shown from a model where a heavy-ion collision is treated as a hydrodynamic system(). The initial shape is extended out-of-plane. By 8 fm/c after the formation time($\tau - \tau_0$), the shape has deformed to an in-plane extended source. In this model, the anisotropy in momentum-space measured by v_2 is dominated by the early stages.

[194], the study of collective flow in nuclear collisions at high energies has attracted increased attention of the experimentalists and the theoreticians as well. In non-central heavy-ion collisions the initial transverse density gradient has an azimuthal anisotropy that leads to an azimuthal variation of the collective transverse flow velocity with respect to the impact parameter plane for the event. As this azimuthal variation of flow is expected to be self-quenching, hence, especially sensitive to the interactions among constituents in the early stage of the collision, when the system at RHIC energies is anticipated to be well above the critical temperature for QGP formation. Figure (3.22) shows the evolution of the source shape calculated from a model where the collision system is described by hydrodynamic equations[195].

Most observables in heavy-ion collisions are integrated over the azimuthal angle and, as such, they are insensitive to the azimuthal asymmetry of the initial source. In this thesis we discuss measurements sensitive to the conversion of the initial spatial

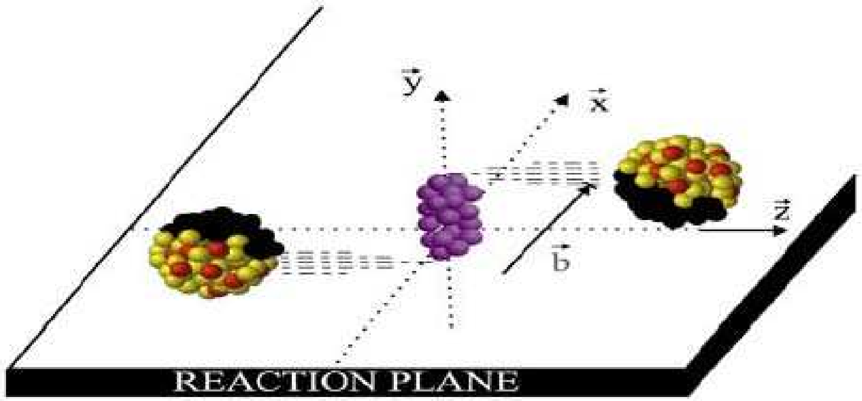

Figure 3.23: Schematic diagram of the Reaction Plane in the heavy-ion collision.

anisotropy to a final momentum-space anisotropy. Multiple interactions are necessary to develop a momentum-space anisotropy from a coordinate-space anisotropy. If each nucleon-nucleon collision is independent, the final momentum distribution will represent a superposition of random collisions and will therefore be isotropic.

The spatial anisotropy can be quantified by estimating the eccentricity ϵ of the initial source,

$$\epsilon = \frac{< y^2 - x^2 >}{< y^2 + x^2 >} \tag{3.36}$$

The event anisotropy can be evaluated with the Fourier expansion of azimuthal distribution of particles[196],

$$\frac{d^3N}{p_T dp_T dy d\phi} = \frac{d^2N}{p_T dp_T dy}\{1 + 2\sum_n v_n \cos[n(\phi - \Psi_{RP})]\} \tag{3.37}$$

The harmonic coefficients, v_n, are anisotropy parameters, p_T, y, and ϕ are the respective transverse momentum, rapidity, and azimuthal angle for the particle, and Ψ_{RP} is the reaction plane (Figure 3.23) angle.[5]. The sine terms which in general appear in Fourier expansions vanish due to the reflection symmetry with respect to the reaction

[5]The reaction plane is defined by the beam axis and the vector connecting the centers of the two colliding nuclei. For high energy collisions, in the laboratory reference frame the Au nuclei are Lorentz-contracted along the beam axis. As such, the vector connecting the colliding nuclei is nearly perpendicular to the beam axis and the reaction plane can be characterized by its azimuthal angle.

plane. It follows that $< \cos n\phi >$ gives v_n:

$$< \cos n\phi >= \frac{\int_{-\pi}^{\pi} \cos n\phi \frac{d^3N}{p_T dp_T dy d\phi} d\phi}{\int_{-\pi}^{\pi} \frac{d^3N}{p_T dp_T dy d\phi} d\phi} = v_n \tag{3.38}$$

where the orthogonality relation between Fourier coefficients $\int_{-\pi}^{\pi} [\cos n\phi \cos m\phi]_{m \neq n} d\phi = 0$ has been used.

Anisotropic flow corresponding to the first two harmonics plays a very important role and we use special terms for them: directed flow and elliptic flow, respectively. The word "directed" (also called sideward flow) comes from the fact that such flow looks like a sideward bounce of the fragments away from each other in the plane of the reaction, and the word "elliptic" is due to the fact that the azimuthal distribution with non-zero second harmonic represents an ellipse.

3.3.2 **Elliptic Flow**

Event anisotropy characterized by v_2, elliptic flow, measures the momentum anisotropy in the transverse plane in non-central heavy ion collisions. In contrast to transverse radial flow from central collisions, elliptic flow established at relatively early stage of the collisions. Therefore it is sensitive to the initial conditions and the possible onset of the hydrodynamics in the collision. Because multiple interactions, which help to achieve the thermalization of the system, mainly happen during the early stage of the system. And also the azimuthal anisotropy in coordinate space is largest thus the pressure gradiant is largest at the beginning of the evolution. Thus v_2 can reveal the information about the thermalization of the system at the early stage. If v_2 is positive, one will expect more particles coming out parallel to the reaction plane and fewer particles coming out perpendicular to the reaction plane.

Elliptic flow has been observed and extensively studied in nuclear collisions from lower relativistic energies on up to RHIC. At top AGS and SPS energies, elliptic flow is inferred to be a relative enhancement of emission in the plane of the reaction. Generally speaking, large values of collective flow are considered signatures of hydrodynamic behavior, while smaller flow signals can have alternative explanations.

The centrality dependence of elliptic flow is of special interest [197,198]. In the low density limit (LDL), the mean free path is comparable to or larger than the system size, and the colliding nuclei resemble dilute gases. The final anisotropy in momentum space depends not only on the initial spatial eccentricity, but also depends on the particle density, which affects the number of rescatterings. A more dilute system (less rescatterings) has more difficulty to transform spatial anisotropy to momentum anisotropy.

Thus in this limit, the final elliptic flow (see a more detailed formula in [199]) is given by:

$$v_2 \propto \epsilon \frac{1}{S} \frac{dN}{dy} \tag{3.39}$$

where dN/dy characterizes density in the longitudinal direction and $S = \pi R_x R_y$ is the initial tranverse area of the overlapping zone, with $R_x^2 \equiv < x^2 >$ and $R_y^2 \equiv < y^2 >$ describing the initial geometrical dimentions of the system in the x and y directions, respectively.

As follows from Equation (3.39), the elliptic flow increases with the particle density. Eventually, it saturates [200] at the hydro limit. In this region, the ratio of v_2 to ϵ is expected to be approximately constant [201] due to the complete thermalization (the mean free path is much less than the geometrical size of the system).

At AGS energies, the elliptic flow results from a competition between the early squeeze-out when compressed matter tries to move out in the unimpeded direction perpendicular to the reaction plane and the late-stage in-plane emission associated with the shape of the participant zone. The squeeze-out contribution to the elliptic flow depends, generally, on the pressure built-up early on, compared to the energy density, and on the passage time for the spectators. When the heated matter is exposed to the vacuum in the transverse direction, expansion happens more rapidly in the exposed direction. At relativistic energies, the Lorentz contracted spectators in the colliding nuclei pass by each other quickly (in a time of the order $2R/\gamma$, where R is the nuclear radius and is the Lorentz contraction factor). When this passage time is short enough, the in-plane (positive) component of elliptic flow dominates.

3.3.3 **Elliptic Flow of Charged Hadrons**

The recent measurement of the v_2 of identified particles shows a mass ordering phenomenon at low p_t range [202]. At a given p_T in this range, the v_2 decreases with increasing particle mass. The hydrodynamic model, which assumes ideal fuid fow, describes the mass ordering of v_2 at low p_T reasonably well [203]. The left plot of Figure (3.24) shows the measured v_2 of $\pi^{\pm}, K_s^0, \overline{p}$ and $\Lambda + \overline{\Lambda}$ together with hydrodynamic calculations. The success of hydrodynamic model in this p_T range indicates that a strong interacting thermalized quark matter has been created. The result from v_2 measurement can constrain the effective Equation of State (EoS) of the nuclear matter created by RHIC. Recent hydrodynamic model study indicates that the nuclear matter created at RHIC has an EoS with a strong first order phase transition between hadron gas and an ideal parton gas. The right plot of Figure (3.24) shows that the EoS Q (QGP EoS) describes the experimental data much better than the EoS H (hadron gas EoS). This seems to indicate that the phase transition has happened at RHIC collisions. At mediate p_T , the hydrodynamic model, whose assumption is no longer valid, gives v_2 much larger than experiment results. In this p_T range, the quark recombination model successfully describes the experimental data. At high p_T , the v_2 of identified particles begins to saturate, which implies jet quenching.

Figure (3.25) shows the scalar product (see chapter 5 for the definition) as a function of p_t for three different centrality ranges in $Au + Au$ collisions compared to

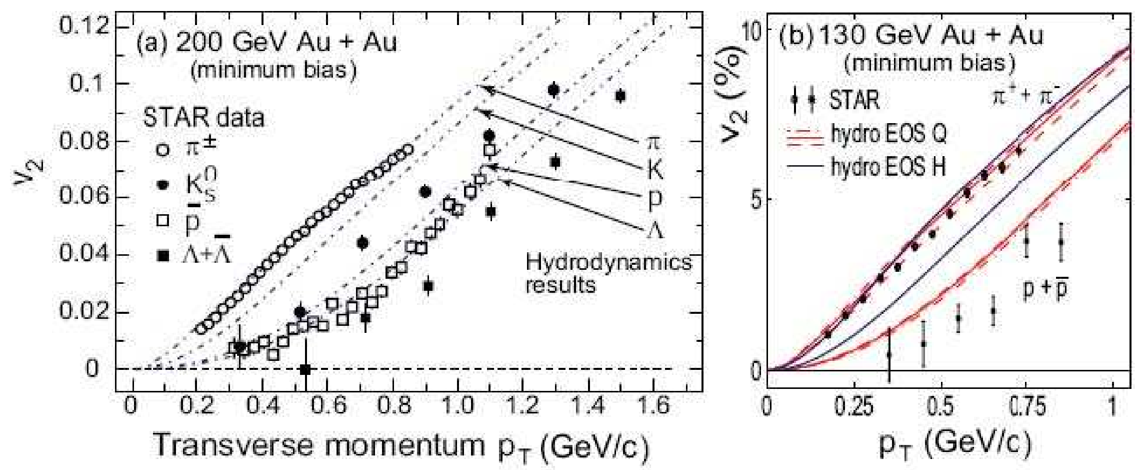

Figure 3.24: STAR experimental results of the transverse momentum dependence of the elliptic flow parameter in 200 GeV $Au + Au$ collisions for charged $\pi^+ + \pi^-, K_s^0$ $\overline{p} and \Lambda$[204]. Hydrodynamics calculations [205,206] assuming early thermalization, ideal fluid expansion, an equation of state consistent with LQCD calculations including a phase transition at T_c=165 MeV (EOS Q in [205]), and a sharp kinetic freezeout at a temperature of 130 MeV, are shown as dot-dashed lines. Only the lower p_T portion ($p_T = 1.5$ GeV/c) of the distributions is shown. (b) Hydrodynamics calculations of the same sort as in (a), now for a hadron gas (EOS H) vs. QGP (EOS Q) equation of state [205,207], compared to STAR v_2 measurements for pions and protons in minimum bias 130 GeV $Au + Au$ collisions [208].

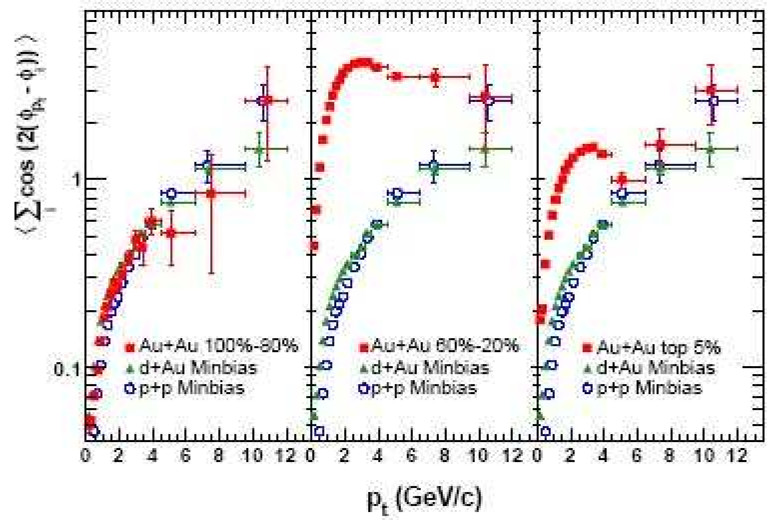

Figure 3.25: Charged hadron azimuthal correlation vs. p_T in Au+Au collisions (squares) as a function of centrality (perpheral to central from left to right) compared to minimum bias azimuthal correlations in $p+p$ collisions (circles) and d+Au collisions (triangles).

minimum bias $p+p$ collisions [209] and $d+Au$ collisions. For $Au+Au$ collisions, in middle central events we observe a big deviation from $p+p$ collisions that is due to the presence of elliptic flow, while in peripheral events, collisions are essentially like elementary $p+p$ collisions. The azimuthal anisotropy goes up to 10 GeV/c but we cannot distinguish whether it is from hydro-like flow or from jet quenching. For p_t beyond 5 GeV/c in central collisions, we again find a similarity between $Au+Au$ collisions and $p+p$ collisions, indicating the dominance of nonflow effects. The scalar product in $d+Au$ collisions is relatively close to that from $p+p$ collisions but there is a finite difference at low p_t. This difference is small if compared to the difference between middle central $Au+Au$ collisions and minimum bias $p+p$ collisions. This indicates that non-flow could dominate the azimuthal correlations in central $Au+Au$ collisions at high p_t. The centrality dependence of the azimuthal correlation in $Au+Au$ collisions is clearly non-monotonic, being relatively small for very peripheral collisions, large for mid-central collisions, and relatively small again for central collisions. This non-monotonic centrality dependence is strong evidence

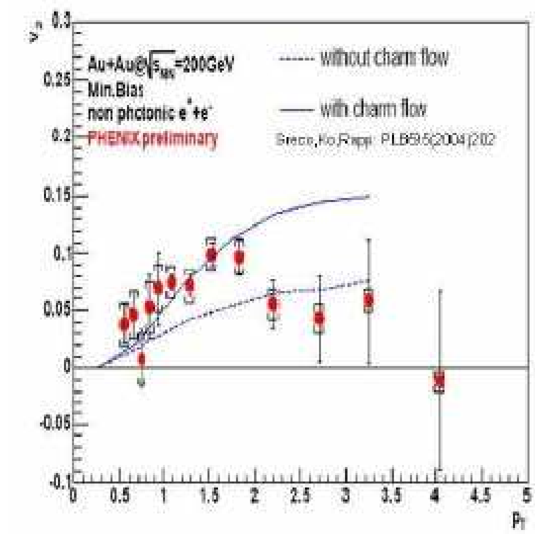

Figure 3.26: The elliptic flow strength v_2 of single electrons from heavy quark decay. The curves on the figure are charm coalescence model predictions()with (solid) and without(dashed)charm quark flow.

that in mid-central collisions (10%-50%) the measured finite v_2 for pt up to 16 GeV/c is due to real correlations with the reaction plane.

Another evidence for the strongly coupled matter formed at RHIC is observed through the heavy quarks flow. Figure (3.26) shows the preliminary data of the elliptic flow strength, v_2, of single electrons from heavy quark decay. The data clearly demonstrates that the v_2 of single electrons is non-zero, and that therefore the parent D meson have non-zero elliptic flow.

3.4 Elliptic Flow of Direct Photons

The two most interesting sources of photons are those where the plasma is directly involved in the emission. These are the thermal radiation from the hot QGP [210] and the radiation induced by the passage of high energy jets through the plasma [211-213]. The thermal radiation is emitted predominantly with low transverse momentum p_T and has to compete with photon emission from the hot hadronic gas at later times [214,215]. Photons from jets are an important source at intermediate p_T , where they compete with photons from primary hard scatterings between partons of the nuclei [216]. They probe the thickness of the medium: the longer the path of the jet, the more photons are emitted.

As we have discussed the hadrons are highly suprressed at high-p_t at RHIC energy, however the direct photons yield is consistent with binary collision scaling.The lack of suppression of direct photons is further evidence in favor of the final-state effect in hadron suppression. In addition to the initially-produced hard photons that should inherently follow binary scaling, there may be other counteracting effects resulting in apparent binary scaling. For example, some fraction of the photons may originate from partons having experienced energy loss, causing an analogous suppression of these photons [217] similar to hadrons. On the other hand, the parton energy loss may enhance the photon yield via Bremsstrahlung while passing through the hot and dense matter [218]. The thermal emission of photons radiated from the hot and dense matter is also expected to increase direct photon yield for central Au+Au collisions [219]. The v_2 measurement of the direct photons could help to confirm that the observed binary scaling of the direct photon excess is attributable to the direct photon production being dominated by the initial hard scattering. The v_2 measurement of the direct photons would give additional and complementary information to help disentangle the various scenarios of direct photon production, as well as to provide more information on the dynamics and properties of the produced hot and dense matter. The v_2 of photons from the initial Compton-like hard scattering is expected to be zero if they do not interact with the hot and dense matter produced during the collision. However when the v_2 of high p_t hadrons is given purely by the parton energy loss, the photons from the parton fragmentation outside of the reaction zone should have v_2 similar to the hadrons at high p_t .

On the other hand, one would expect that the photons originating from Bremsstrahlung due to the passage of partons through the hot and dense matter should have the opposite (negative) sign in v_2 compared with hadrons, because the parton energy loss is larger in the long axis of the overlapping region (out-of-plane). Finally, the photons from the thermal radiation should reflect the dynamical evolution of the produced hot and dense matter. There are recent theoretical predictions for different mechanisms [220].

To summarize, studying the v_2 of inclusive or direct photons is a useful tool to disentangle the different production mechanisms of the photon.It is predicted that the v_2 is zero for photon orignated from Coulomb scattering, greater than zero for the decayed photons, and less than zero for the radiated photons “Bremsstrahlung”. The measurements of the v_2 of inclusive photons is one of the main point in this dissertation.

Chapter 4

Experiment

"Despite the mathematical beauty of some of its most complex and abstract theories, including those of elementary particles and general relativity, physics is above all an experimental science."

R. Resnick, D. Halliday, and K. Krane

In the collider experiment the accelerator and the detector setup are closely connected. The required components for each detector and its granularity are heavily controlled by the kind of the collision system and by the top available energy, which can be reached by the accelerator. The hardware trigger system for any detector is designed considering the highest luminosity, which can be delivered by the accelerator.

In this chapter we overview the experimental setup used to gather the data for the analysis presented in this work. Simple description of the accelerator complex at Brookhaven National Laboratory is presented in the first section. The general conditions of the experiment and the conceptual design of the detector components are discussed in the second and third sections respectively. The specific goal for each detector at RHIC is mentioned in the fourth section when we emphasize the role of each detector complementing the ability to detect the QGP signal. In section five an overview of STAR detector is presented, we will focus on the BEMC, main TPC, and Forward TPC, which are the key subsystems for the presented analysis.

Accelerator	Beams	$\sqrt{s_{NN}}$[GeV]	Startup year
AGS,BNL	$^{16}O,^{28}Si$	5.4	1986
SPS,CERN	$^{16}O,^{32}S$	19.4	1986
AGS,BNL	^{197}Au	4.9	1992
SPS,CERN	^{208}Pb	17.3	1994
RHIC,BNL	^{197}Au	130	2000
RHIC,BNL	^{197}Au	200	2001
RHIC,BNL	^{197}Au	62.5	2004
LHC,CERN	^{208}Pb	5500	2007

Table 4.1: Heavy-ion accelerators described in terms of accelerated nuclei and available energy.

4.1 The Relativistic Heavy Ion Collider

The Relativistic Heavy Ion Collider (RHIC) is designed to accelerate heavy ions to nearly the speed of the light in two concentric collider rings. The RHIC storage ring is 3.83km in circumference and is designed with six interaction points, at which beam collisions are possible. Up to 112 particle bunches per ring can be injected, in which case the time interval between bunch crossings at the interaction points is 106ns. Running at approximate luminosity $2 \times 10^{26} cm^{-2}s^{-1}$ using Au+Au ions, for p+p collisions it is $2 \times 10^{32} cm^{-2}s^{-1}$, RHIC can provide beam energies ranging from 30GeV/u to 100GeV/u. This corresponds to $\sqrt{s_{NN}}$ energies ranging from 60GeV to 200GeV. Until the Large Hadron Collider (LHC) at CERN is complete, RHIC remains the highest energy collider in existence, taking Au ions to 99.995% the speed of light. A summary of the development of heavy-ion colliders is given in table(4.1).

RHIC is also capable of accelerating polarized and unpolarized proton beams to a maximum energy of 250GeV/u. Besides supplying important baseline information with respect to $A + A$ collisions, the study of $p + p$ collisions will provide data on the proton spin problem where it has been shown that the valance quarks of the proton do not provide the total spin observed [221]. Collision of asymmetric species, i.e. different species in the two beams $(d + Au)^1$, is also possible due to independent

[1] This happened during the third RHIC beam period, where d+Au collisions have been examined

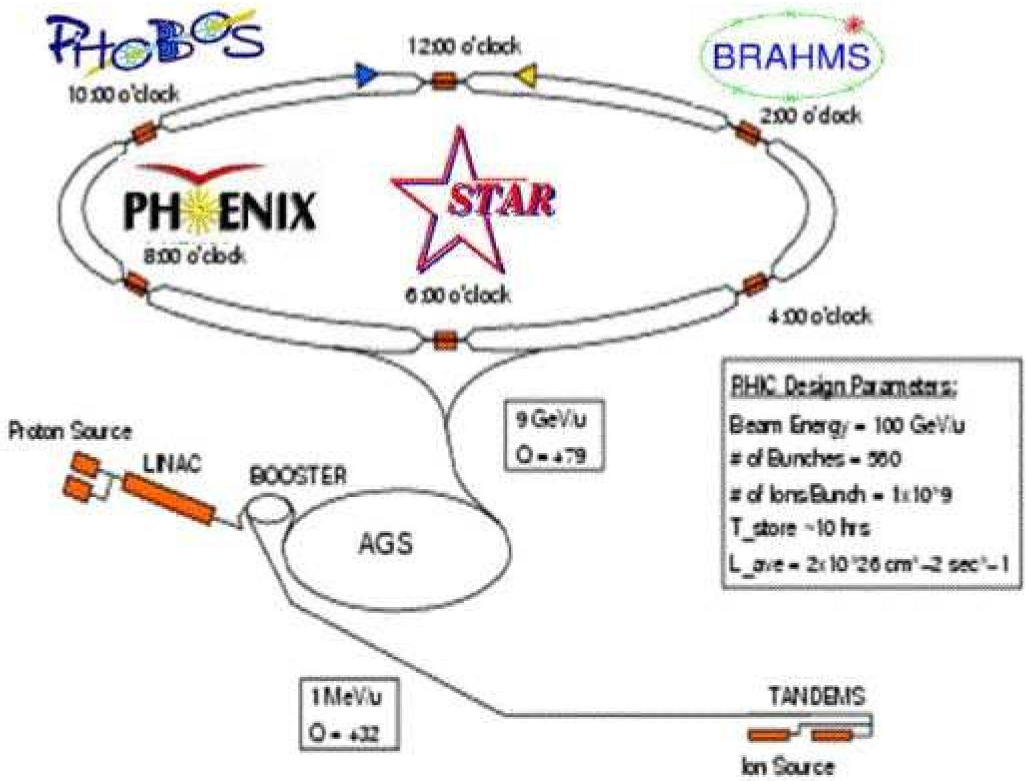

Figure 4.1: RHIC facility at Brookhaven National Laboratory(**?**).

rings with independent steering magnets. This diversity allows the study of colliding systems as a function of both energy and system size.

Figure (4.1) shows the layout of RHIC complex. The path of the Au atoms begins in the Pulsed Sputter Ion Source in the Tandem Van de Graaff facility with a charge of -1. These atoms are accelerated and passed through two thin Au foils that strip the Au atoms of some electrons, leaving them with a net charge of +32. The Booster Synchrotron takes the 1 MeV/u Au beam and accelerates it to 95 MeV/u and further strips the ions to a net charge of +77. The beam is then fed into the AGS where it is bunched and accelerated to 10.8 GeV/u.

Ions begin at the Pulsed Sputter Ion Source while protons begin at the Proton LINAC. The bunched beam is extracted from the AGS to RHIC (AtR) line via a

to study the effects of cold nuclear matter at $\sqrt{s_{NN}}$=200GeV(see section). The choice of deuterons instead of protons was mainly motivated by technical reasons. The mass/charge ratio is similar to gold; this makes it possible to adopt many accelerator setting from $Au + Au$

fast extraction beam (FEB) system. The FEB system is capable of performing single bunch multiple extraction of a heavy ion beam or a high intensity proton beam at a rate of 30Hz [222]. Multiple AGS bunches are injected into a single RHIC bunch and put into a waiting radio frequency (r f) bucket through the AtR. The Au atoms are stripped of their last two electrons and are injected into RHIC with a charge of +79. RHIC is designed to handle up to 60 bunches where each bunch contains approximately 109 Au ions. Once in RHIC, the Au bunches are accelerated to the final collision energy and stored for data taking.

The first physics run took place in 2000, with $Au + Au$ collisions at 130GeV per nucleon. The following four running periods include Au+Au collisions at 200, 62.4, and 19.6GeV/nucleon, $Cu+Cu$ collisions at 200, 62.4, and 22.4GeV/nucleon, $d+Au$ collisions at 200GeV/nucleon, and polarized $p+p$ collisions at 200GeV. The analysis presented in this thesis is based on data acquired during run IV, the specifications of which are discussed in chapter 5.

4.2 Experimental Conditions

The technique used in experiments studying relativistic nucleus-nucleus collisions are similar to those used in high energy elementary particle physics experiments. The primary difference is that the particle multiplicities and the background for various processes differ between the nuclear and particle physics environments. For central collisions, with impact parameters near zero, the particle multiplicity scale approximately as the mass of the colliding system and therefore, with nuclear masses around 200, can be a factor of 200 times higher in collisions of heavy nuclei compared to collisions between protons at the same energy. The multiplicities scale weakly as a function of energy with $dn/dy(\mathrm{y}_{cm}) \sim ln\sqrt{s}$. Likewise, the combinatorial backgrounds underlying process such as Drell-Yan production, particle and resonance decays, and photon production increase more than linearly with (and usually as the square of) increasing primary particle multiplicities, complicating reconstruction of these signals.

4.3 Detector Components

The types of detectors in the collider experiments can be divided into four categories: detectors for charged particle tracking, calorimeter for energy measurements; detectors for particle identification; and photon detectors. In contrast to the high energy physics environment, at the heavy ion colliders: the p_T of the particles of interest is typically lower; the luminosities are considerably lower, allowing the use of slower detectors and readout times; while the particle multiplicities are considerably higher requiring finer segmentation of detectors and larger event sizes. Tracking detectors utilize the ionization of a charged particle traversing a medium in order to determine its trajectory. For tracking near the primary collision region within 5 to 10cm, where particle densities approach $\sim$ 100 to 1000 cm^{-2}, silicon detectors (pixels, strips, drift) [223] with excellent position (20 μ) and double track (200 μ) resolution are used. Measurements close to the primary interaction are particularly important for detecting decays of short-lived strange and charm particles, of extreme importance in quark-gluon plasma searches. For large area tracking away from the interaction region and at more moderate particle densities of $\sim$ 1cm^2, time-projection chambers and other types of tracking detectors are used [224]. The calorimeters used at the heavy ion colliders are of two basic types. Conventional sampling calorimeters [225] can be used for electromagnetic and hadronic energy determination, and measurements of jets. Highly segmented calorimeters can be used, in addition to the above measurements, to measure high-energy particles and photons. Particle identification of charged particles can be accomplished using ionization energy loss, Cerenkov radiation, transition radiation, or time-of-flight techniques. At higher momenta, combinations of these techniques are sometimes necessary for best results, especially when measuring over a wide range of p_T over which any single technique may not be applicable. Highly segmented photon detectors will be utilized for the measurements of photon radiation. Detectors from new types of materials have been developed [226] for higher efficiencies and with smaller Moliere radius to be able to improve performance and to more finely segment photon detector systems.

4.4 RHIC Detectors

Currently, there are four major experiments at RHIC. The two largest detectors, STAR (Solenoidal Tracker at RHIC) and PHENIX (Pioneering High Energy Nuclear Interaction Experiment), are located at the 6 and 8 o'clock positions, respectively. The smaller experiments, BRAHMS (Broad Range Hadron Magnetic Spectrometers) and PHOBOS, are located at the 2 and 10 o'clock positions, respectively. The four experiments were designed with some overlap and some complementarity in the physics processes they could measure. In this way it is frequently possible for one experiment to crosscheck the results of another, yet each experiment has its own area of specialization.

The BRAHMS experiment is designed to measure $\pi^{\pm}$, $p^{\pm}$, $k^{\pm}$ in the region $0 < |y| < 4$ and $0.2 < P_T < 3$ GeV/c. Having two detector arms, one at forward rapidity and one near mid-rapidity, BRAHMS is able to provide information on baryon-poor and baryon-rich regions of particle production.

The PHOBOS experiment centers around a search for fluctuations in the number of produced particles and their angular distributions as a way of identifying a phase transition from normal nuclear matter to a QGP state. The detector is able to study 1% of the produced particles in detail while also offering a global picture of the collision event. PHOBOS measures quantities such as the temperature, size, and density of the collision fireball.

The PHENIX experiment specializes in examining leptons and photons coming from the collision fireball. Besides the quest to help identify the existence of QGPs, PHENIX also hopes to aid in uncovering the reasons behind the proton's spin structure, since the three valence quarks are known to not carry all of the spin. There are over 430 physicists working with this detector.

The STAR experiment is composed of 52 institutions from 12 countries, with a total of 550 collaborators. STAR is designed to give information on many observables, both inclusively and on an event-by-event basis. Due to the significantly increased particle production at RHIC as compared to previous colliders and also the hard parton-parton scattering in heavy ion collisions, STAR was designed to enable measurements of observables that help determine global variables such as entropy, baryochemical and strangeness chemical potentials, temperature, fluctuations, and particle and energy flow. High transverse momentum p_T processes are also examined via high p_T jets, mini-jets, and single particles. The STAR experiment, through which the measurement for this thesis was made, is described in more detail in the following two sections.

4.5 Solenoidal Tracker at RHIC

STAR was constructed to investigate the behavior of strongly interacting matter at high energy density and to search for signatures of quark-gluon plasma (QGP) formation. Key features of the nuclear environment at RHIC are a large number of produced particles (up to approximately one thousand per unit pseudo-rapidity) and high momentum particles from hard parton-parton scattering. STAR measures many observables simultaneously to study signatures of a possible QGP phase transition and to understand the space-time evolution of the collision process in ultra-relativistic heavy ion collisions. The goal is to obtain a fundamental understanding of the microscopic structure of these hadronic interactions at high energy densities.

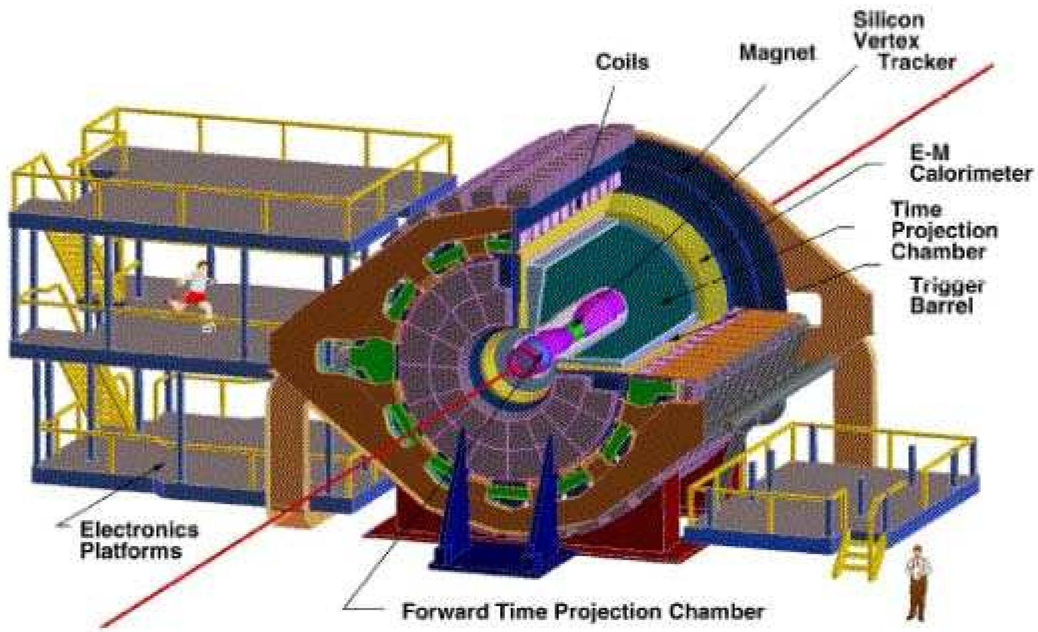

Figure 4.2: Perspective view of the STAR detector, with a cutway for viewing inner detector systems.

4.5.1 Detector Overview

STAR was designed primarily for measurements of hadron production over a large solid angle, featuring detector systems for high precision tracking, momentum analysis, and particle identification at the center of mass (c.m.) rapidity. The large acceptance of STAR makes it particularly well suited for event-by-event characterizations of heavy ion collisions and for the detection of hadron jets.

The layout of the STAR experiment [227] is shown in Figure (4.2). A cutaway side view of the STAR detector as configured for the RHIC 2001 run is displayed in Figure (4.3). A room temperature solenoidal magnet [228] with a maximum magnetic field of 0.5 T provides a uniform magnetic field for charged particle momentum analysis. Charged particle tracking close to the interaction region is accomplished by a Silicon Vertex Tracker [229] (SVT) consisting of 216 silicon drift detectors (equivalent to a total of 13 million pixels) arranged in three cylindrical layers at distances of approximately 7, 11 and 15 cm from the beam axis. The silicon detectors cover

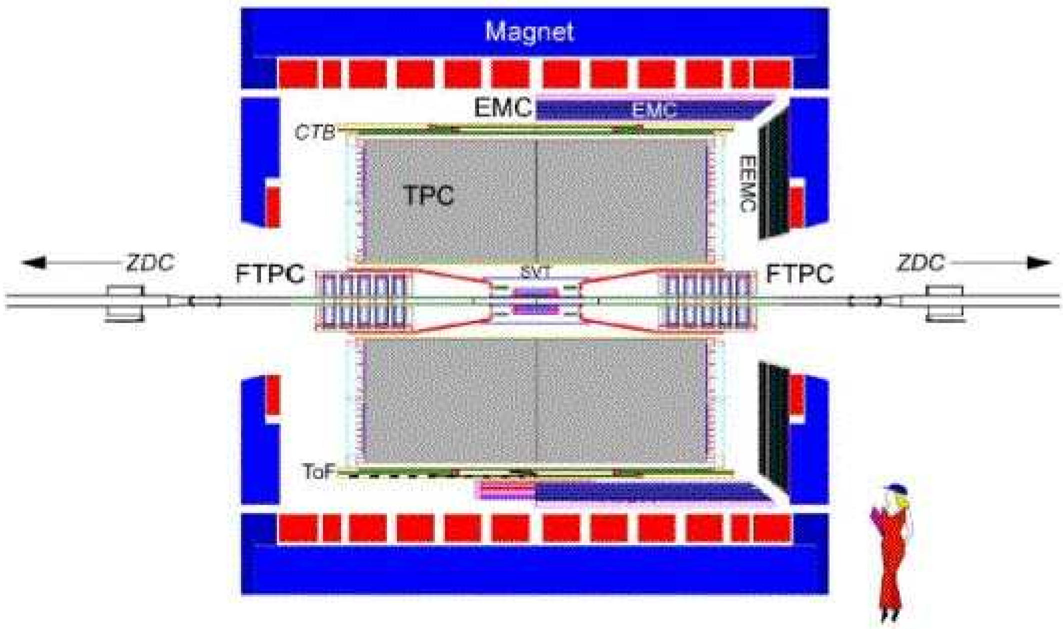

Figure 4.3: Cutway side view of the STAR detector.

a pseudo-rapidity range $|\eta| <= 1$ with complete azimuthally symmetry $\Delta\phi = 2\pi$. Silicon tracking close to the interaction allows precision localization of the primary interaction vertex and identification of secondary vertices from weak decays of, for example, Λ, Ξ, and Ωs. A large volume Time Projection Chamber [230] (TPC) for charged particle tracking and particle identification (Figure 4.4) is located at a radial distance from 50 to 200 cm from the beam axis. The TPC is 4 meters long and it covers a pseudo-rapidity range $|\eta| <= 1.8$ for tracking with complete azimuthal symmetry $\Delta\phi = 2\pi$ providing the equivalent of 70 million pixels via 136,608 channels of front end electronics [231] (FEE). Both the SVT and TPC contribute to particle identification using ionization energy loss, with an anticipated combined energy loss resolution (dE/dx) of 7% (σ). The momentum resolution of the SVT and TPC reach a value of δp/p = 0.02 for a majority of the tracks in the TPC. The δp/p resolution improves as the number of hit points along the track increases and as the particle's momentum decreases, as expected.

To extend the tracking to the forward region, a radial-drift TPC (FTPC) [232] is

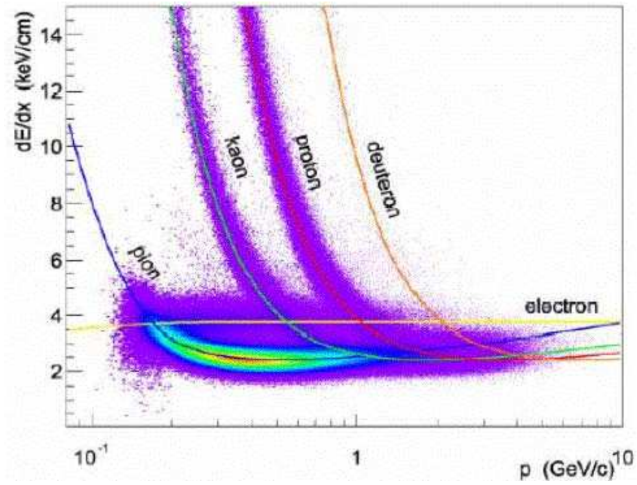

Figure 4.4: Particles identification using the STAR-TPC.

installed covering $2.5 < |\eta| < 4$, also with complete azimuthal coverage and symmetry. To extend the particle identification in STAR to larger momenta over a small solid angle for identified single-particle spectra at mid-rapidity, a time-of-flight (TOF) patch covers -1$< \eta < 0$ and $\Delta\phi = 0.04\pi$. About 10 percent of the full-barrel electromagnetic calorimeter [233] (EMC) shown in Figure (4.3). The EMC covers -1 $< \eta <$1 and $\Delta\phi = 2\pi$ and an endcap electromagnetic calorimeter [234] (EEMC) obtains an eventual coverage of -1 $< \eta<$ 2 and $\Delta\phi = 2\pi$. This system allows measurement of the transverse energy of events, and trigger on and measure high transverse momentum photons, electrons, and electromagnetically decaying hadrons. The EMC's include shower-maximum detectors to distinguish high momentum single photons from photon pairs resulting from π^0 and η meson decays. The EMC's also provides prompt charged particle signals essential to discriminate against pileup tracks in the TPC, arising from other beam crossings falling within the 40 μsec drift time of the TPC, which are anticipated to be prevalent at RHIC pp collisions luminosities $\cong 10^{32} cm^{-2} s^{-1}$.

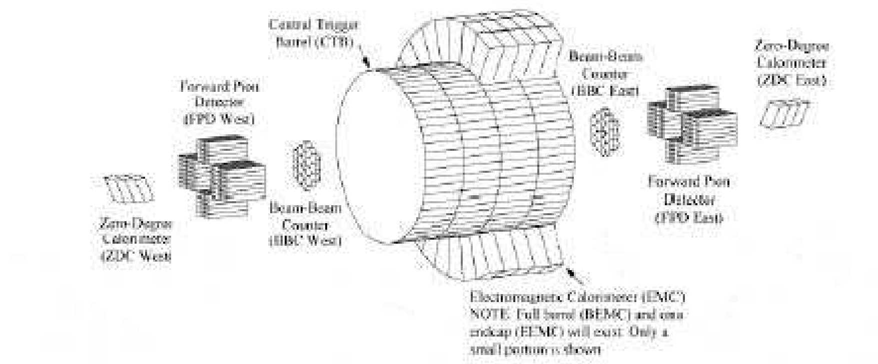

Figure 4.5: STAR Detector trigger components.

4.5.2 **Data Flow**

The STAR Trigger

After a collision, the detector must very quickly decide if the collision was of interest and should be recorded. The decision must be made before the particle signals have cleared from the STAR electronics. We call the detectors, electronics, and software that make this decision the trigger. A trigger menu defines a set of trigger conditions which, if satisfied, allow an event to be passed to the event filter. Trigger conditions are given in terms of logical combinations of trigger elements. A trigger element represents a physical object (e.g. an electron, or missing energy). STAR built a complex triggering system which enable data acquisation with multiple triggering scheme in parallel. The STAR Trigger is designed to facilitate the search for new states of matter such as the quark-gluon plasma and the quest to understand the interior of hadrons. It is a pipelined system in which digitized signals from the fast trigger detectors are examined at the RHIC crossing rate[2] (∼10MHz). This information is used to determine whether to begin the amplification-digitization-acquisition (ADA) cycle for slower, more finely grained detectors. The slow detectors[3] provide

[2]Typically 9.37 MHz during the 130 GeV per nucleon pair AuAu running in Summer 2000.

[3]Fast detectors are fully pipelined. Slow detectors are not and include the central Time Projection Chamber (TPC), Silicon Vertex Tracker (SVT), Forward TPC (FTPC), Shower Max Detector (SMD), Photon Multiplicity Dectector (PMD), Time-of-Flight-patch (TOFp).

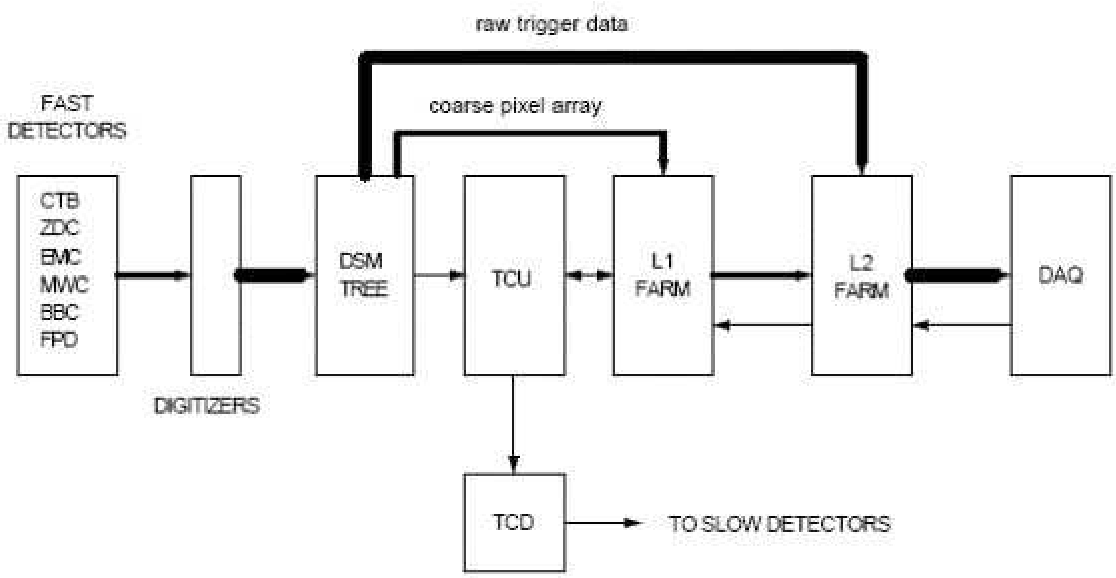

Figure 4.6: Data flow through the trigger. See text for definition of acronyms.

the momentum and particle identification on which our physics conclusions are based, but they can only operate at rates of $\sim$ 100Hz. Interaction rates approach the RHIC crossing rate for the highest luminosity beams, so the fast detectors (Figure 4.5) must provide means to reduce the rate by almost 5 orders of magnitude. Interactions are selected based on the distributions of particles and energy obtained from the fast trigger detectors. Interactions that pass selection criteria in four successive trigger levels are sent to storage at a rate of $\sim$5Hz($\sim$50MB/s). The final trigger decision is made in Level 3 based on tracking in the slow detectors. The first three levels, 0,1,and 2, are based on fast information.

Data flow through the trigger (TRG) is shown in Figure (4.6). Output from DSM tree is fed to the Trigger Control Unit (TCU) where it is combined with detector status bits to act as an 18 bit address to a lookup table (LUT) which holds the trigger word that goes with each bit combination. The trigger word then acts as an address into the Action World LUT which holds the information on which detectors are to be involved and what action is to be taken for this trigger. This DSM-based decision tree constitutes Level 0 of the trigger and is constrained to issue a decision within 1.5μs from the time of the interaction. When an interaction is selected at Level 0, each STAR detector designed to participate in this type of event is notified using a 4-bit Trigger Command and told to identify this event with a 12-bit token [235].

While the amplification/digitization cycle is proceeding in the slow detectors, the fast detector information is gathered by VME processors and examined in a coarse pixel array (CPA) at Level 1. The cells of Level 1 have $\delta\eta\sim0.5$ and $\phi\sim\pi/2$, suitable to respond to gross spatial symmetries in particle distributions typical of beam-gas background, which could lead to Level 1 aborts. Interactions not aborted by Level 1 continue their data acquisition cycle while the raw trigger dataset is collected in the memory of one of several CPUs that continue the Level 2 farm. This raw data set forms a fine pixel array whose pixels are of suitable size for jet isolation or for refinement of particle topologies useful in selecting specific interaction mechanisms. When an interaction is accepted at Level 2, the trigger system notifies the central Data Acquisition (DAQ) system and relinquishes control of the proto-event to DAQ.

Data flow through the trigger pipeline is controlled via a 12-bit token, which is issued for each interaction that is accepted at Level 0. This token guarantees that the resources are available in the trigger system to complete a Level 2 decision to abort or to hand off the event to DAQ within 5ms of the occurrence of the interaction. All of the raw trigger detector data and the results from Level 1 and Level 2 analyses are packaged and sent to DAQ with the token. The token stays with the event and is used as an identifier within DAQ to organize collection of all the fragments from each STAR detector. Once DAQ either accepts and stores the event or aborts it, the token is returned to the trigger and recycled.

The goals of the trigger system can be summarized as follows: • Select central collisions in AA and pA interactions based on charged particle multiplicity in the TPC acceptance. These involve the largest number of nucleons and are expected to maximize the collective effects. •Select ultra-peripheral collisions. These represent specific elementary processes which may be enhanced in AA collisions. • Select jet events. Jets reveal internal structure. • Select events based on bunch polarization. Polarization provides a sensitive probe of spin structure. • Select Cosmic ray events. Useful for system debugging and calibration. • Adapt to new physics. To explore new territory and select specific rare interactions. • Operate for pp, pA, and AA interactions. The STAR research program investigates such interactions for spin and QGP(Quark Gluon Plasma) studies. • Issue triggers when requested by different STAR detectors. Necessary for calibration of individual detectors. • Accommodate new detectors. To support STAR's vigorous program. • Reject background. Expect beam-gas rate of 100Hz at maximum luminosity. • Minimize trigger related deadtime. Maximize beam use. • Open TPC amplifier grid in <1.5μs. Lose 2% of the data per μs delay. • Must allow understanding of any trigger bias introduced in event selection.

DAQ

The design and implementation of the STAR DAQ system [236,237] was driven by the characterstics of STAR's main detectors, a large Time Projection Chamber(TPC), and to a lesser degree two smaller Forward TPCs (FTPC) and a Silicon Vertex Tracker(SVT). Together these detectors produce 200MB of data per event and are able to read out events at 100Hz. The RHIC Computing Facility (RCF) manages the storage of raw data for all of the RHIC experiments using an HPSS hierarchical storage system. By balancing the expected rate of offline data analysis with the rate of data production, resources were allocated to STAR to support sustained raw data rates up to 30MB/sec for steady rate operation. The central task of the STAR DAQ system is then to read data from the STAR detectors at rates up to 20,000MB/sec, to reduce the data rate to 30MB/sec, and to store the data in the HPSS facility. 200MB events are reduced to 10MB by zero suppression performed in hardware using cus-

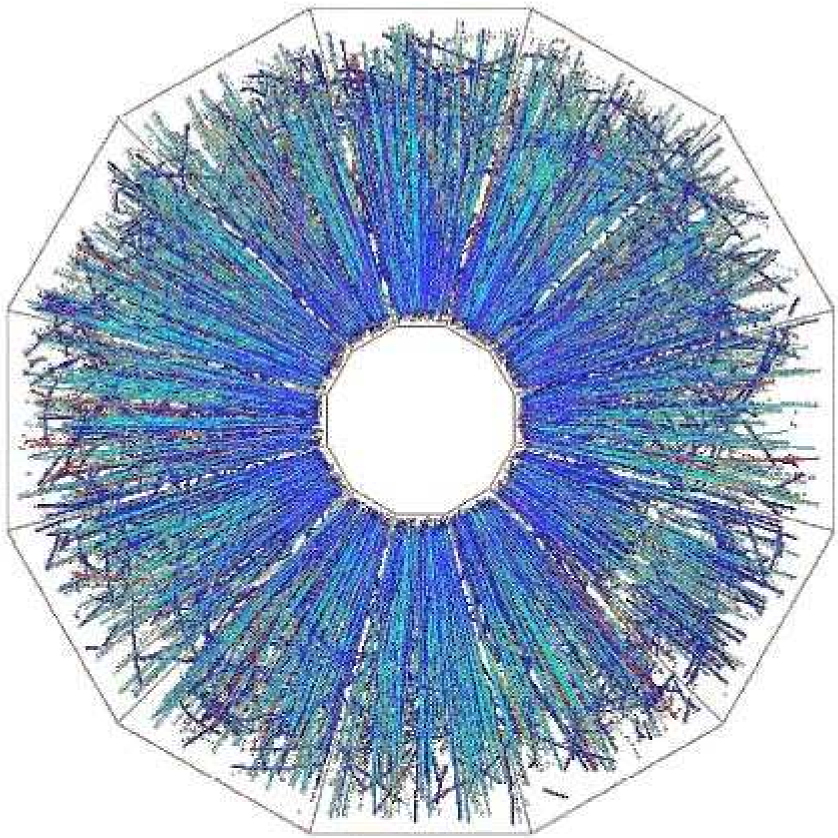

Figure 4.7: Beam,s eye view of a central event in the STAR TPC. This event was drawn by the STAR level-3 online display.

tom designed ASICs. A Level 3 Trigger (Figure 4.7) reconstructs tracks in real time (within 200ms) and provides a physics-based filter to further reduce the sustained output data rate to ∼30MB/sec. Built events are sent via Gigabit Ethernet to the RCF and stored to tape using HPSS.

The management of events within the DAQ system (Figure 4.8) can be described in two phases according to whether the build decision for that event has been made by L3. Before the decision, the Global Broker (GB) handles the overall management of the event. At the same time as the data are read from the detectors into the DETs, the GB receives a token and trigger detector data from the Trigger/DAQ Interface (TDI) via a Myrinet network. The GB assigns L3 processors to analyse the event and wait for an event decision. If the event is rejected by L3, GB instructs the DETs

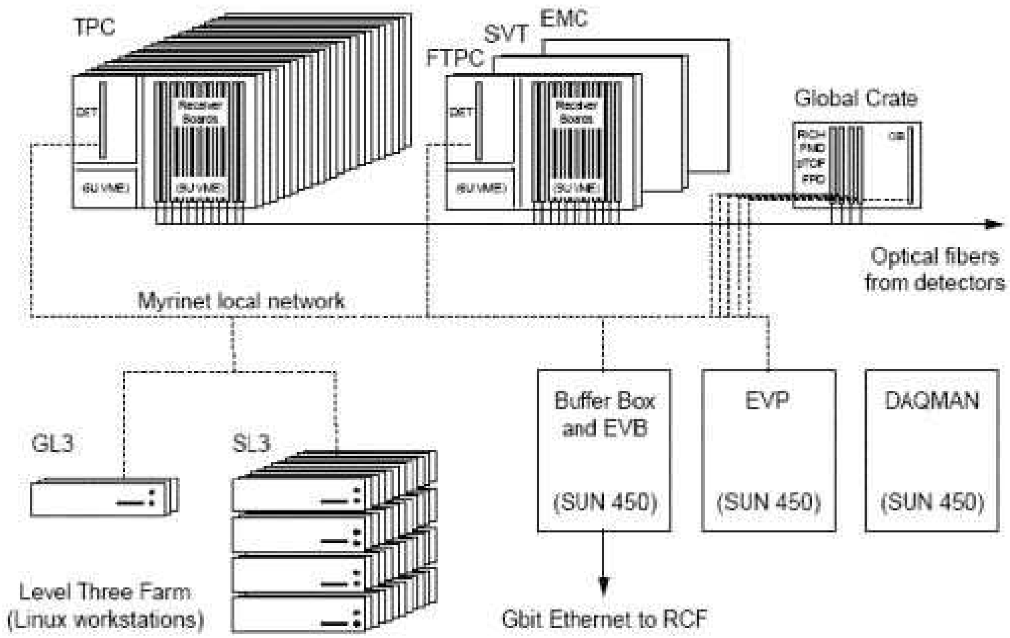

Figure 4.8: Schematic Overview of the STAR DAQ.

to release the buffers associated with the event and returns the token to TDI for re-use. If the event is accepted by L3, responsibility for the management of the event is transffered to the Event Builder (EVB). The EVB collects and formats all of the contributions. At this time, EVB instructs the DETs to release the buffers associated with the event and passes the event to Spooler(SPOOL) which handles the writing of the event to RCF. When the event is written, EVB returns the token to the TDI.

4.5.3 Trigger Detectors

The trigger detectors in STAR are all fast detectors, fully pipelined with short readout times. There is a central trigger barrel (CTB) around the TPC at $|\eta|$ <1, the beam-beam counters (BBCs) at both sides of the STAR detector and the zero degree calorimeters (ZDC) in the accelerator tunnel on both sides of the interaction area.

The CTB (Figure 4.9) and the BBC (Figure 4.10) consist of plastic scintillators read out via photomultipliers. They are used to register charged particles and to provide a first estimate of the multiplicity of the event. The ZDCs (Figures 4.12 and

4.13) detect neutrons that did not participate in the collision and thus fly in beam direction. The ZDCs are located behined the first set of magnets in the accelerator tunnel where all charged particles are deflected by the magnetic field.

By forming a concidence between the ZDCs, the vertex position can be derived from flight time differences. Howerver, this is only possible if neutrons are detected on both sides of the interaction region. In d+Au collisions, this is usually not the case, so a vertex determination with the ZDCs in general not possible in these events. Each experiment at RHIC has a complement of ZDC's for triggering and cross-calibrating the centrality triggering between experiments [238]. Displayed in Figure (4.11) is the correlation between the summed ZDC pulse height and that of the CTB for events with a primary collision vertex successfully reconstructed from tracks in the TPC. The largest number of events occurs for large ZDC values and small CTB values (gray region of the plot). From simulations these correspond to collisions at large impact parameters, which occur most frequently and which characteristically leave a large amount of energy in the forward direction (into the ZDC) and a small amount of energy and particles sideward (into the CTB). Collisions at progressively smaller impact parameters occur less frequently and result in less energy in the forward direction (smaller pulse heights in ZDC) and more energy in the sideward direction (larger pulse heights in CTB). Thus, the correlation between the ZDC and CTB is a monotonic function that is used in the experiment to provide a trigger for centrality of the collision. The ZDC is double-valued since collisions at either small or large impact parameter can result in a small amount of energy in the forward ZDC direction.

A minimum bias trigger was obtained by selecting events with a pulse height larger than that of one neutron in each of the forward ZDC's, which corresponds to 95 percent of the geometrical cross section. Triggers corresponding to smaller impact parameter were implemented by selecting events with less energy in the forward ZDCs, but with sufficient CTB signal to eliminate the second branch at low CTB values

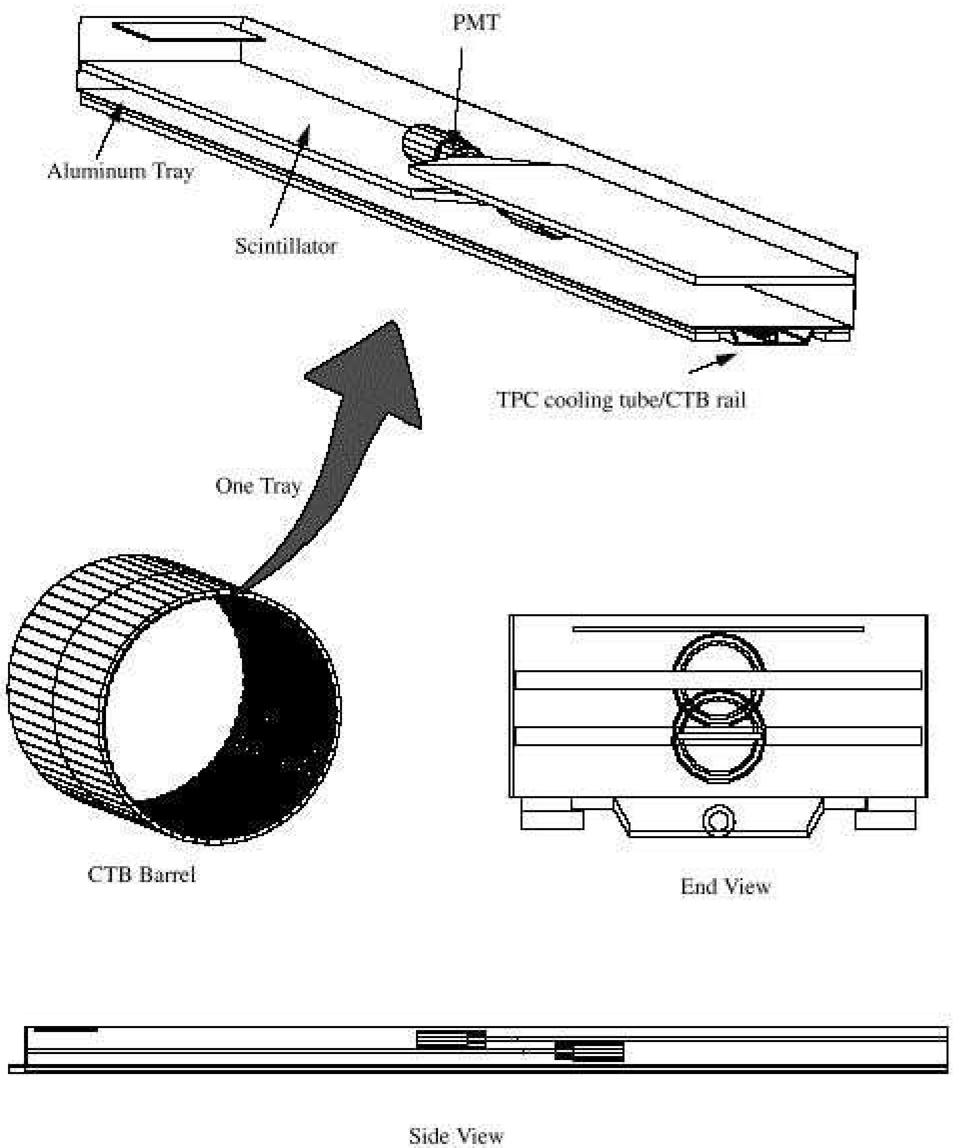

Figure 4.9: The Central Trigger Barrel at STAR.

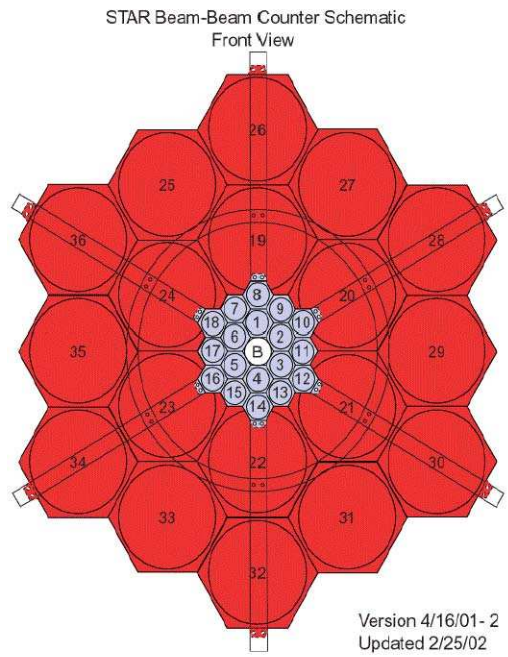

Figure 4.10: Schematic front-view of the STAR Beam-Beam Counter.

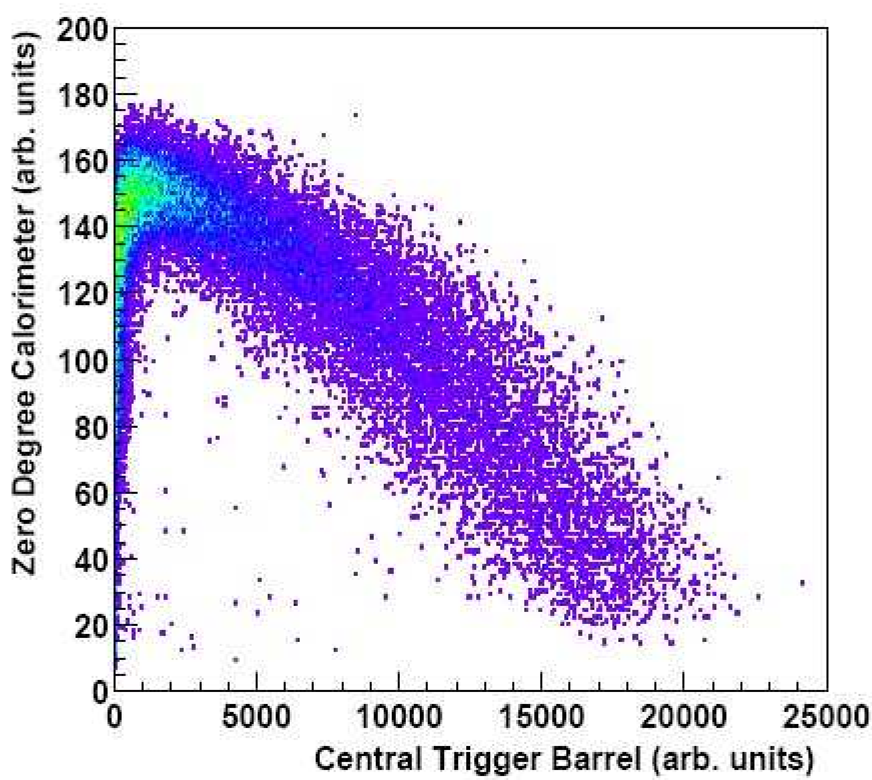

Figure 4.11: Correlation between the summed pulse heights from the Zero Degree Calorimeters and the Central Trigger Barrel for events with a primary collision vertex successfully reconstructed from tracks in the Time Projection Chamber.

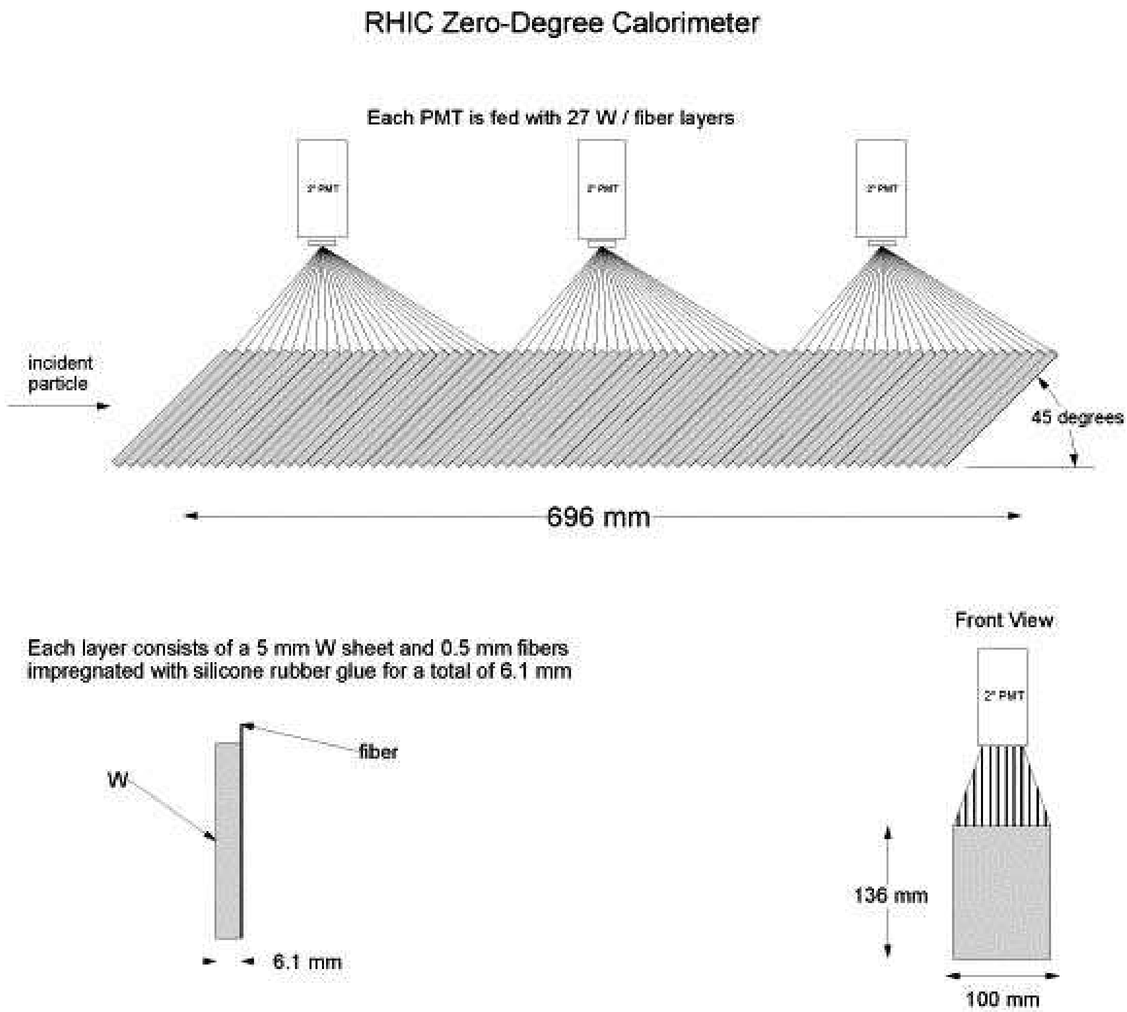

Figure 4.12: Zero Degree Calorimeters.

shown in Figure (4.11).

4.5.4 Calorimeters

The STAR Barrel EMC consists of sampling towers, shower maximum detector, and a preshower detector. The description of these components is given in the following sections.

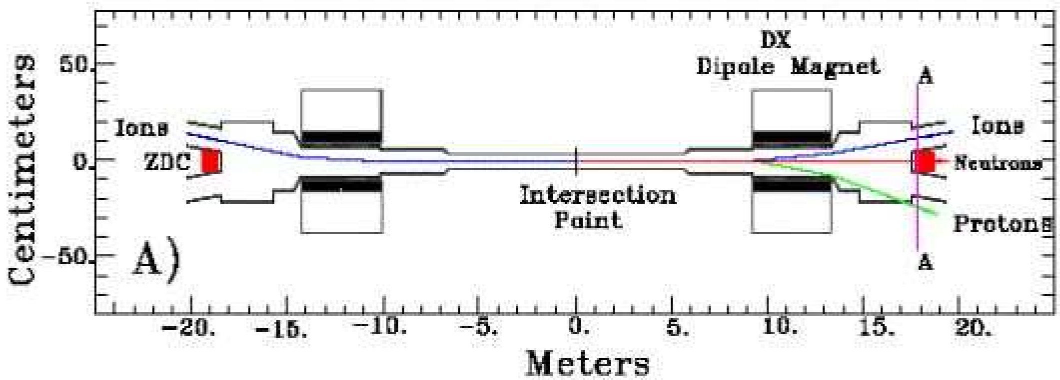

Figure 4.13: Plan view of the collision region "beam's eye" view (section A-A) of the ZDC location indicating deflection of protons and charged fragments downstream of the dipole magnet.

Mechanical Structure

The STAR Barrel EMC (BEMC) is a sampling calorimeter and consists of layers of lead and scintillator. It covers more than 100 m^2 of area outside the TPC for $|\eta| < 1$. The Barrel calorimeter includes a total of 120 calorimeter modules, each subtending 6^0 in ϕ (0.1 radian) and 1.0 unit in η. The modules are mounted 60 in ϕ by 2 in η (Figure 4.14). Each module is $\sim$ 26 cm wide by $\sim$ 293 cm long with an active depth of 23.5 cm or 21 radiation lengths (X_0) and about 6.6 cm in structural plates (of which 1.9 cm lies in front of the detector). A module is further divided into 40 towers, 2 in ϕ and 20 in η, with each tower being 0.05 in $\Delta\phi$ by 0.05 in $\Delta\eta$. The calorimeter thus is physically segmented into a total of 4800 towers, each of which is projective and pointing back to the interaction diamond. Figure 4.15 shows a side view of a module illustrating the projective nature of the towers in η-direction.

Each module consists of a lead-scintillator stack and shower maximum detectors located $\sim$ 5 radiation lengths from the front of the stack (Figure 4.15). There are 20 layers of lead and 21 layers of scintillator. Lead layers are 5 mm thick; 2 layers of scintillator located in front of the stack and used in the preshower detector are 6 mm thick, and the remaining 19 scintillator layers are 5 mm thick. The stack is held together by 30 straps connecting the non-magnetic front and back plates of

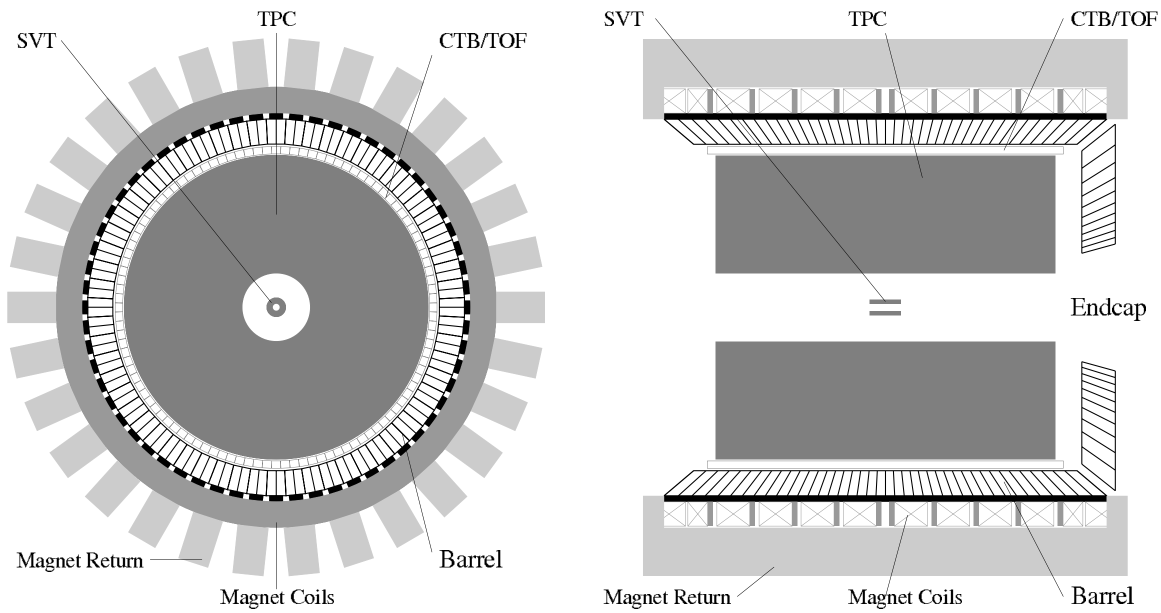

Figure 4.14: Cross sectional view of the STAR detector. The barrel EMC covers $|\eta| < 2$ and 2π in azimuth.

a calorimeter module. Figure 4.16 shows an end view of a module along with the mounting system and the compression components.

Optical Structure

There are 21 active scintillating layers in the barrel calorimeter. The scintillator layers alternate with 20 layers of lead absorber plates. The plastic scintillator layers are manufactured in the form of "mega-tile" sheets with 40 optically isolated area segments ("tiles") in each layer. The layout of the 21^{st} mega-tile sheet is illustrated in figure 4.15. The signal from each scintillating tile is read-out with a wavelength shifting (WLS) fiber embedded in a "σ-groove" that is machined in the tile (Figure 4.17). The optical isolation between individual tiles in a given layer is achieved by carving 95% of the depth through the scintillator sheet and filling the resulting groove with opaque, silicon dioxide loaded epoxy. The potential optical cross talk between adjacent tiles as a result of the remaining 5% of the scintillator thickness is cancelled to the level of $< 0.5\%$ by a thin black line painted at the location of the isolation

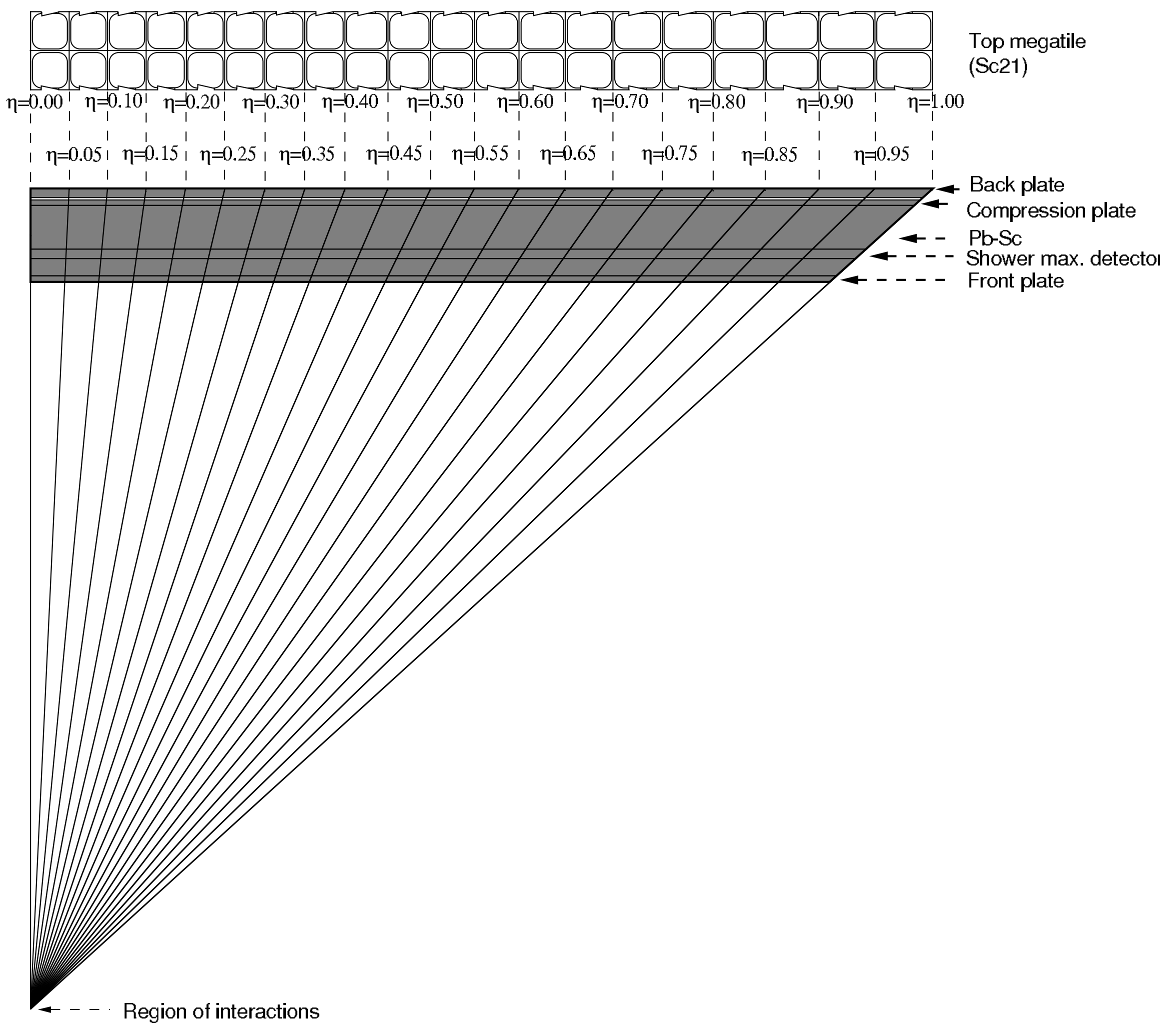

Figure 4.15: Side view of a calorimeter module showing the projective nature of the towers. The 21^{st} megatile layer is also shown.

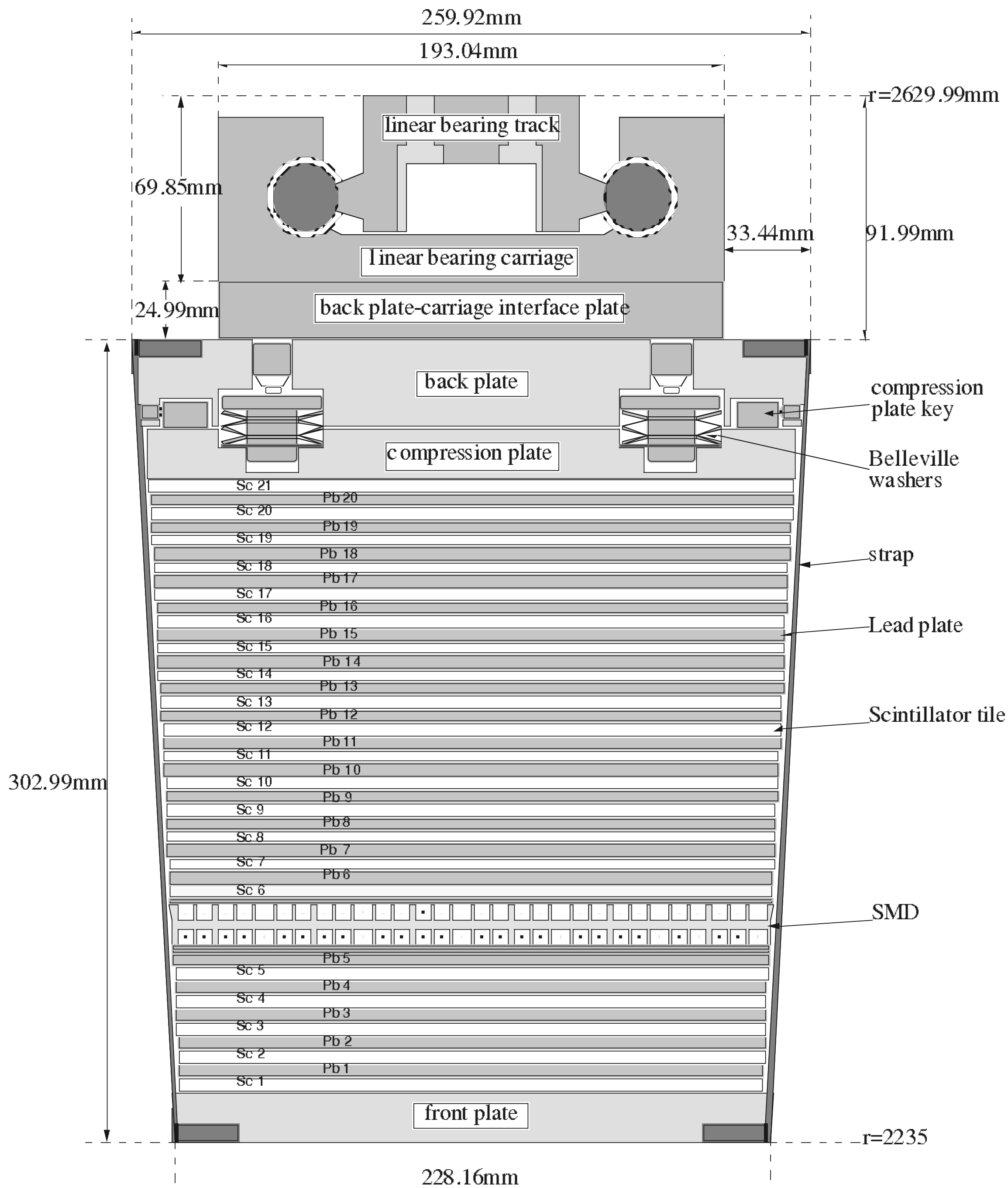

Figure 4.16: End view of a calorimeter module showing the mechanical assembly including the compression components and the rail mounting system. Shown is the location of the two layers of shower maximum detector at a depth of approximately $5X_0$ from the front face at $\eta = 0$.

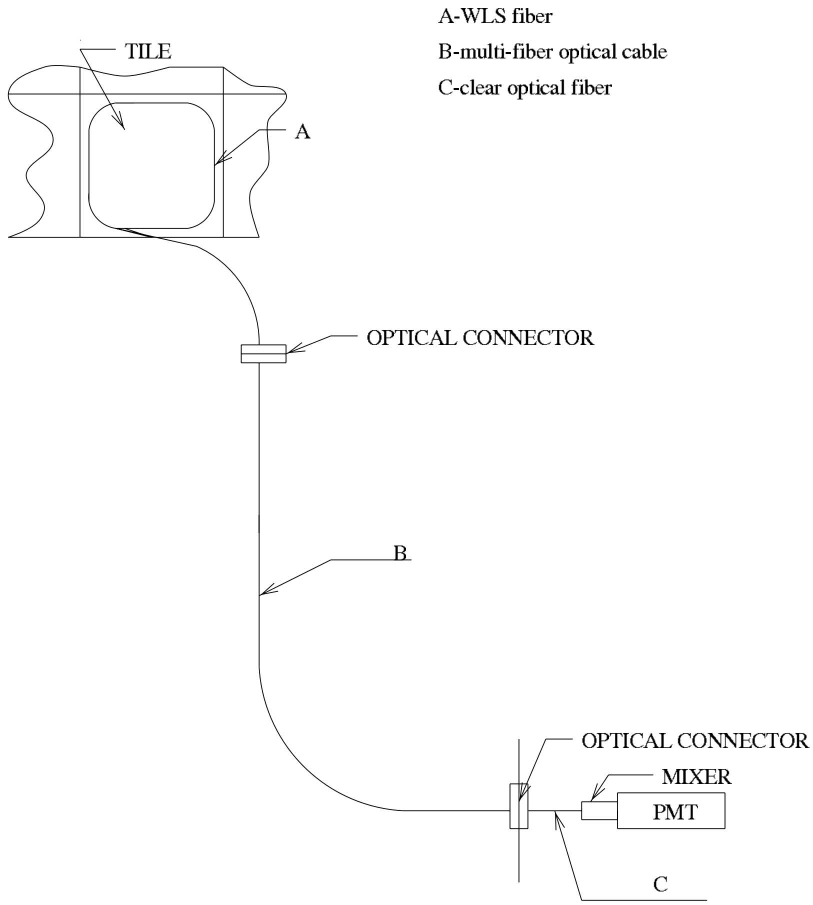

Figure 4.17: A diagram of tile/fiber optical read-out scheme of Barrel EMC.

grooves on the uncut scintillator surface.

A total of 840 different tile shapes (420 plus their mirror image) were machined in the layers of each module. The machined, unpolished mega-tile edges are painted white with Bicon BC620 reflective paint. White bond paper, which has good diffuse reflectivity and, most important, a high coefficient of friction, is used on both surfaces of the mega-tile as a diffuse reflector between calorimeter layers.

After exiting the scintillator the WLS fiber is routed along the outer surface of the lead scintillator stack, under the module's light tight cover and terminate in a multi-fiber optical connector at a back-plate of the module. A 2.1 m long multi-fiber optical cable of clear fibers connected with mating optical connectors, carries the light from the optical connector through the magnet structure to decoder boxes mounted on the outer surface of the STAR magnet, where the light from 21 tiles composing a single tower is merged onto a single photo multiplier tube (PMT).

The photo multiplier tubes used for the EMC towers are Electron Tube Inc. model 9125B. PMT's are powered by Cockroft Walton bases that are remotely controlled by the slow control software written in LabView.

Shower Maximum Detector

A shower maximum detector (SMD) is used to provide fine spatial resolution in a calorimeter which has segmentation (towers) significantly larger than an electromagnetic shower size. While the barrel EMC towers provide presice energy measurements for isolated electromagnetic showers, the high spatial resolution provided by the SMD is essential for π^0 reconstruction, direct γ identification, and electron identification. Information on shower position, shape, and, from the signal amplitude, the electromagnetic shower longitudinal development are provided.

Figure 4.18 shows the conceptual design of the STAR BEMC SMD. It is located ~ 5 radiation lengths deep in the calorimeter modules at $\eta = 0$ including all material immediately in front of the calorimeter[4]. A two sided aluminum extrusion provides ground channels for two independent planes of proportional wires. Independent printed circuit (PC) board cathode planes with strips etched in the η and ϕ directions respectively allow reconstruction of a two dimensional image of the shower as shown schematically in Figure 4.18.

The SMD is a wire proportional counter – strip readout detector using gas amplification. The basic structure of the detector is an aluminum extrusion with 5.9 mm wide channels running in the η direction. A cross sectional view of the detector is shown in Figure 4.19 and the design parameters are summarized in table 4.2.

In the center of the extrusion channels are 50 μm gold plated tungsten wires. The

[4]The depth of the shower maximum detector varies from $4.6X_0$ to $7.1X_0$ counting only the calorimeter material as η varies from 0 to 1

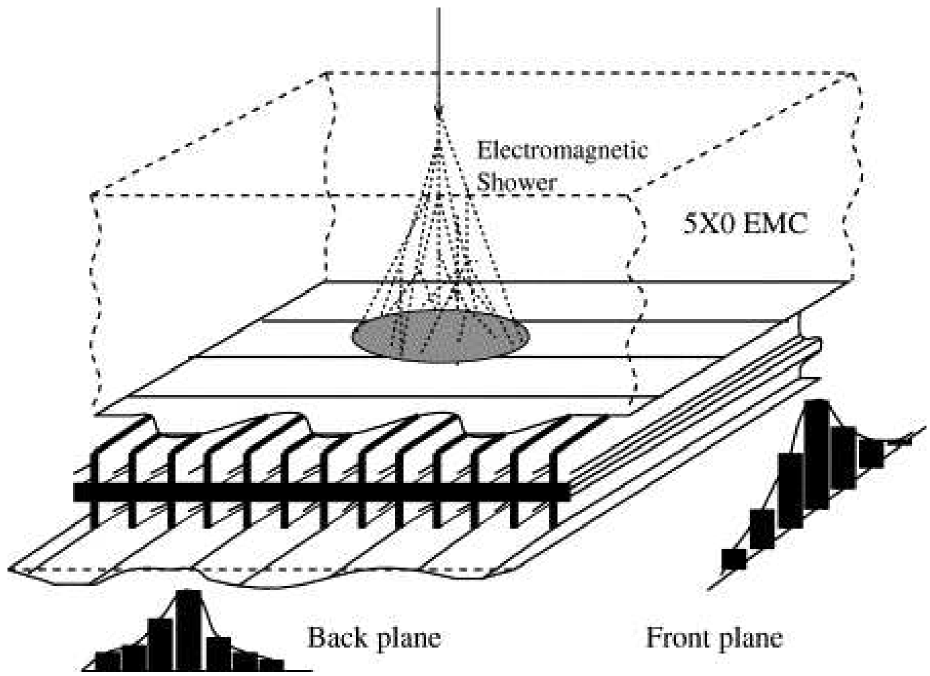

Figure 4.18: Schematic illustration of the double layer STAR BEMC SMD. Two independent wire layers separated by an aluminum extrusion image electromagnetic showers in the η and ϕ directions on corresponding pad layers.

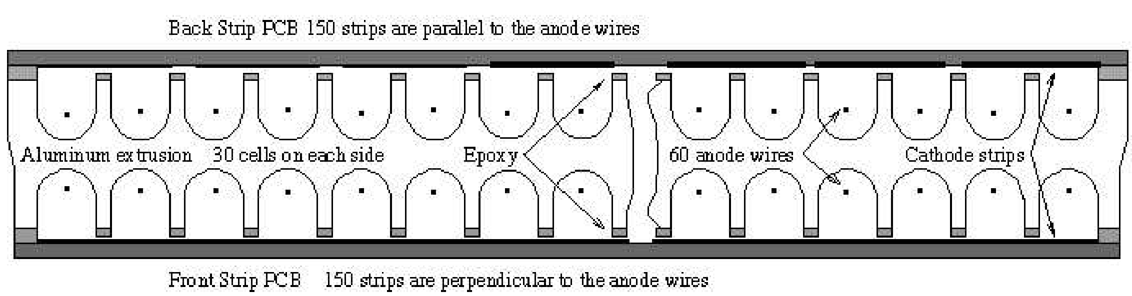

Figure 4.19: Cross sectional view of the SMD showing the extruded aluminum profile, the wires and cathode strips.

SMD Design Parameters	
Chamber Position Inside EMC	$\sim 5X_0$ at $\eta = 0$
Rapidity Coverage (Single Module)	$\Delta\eta = 1.0$
Azimuthal Coverage (Single Module)	$\Delta\phi = 0.105$ (6^0)
Occupancy (pp)	$\approx 1\%$
Occupancy (Au+Au)	> 5 to $\sim 25\%$
Chamber Depth (Cathode to Cathode)	20.6 mm
Anode Wire Diameter	50 μm
Gas Mixture	90%-Ar / 10%-CO_2
Gas Amplification	~ 3000
Signal Length	110 ns
Strip Width (Pitch) in η for $\|\eta\| < 0.5$	1.46 (1.54) cm
Strip Width (Pitch) in η for $\|\eta\| > 0.5$	1.88 (1.96) cm
Strip Width (Pitch) in ϕ	1.33 (1.49) cm
Number of Strips per Module	300
Total Number of Modules	120
Total Number of Readout Channels	36000

Table 4.2: STAR Barrel EMC SMD Design Parameters.

detector strips sense the induced charge from the charge amplification near the wire. Strips perpendicular to the wires provide an image of the shower spatial distribution in the η direction. The other set of strips is parallel to the wires; these provide shower coordinate measurements in the ϕ direction. Signals from the cathodes propagate along a transmission line plane in the printed circuit boards to reach the front end electronics (FEE) board. At the FEE board, amplified cathode strip signals are buffered in a switched capacitor array before being multiplexed 80 : 1 to external digitizer crates mounted outside the STAR magnet.

Preshower Detector

The first two scintillating layers of the calorimeter have separate readout fibers. The scintillation light from these two layers of each tower is brought to the multi anode phototubes located in the PMT decoder boxes. A total of 300, 16 pixel multi anode PMT's are used to read 4800 fiber pairs providing the tower preshower signals. Preshower readout electronics were not installed until the RHIC physics run IV.

Barrel EMC Electronics

The BEMC electronics includes trigger, readout of phototubes and SMD, high voltage system for the phototubes, low voltage power, calibration controls, and interfaces to the STAR trigger, DAQ and slow controls. Front end electronics including signal processing, digitization, buffering, formation of trigger primitives, and the first level of readout is located in custom EMC crates located on the outside of the magnet iron. SMD front end electronics including preamplifiers and switched capacitor arrays reside on the EMC modules inside the STAR magnet. Schematic view of the BEMC electronics installed on the magnet steel is shown in Figure 4.20.

4.5.5 Time Projection Chambers (TPCs)

The Time Projection chamber (TPC), first proposed by David Nygren in the late 1970s, exploits the fact that particles traversing a gas volume will ionize some of the gas atoms or molecules, thus creating positive ions and electrons. In an electric field, the electrons and ions will drift along the electric field lines. The electrons are collected with readout devices that measure two-dimensional position information. By measuring the time difference from the passage of the particle to the arrival of the charge at the readout, the third coordinate can be determined. Thus a three-dimensional reconstruction of particle trajectories is possible with a single readout plane. The time when the particles passed through the TPC has to be provided by external detectors, typically by the trigger system of the experiment.

Most TPCs operate in a constant electric field, which leads to a linear dependence of the drift distance on time. This facilitates the track reconstruction and the calibration of the detector. More complicated geometries are possible and have been successfully applied, for example in the TPC of the CERES experiment at CERN [239].

The charge of the traversed particle is determined via the sign of the curvature of

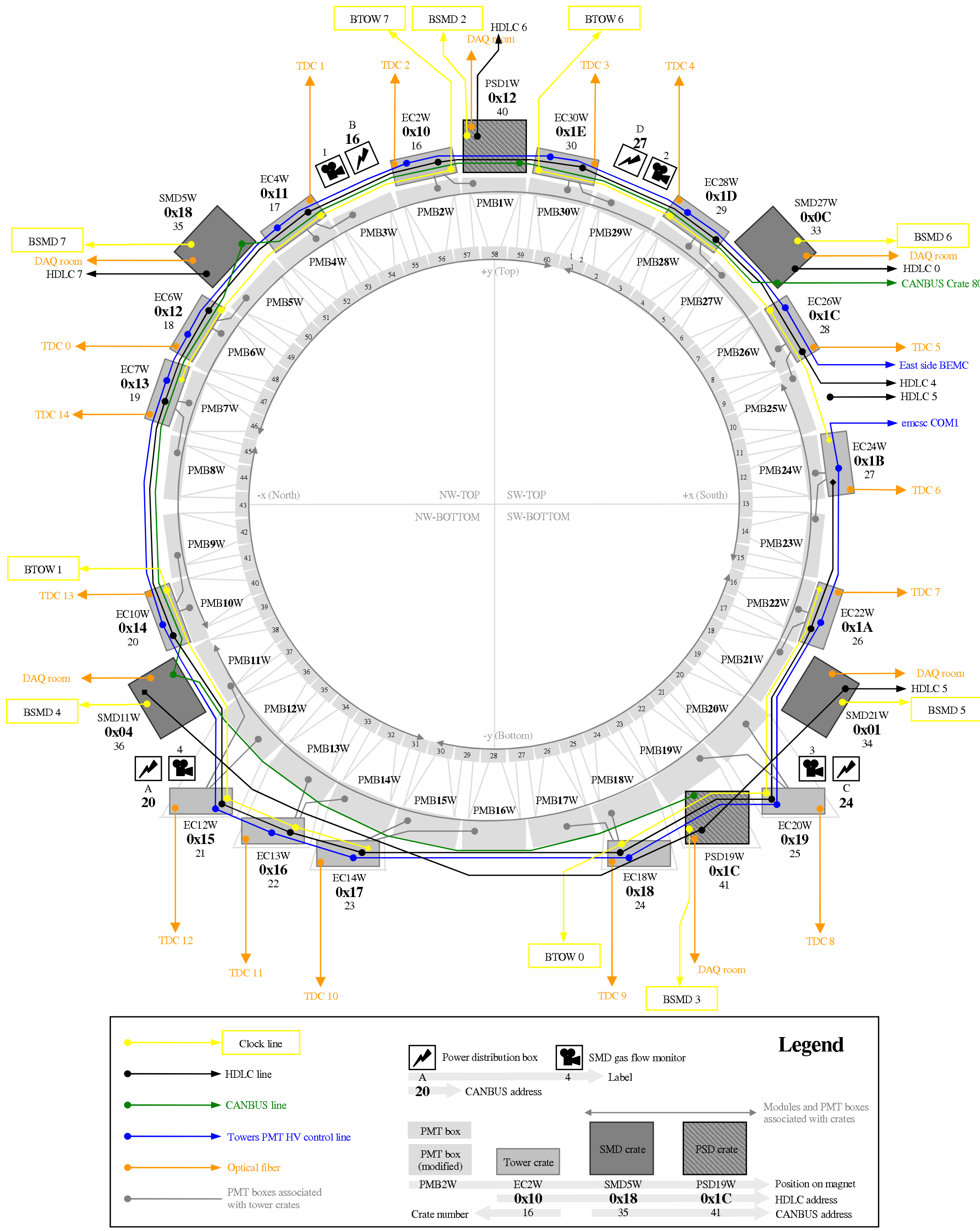

Figure 4.20: Schematic view of the BEMC electronics as seen from the West (positive z direction). During d+Au 2003 and p+p 2004 runs West half of the barrel was fully instrumented.

the particle track in the magnetic field. The transverse momentum p_t (the momentum perpendicular to the beam axis) is given by p_t=0.3q B ρ (GeV/c) where q is the charge of the particle, B is the magnetic field in T parallel to the beam axis and ρ is the helix radius of the trajectory of the particle in m.

The particle can be identified via their specific energy loss in the detector volume. The energy loss per distance traveled is given by the Bethe-Bloch formula:

$$\frac{dE}{dx} \approx Kz^2\frac{Z}{A}\frac{1}{\beta^2}(\frac{1}{2}ln\frac{2m_ec^2\beta^2\gamma^2T_{max}}{I^2} - \beta^2) \tag{4.1}$$

Where K $\sim$ 0.31MeVcm^2, and β and γ are the usual relativistic variables. T_{max} is the maximum kinetic energy imparted to a free electron in a single collision, and I is the mean excitation energy. This formula has been implemented in the STAR analysis in order to detrmine the particle identification of low transverse momentum particles.

Main TPC

The main tracking detector in STAR is the Time Projection Chamber (TPC). With a long cylinder of length of 4.2 m and diameter of 4m it is the world's largest TPC currently in operation (Figure 4.21).

The cylinder is concentric with the beam line, and the inner and outer radii are 0.5 and 2.0m.The acceptance of the detector is full coverage in the azimuth and $\pm$2 unites in pseudorapidity η around mid-rapidity for the inner radius and $\pm$1 unit for the outer radius. Requiring good p_T resolution through the number of 15 hits on each track limits the pseudorapidity coverage to $\pm$ 1.4units. The gas used in the drift volume is P10, a mixture of 90% Ar and 10% CH4 at 2 mbar above atmospheric pressure. The readout is situated at both ends of the TPC and is at ground potential, the drift field is created by applying -31kV at a thin cathode membrane in the center of the TPC. This causes the electrons created by the passage of ionizing particle to drift toward the readout plane.

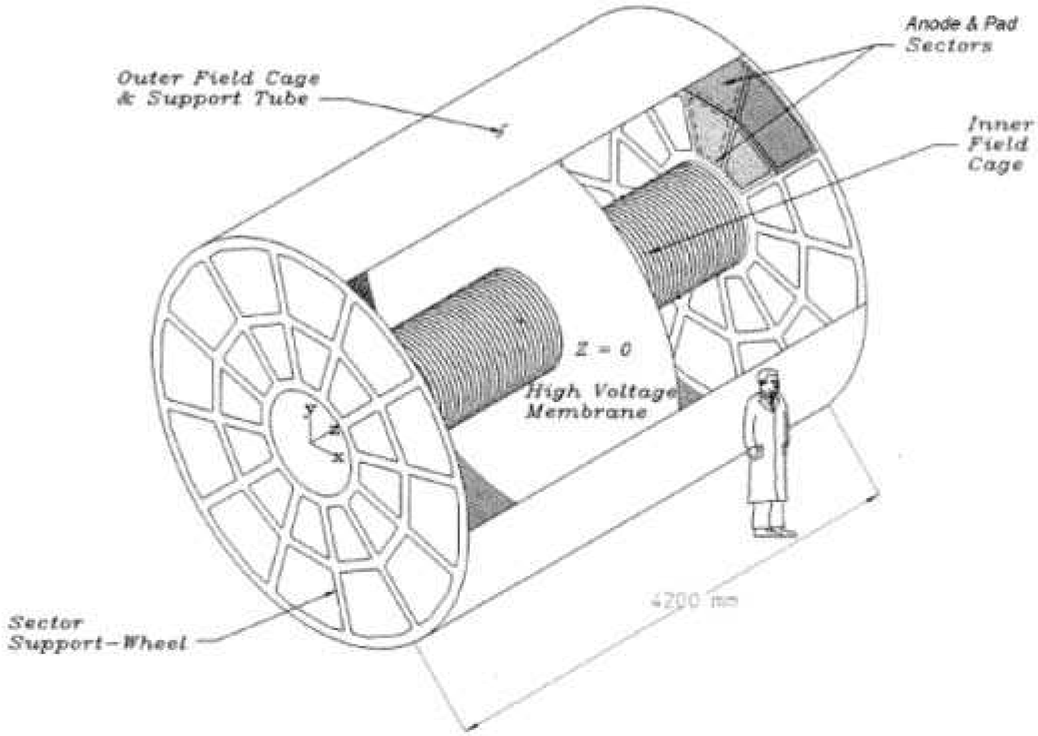

Figure 4.21: Side view of STAR-TPC.

TPC consists of 12 sectors in the ϕ-plane. Each of the 12 sectors is subdivided into inner and outer subsectors characterized by a change in the readout pad row geometry. The pad design consists of straight rows of pads in each subsector and is shown in Figure (4.22). The design of the sub sectors was intended to enhance the event reconstruction in two important ways. The inner sector, where the track/hit density is highest, uses a smaller size pad, 2.85 by $11mm^2$, in 13 rows to improve the hit resolution. This improves tracking by reducing the occurrence of split tracks which can be essential to many analyses including weak decay particle reconstruction and HBT etc. In the outer sector, where the hit occupancy is relatively low, the pad geometry is optimized for particle identification. Thus the pad size is increased to improve the measurements of the gas ionization. The outer sector consists of 32 rows of pads of 6.2 by 19.5 mm^2. The TPC gas chamber is surrounded by both an inner and outer field cage which controls the voltage drop and subsequent electric field between the high voltage central membrane and the multi-wire proportional chamber (MWPC)

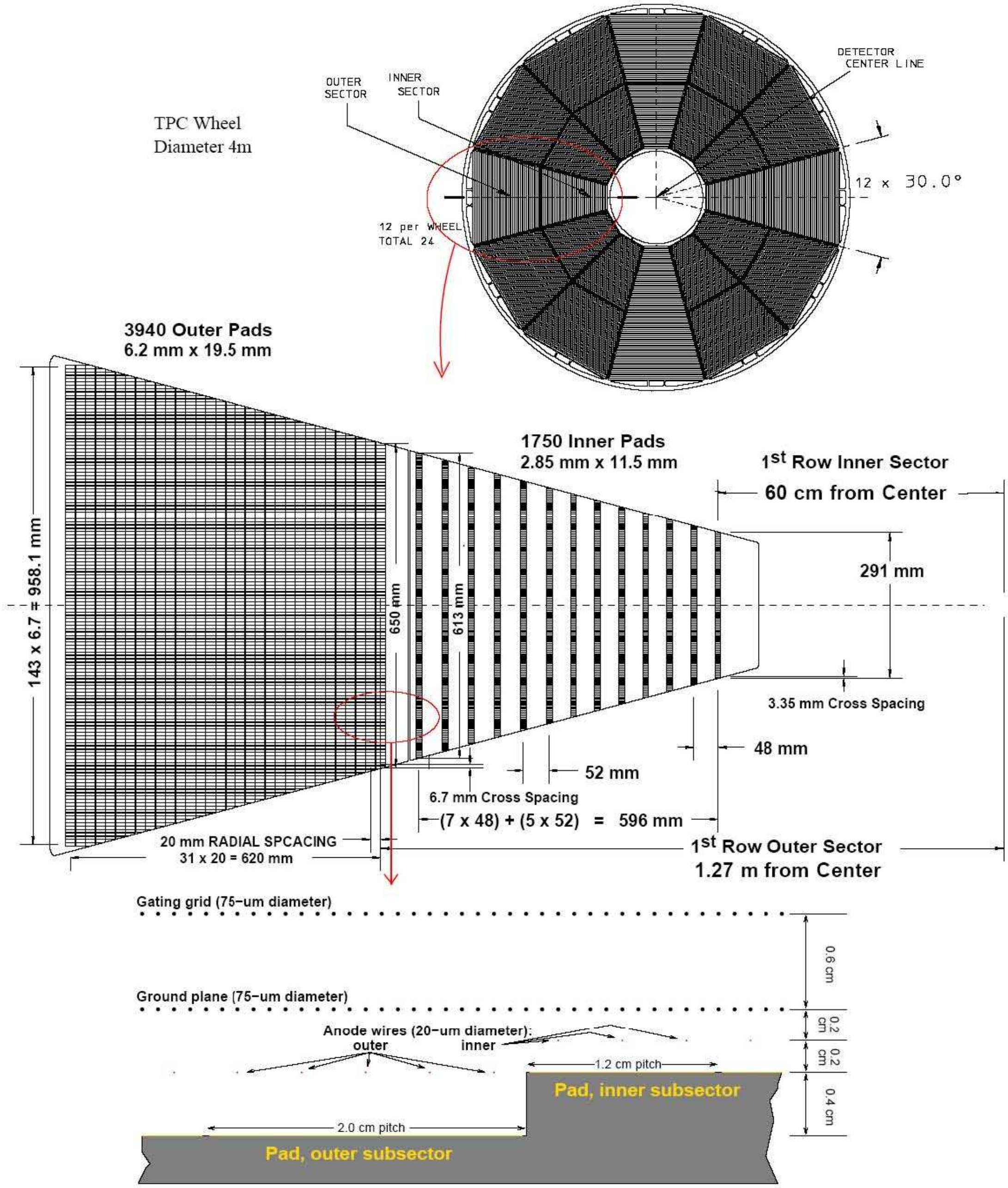

Figure 4.22: Sectors of the STAR-TPC.

and gating grids located just above the pad array for the two sections of each sector at the TPC endcap. The electrons produced from particles ionizing the gas as they traverse the detector drift towards the end of TPC and are amplified as an avalanche of electrons by the MWPC. These charges are imaged onto the pads and read out with a sampling rate of 100MHz, binned into 512 time buckets. The electrode geometry of the MWPC is shown in figure 2.8 and again shows a change in design elements between the inner and outer sub sectors. The choice of drift gas was based on several features necessary for optimal TPC performance. Among them were the constraints that the gas be under atmosphere pressure, and that the gas must have a drift velocity v_{drift}>2cm/μs in an electric field E<300V/cm. A mixture of 90% argon to 10% methane (P10) was selected. The drift speed of P10 at 130 V/cm is 5.5cm/μs. Also of important is the signal broadening introduced to the hit reconstruction by diffusion of the drift electrons in the gas chamber. The diffusion coefficient for P10 in the beam direction are 320μm/$\sqrt{}$cm and in the transverse direction is about 540μm/$\sqrt{}$cm which correspond to signal widths of 0.3cm and 0.8cm respectively.

Forward TPC (FTPC)

The Forward Time Projection Chambers (FTPCs) is constructed to extend the acceptance of the STAR experiment. They cover the pseudorapdiity $2.5 < |\eta| < 4$ on both sides of STAR and measure momenta and production rate of positively and negatively charged particles as well as neutral strange particles. Also due to the high multiplicity, approximately 1000 charged particles in a central $Au+Au$ collision, event-by-event observables like<p_t>, fluctuations of charged particle multiplicity and collective flow anisotropies can be studied. The increased acceptance improves the general event characterization in STAR and allows the study of asymmetric systems like p+A collisions.

The FTPC concept was determined mainly by two considerations: Firstly by the

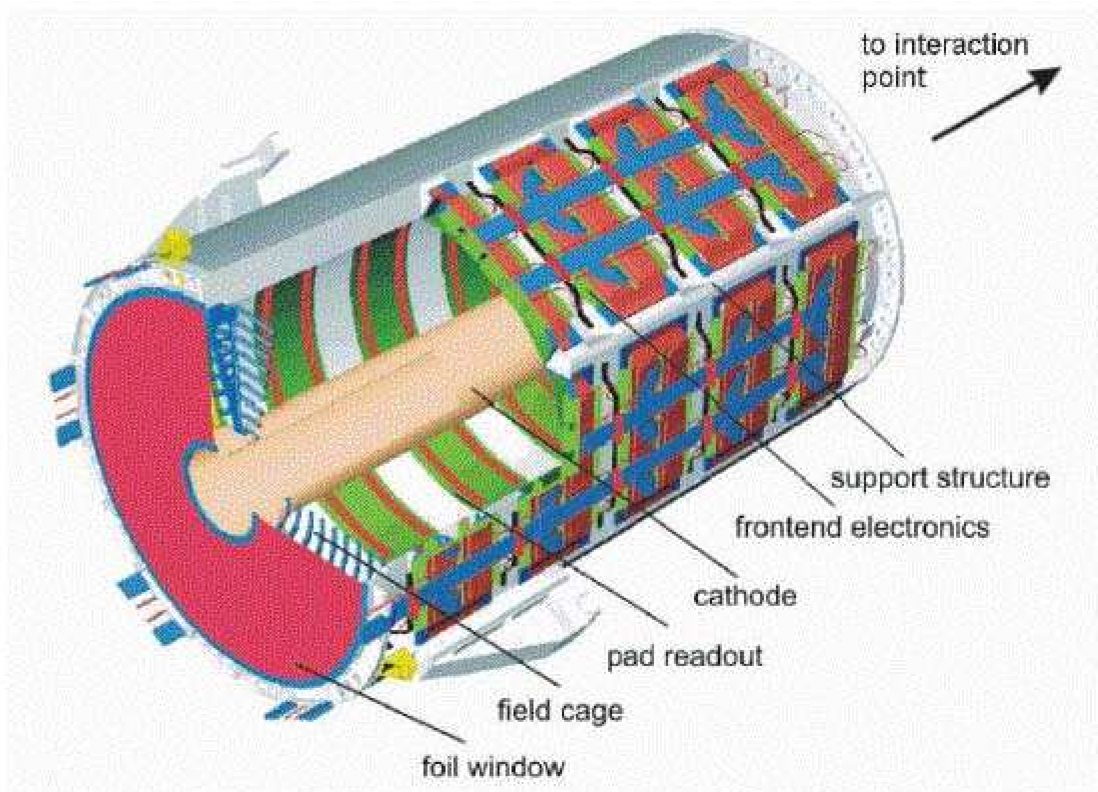

Figure 4.23: Layout of the forward TPCs. The field cage with potential rings at the endcaps,the padrows on the outer surface of the gas volume and the frone end electronics are shown. The readouts boards which are situated at the left end of the detector are nont included in the drawing.

high particle density with tracks under small angles with respect to the beam direction and secondly by the restricted available space inside the TPC [240], where the FTPCs are located. The final design is shown in Figure (4.23).

It is a cylindrical structure, 75 cm in diameter and 120 cm long, with a radial drift field and readout chambers located in 5 rings on the outer cylinder surface. Each ring has two padrows and is subdivided azimuthally into 6 readout chambers.

The drift toward the detector endcaps, as in main TPC, is not practical, since the long drift path leads to cluster broadening which reduces the two-track separation. Moreover the short projected length of low-angle tracks on the endcap makes the resolution of individual hits difficult. So the radial drift configuration was chosen to improve the two-track separation in the region close to the beam pipe where the particle density is highest. Due to the magnetic field parallel to the detector axis and thus perpendicular to the electric field, the drifting charge clouds get deflected by the Lorentz force (E×B). The radial drift spreads clusters originating from near the inner radius of the detector apart, thus leading to improved two-track separation in the area with the highest track density. The short drift distance (∼23cm) in the radial geometry permits the use of a slow gas mixture with small diffusion, which is important for good cluster separation. After exetensive measurements an Ar/CO_2(50/50) mixture was selected which has a low diffusion coefficient for electrons and a small Lorentz angle[241, 242].

The field cage is formed by the inner HV-electrode, a thin metalized plastic tube, and the outer cylinder wall at ground potential. The field region at both ends is closed by a planar structure of concentric rings, made of thin aluminum pipes. The front end electronics (FEE), which amplifies, shapes, and digitizes the signals, is mounted on the back of the readout chambers. Each particle trajectory is sampled up to 10 times. The ionization electrons are drifted to the anode sense wires and induced signals on the adjacent cathode surface are read out by 9600 pads (each1.6×20 mm^2). Curved readout chambers are used to keep the radial field as ideal as possible. A two-track separation of 1-2 mm is expected, which is an order of magnitude better than in all previously built TPCs with pad readout.

In order to use the recorded data for physics analysis, the particle tracks in the detector have to be reconstructed. This requires a calibration of the detector parameters and an understanding of effects caused by mechanical and electronic imperfections. The FTPCs have a laser system that is used to measure the drift velocity. This determines the relation between the measured time and the radial position of the particle track. Also the deflection angles due to Lorentz force are determined this way. The reconstruction of particle tracks proceeds in two steps, namely the finding of charge cluster, which is done for each padrow, and the combination of clusters from all rows into tracks. A complete summary of the detector parameters can be found in [243].

Chapter 5

Analysis and Results

"No amount of experimentation can prove me right;

a single experiment can prove me

worong."

Albert Einstein

This chapter is dedicated to a detailed description of the v_2 of inclusive photons analysis, the new clustering finder algorithm for π^0 reconstruction and presentation of their results. For the v_2 of inclusive photons determination the standard method is used. The analysis includes the reaction plane determination using the tracker detectors TPCs at mid-rapidity and forward/backward rapidity, the recentering for the reaction plane, and correction for the reaction plane resolution. The photon identification using the BEMC and the quality assurance of the BEMC are also discussed. The azimuthal correlation of origin not related to the reaction plane "non-flow" is also studied. The scalar product method is used to estimate the contribution of the non-flow to the azimuthal correlation. The results of the scalar product method for $p+p$ and $Au+Au$ at the same $\sqrt{s_{NN}}$ using the tracker detectors at two different pseudorapidity regions are also presented.

Unlike the low multiplicity collision, in the high multiplicity collisions system the direct photon measurements can only be done on statistical basis. So the first step toward any direct photons measurements is to extract the π^0 contribution. Reconstructing the invariant mass through its highest decay channel 2γ identifies the π^0. The analysis of π^0 invariant mass reconstruction includes the electromagnetic shower characteristics, π^0 decay kinematics, and the new cluster finder algorithm. Finally the π^0 peak for all different system at RHIC energy is presented.

5.1 Data and Detector Descriptions for Run IV

All raw data coming from the detectors are assembled. Collections of events over a certain peroid of time represent the individual runs. Within one run the global settings of the data acquisition, e.g. the prescale factors of the triggers, and of the detectors remain unchanged. Runs are subdivided into segments to keep the size of the output files low, and to make parallel processing during the offline production possible, where the raw data are converted into quantities with more physical meaning.

5.1.1 Trigger

The typical luminosity that is achievable at RHIC is much higher than the event sampling rate of slow tracking detectors, such as the STAR TPC. As it is mentioned in the previous chapter, The slow STAR detector subsystems only operate at rates of about 100 Hz. Collision interaction rates approach the RHIC crossing rates (up to ∼10 MHz) for the highest luminosity beams, so fast detectors, such as the CTB, must provide means to reduce the rate by almost 5 orders of magnitude. Interactions are selected based on the distributions of particles and energy obtained from the fast trigger detectors.

One of interest to this analysis is the minimum bias trigger configuration, the goal of which is to maximize acceptance of inelastic $Au + Au$ interactions at all impact parameters. The trigger conditions were defined in real-time data-taking by a logical combination of information from the fast trigger detectors. The trigger detectors in the 2004 run consisted of the east and west ZDCs and the CTB. Minimum-bias triggered events are defined as ones in which the two ZDCs are above threshold (ADC > 5) and the sum of all CTB slats have ADC > 75. The CTB portion of the minimum bias trigger condition was imposed in order to reject non-hadronic events.

For the 2004 Au+Au run, additional timing information from the ZDC was available. Using the independent timing information from the east and west ZDCs, one can locate the approximate position of the collision along the beam direction [244]. This allowed for selection of events that satisfied a vertex position along the beam direction of less than 30 cm from the center of the TPC.

Selecting events that occur near z = 0 cm allows for the same acceptance on the left and right portions of the STAR detector. Maximizing acceptance ensures that most of the detector volume of STAR subsystems, such as TPC, is used.

The L0 high tower trigger concentrates only on the γ/π^0/electron with high energy and select every event which has a tower above some transverse energy[1] threshold $E_{T,thresh.}$ .The energy threshold is the only free parameter in this algorithm which allows to vary trigger efficiency and rejection rate. This algorithm will be refered to as the L0 high tower algorithm in the following. The algorithm is shown schematically in Figure (5.1)

5.1.2 The BEMC Performance in Run IV

Although the calorimeter was described in detail in the previous chapter, however, some problems have arised during the real-time run. In this section we address some technical issues, which have impact on the analysis performed in this dissertation.

[1]The BEMC is (should be) calibrated in transverse energy E_T due to the demands of the high-p_T and spin working groups. The raw ADC values on which the L0 decision is based are thus also proportional to E_T . A conversion to E is not possible on the L0 trigger level. Due to the limited capabilities on the L0 trigger level the 10-bit ADC values are shifted and reduced to 6-bit values ADC$_{trg}$.

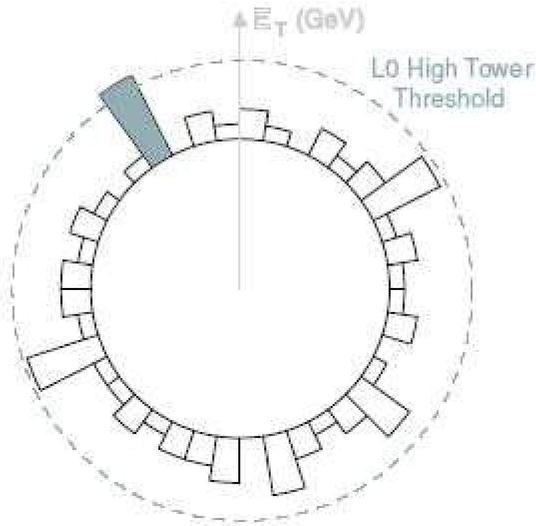

Figure 5.1: Schematic illustration of the L0 High Tower algorithm. The event is accepted because the filled tower is above threshold.

Acceptance

The nominal BEMC coverage for run 4 was $\sim 3/4$, i.e. 72 modules out of the 120 total. Various technical problems reduced this coverage significantly. They can be roughly divided in two categories, one affecting single towers and being quite stable in the run. The second affects large areas at once and varies with time, we first focus on this effect.

In the front end electronic for the 160 towers are installed in the Tower Digitizer Crates. The power supplies of these crates developed a high failure rate during the run, with ~ 1 failure per week. The available spares and the time needed for repair of the broken power supplies would not have allowed to replace all failed ones. It was decided to drop the support of the east half of BEMC, thereby reducing the number of working modules to the 60 of the west half. With the freed power supplies of the east half crates enough power supply spares were available to replace the failing ones in the west half. The replacement was however only possible during the scheduled access periods every two weeks since the replacement procedure required access to the platform and consequently interruption of the beam. This resulted in extended periods with non-working crates and thus reduced BEMC coverage. The 160 towers of one crate correspond to $\sim 3\%$ of all towers and $\sim 7\%$ of the working towers.

The other category of BEMC hardware failures affects single towers only. Several failure modes have been identified so far by analyzing the single tower ADC spectra in the recorded data: • dead channels (no signal) • hot channels (high values for every event) • channels with very low/high gain (large shift of pedestal peak) • noisy channels (large width of the pedestal peak) • channels with bit failure (always set/never set) • adjacent tower FEE channels giving the same ADC value for every event

Tower Energy Calibration

During the data analysis another problem with the BEMC based triggers became visible: the individual tower calibration. Due to the accidental loss of the west half high voltage settings for the individual photomultiplier tubes between the FY03 and FY04 runs the whole calibration of the BEMC had to be redone in the first weeks of the FY04 run. The goal is a calibration in transverse energy, i.e. a measured ADC value translates to the same E_T independent of the actual tower. A proper calibration is crucial for triggering , especially on L0 where the raw ADC values are used as input. As will be shown later in this section the calibration for the FY04 run did not achieve this goal, thereby decreasing the detection and increasing the analysis of equilization complexity.

The calibration scheme employed in STAR is based on ADC slope equilibration for the inter-tower-calibration and the BEMC response of minimum ionizing particles or electrons for setting the absolute energy scale.The calibration process starts by obtaining such ADC spectra for every (working) tower. To calibrate the towers relative to each other assumptions have to be made how the ADC spectra in neighboring towers relate to each other. Obviously the collisions are rotation symmetric in azimuthal (ϕ). This allows a grouping of the towers into rings of 120 towers in ϕ times 1 tower in η. After pedestal subtraction the slope of the ADC spectrum is fitted for each tower in the rings. The HV setting of the PMTs is then adjusted in an iterative process until the fitted slope are the same for each tower in the rings.

Calibrating the rings to each other requires another assumption. It is known from earlier measurements that the transverse energy in $Au+Au$ collisions is roughly independent of pseudorapidity η in the BEMC range -1< η <1. Thus equilibrating the fitted ADC slopes of all rings will result in the desired E_T calibration, i.e.

$$ADC \sim E_T = E\sin(\theta) \tag{5.1}$$

where θ is the polar angle measured relative to the beam axis ($\eta = -ln\tan(\theta/2)$)

After this step, all towers of the BEMC are calibrated relative to each other, i.e. they produce the same ADC value for the same deposited transverse energy E_T . What still needs to be done is a determination of the absolute energy scale. The STAR software supports not only a linear mapping but higher order corrections as well, leading to the equation

$$E = \sum_{i=0}^{4} (ADC)^i c_i \tag{5.2}$$

to calculate the energy E from the measured ADC values using the calibration constants c_i for each of the 4800 towers. However currently only a linear mapping (i.e. only c1$\neq$ 0) is used. The HV were set such that the maximum energy is 64 GeV, a requirement for $p+p$ jet spin physics at $\sqrt{s}$ = 500 GeV. By mistake the actual calibration during the FY04 run was for a maximum energy of 32 GeV.

Two different methods are used in STAR to determine the energy scale. Both require a combination of particles measured in the TPC with the BEMC tower data. Either one selects electrons using the momentum and dE/dx information and adjusts the high-voltages so that the ratio of energy measured in the BEMC to the TPC

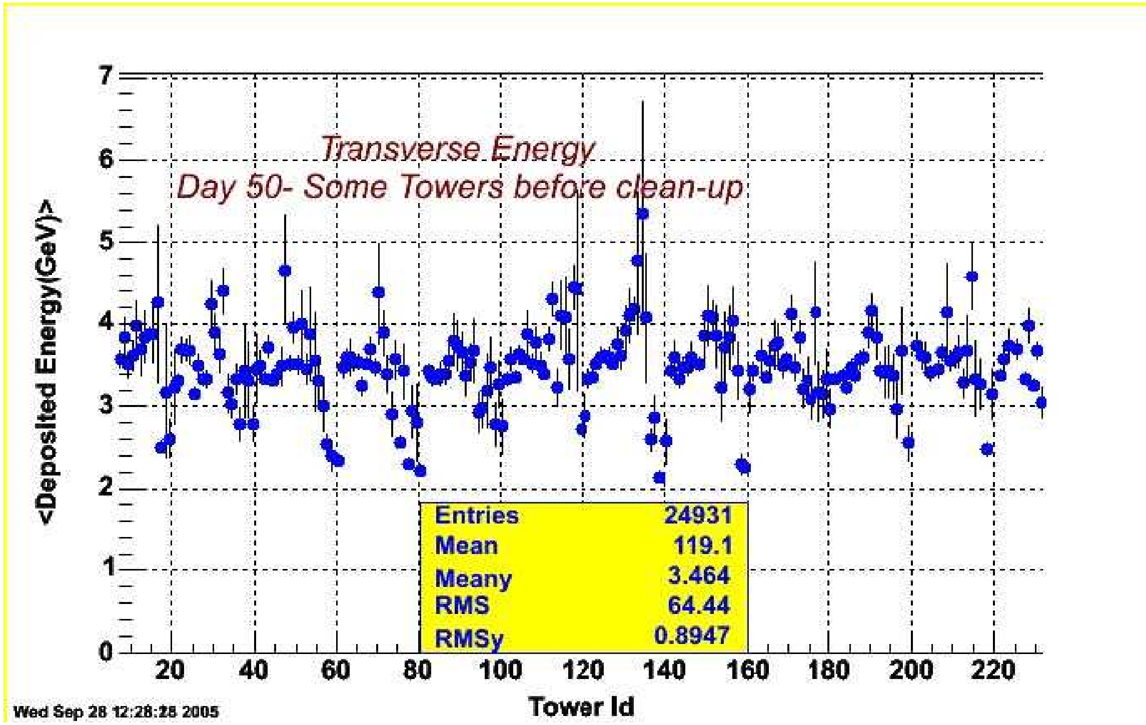

Figure 5.2: The deposited average transverse energy vs. some towers Id with $E \geq$3GeV for one day of the run period. It is obvious there is a structure in the distribution with a period of 20-towers.

momentum E_{tower}/p peaks at one. This requires however a large statistics dataset with both TPC and BEMC information due to the low number of (high-p_T) electrons in the collisions. This electron calibration is therefore only used for the offline calibration after the run.

During the run, a different approach is used to obtain a calibration. It is based on the BEMC response of hadrons which do not shower in the calorimeter. By selecting particles with more than 1 GeV/c momentum, the energy loss in the BEMC material is essentially the one of minimum ionizing particles. However the observed structure is usually quite broad and thus the precision of this calibration is not as good as that achievable with electrons. The big advantage is however the much smaller number of events needed. Such a calibration was done at the beginning of the FY04 run, using L3 tracking information, and used in the trigger levels L2 and L3.

It was planned to calibrate the BEMC in transverse energy E_T and during the run it was assumed that this had happened. In this case the minimum transverse energy E_T triggered by L0 should be independent of η with some spread due to a non-perfect calibration. But after the run and the first data production enough statistics was available to perform analysis, we found that this distribution is far from being independent of η. Accidentally the BEMC group introduced an additional factor $\sin(\theta)$ into Equation (5.1) resulting in

$$ADC \sim E_T \sin(\theta) = E \sin^2(\theta) \tag{5.3}$$

At $\eta = 1$ the energy threshold is effectively increased by a factor $1/\sin(\theta) = 1.54$, shifting it from $E_T \approx 3.5$ GeV at $\eta = 0$ to $E_T \approx 5.4$ GeV at $\eta = 1$ (Figure 5.2). Obviously such an unexpected shift in the trigger threshold has a huge influence on the trigger efficiency of the L0 trigger. Steps have been taken to introduce additional QA measures during the run to prevent such a mistake in future.

5.1.3 Centrality Bins

In a relativistic heavy ion collision, the event centrality is determined by the impact parameter b, which is the distance between the centers of two colliding nuclei [245]. The impact parameter b is not directly observable but it is correlated with the multiplicity of produced particles in each event. The higher the multiplicity, the smaller the impact parameter and the more central the collision. In STAR, the reference multiplicity is used as a standard to all analyses in the determination of the centrality. The reference multiplicity is defined as the number of tracks satisfying the following requirements: • Flag>0 (a basic track reconstruction quality requirement) • Distance of Closest Approach (DCA) to the primary vertex $<$ 3cm • Number of fit points $\geq$10 • -0.5 $< \eta <$0.5

The reference multiplicity distribution is binned into percentiles of the total cross section. Each percentile range corresponds to a range of centrality and defines each

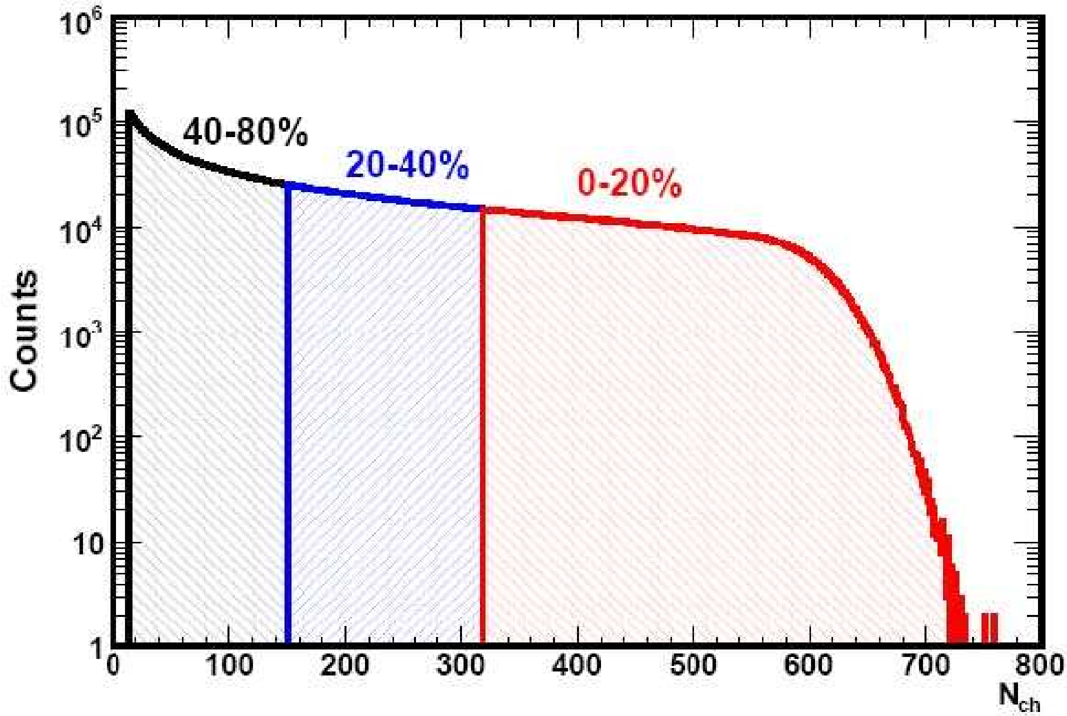

Figure 5.3: The STAR reference multiplicity distribution for Au+Au 200 GeV minimum biased events. The reference multiplicity is not the multiplicity of the event. It is solely used for the determination of the centrality.

centrality bin. The average number of binary collisions N_{bin} (number of binary collisions) and the average number of participants N_{part} (number of participants) for each percentile can be calculated using Glauber model. However, two methods are used to calculate the N_{bin} and N_{part}. One is called Optical Glauber approach and the other is called Monte Carlo Glauber approach. The difference between these two is negligible for central Au+Au collisions, but is significant for peripheral Au+Au collisions [246]. Thus, in this analysis, only events within the centrality interval from 0 to 80% are selected. Table (5.1) lists the STAR centrality definition for year 2004 $Au + Au$ 200 GeV experiment [247]. Figure (5.3) shows the reference multiplicity and centrality distributions for $Au + Au$ 200 GeV minimum biased events.

centrality	N_{par}	N_{bin}	Reference Multiplicity
0-5%	352.4+3.4-4.0	1051.3+71.5-71.1	≥520
5-10%	299.3+6.6-6.7	827.9+63.9-66.7	441-520
10-20%	234.6+8.3-9.3	591.3+51.9-59.9	441-319
20-30%	166.7+9.0-10.6	368.6+41.1-50.6	319-222
30-40%	115.5+8.7-11.2	220.2+30.0-38.3	222-150
40-50%	76.6+8.5-10.4	123.4+22.7-27.3	150-96
50-60%	47.8+7.6-9.5	63.9+14.1-18.9	96-57
60-70%	27.4+5.5-7.5	29.5+8.2-11.3	57-31
70-80%	14.1+3.6-5.0	12.3+4.4-5.2	31-14

Table 5.1: The STAR centrality definition for year 2004 Au+Au 200 GeV experiment.

5.2 Event-wise Azimuthal Anisotropy of Inclusive Photons

5.2.1 Events Selection

We address in this section the general characteristics of the selected events used in this analysis. In year 2004, about 80 million Au+Au collisions were recorded by STAR. By the time this analysis was done, about 10.6 million events with valid BEMC information were processed by the STAR production team.

After various event selection and cuts about 10.2 million minimum biased, high tower, and central events were used to produce the results presented in this dissertation.

Primary Vertex Based Selection

Our analysis was restricted to events with a primary vertex within ±25 cm and ±80cm of the center of the TPC for the analysis of Au+Au and p+p data respectively. Studies found that events with vertex Z outside this range have much larger fraction of photon conversion electrons [248]. Figure (5.4) shows the longitudinal position distribution of primary vertices for $Au + Au$ collision. The number of events and its percentage according to its trigger identification are listed in table(5.2). About 84% of the total number of events have a primary vertex that lies within ±25cm of the TPC center along the beam line for $Au + Au$ collisions. The events with primary

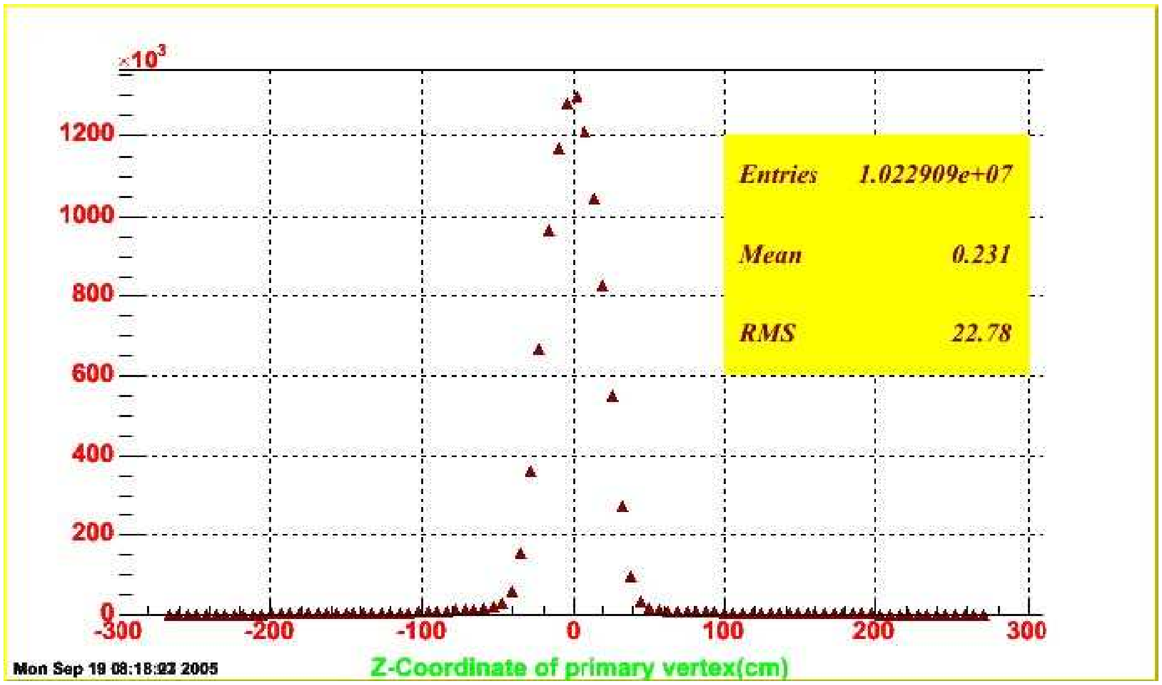

Figure 5.4: Primary vertex distribution along the beam direction from the center of the TPC for the 2004 $Au + Au$ run

Trigger Id	Number of events	Percentage
Minimum Bias	4.82M	47.18%
High Tower1	1.21M	11.83%
Central	2.46M	24.06%
Minimum Bias and Central	11.75k	0.11%
Minimum Bias and High Tower1	64.62k	0.63%
High Tower1 and Central	91.16k	0.89%
Other	1.56M	15.27%

Table 5.2: Used data "$Au + Au$" percentage according to the trigger setup.

Trigger Id	Number of events	Percentage
Minimum Bias	3.96M	46.14%
High Tower1	1.02M	11.90%
Central	2.24M	26.05%
Minimum Bias and Central	11.08k	0.13%
Minimum Bias and High Tower1	54.46k	0.62%
High Tower1 and Central	86.66k	0.89%
Other	1.21M	14.12%

Table 5.3: Used data "$Au + Au$" percentage according to the trigger setup after $z \leq |25|$ cut.

Trigger Id	Number of events	Percentage
Minimum Bias	2.015M	33.47%
High Tower1	1.36M	22.59%
High Tower2	5.5k	0.09%
Minimum Bias and High Tower1	158	2.6×10^{-3}%
Minimum Bias and High Tower2	14	2×10^{-4}%
High Tower1 and High Tower2	13.4k	0.21%
Other	2.55M	41.19%

Table 5.4: Used data "$p+p$" percentage according to the trigger setup after $z \leq |80|$ cut.

vertex $\pm$25 cm which were selected for this analysis are tabulated in (5.3) and shown in Figure(5.5).

In the scalar product method the $p+p$ data is also used . For $p+p$ collisions, 6.08 Million events at $\sqrt{s_{NN}}$=200GeV from the same 2004 run period with a primary vertex $\pm$80cm along the beam line are used in this analysis. Classification of the events according to the trigger setup is shown in table(5.4).

5.2.2 **Elliptic Flow of Inclusive Photons**

The Standard Method

The standard method [249] correlates each particle with the event plane determined from the full event minus the particle of interest. Since the event plane is only an approximation to the true reaction plane, one has to correct for the smearing by

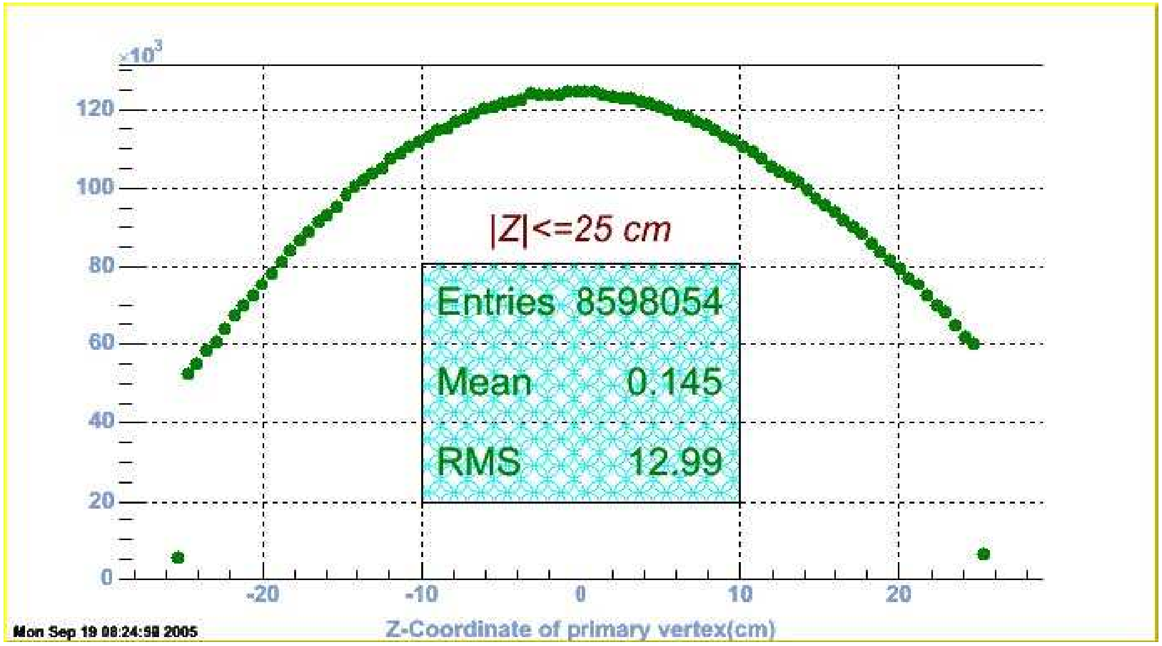

Figure 5.5: Primary vertex distribution along the beam direction from the center of the TPC for the 2004 $Au + Au$ run after $|z| \leq$25cm

dividing the observed correlation by the event plane resolution, which is the correlation of the event plane with the reaction plane. In order to make this correction the full event is divided up into two subevents, and the square root of the correlation of the subevent planes is the subevent plane resolution. The full event plane resolution is then obtained using the equations in Ref. [253], which describe the variation of the resolution with multiplicity.

- **Event plane reconstruction**

Tracks with p_t <2.0GeV/c were selected in order to have constant tracking efficiency. They also have number of fit points >15 to insure good resolution in the momentum measurements. The tracks, which passed the above-mentioned criteria, were used to determine the event plane in the main TPC and the FTPC. To avoid the autocorrelations with the reaction plane only the east side of the main TPC was used, hence the BEMC reside in the west side of STAR detector. Since both sides of FTPC are far in pseudorapidity from the BEMC location, both sides were used for the event plane determination. The FTPC is used in the event plane determination to reduce the effect of the so-called "non-flow" contributions.

Each event is subdivided randomly into two sub-events. In each subevent the azmiuth location of each passed criteria track is determined by the detector coordinate. The reaction plane is determined in each event according to Equations(5.4 and 5.5) for TPC and FTPC respectively:

$$\Psi_{RE} = \frac{1}{2} arctan(2\{\frac{\sum_i \sin 2\phi_{1i} + \sum_i \sin 2\phi_{2i}}{\sum_i \cos 2\phi_{1i} + \sum_i \cos 2\phi_{2i}}\}) \tag{5.4}$$

$$\Psi_{RE} = \frac{1}{2} arctan(2\{\frac{\sum_i \sin 2\phi_{W1i} + \sum_i \sin 2\phi_{W2i} + \sum_i \sin 2\phi_{E1i} + \sum_i \sin 2\phi_{E2i}}{\sum_i \cos 2\phi_{W1i} + \sum_i \cos 2\phi_{W2i} + \sum_i \cos 2\phi_{E1i} + \sum_i \cos 2\phi_{E2i}}\}) \tag{5.5}$$

where each sum goes over all the particles used in the sub-event plane azimuthal angle determination, while ϕ_i is the azimuthal angle of the ith particle. The W and E in Equation (5.5) stand for the West and East FTPCs. Figures (5.6-5.9) show the event plane distribution for the event palne reconstructed using the TPC tracks and FTPCs tracks. Figures 5.6 and 5.8 are for the minimum bias data and Figures (5.7 and 5.9) for the high tower trigger data. It is obvious the distribution depends on the acceptance of the used detector rather than the data type.

In the ideal case of the full acceptance detector the distribution of the reaction plane is flat. In practice, due to some bad sectors during the run and the dead area between the sectors the distribution may be not flat. One has to remove these biases in the reaction plane distribution. Removing these biases is done through a re-centering procedure described next.

•Event plane recentering

Biases due to the finite acceptance of the detector, which cause the particles to be azimuthally anisotropic in the laboratory system, can be removed by making the

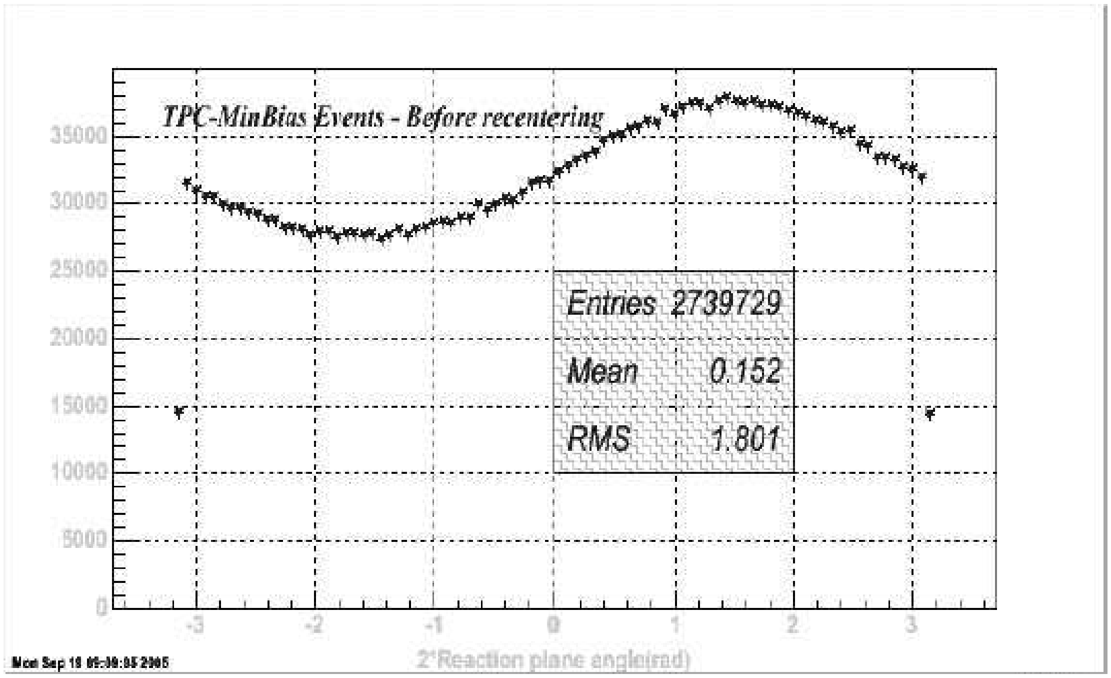

Figure 5.6: Event plane angle distribution before recentering “Minimum Bias-TPC”

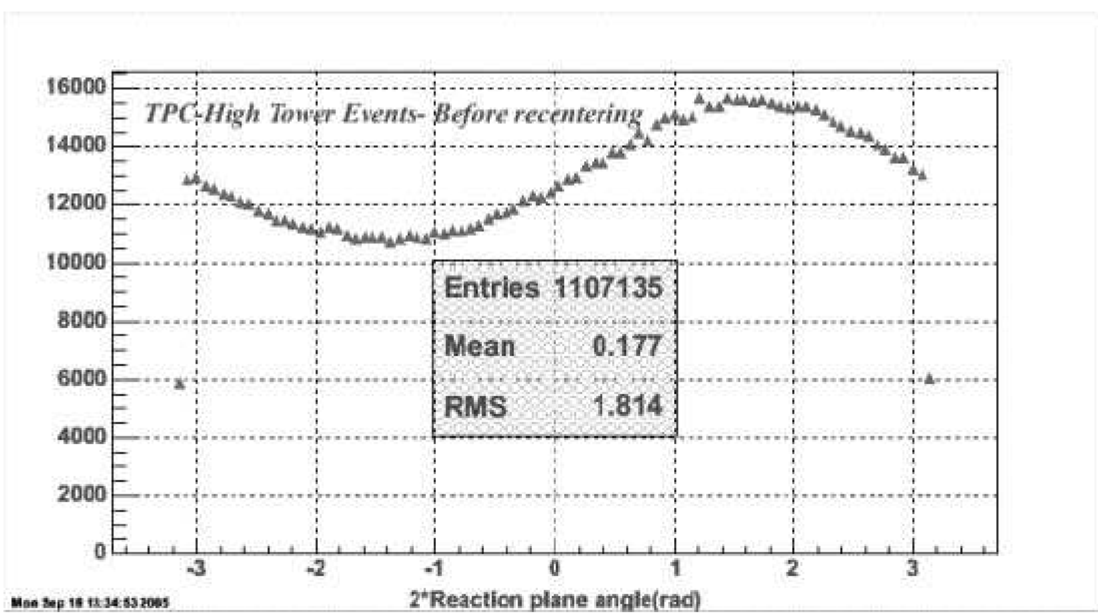

Figure 5.7: Event plane angle distribution before recentering “High Tower-TPC”

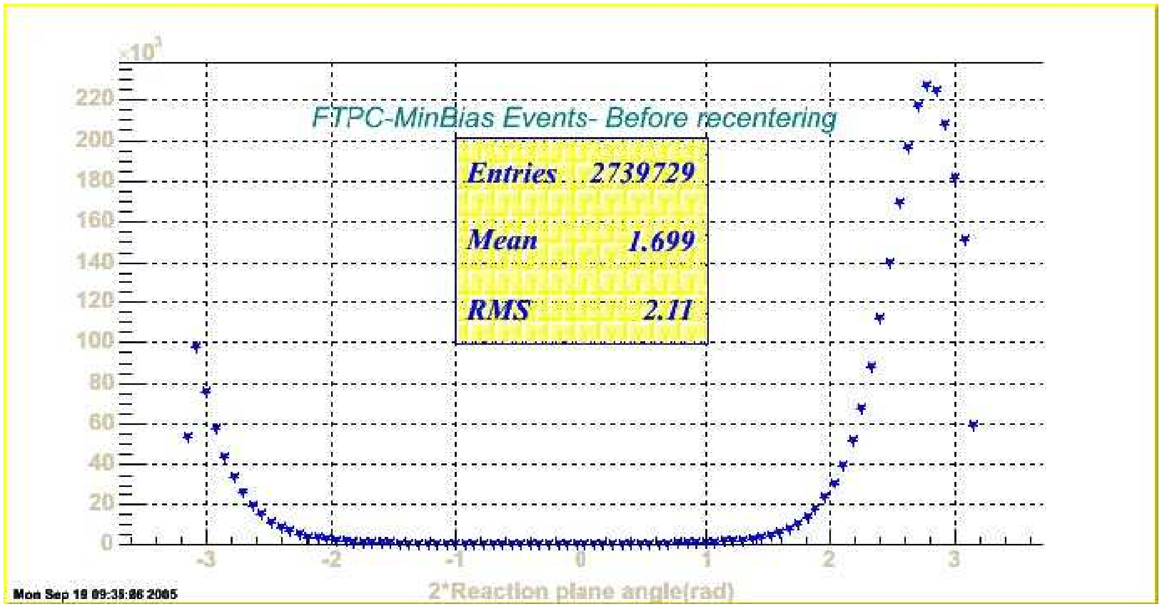

Figure 5.8: Event plane angle distribution before recentering "Minimum Bias-FTPC"

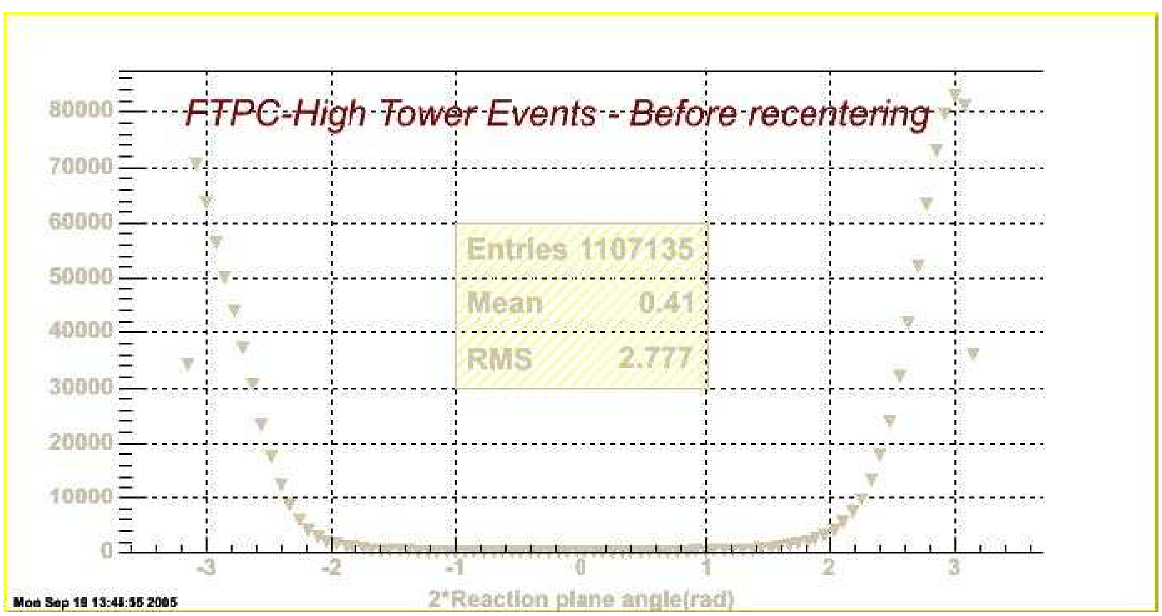

Figure 5.9: Event plane angle distribution before recentering "High Tower-FTPC"

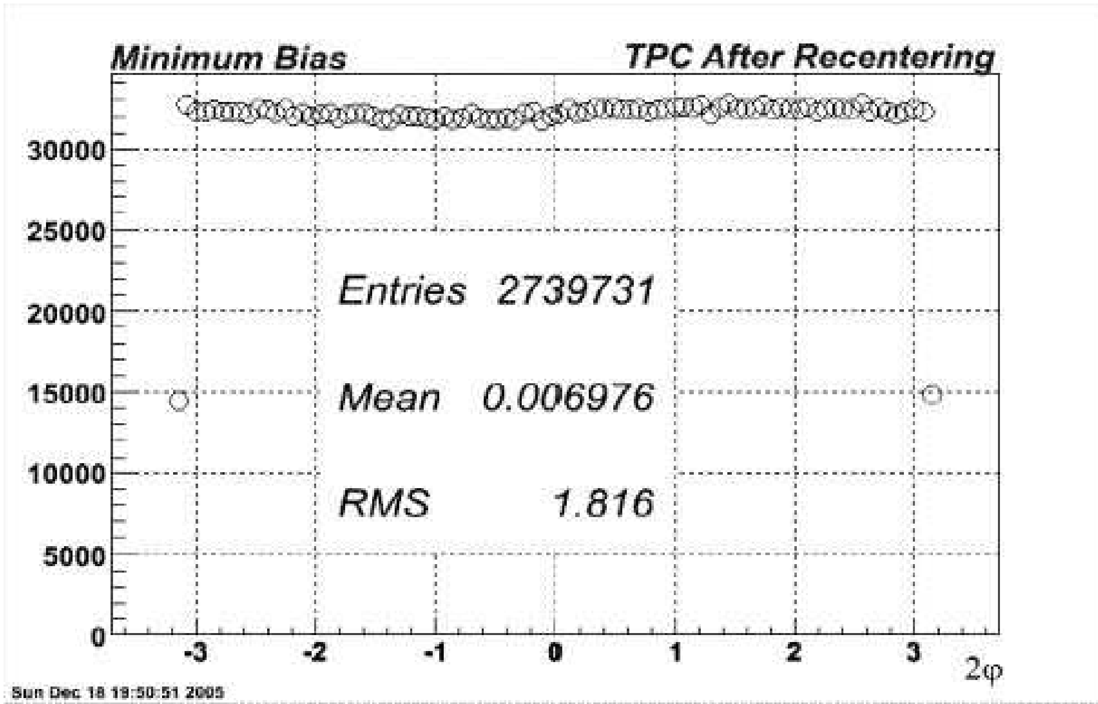

Figure 5.10: Event plane angle distribution after recentering “Minimum Bias-TPC”

distribution of event planes isotropic in the laboratory. Different methods exist to remove the effects of anisotropy. Each method has advantages along with disadvantages. The simplest technique is to recenter [250-252] the distributions (X_n, Y_n) (Eqs. 5.4 and 5.5) by subtracting the (X_n, Y_n) values averaged over all events, where $X_n = \sum \cos(n\phi)$ and $Y_n = \sum \sin(n\phi)$ and the sum goes over the number of used tracks. In order to remove the acceptance bias, the recentering is done using the minimum bias events on day-by-day basis. Since the track reconstruction efficiency changes with collision centrality, the recentering procedure is carried out as a function of reference multiplicity. The event plane is recenterd by replacing the cosine and sine terms in Equtions (5.4 and 5.5) according to Equation (5.6).

$$\sin 2\phi \rightarrow \sin 2\phi - M < \frac{\sin 2\phi}{M} > \qquad \cos 2\phi \rightarrow \cos 2\phi - M < \frac{\cos 2\phi}{M} > \tag{5.6}$$

where M is the number of tracks in each sub-event.

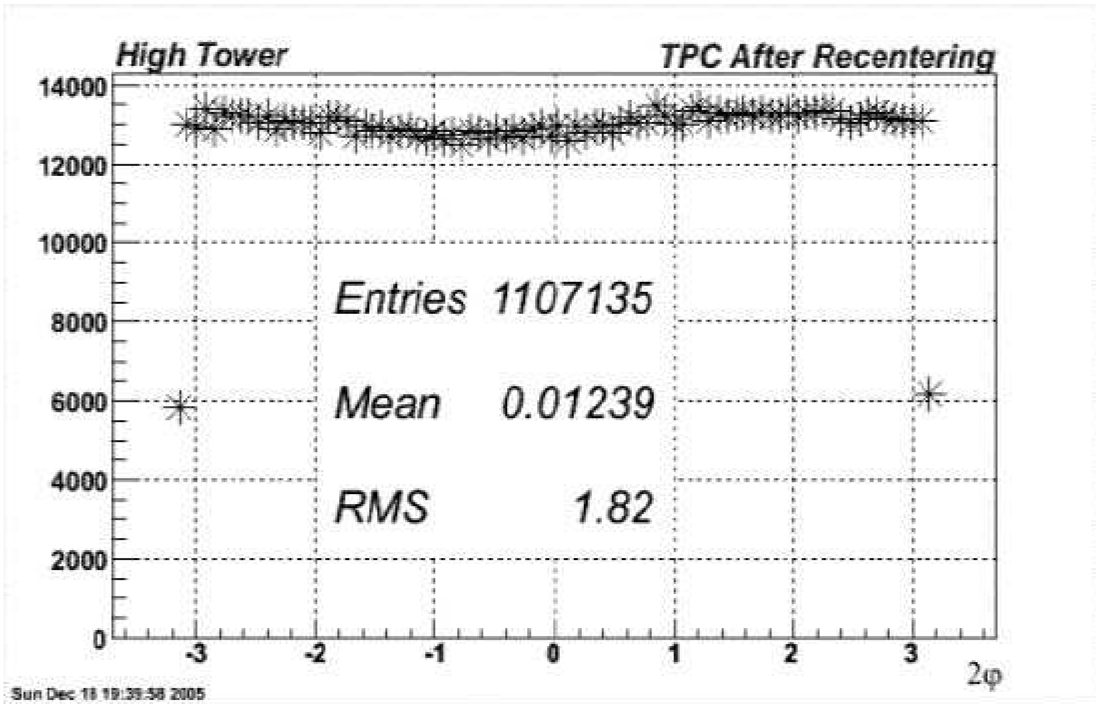

Figure 5.11: Event plane angle distribution after recentering “High Tower-TPC”

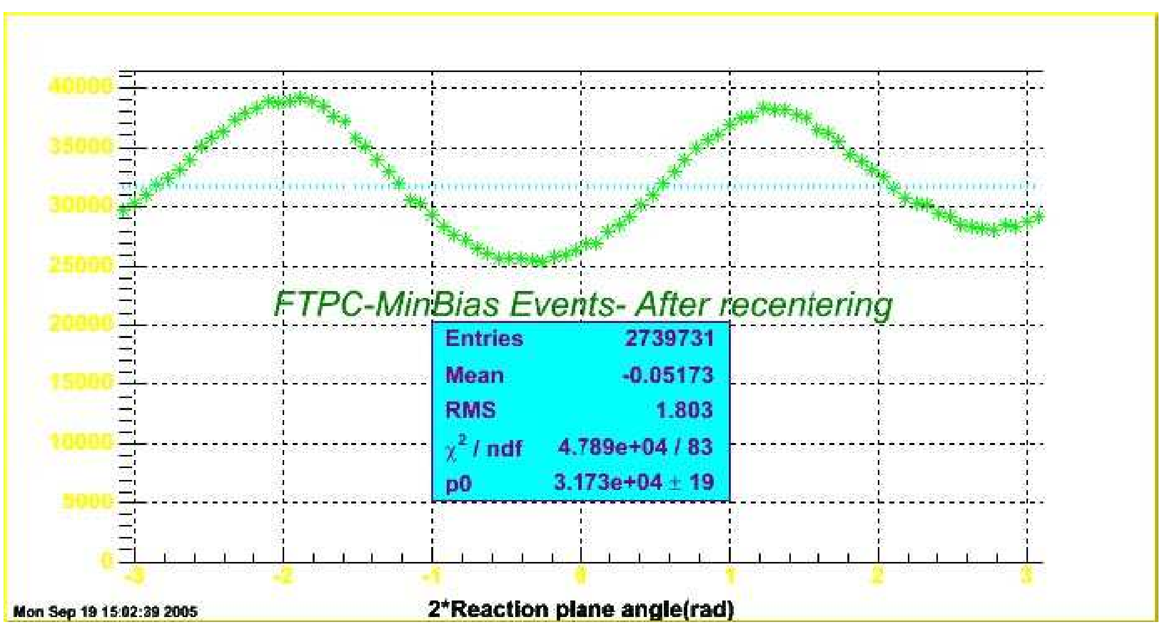

Figure 5.12: Event plane angle distribution after recentering “Minimum Bias-FTPC”

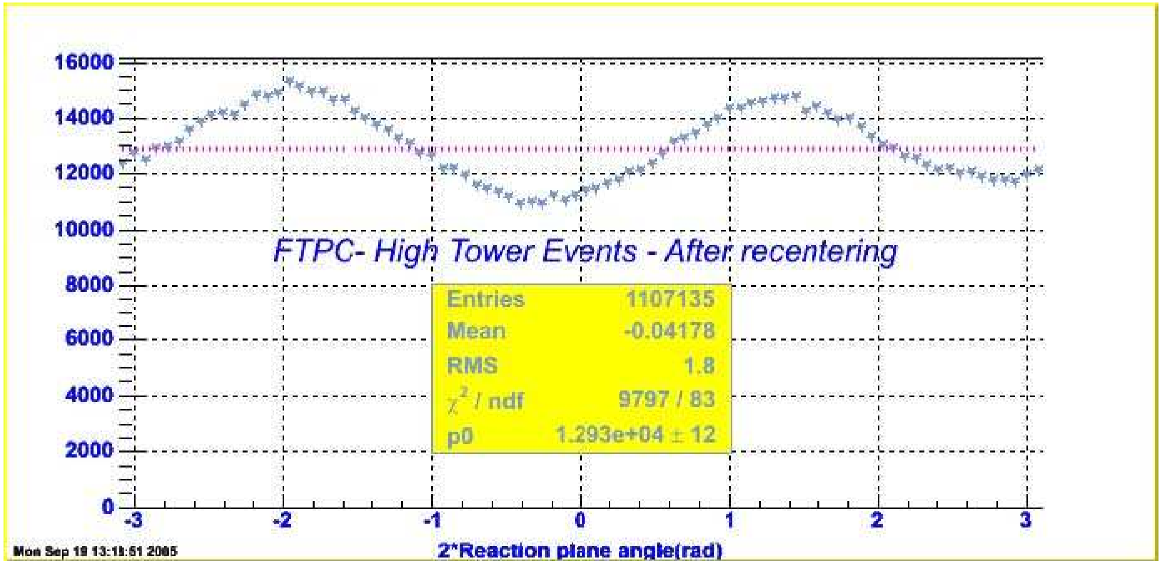

Figure 5.13: Event plane angle distribution after recentering “High Tower-FTPC”

It is obvious form Figures (5.10-5.13) that the distribution of the event plane angle exhibit more uniformity than before recentering. The fact that the cosine of the mean angle of the distribution is fairly small indicates the negligible bias due to the detector acceptance.

•Photons from the BEMC

While charged particles are detected using tracking detectors, photons are detected using the electromagnetic calorimeter. When a photon hits the BEMC, it deposits all of its energy in different parts of the calorimeter: preshower, SMD, and sampling towers. Usually hits, that appear to be produced by the same photons, are grouped into clusters. Clustering is usually done independently for towers and SMD η-and ϕ-planes. Clusters are then matched together to form BEMC points, from which energies and coordinates of photon candidates are determined. In the case of high statistics, in order to reduce the hadronic rejection factor and to enhance the purity of the photon samples, the BEMC points were required to have clusters in both SMD η-and ϕ-planes.

However, because of the limitation of the available produced high tower data for

$Au + Au$ and $p + p$ collisions by the time when this analysis is done, the photon are detected without clustering. We simply assume the neutral tower energy is the full energy of the candidate photon. The position of the photon is determined by the coordinate of the tower. Of course this method is an oversimplification for measurements and correction must be done to estimate the hadronic background and the right energy/position of the photon. However, for the elliptic flow measurements at high p_t the hadronic contribution are really small since the probability of the hadrons to deposit a high energy in the calorimeter is small. In addition to, the small value of Moliere radius of the electromagnetic shower compared to the tower size make the energy leakage has no large effect on the corrected photon's energy. The high suppression factor of π^0 at high p_t increase the probability of the dominance of direct photons at higher energy (chpater 3).

Each track is extrapolated to the BEMC face and the charged particle veto cut for the target tower is used. To enhance the purity of the photon samples a minimum energy condition is required in the tower. For the minimum bias data the transverse energy threshold is 0.1 GeV and for the high tower data is 3GeV[2]

In the course of this analysis another problem arises which is the absence of the status table of the towers. Due to many reasons the distribution of the photons in the calorimeter can be non-uniform. The non uniformity in the calorimeter can lead to a strong bias in the results.

•**Quality Assurance of the BEMC**

To assure high quality of the BEMC, the distribution of the average deposited transverse energy in the pseudorapidity and the azimuthal directions is studied very carefully. Moreover, the distribution of the transverse energy in tower by tower for each day of the run period is done separately (Figure 5.14). Selected towers are the

[2]As it is discussed in section 5.1, the hardware trigger was set to $E\sin^2(\theta)$ instead of $E\sin(\theta)$ in run IV. The towers at high pseudorapidity is affected by $E_T \geq$3GeV more than the towers at lower pseudorapidity.However, due to the independence of v_2 on the pseudorapidity "$-1 \leq \eta \leq 1()$", the E_T cut will not induce any bias in the results.

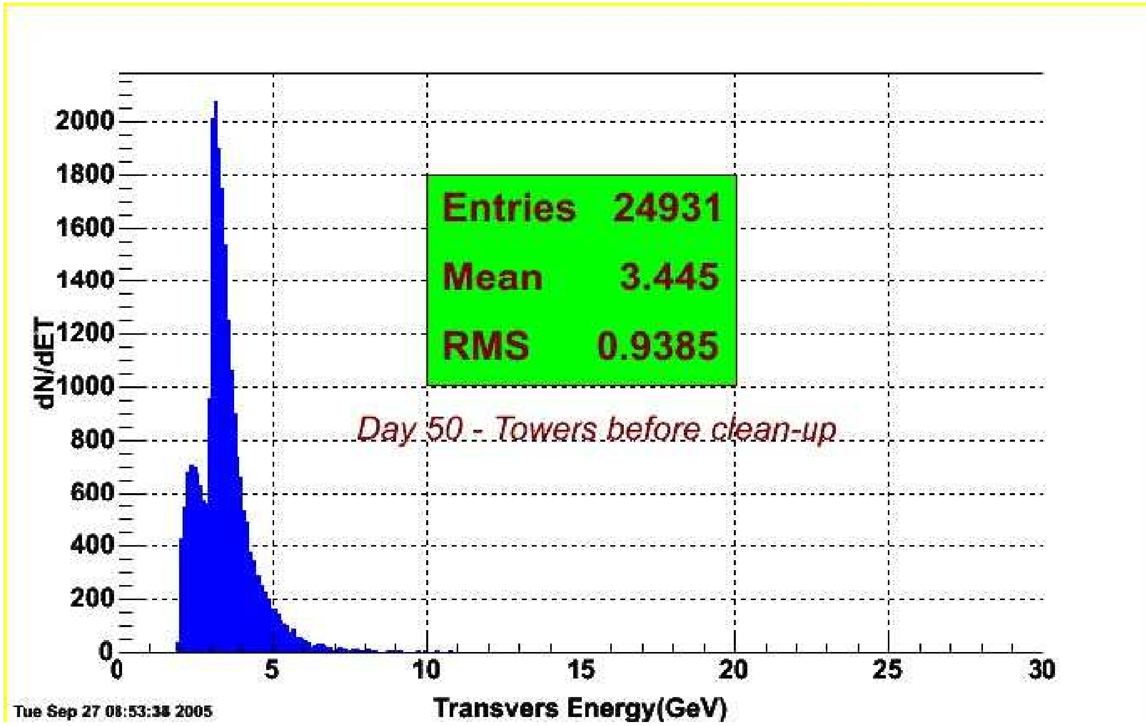

Figure 5.14: The distribution of the transverse energy deposited in the calorimeter for one day (Day 50) of IV run for the high tower data. The little peak is due to the non-high towers and some of the high towers mainly at high η.

towers with average transverse energy within 1.6σ of the mean distribution over all towers (Figure 5.15). This requirement is applied for the minimum bias data and high tower data separately. Indeed applying such requirement remove all the biases from the photons distribution in the calorimeter. The distribution of the average deposited transverse energy looks fairly flat in the pseudorapidity and azimuthal directions as well as in the tower Id (Figures 5.16-5.18).

•Elliptic Flow of inclusive Photons

After finding the event plane and the azimuthal direction and the energy of the candidate photons, the v_2, integrated over the BEMC pseudorapidity range, of the inclusive photons is determined using the following equation:

$$v_2^{observed} = < \cos(2\phi_\gamma - 2\Psi_{RE}) > \tag{5.7}$$

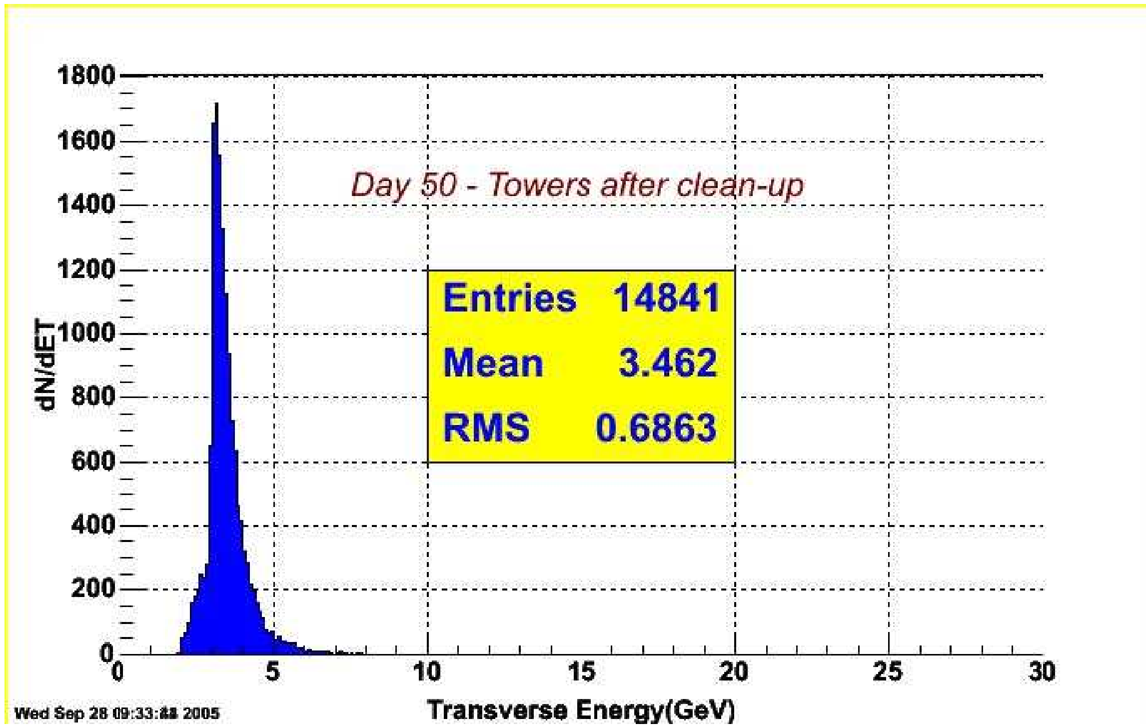

Figure 5.15: The distribution of the transverse energy deposited in the calorimeter for one day (Day 50) of IV run for the high tower data after imposing 1.6σ cut.

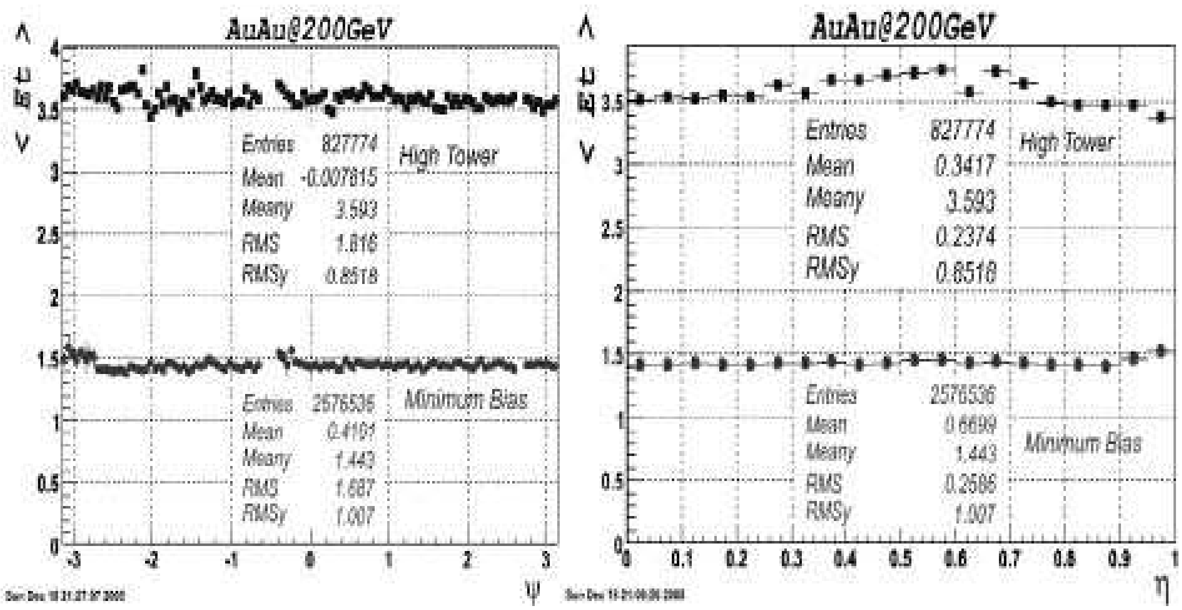

Figure 5.16: η (Right)and ϕ (Left) distribution for the transverse energy deposited in the calorimeter.

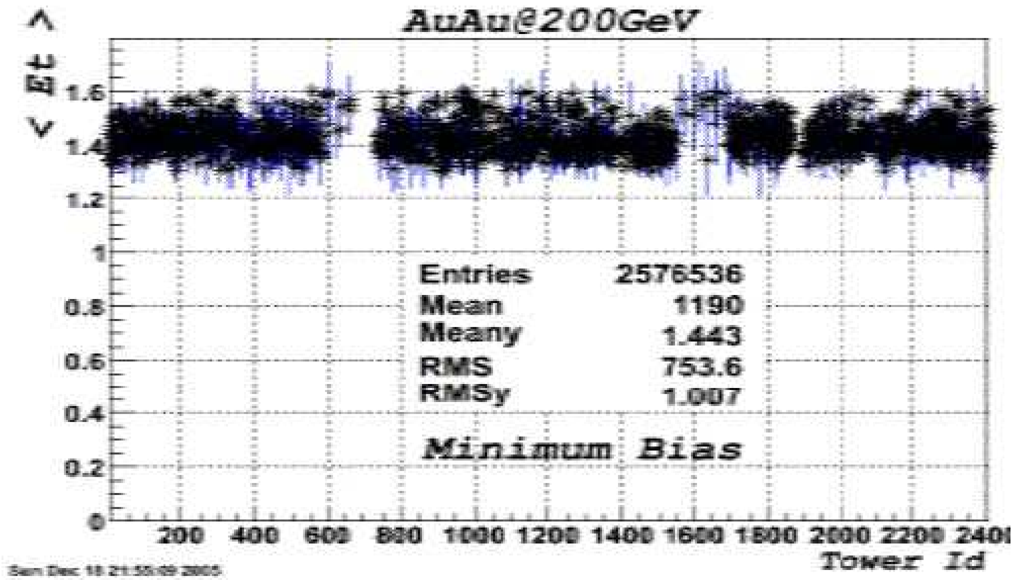

Figure 5.17: Transverse energy distribution vs. tower Id-Minimum Bias data

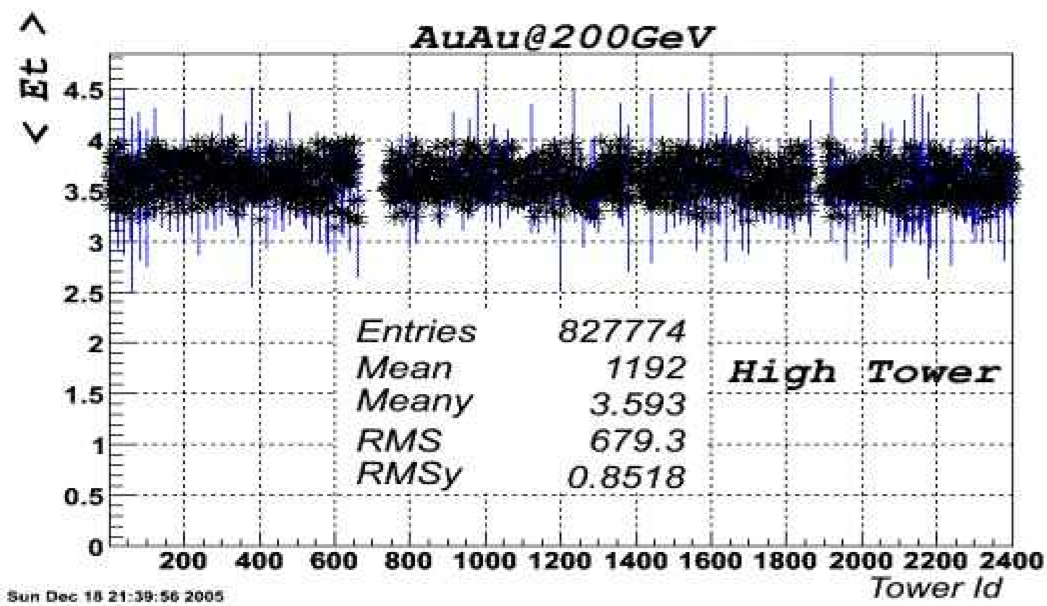

Figure 5.18: Transverse energy distribution vs. tower Id- High Tower data

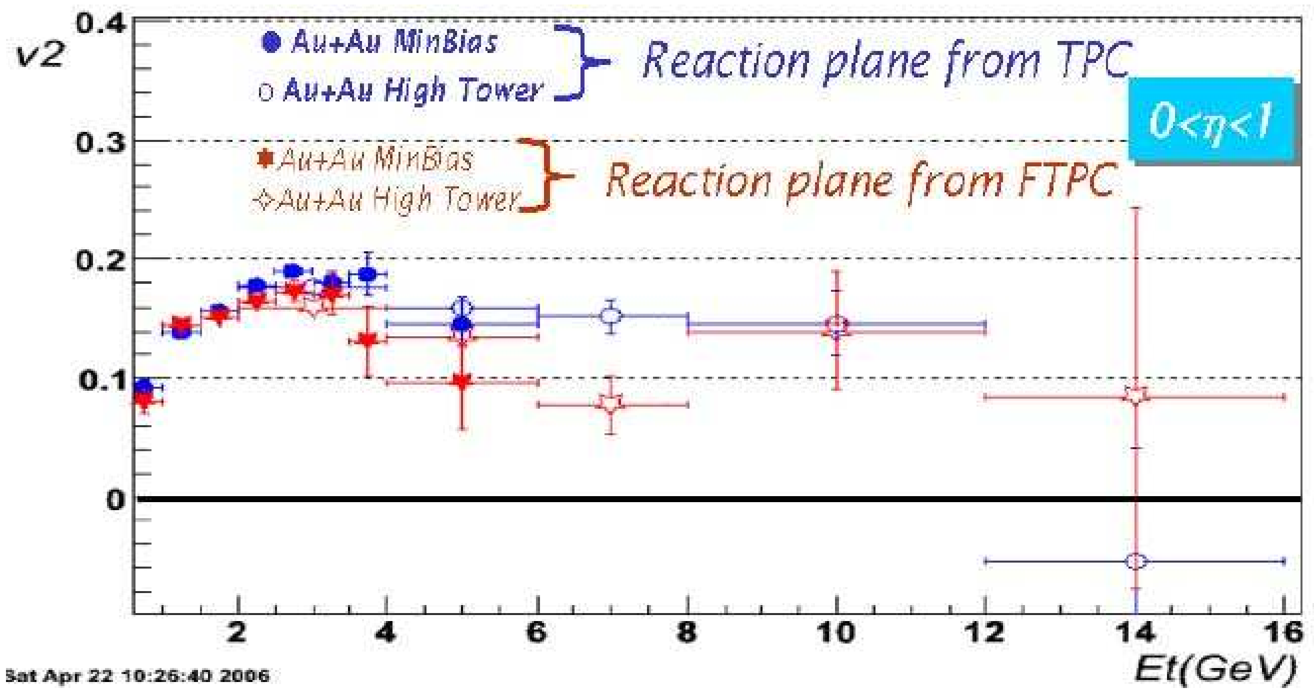

Figure 5.19: Elliptic flow of inclusive photons. Event plane was determined by TPC and FTPC separately.

The value obtained by Equation (5.7) is the observed v_2. The observed v_2 is divided by the reaction plane resolution to get the corrected value of v_2:

$$v_2 = \frac{< \cos(2\phi_\gamma - 2\Psi_{RE}) >}{\sqrt{\cos(2(\phi_1 - \phi_2))}} \tag{5.8}$$

where ϕ_1 and ϕ_2 are the event plane angles obtained from the sub-events. The resolutions for TPC are 0.44, 0.46 and for FTPC are 0.26,0.26 for the minimum bias and high tower events respectively.

Figure (5.19) shows the elliptic flow of inclusive photons integrated over unit pseudorapidity (0< η <1) with a reaction plane determination from the TPC and FTPCs. The fairly nice matching between the two different data sets, minimum bias and high tower, is obvious in the region of overlap (~3GeV). At low and intermediate transverse energy, the v_2 behaivour of inclusive photons is similar with that of the other mesons, which indicates either the dominance of the decayed photons in that range or the high contamination from the hadronic background due to the used photon identification method. Although at high transverse energy the statistical error bars are large but it is clear that v_2 tend to decrease with the transverse energy. The finite value of v_2 of inclusive photons at high transverse arises the question of the non-flow effect at high transverse energy. The scalar product method is suggested to estimate the contribution of the non-flow effect. The comparison of the scalar product method result between the different sizes of collision system can enlighten the effect of collective motion and/or the medium modification.

5.2.3 The Scalar Product Method

In order to estimate the contribution of the so-called "non-flow[3]" we used the scalar product method [253]. The scalar product results are expected to be the same for all collision system in the case of only "non-flow". The difference in the results using the scalar product method is indicative of collective motion and/or effects of medium modification. The performed measurements using the scalar product method are done using the TPCs traking detector at mid-rapidity and at forward/backward rapidity. The contribution of the non-flow is expected to be small or zero at the forward/backward pseudorapidity regions (FTPCs). It is interesting to study how elliptic flow evolves from $p + p$ collisions, in which non-flow dominates, to $Au + Au$ where flow dominants. To do such a comparison, we calculate the azimuthal correlation of particles as a function of p_t with the entire flow vector of all particles used to define the reaction plane(scalar product). The correlation in $Au + Au$ collisions, under the assumption that non-flow effects in $Au + Au$ collisions are similar to those in $p + p$ collisions, are the sum of the flow and non-flow contribution and are given

[3]The non-flow refers to the azimuthal correlations which are unrelated to the reaction plane. There are several possible sources for the non-flow like resonance deacy, (mini)jets, strings, quantum statistics effects, final state interactions (particularly Coulomb effects), momentum conservation, etc.

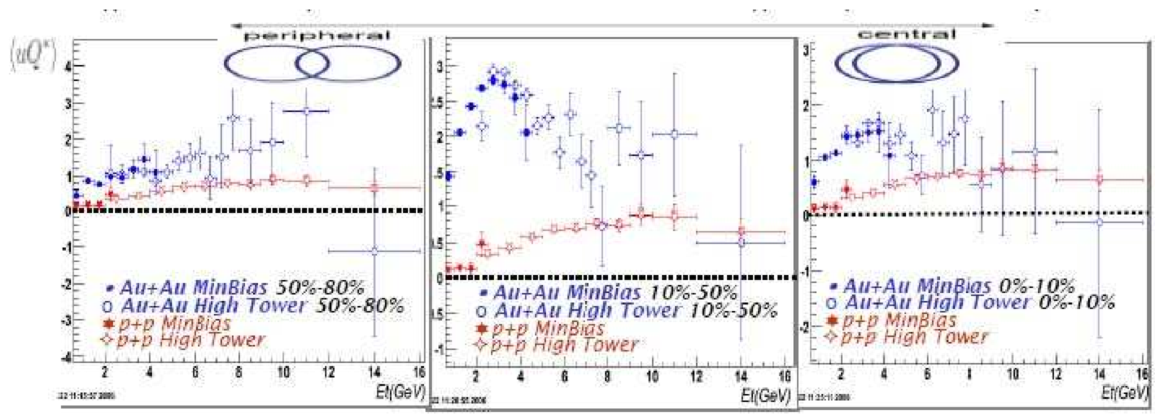

Figure 5.20: Azimuthal correlation of inclusive photons in $Au + Au$ and $p + p$ using the TPC tracks.

by:

$$< uQ^* >=< \sum_i \cos 2(\phi^{\gamma}_{p_t} - \phi_i) >= M v_2(p_t)\overline{v_2} + \{non - flow\} \tag{5.9}$$

where ϕ^{γ}_{pt} is the azimuthal angle of the photon from a given p_t bin, and ϕ_i is the azimuthal angle of the ith particle in the sub-event. In Equation(5.9)$u = \cos\phi + i \sin\phi$ is the unit vector. If Q is replaced by its unit vector, both Equations (5.7 and 5.9) are identical. The first term in right hand side of Equation (5.9) represents the elliptic flow of particles with a given p_t, and $\overline{v_2}$ is the average flow of particles used in the sum; M is the multiplicity of particles used in the sum, which in this work is performed over particles in the region p_t ≤2GeV/c and 2.6 $< |\eta| <$ 4.0 for FTPC and 0$< \eta <$1 for TPC.

Figures (5.20 and 5.21) show the azimuthal correlation as a function of transverse momentum using the TPC and FTPCs tracks respectively. In Figures (5.20 and 5.21) there are three different centrality ranges in $Au + Au$ collisions compared to minimum bias minimum bias and high tower $p + p$ collisions . As we predicted the contribution of non-flow at high pseudorapidity is negligble since the signal of the azimuthal corellation in the case of $p + p$ in the FTPC is zero within the error bars. We observe that the azimuthal correlation in peripheral Au+Au collisions and $p + p$ collisions are similar to each other except at low and mid p_t (<∼4 GeV/c), where the difference

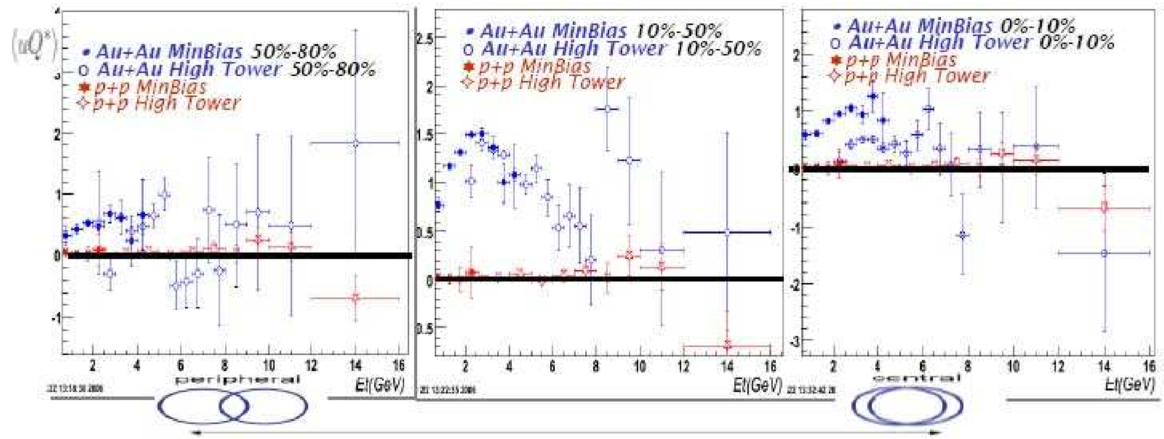

Figure 5.21: Azimuthal correlation of inclusive photons in $Au + Au$ and $p + p$ using the FTPC tracks.

is small compared to the difference between mid-central $Au + Au$ collisions and the other two cases. This is suggestive of a relatively small flow contribution in very peripheral $Au + Au$ collisions. In mid-central events, the azimuthal correlations in $Au+Au$ collisions is very different from that in $p+p$ collisions, both in magnitude and p_t-dependence. For the most central $Au + Au$ collisions, the magnitude of the correlation at low-p_t is also different from $p + p$, however, for particles with $p_t \sim 6$ GeV/c, the correlation in $p + p$ and $Au + Au$ becomes the same within errors. This indicates that non-flow could dominate the azimuthal correlations in central $Au + Au$ collisions at high p_t. The centrality dependence of the azimuthal correlation in $Au + Au$ collisions is clearly non-monotonic, being relatively small for very peripheral collisions, large for mid-central collisions, and relatively small again for central collisions. This non-monotonic centrality dependence is strong evidence that in mid-central collisions (10%-50%) the measured finite v_2 for p_t up to $\sim$8 GeV/c is due to real correlations with the reaction plane. We observe also some points with negative value which may reflect the fact that the radiative photons have negative v_2 due to the more radiation along the long axis of the medium-penterated fast partons.

5.3 π^0 Reconstruction

Although, the physics of π^0 is very important on the elementary particle physics and heavy-ions physics but in many cases the extraction the π^0 contribution to some measurements, like inclusive photons,is extremely important too. The main problem in the measurement of direct photons is to separate the signal from the contribution of radiative decays (mainly π^0, $\eta \rightarrow \gamma\gamma$) in the inclusive photon spectrum. A widely used strategy in nucleon-nucleon collisions is to identify direct photons at large transverse momenta via the jet topology: A cone of hadronic particles back-to-back with an isolated photon is characteristic for hard Compton scattering or $q\overline{q}$ annihilation. However, such requirements bias the measurement and basically exclude other processes, such as Bremsstrahlung. In the low multiplicity environment of nucleon-nucleon collisions it is also possible to identify photons from hadronic decays directly by an invariant mass analysis of photon pairs.

In heavy ion collisions the situation is more complicated, besides the increased number of possible sources of direct photons, the large multiplicity especially in central events does not allow to use the techniques mentioned above for elementary reactions. Instead the inclusive photons are measured and on a statistical basis compared to the expectation from hadronic decays, which is determined based on the measurement of π^0s in the same event sample. This eliminates a large fraction of the systematic errors, e.g. for normalization and centrality selection.

The decay of the π^0 is the largest contribution to the background for the direct photon measurement. The second most important contribution to the decay background after the π^0 is formed by the two photon decay of the ηmeson ($\eta \rightarrow \gamma\gamma$). The measurement of the η via this decay channel is complicated by the smaller production rate of the η, the smaller BEMC acceptance (Only the west half in STAR BEMC is working by the time of this analysis was done) for the two decay photons at low p_T, the larger decay width, and the smaller branching ratio compared to the π^0 measurement via this channel. This leads to a smaller signal to combinatorial background rate in the invariant mass analysis.

Neutral pions are detected via their 2γ decay channel. Due to the relatively short mean lifetime of neutral pions of about 10^{-16} s, typical of electromagnetic decays, the pions decay before escaping from the collision region. This makes the decay vertex well known and the pions can be reconstructed via an invariant mass analysis of photon pairs measured.

5.3.1 Invariant Mass Analysis

The invariant mass of a particle pair is given by the absolute value of its four-momentum $P_{12} = P_1 + P_2$. As photons are massless particles this reduces to the determination of the energy E and the opening angle θ between the two photons:

$$m_{\gamma\gamma} = \sqrt{(P_{\gamma 1} + P_{\gamma 2})^2} = \sqrt{E_{\gamma 1} E_{\gamma 2}(1 - \cos\theta_{12})} \tag{5.10}$$

For a photon pair originating from a π^0 decay this invariant mass is identical to the π^0 rest mass of 134.9766 MeV/c^2 [254]. However, due to the finite energy and position resolution in the detection of the photon pair, the actual reconstructed value is smeared around a mean value, which can deviate from the nominal value. The reconstructed peak position is also influenced by the high multiplicity in a heavy ion collision, where overlapping clusters can shift the measured energy of the single photon. With the invariant mass analysis the π^0 cannot be identified uniquely since all possible photon-photon combinations have to be considered. This leads to a large combinatorial background, which increases quadratically with the multiplicity. [4]

The π^0 yield is instead determined on a statistical basis, with the background contribution established via a mixed event technique. One possibility to reduce the combinatorial background is to make use of the phasespace distribution of the photons

[4] For a given multiplicity N the number of possible pair combinations is $N_{pair} = \frac{N}{2}(N-1)$.

in a π^0 decay. The probability for a decay photon to carry a fraction x of the pions energy is the same for all values of x. Expressed in terms of the asymmetry α of the two photon energies defined by Equation (5.11), this is equivalent to a flat distribution of α.

$$\alpha = |\frac{E_1 - E_2}{E_1 + E_2}| \tag{5.11}$$

For random combinations within one event the asymmetry is not flat. As the energy spectrum of all detected particles is steeply falling, pair combinations containing one hit with lower energy are more probable. This leads to an increase of photon pairs with large asymmetry, where the asymmetry distribution for photons from π^0s is nearly flat.

5.3.2 π^0 Decay Kinematics

If the π^0 is moving with a velocity different from zero (lab frame), the two gamma rays can obviously not both be emitted along the direction of motion of the original particle. This follows from conservation of energy and momentum. If the two photons move in the same direction, their total energy is equal to their total momentum and is equal to the sum of the two frequencies. This is only possible if the mass of the decaying particle is zero, which we know not be the case. Therefore, there must be a certain minimum angle between the two directions of emission of the photons. Intuitively, this angle is obtained in the symmetric case. From Equation(5.10), it follows that the minimum opening angle depends on the total energy of π^0 through the following equation:

$$\theta_{min} = 2\sin^{-1}(m_{Inv.}/E) \tag{5.12}$$

Figure (5.22) shows the energy dependence of the minimum openeing angle between the two decayed photons. It is also of some interest to compute the angular correlation function of the two γ-rays emitted under the assumption that all decay

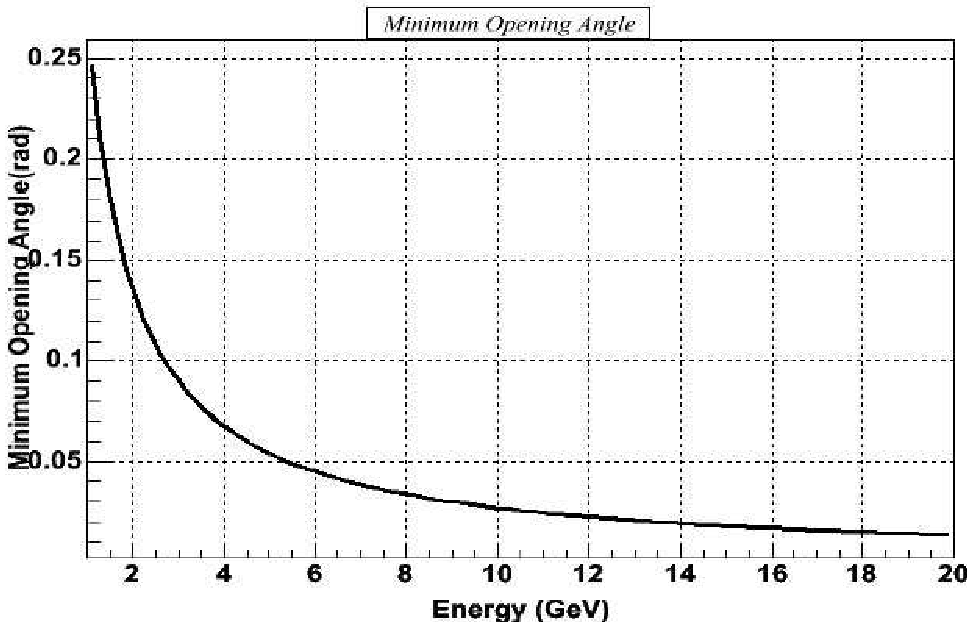

Figure 5.22: The minimum opening angle vs. the total energy of π^0.

directions are equally probable in the Lorenz frame where the decaying particle is at rest. the correlation fuction is given by the following equation:

$$W(\phi) = \frac{(1-v^2)\cos(\phi/2)\theta\{v^2-\cos^2(\phi/2)\}}{2v\sin^2(\phi/2)\sqrt{v^2-\cos^2(\phi/2)}} \tag{5.13}$$

It is clear that the correlation function goes over into a δ-function both in the limit when v becomes very small and when it is very close to one. In the first case, the δ-function appears at $\phi = \pi$, while the δ-function in the second case appears for ϕ=0. This is physically reasonable as v=0 corresponds to the particle being at rest, in which case the two photons must be emitted in opposite directions. When the velocity v is equal to the velocity of light, the rest mass of the decaying particle must be zero and, according to our previous discussion, the two photons have both to be emitted in the forward direction.

Even for intermediate velocities, the distribution $W(\phi)$ in Equation (5.13) is very heavily peaked but around the minimum opening angle given by Equation (5.12) . As an illustration of this one excample is plotted in Figure(5.23). Consequently, if a

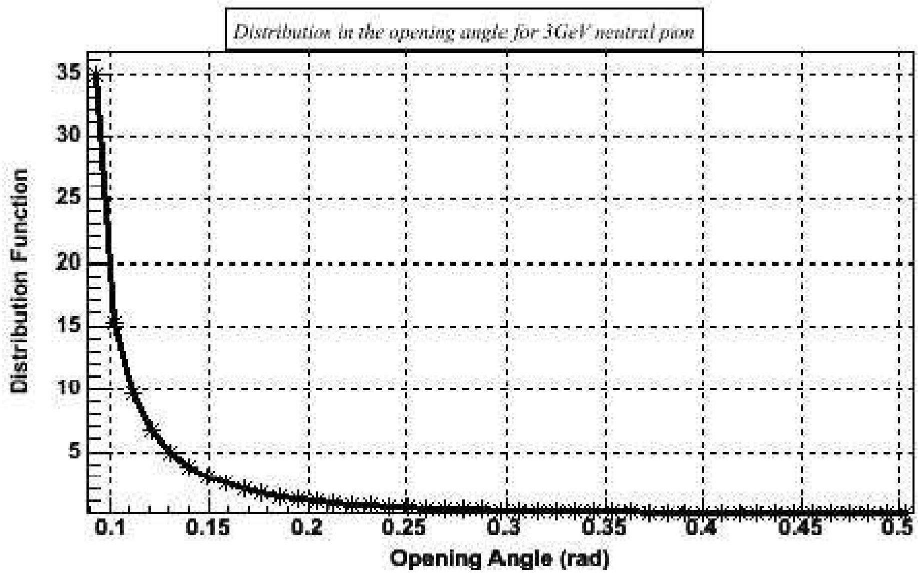

Figure 5.23: The distribution of $\gamma\gamma$ in the openenig angle for 3GeV π^0.

neutral particle decays into two photons and if the distribution is isotropic in the rest frame of the decaying particle, the angle between the two photons in the laboratory system is practically always given by the minimum angle in Equation(5.12). This is particularly true if the velocity v is either small compared to one or very close to one.

5.3.3 Electromagnetic Shower Characteristics

Since the EM shower development is primarily determined by the electron density in the absorber medium, it is to some extent possible, and in any case convenient, to describe the shower characteristics in a material-independent way. The units that are frequently used to describe the characteristic shower dimensions are the radiation length (X_0) for the longitudinal development and the Molière radius (ρ_M) for the transverse development. The radiation length is defined as the distance over which a high-energy (> 1 GeV) electron loses on average 63.2% (1 - 1/e) of its energy to bremsstrahlung. The average distance that very high-energy photons travel before converting into an e^+e^- pair equals $\frac{9}{7}(X_0)$. The Molière radius is defined by the ratio of X_0 and ϵ_c, where ϵ_c is the electron energy at which the losses through radiation and

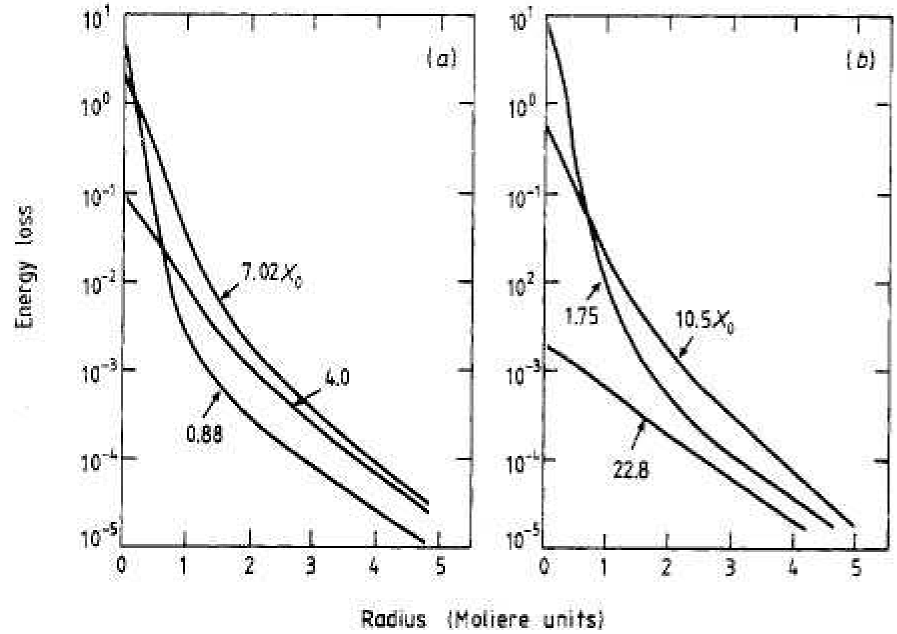

Figure 5.24: The lateral distribution of the energy deposited by a 1GeV EM showe in lead, at various depths.

ionization are the same. For approximate calculations, the following relations hold:

$$X_0 \approx 180A/Z^2(gcm^{-2}) \qquad \rho_M \approx 7A/Z(gcm^{-2}) \tag{5.14}$$

Expressed in these quantities, the shower development is approximately material independent.

Figure (5.24) shows the lateral distribution of the energy deposited by an EM shower in lead, at various depths. The lateral shower profile is characterized by two distinguished components (note the logarithmic ordinate). The radial profile shows a pronounced central core surrounded by a halo. The central core disappears beyond the shower maximum. Two effects cause the lateral spread of an EM shower (i) Electrons move away from the axis by multiple scattering. (ii) In the energy region where the total cross section is minimal, bremsstrahlung photons may travel quite far from the shower axis, in particular if they are emitted by electrons that themselves travel under a considerable angle with this axis. The first process dominates in the early stages of the shower development, while the second process is predominant beyond the shower maximum, particularly in high-Z media.

Figure (5.24) shows also that EM showers are very narrow, especially in the first few radiation lengths. The Moliere radius of lead is 1.7 cm. With a sufficiently fine-grained calorimeter, the showering particle can therefore be localized with a precision of 1 mm.

The physics of the longitudinal and transverse development of photon shower is very well established. When the photon of the shower reach the critical energy, radiation (pair production) ceases and the energy is deposited as ionization (Compton or photoelectric). Almost all of the shower energy ∼90% is deposited in a cylinder of radius ρ_M. and ∼99% of the shower energy is deposited in a cylinder of radius $3.5\rho_M$ .In lead, the critical energy is 7.4MeV, the radiation length is 5.6mm, the molière raidus is 16.0mm and the nuclear interaction length[5] is 170mm.

5.3.4 New Clustering Algorithm

Motivation

Two main reasons have motivated us to develop a new cluster algorithm to replace the current cluster finder in STAR BEMC. Very pronounced persistence peak in the real data at low invariant mass region was the first reason (Figures 5.25 and 5.26). Secondly, the failure of the current cluster algorithm to show the invariant mass π^0 peak in the high multiplicity collision system (Figure 5.27). Figures(5.25 and 5.26) show a clear peak in minimum bias and high tower $d + Au$ data at the low invariant mass region. This peak is clearly due to the photon candidate cluster splitting. The existence of cluster splitting in the current cluster finder smears the π^0 peak in the high multiplicity collision system and it is believed as the reason for the nonexist π^0

[5]The nuclear interaction length of an absorber medium is defined as the average distance a high-energy hadron has to travel inside that medium before a nuclear interaction occurs.

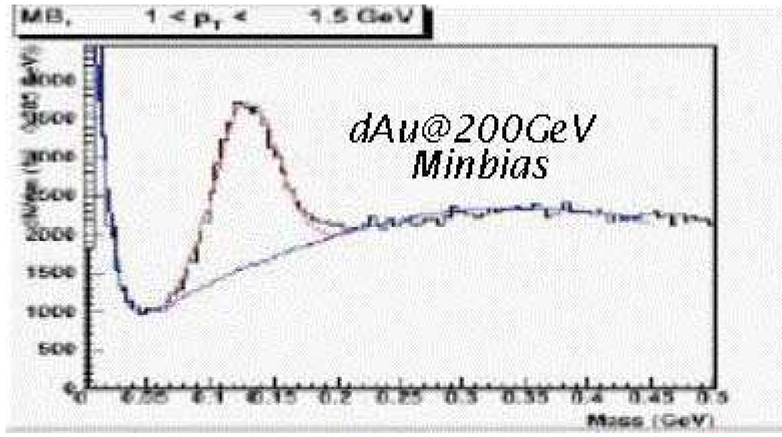

Figure 5.25: $M_{\gamma\gamma}$ in dAu minimum bias data.

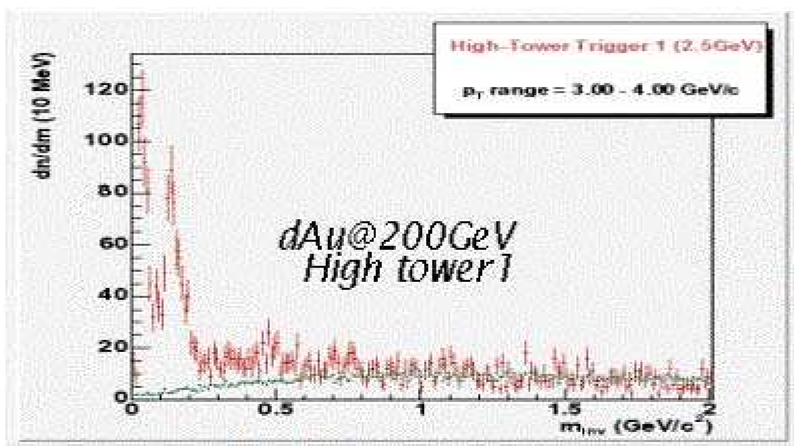

Figure 5.26: $M_{\gamma\gamma}$ in dAu High Tower data.

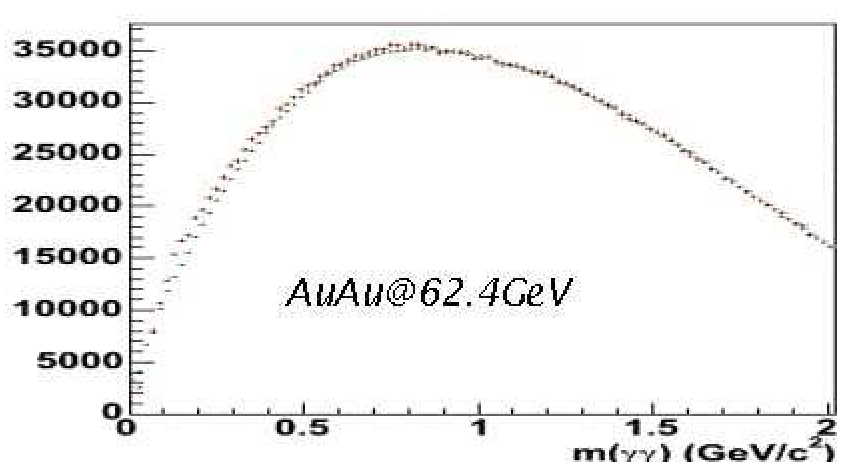

Figure 5.27: $M_{\gamma\gamma}$ in $Au + Au$ at $\sqrt{s_{NN}}$ =62.4GeV data.

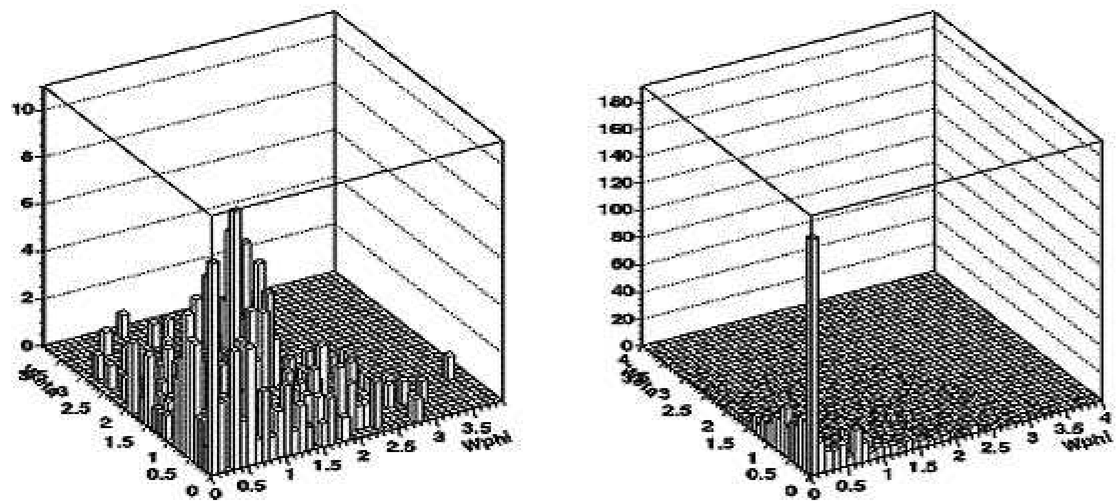

Figure 5.28: The effective shower width for the electrons and the charged hadrons. $W_{eta} = W_{phi} = \frac{\sum_i r_i E_i}{\sum_i E_i}$, where E_i represented the energies deposited in individual strip i and r_i indicated the distance between the strip i and the center of the cluster.

peak in such system (Figure 5.27).

Transverse Shower Shape Study

It is crucial for direct photons identification to use the same algorithm for inclusive photons and π^0 and also it is important to have the same cluster algorithm for all different collisions system to reduce the systemic errors. This is impossible without having transverse shower shape study. It is clear from the SMD strips width that the distinction between two adjacent photon showers and one photon shower is difficult without the Preshower.

In Figure(5.28),the effective shower width in η and ϕ is shown for very selective electrons (left panel) and for the charged hadrons (right panel). The electrons were identified by the usuall method dE/dx using the TPC, and further more the electrons sample is filtered out by the E/p method using the BEMC. Altough the effective width of the electrons is greater than that of hadrons hence the hadrons usually do not shower in the electromagnetic calorimeter. However,the efficeincy/purity of the effective width cut is small due to the size of the SMDs strips and compact nature of the electromagnetic shower.

STAR BEMC Position and Granularity Reviews

The calorimeter has a total depth of approximately $20X_0$ at η=0. The nearly projective tower size is approximately 6-8ρ_M in η and in ϕ. The energy resolution for the tower is very good. SMDs (two layers of gas wire pad chambers) are located nearly at $5x_0$. The SMDs spatial resolution is very good and the energy resolution is bad. Each SMD plane consists of 150 strips, and each strip scans two towers (The η strips scan two towers in ϕ and each ϕ strip scans two towers in η). The strip width is approximately one moliere radius. The distance between the interaction point and the STAR BEMC face at η=0 is ∼2.2m. The calorimeter coverage is full in the azimuthal and one unit in pseudorapidity (∼2.93m). The very important part of the BEMC the Preshower was not ready yet for the data analysis during the 2004 run. The Preshower is supposed to enhance the ability of the BEMC for the γ/π^0 and electron/hadron disrimination.

Clustering Algorithm

The detail of new cluster algorithm is summarized in the following points:

• The central strip of each cluster is included completely in one tower to avoid cluster splitting candidate signals.

• The cluster size is three strips in Eta and seven strips in phi to have fine resolution in one plane and to reduce the cluster splitting by the other plane.

• The minimum distance between two points is two strips in η and/or three strips in phi to resolve the two decayed photons of π^0 at high-p_t.

• The distance between the center of the tower to the point's position is <0.03 to reduce the cluster splitting across the towers.

• The x and y components of the point position are determined from the ϕ-strips coordinate due to the high resolution of the ϕ strips in these directions.

• The z-component of the point position is determined from the η-strips coordinate due to the high resolution of the η strips in the z-direction.

• The energy assigned for the point depends only on the relative position to the center of the tower if the separation between the two points is greater than the width of two towers. In case of separation less than the width of two towers the assigned energy depends also on the separation between the two points.

GEANT Detector Simulation

The passage of particles through the detector material is simulated using the standard GEANT software package developed and maintained by the CERN Application Software Group. GEANT is a highly developed library that models electromagnetic and nuclear interactions of particles with matter. With GEANT we can track the particles through the experimental setup and simulate the detector response.

The STAR detector is described by a highly detailed three dimensional model that is built using pre-defined geometrical primitives of specified material. The GEANT model of STAR is organized in a tree-like structure allowing for easy navigation along an arbitrary trajectory. GEANT models the propagation of particles through the detector representation by simulating multiple scattering, energy loss, conversion, and particle decay along each step of the particle trajectory. The output of GEANT is a full simulation of the propagation of a given particle type through the detector volume. More information on GEANT can be found in Ref. [255].

Cluster Splitting

To check for the cluster splitting in the above-mentioned algorithm, we simulated 5k π^0 for each unit of transverse momentum between 1GeV/c and 15GeV/c. The results of the clustering algorithm is compared with the ideal case of the π^0 through its highest decay channel (2γ). Figure (5.29) shows such comaprison of α vs. θ for

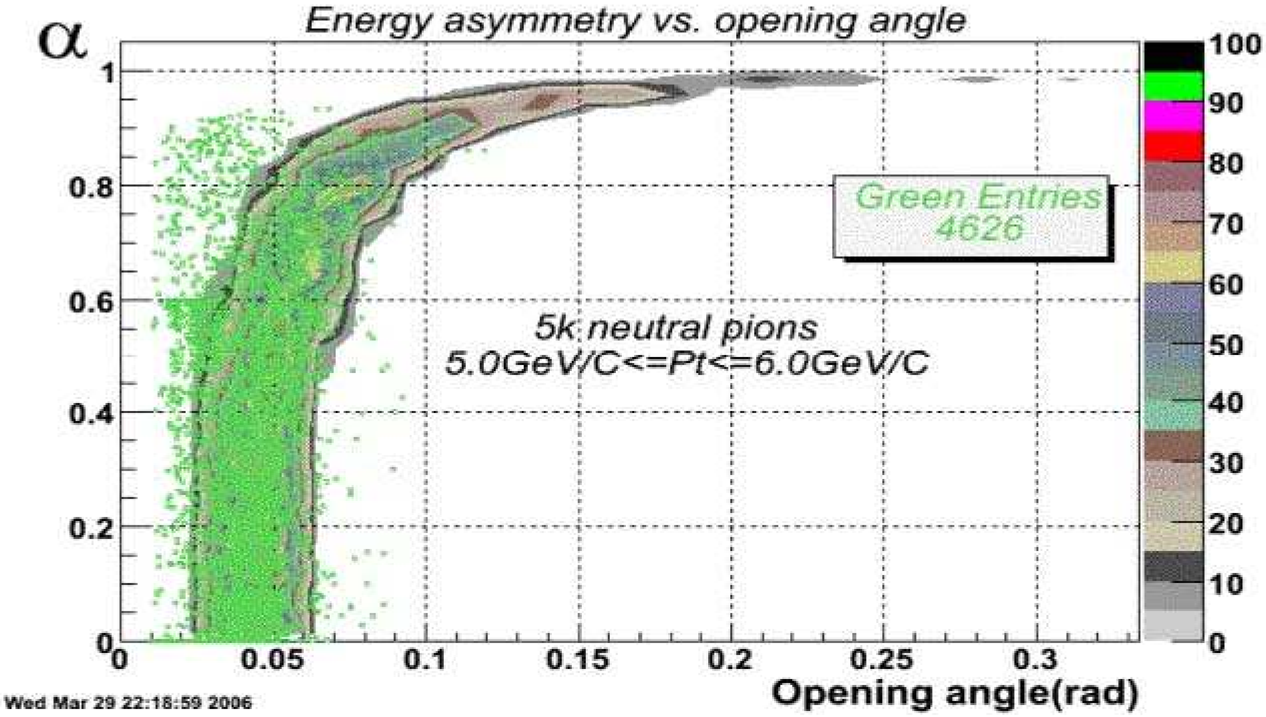

Figure 5.29: The energy asymmetry vs. the opening angle of 2γ for π^0 with 5GeV/c$\leq$ p_t $\leq$6GeV/c. The band represent the ideal case result and the dots represent the cluster algrithm result.

the 5GeV/c$\leq p_t \leq$6GeV/c bin.Theoretically the relation between α-θ is given by:

$$\alpha = \sqrt{1 - m^2_{Inv.}/E^2 \sin^2(\theta/2)}. \tag{5.15}$$

It is obvious that there is a cluster splitting since not all the dots fall inside the band. The inavariant mass is shown in Figure (5.30) where the cluster splitting clearly cause the low invariant mass peak.

Cluster Splitting Consequences

To study the low invariant mass peak position we simulated 5k of γ for each momentum bin over the range of 1GeV/c$\leq p_t \leq$15GeV/c. We have observed that the position of the low invariant mass peak moves towrad higher invariant mass region with the energy of the simulated photons. Figures (5.31, 5.32) show the effect of cluster splitting. At high energy the cluster splitting creates fake π^0 since some of

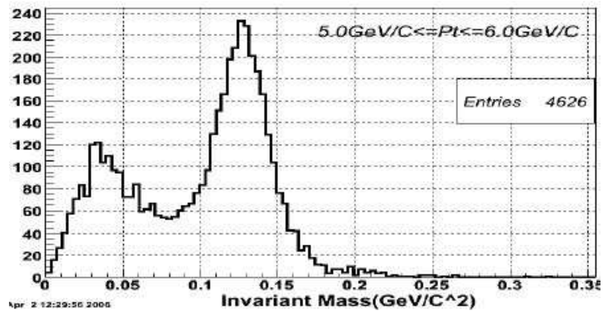

Figure 5.30: $M_{\gamma\gamma}$ for 5k simultaed π^0 with unifrom distribution in transverse momentum 5GeV/c$\leq p_t \leq$6GeV/c.

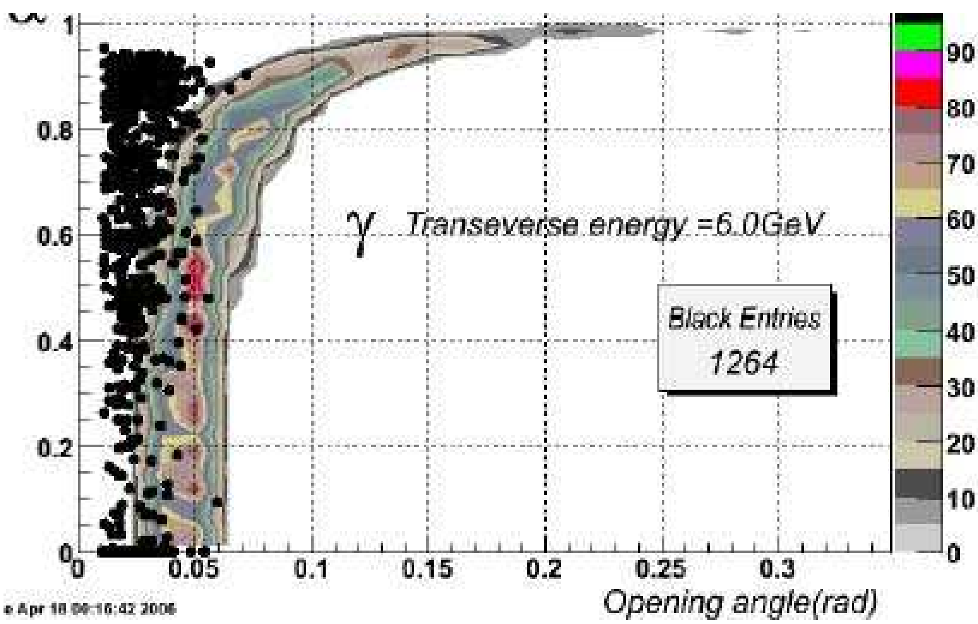

Figure 5.31: $M_{\gamma\gamma}$ for 5k simultaed γ with transverse momentum 6GeV/c.

the entries in figure (5.32) show in the π^0 invarinat mass region.

Cluster Splitting Removal

The basic idea is to use the π^0 kinematics decay to supress the cluster splitting. Therefore, the method here is just valid for the π^0 reconstruction only and it is not valid as a general photon detection algorithm. The conditions and requiremnets for the cluster splitting suppression enlisted in table (5.5).

Figures (5.33-5.36) show the results after using the cluster splitting conditions.

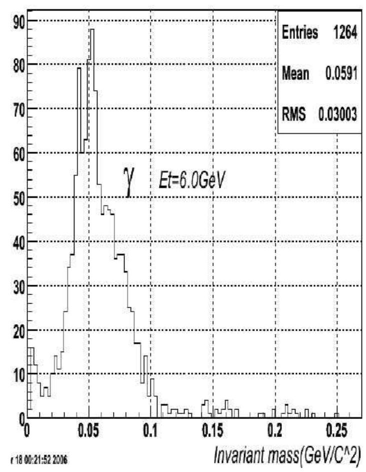

Figure 5.32: $M_{\gamma\gamma}$ for 5k simultaed γ with p_t=6GeV/c.

conditions	Requirements
Adjacent Towers and E_γ <10GeV	$E_{Tower} \geq$1.2GeV, $\alpha_{Tower} \leq 0.6$
Adjacent Towers and E_γ >4GeV	$E_{Point_1} + E_{Point_2} > 5.5$GeV
Adjacent Towers and E_γ >10GeV	$E_{Tower} \geq$3GeV, $\alpha_{Tower} \leq 0.6$
Same Tower	E_{Tower} >10GeV
Same Module and Same Sub	E_{smds} >0.25GeV, α_{SMDs} <0.6
Adjacent Modules and $TowerId_2 = TowerId_1 + 20$	α_{Tower} ≤0.35

Table 5.5: Cluster Splitting Removal

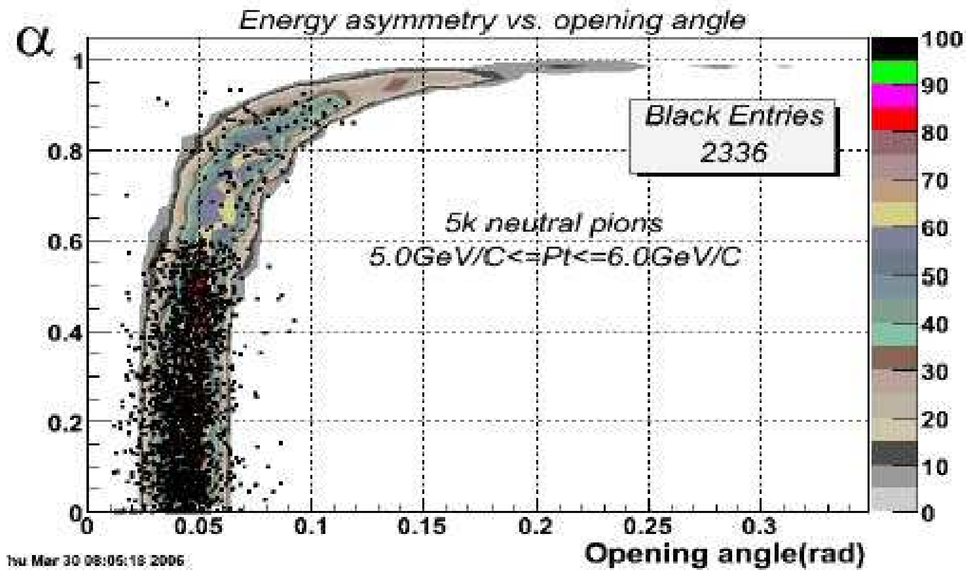

Figure 5.33: The energy asymmetry vs. the opening angle for π^0 with 5GeV$\leq$p$_t\leq$6GeV/c for the survived pairs after the cluster splitting removal cut is used.

Figures(5.35, 5.36) show the comparison between the effect of the cluster splitting removal and the use of the energy asymmetry cut. The energy asymmetry cut reduces the efficiency more than the cluster splitting removal. In addition to, the cluster splitting is more suppressed by the cluster splitting removal than by the asymmetry cut.

Results

The following figures represent the results of π^0 invariant mass peak from simulation and all different collision systems at RHIC using the STAR BEMC.The π^0 is obtained in all results and no low invarinat mass peak is observed. Due to technical reasons for we couldn't purse the analysis further toward the π^0 spectrum in AuAu at $\sqrt{s_{NN}}$=200GeV.

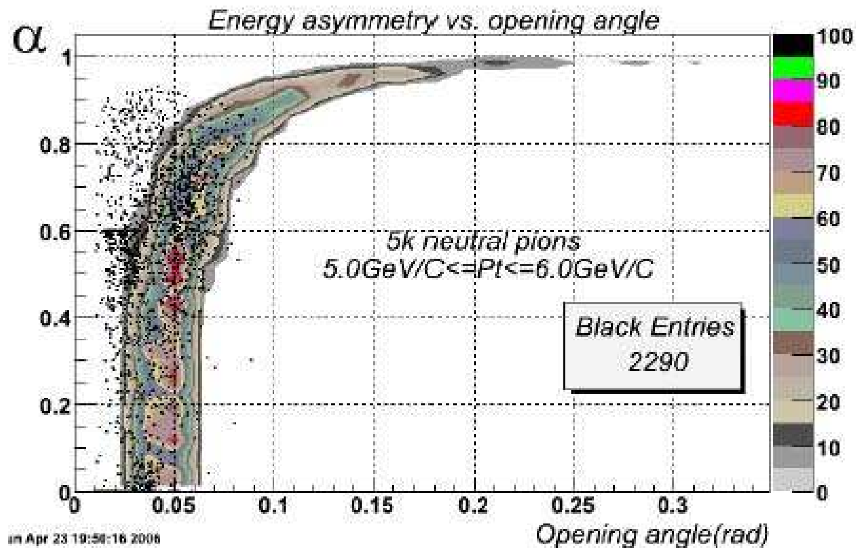

Figure 5.34: The energy asymmetry vs. the opening angle for π^0 with 5GeV$\leq$p$_t$$\leq$6GeV/c for the rejected pairs after the cluster splitting removal cut is used.

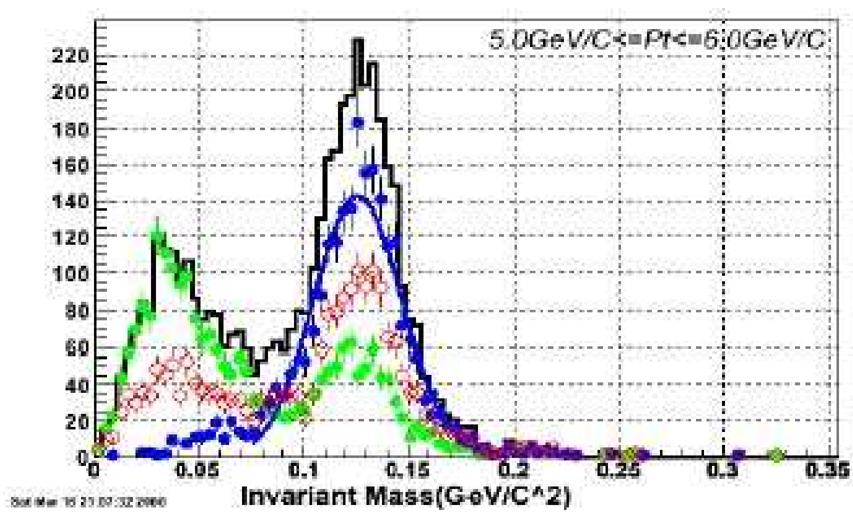

Figure 5.35: $M_{\gamma\gamma}$ for the accepted pairs of 5k simultaed π^0 with unifrom distribution in transverse momentum 5Gev$\leq$ p$_T$$\leq$6GeV."all pairs(Black Line), accepted(Filled Circles),(Opened Circles) rejected,(Red filled Circles) asymmetry cut".

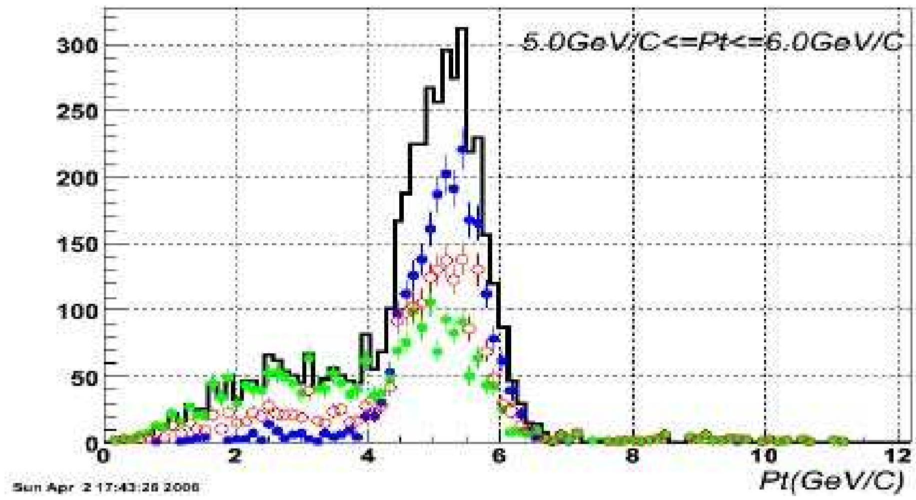

Figure 5.36: The momentum distribution of all pairs(Black Line), accepted(Filled Circles),(Opened Circles) rejected,(Red filled Circles) asymmetry cut.

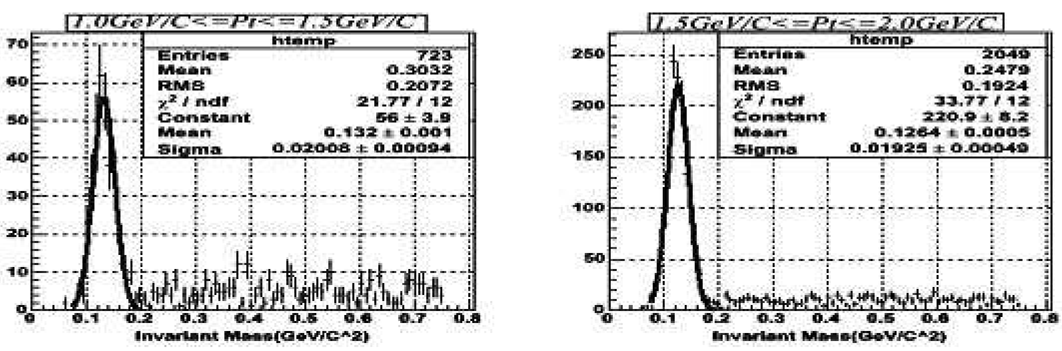

Figure 5.37: Simulation: $M_{\gamma\gamma}$(left) 1.0GeV/c$\leq$ p$_t$$\leq$1.5GeV/c (right)1.5GeV/C$\leq$ p$_t$$\leq$2.0GeV/c.

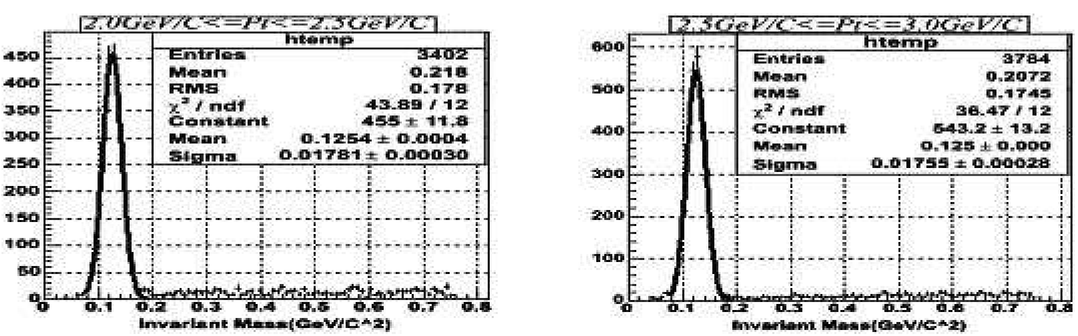

Figure 5.38: Simulation:$M_{\gamma\gamma}$(left) 2.0GeV/c$\leq$ p$_t$$\leq$2.5GeV/c (right)2.5GeV/c$\leq$ p$_t$$\leq$3.0GeV/c.

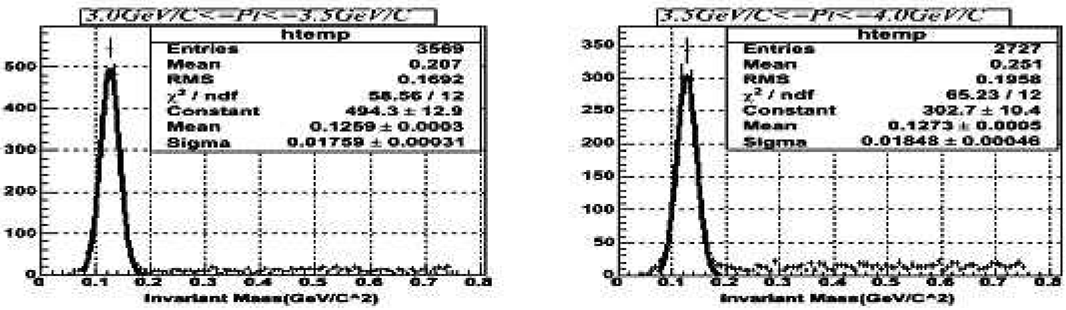

Figure 5.39: Simulation:$M_{\gamma\gamma}$(left) 3.0GeV/c$\leq$ p$_t$$\leq$3.5GeV/c (right)3.5GeV/c$\leq$ p$_t$$\leq$4.0GeV/c.

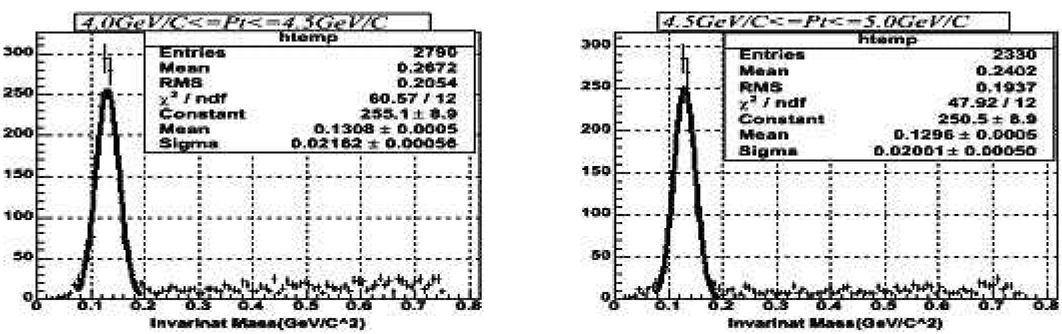

Figure 5.40: Simulation:$M_{\gamma\gamma}$(left) 4.0GeV/c$\leq$ p$_t$$\leq$4.5GeV/c (right)4.5GeV/c$\leq$ p$_t$$\leq$5.0GeV/c.

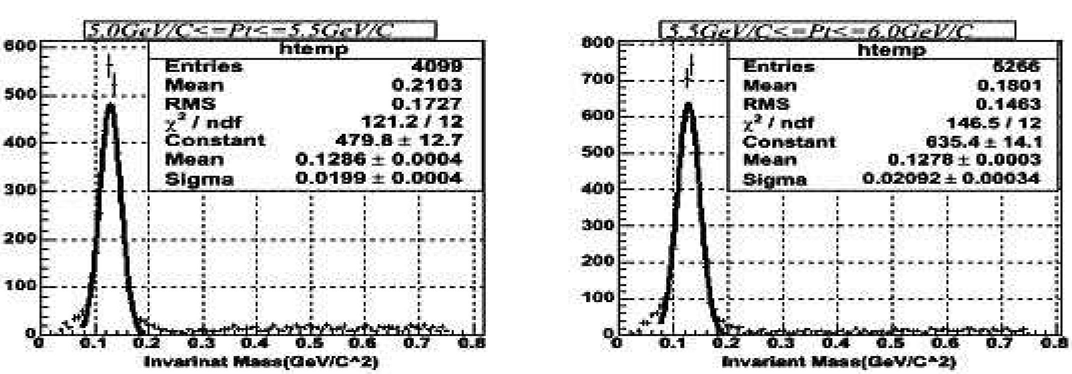

Figure 5.41: Simulation:$M_{\gamma\gamma}$(left) 5.0GeV/c$\leq$ p$_t$$\leq$5.5GeV/c (right)5.5GeV/c$\leq$ p$_t$$\leq$6.0GeV/c.

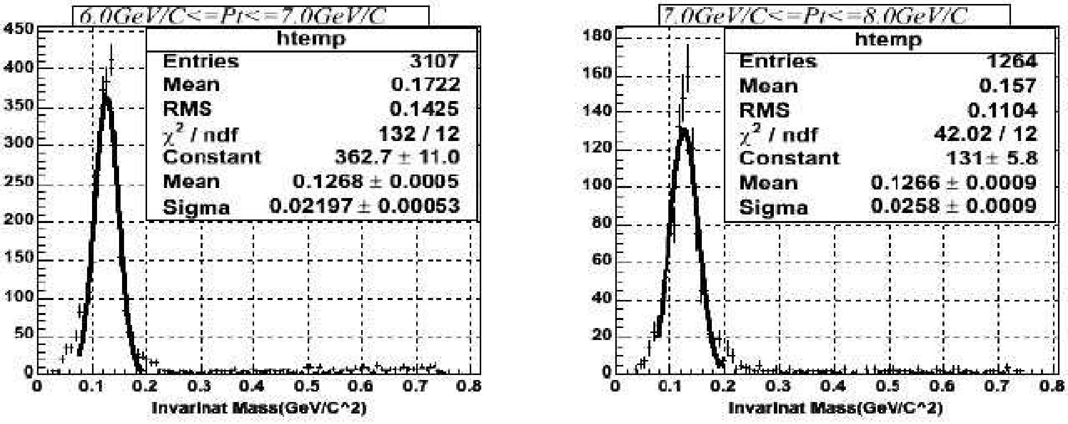

Figure 5.42: Simulation:$M_{\gamma\gamma}$(left) 6.0GeV/c≤ p_t≤7.0GeV/c (right)7.0GeV/c≤ p_t≤8.0GeV/c.

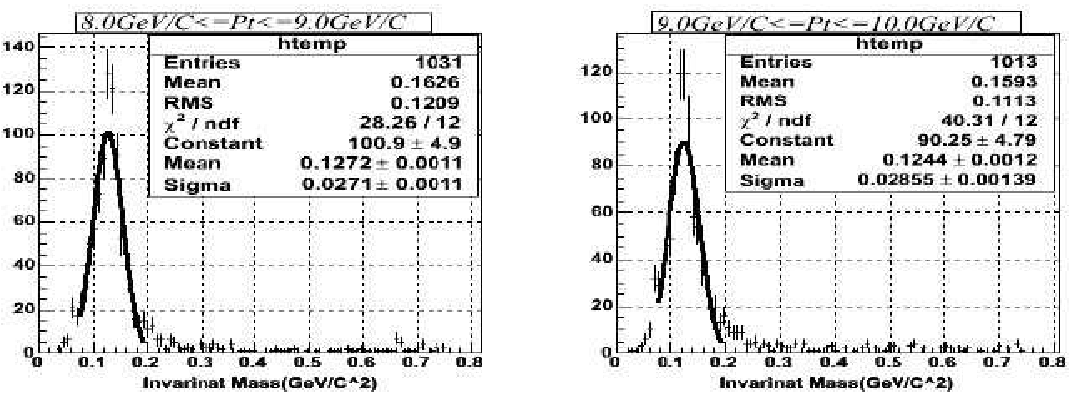

Figure 5.43: Simulation:$M_{\gamma\gamma}$(left) 8.0GeV/c≤ p_t≤9.0GeV/c (right)9.0GeV/c≤ p_t≤10.0GeV/c.

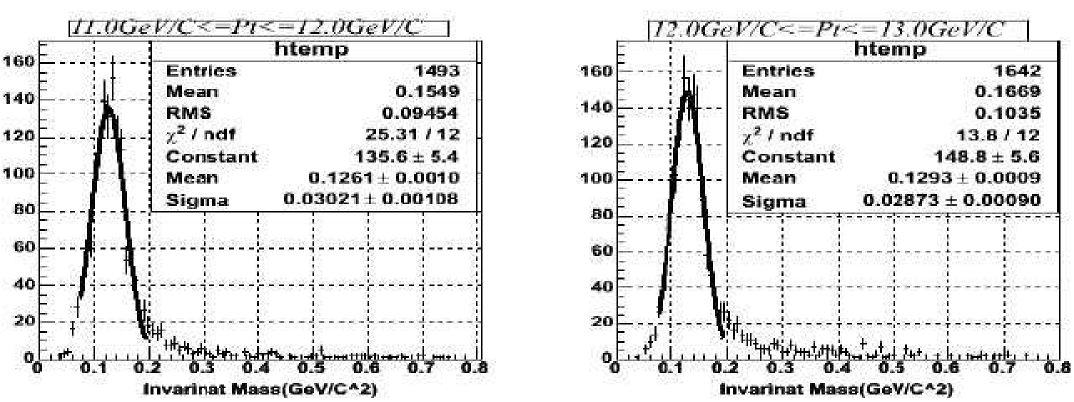

Figure 5.44: Simulation:$M_{\gamma\gamma}$(left) 11.0GeV/c≤p_t≤12.0GeV/c (right)12.0GeV/c≤p_t≤13.0GeV/c.

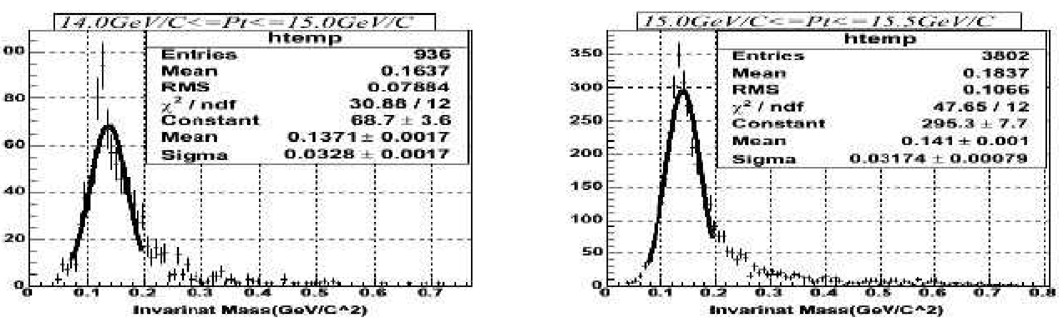

Figure 5.45: Simulation:$M_{\gamma\gamma}$(left) 13.0GeV/c$\leq$p$_t\leq$14.0GeV/c (right)14.0GeV/c$\leq$p$_t\leq$15.0GeV/c.

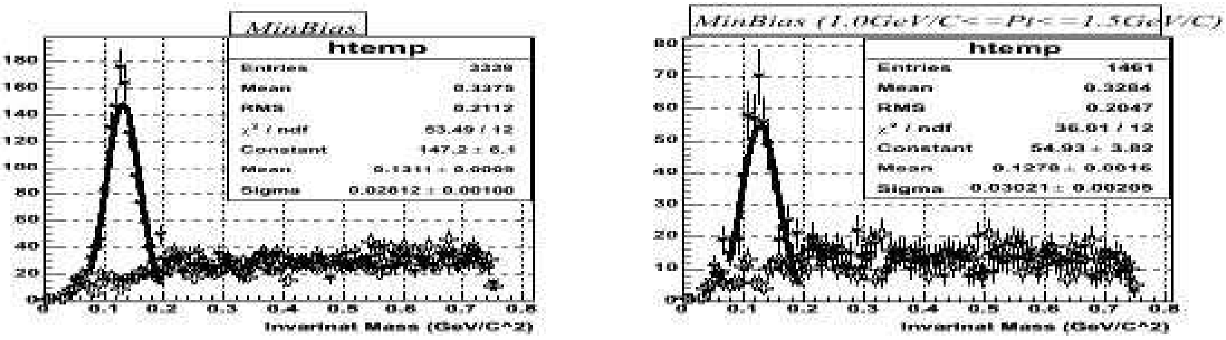

Figure 5.46: pp $\sqrt{s}$=200GeV,data minimum bias data:$M_{\gamma\gamma}$

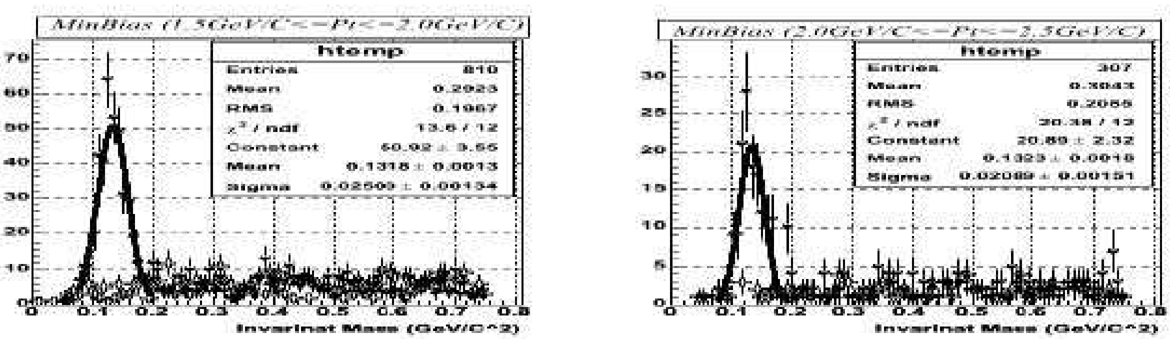

Figure 5.47: pp $\sqrt{s}$=200GeV,minimum bias data:$M_{\gamma\gamma}$

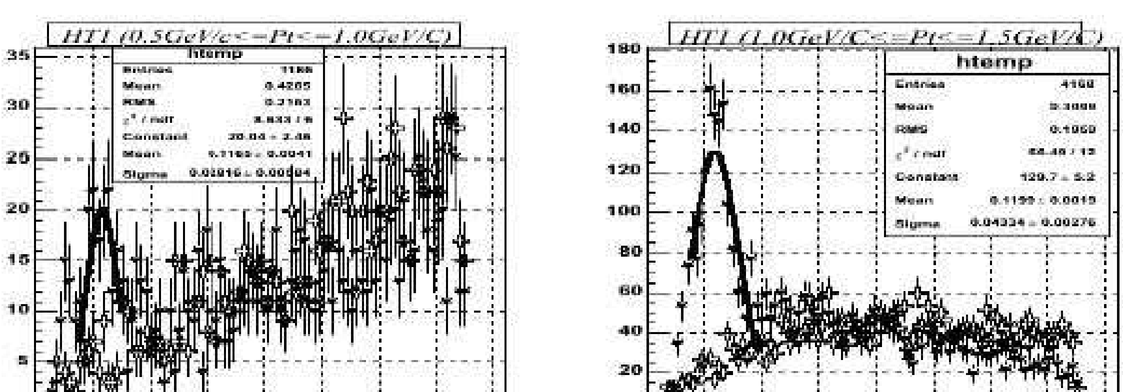

Figure 5.48: pp $\sqrt{s}$=200GeV,high tower data:$M_{\gamma\gamma}$

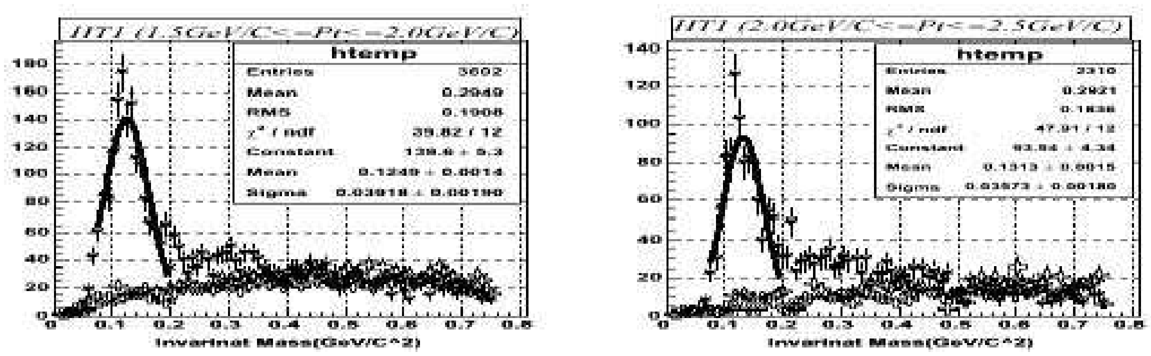

Figure 5.49: pp $\sqrt{s}$=200GeV,high tower data:$M_{\gamma\gamma}$

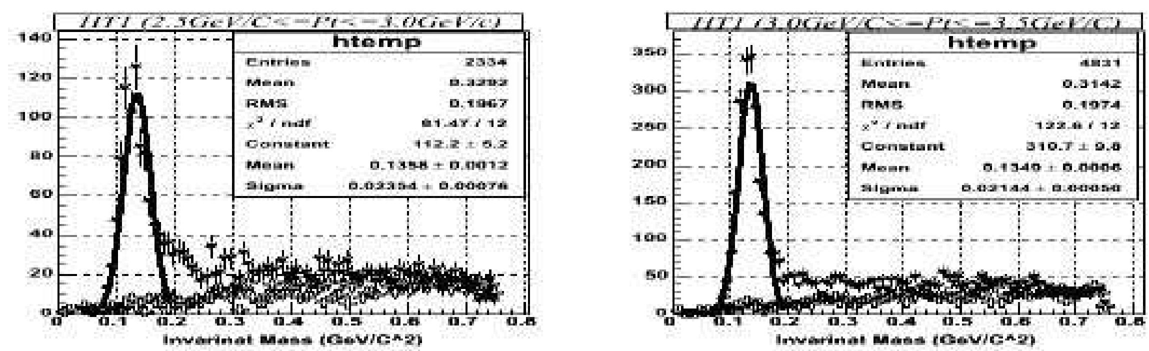

Figure 5.50: pp $\sqrt{s}$=200GeV,high tower data:$M_{\gamma\gamma}$

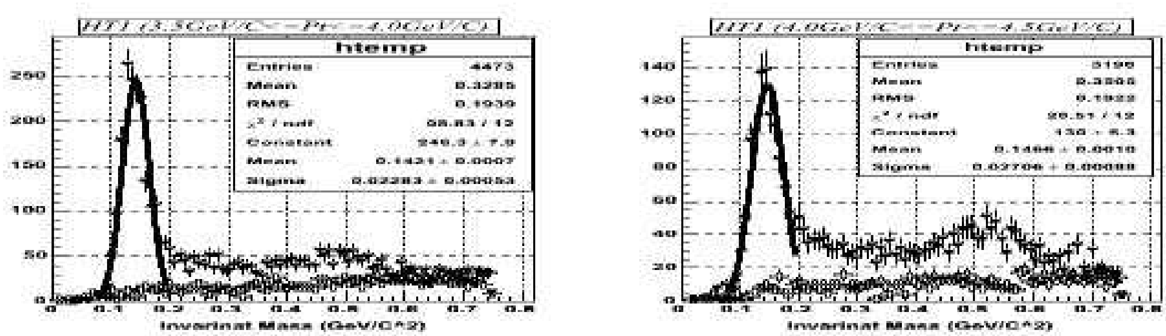

Figure 5.51: pp$\sqrt{s}$=200GeV, high tower data:$M_{\gamma\gamma}$

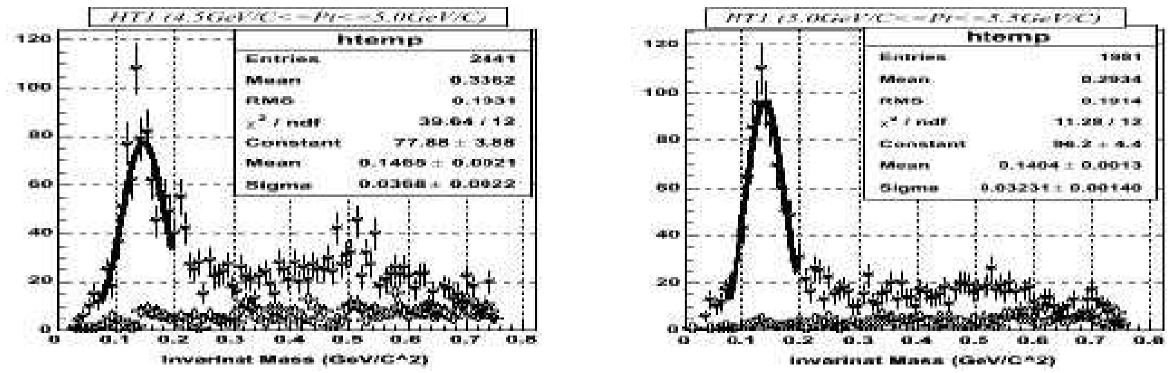

Figure 5.52: pp $\sqrt{s}$=200GeV,high tower data:$M_{\gamma\gamma}$

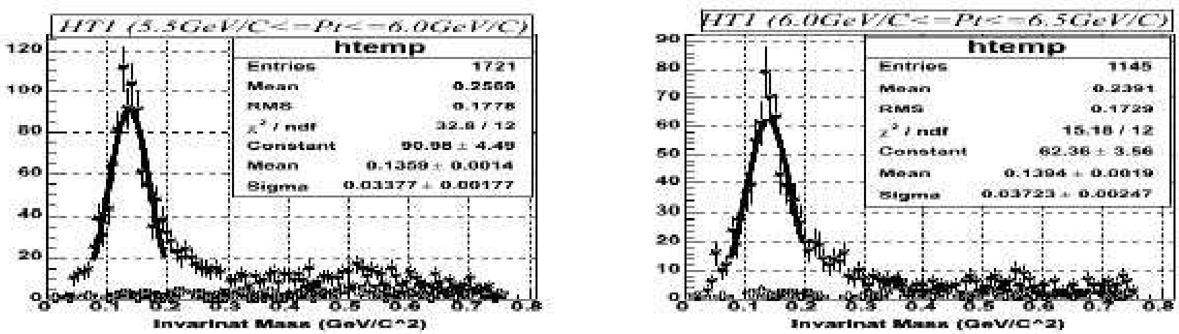

Figure 5.53: pp $\sqrt{s}$=200GeV,high tower data:$M_{\gamma\gamma}$

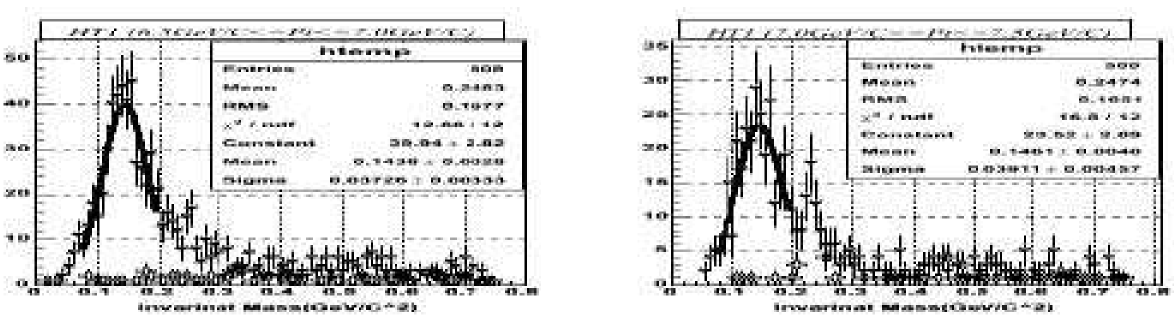

Figure 5.54: pp$\sqrt{s}$=200GeV, high tower data:$M_{\gamma\gamma}$

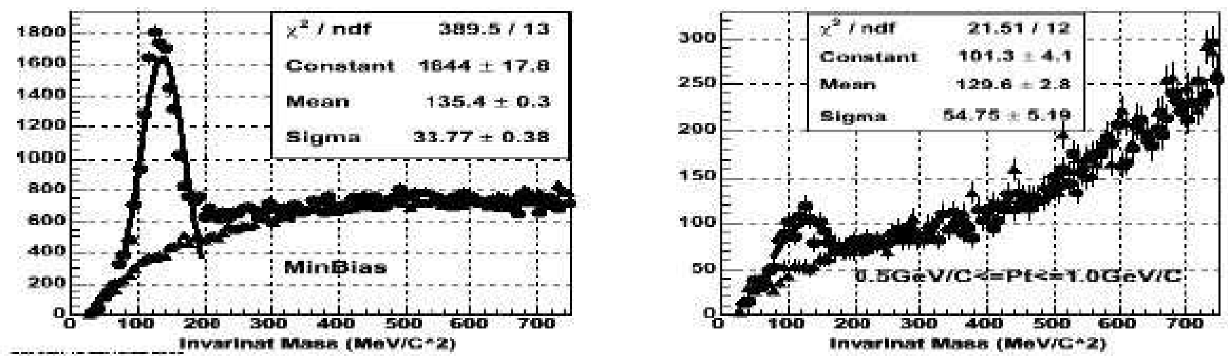

Figure 5.55: dAu at $\sqrt{s_{NN}}$=200 GeV, minimum bias data:$M_{\gamma\gamma}$

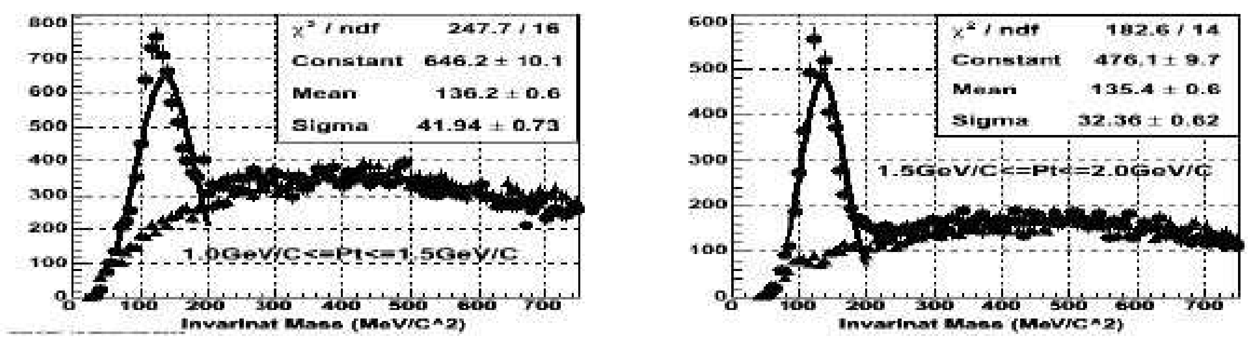

Figure 5.56: dAu at $\sqrt{s_{NN}}$=200 GeV,minimum bias data:$M_{\gamma\gamma}$

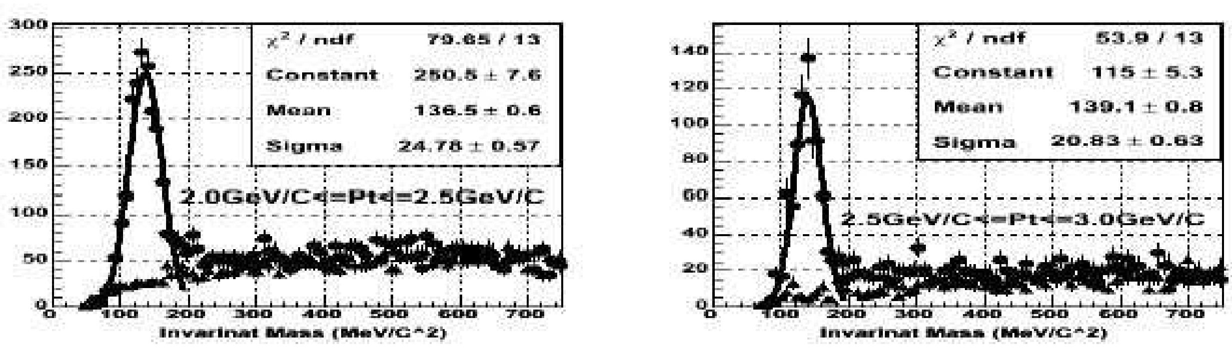

Figure 5.57: dAu at $\sqrt{s_{NN}}$=200 GeV,minimum bias data:$M_{\gamma\gamma}$

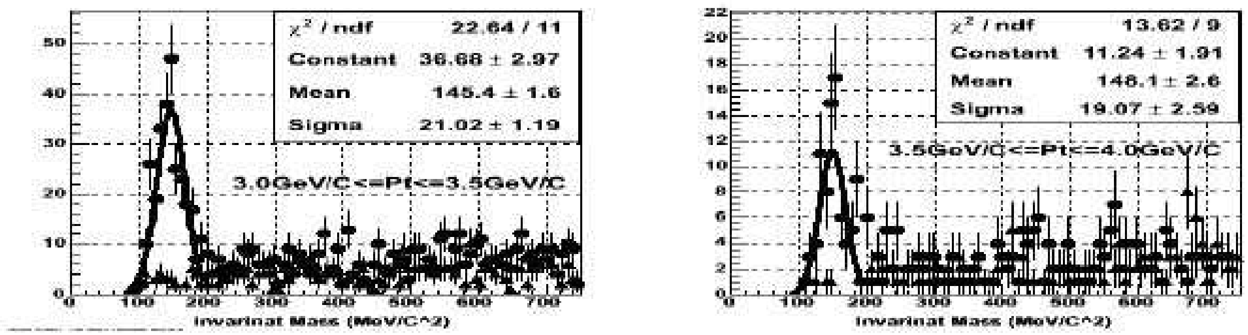

Figure 5.58: dAu at $\sqrt{s_{NN}}$=200 GeV,minimum bias data:$M_{\gamma\gamma}$

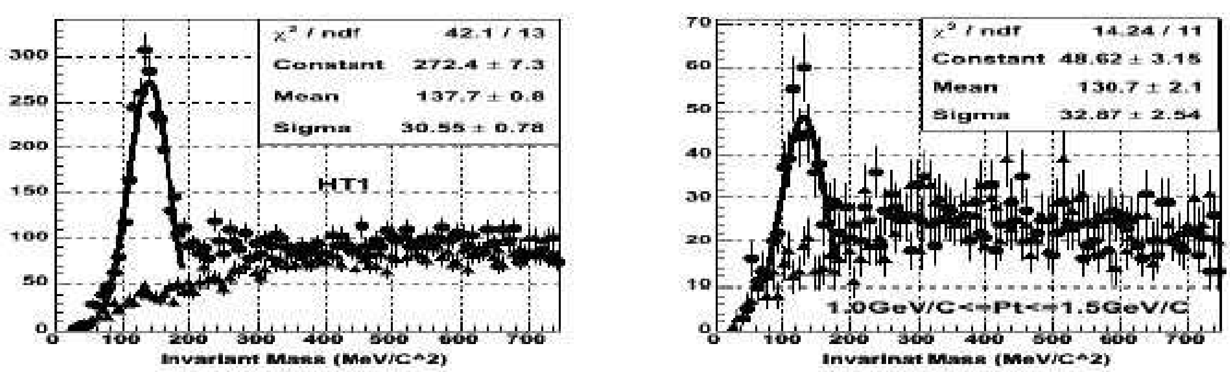

Figure 5.59: dAu at $\sqrt{s_{NN}}$=200 GeV,high tower1 data:$M_{\gamma\gamma}$

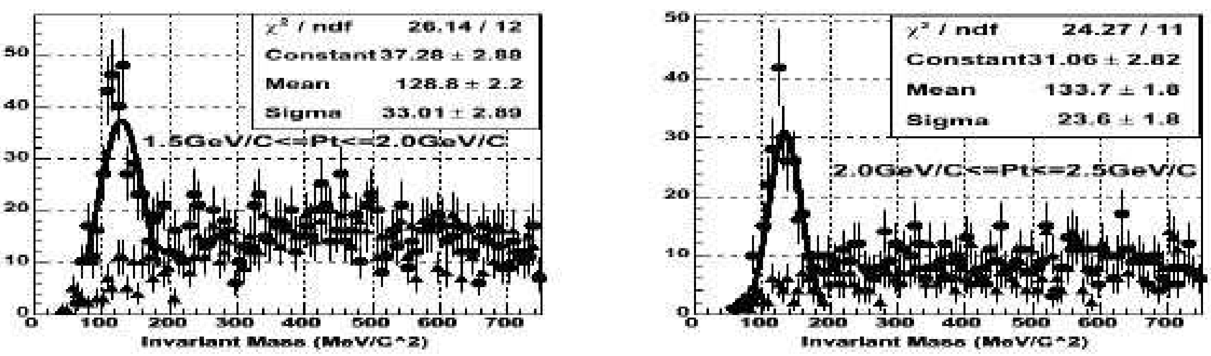

Figure 5.60: dAu at $\sqrt{s_{NN}}$=200 GeV, high tower1 data:$M_{\gamma\gamma}$

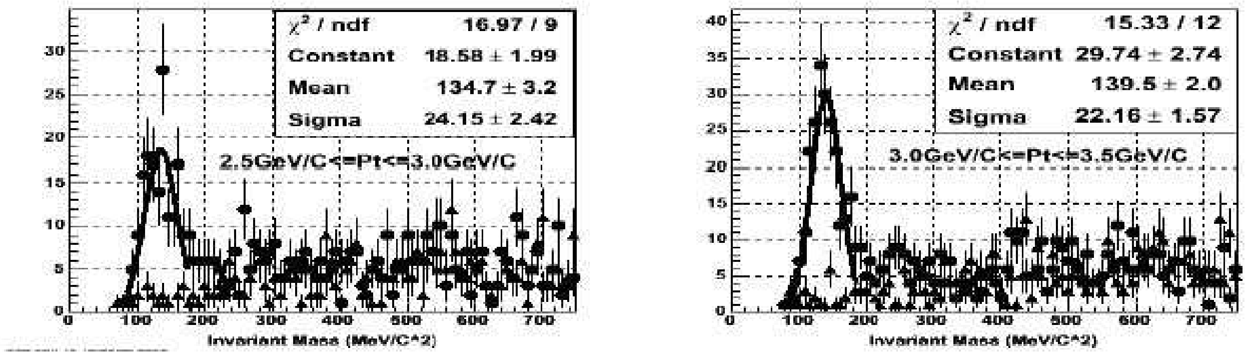

Figure 5.61: dAu at $\sqrt{s_{NN}}$=200 GeV,high tower1 data:$M_{\gamma\gamma}$

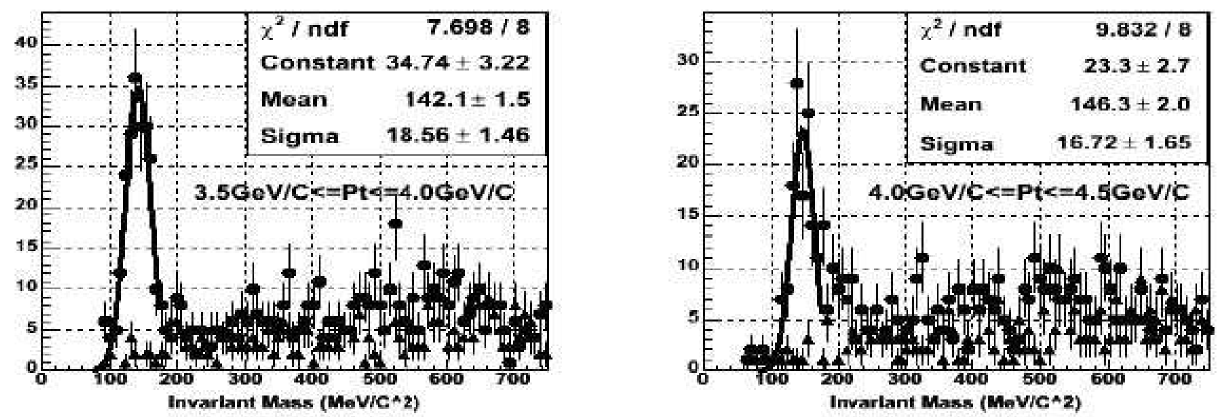

Figure 5.62: dAu at $\sqrt{s_{NN}}$=200 GeV,high tower1 data:$M_{\gamma\gamma}$

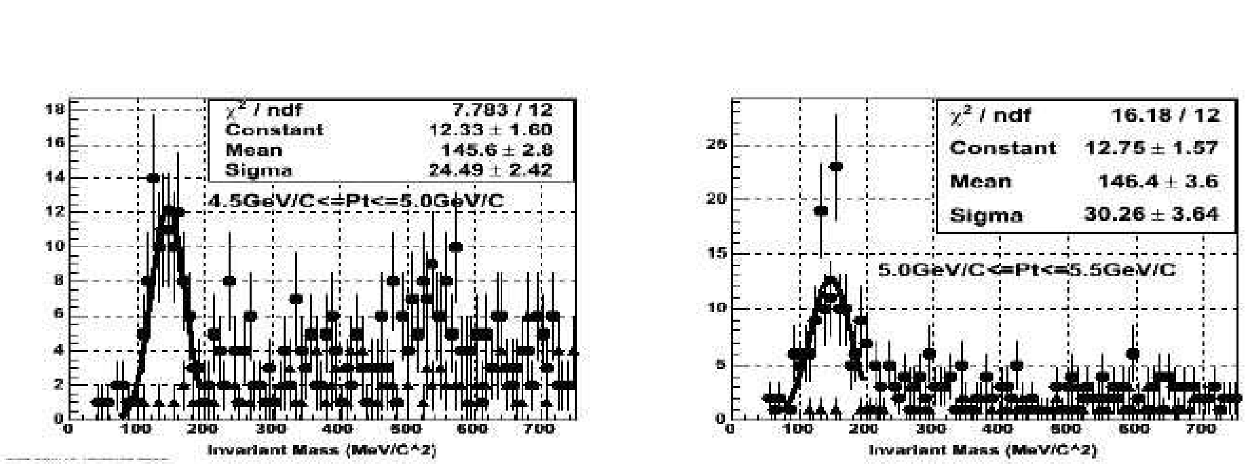

Figure 5.63: dAu at $\sqrt{s_{NN}}$=200 GeV, high tower1 data:$M_{\gamma\gamma}$

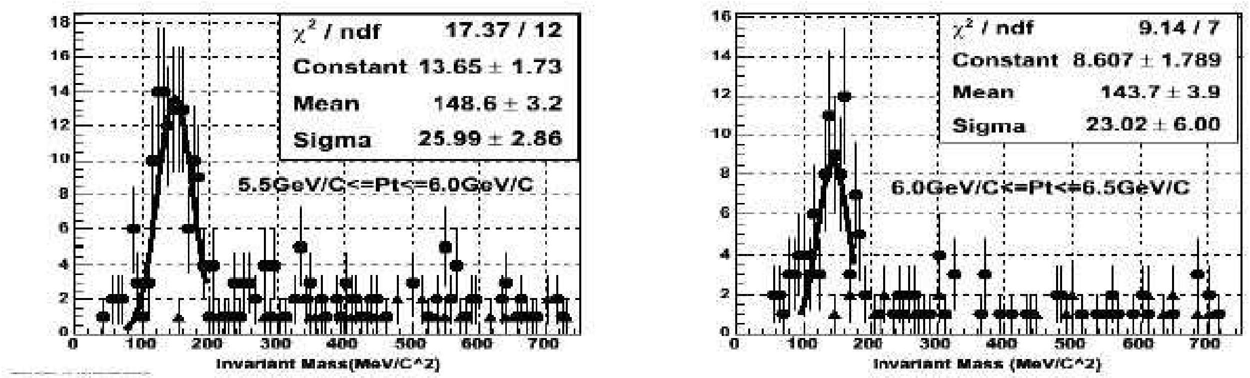

Figure 5.64: dAu at $\sqrt{s_{NN}}$=200 GeV,high tower1 data:$M_{\gamma\gamma}$

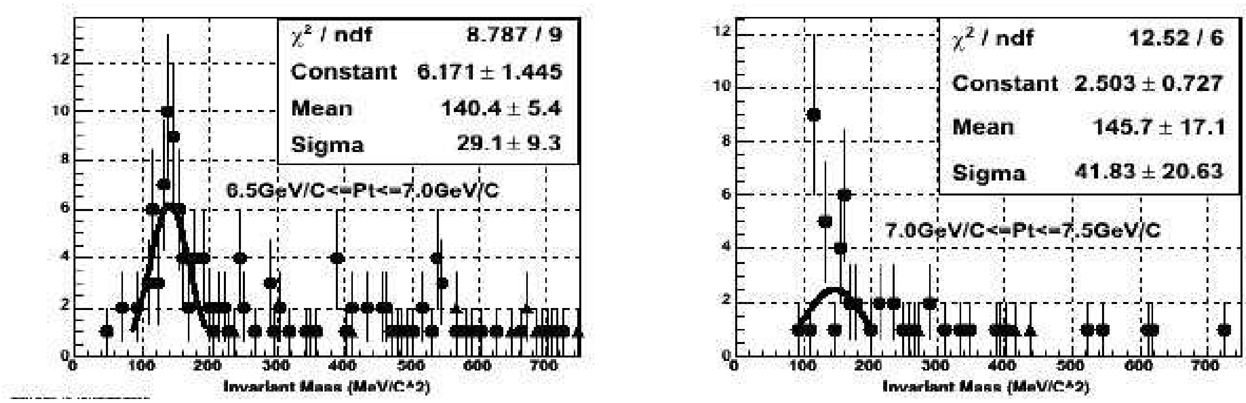

Figure 5.65: dAu at $\sqrt{s_{NN}}$=200 GeV,high tower1 data:$M_{\gamma\gamma}$

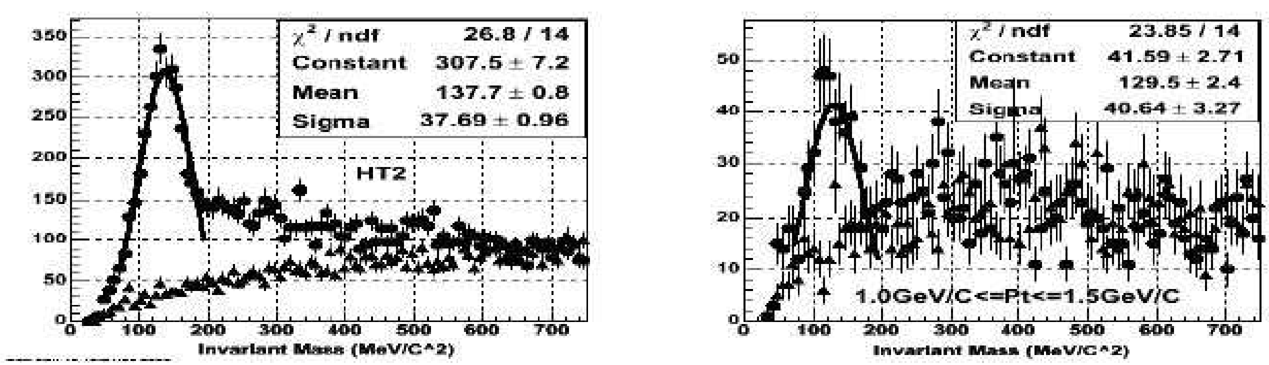

Figure 5.66: dAu at $\sqrt{s_{NN}}$=200 GeV,high tower2 data:$M_{\gamma\gamma}$

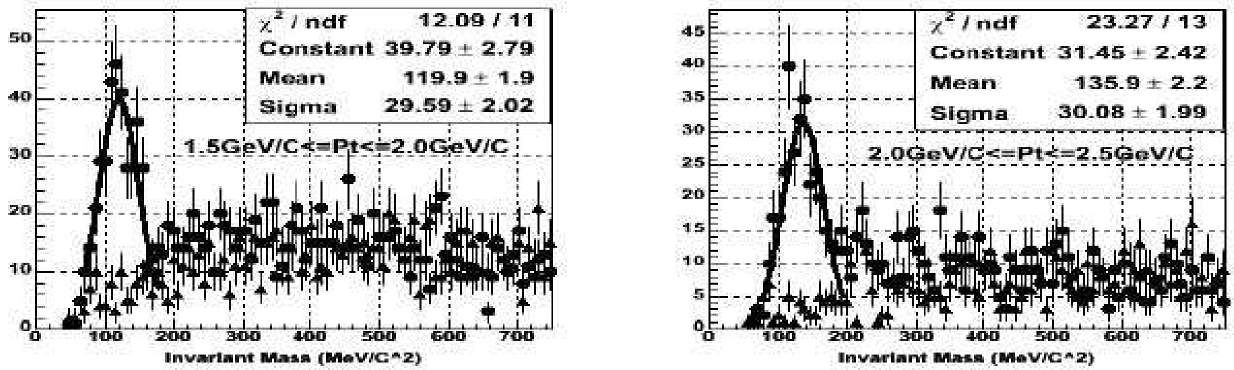

Figure 5.67: dAu at $\sqrt{s_{NN}}$=200 GeV,high tower2 data:$M_{\gamma\gamma}$

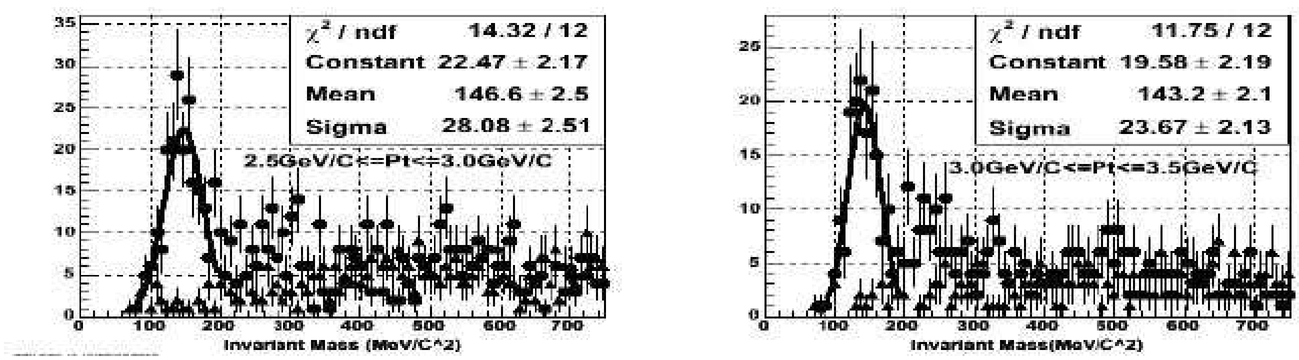

Figure 5.68: dAu at $\sqrt{s_{NN}}$=200 GeV,high tower2 data:$M_{\gamma\gamma}$

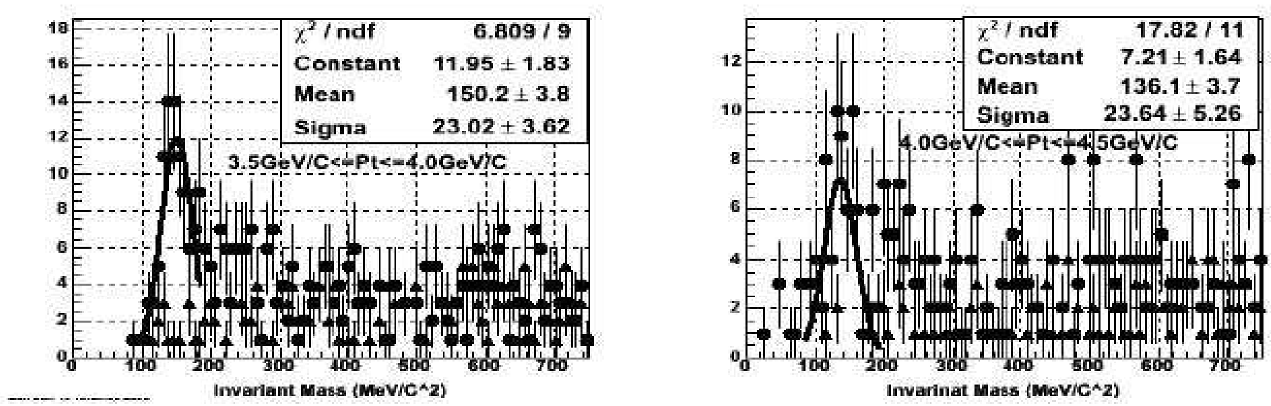

Figure 5.69: dAu at $\sqrt{s_{NN}}$=200 GeV,high tower2 data:$M_{\gamma\gamma}$

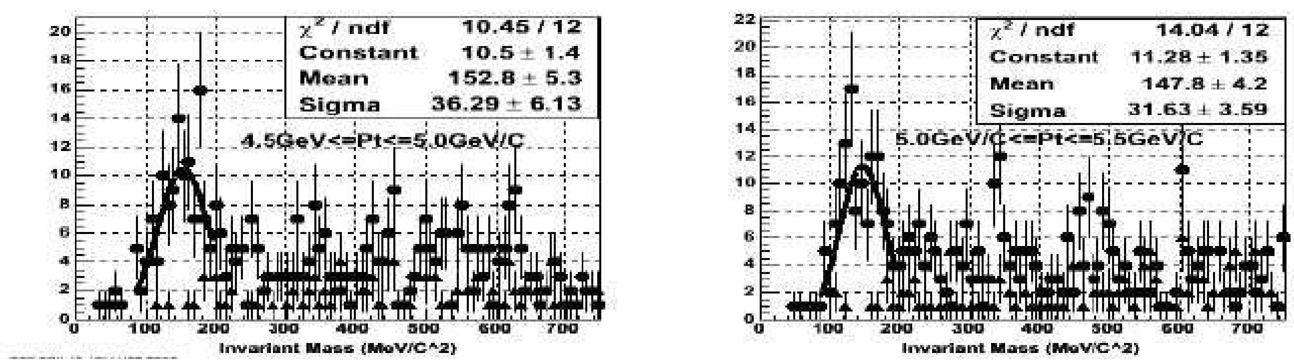

Figure 5.70: dAu at $\sqrt{s_{NN}}$=200 GeV,high tower2 data:$M_{\gamma\gamma}$

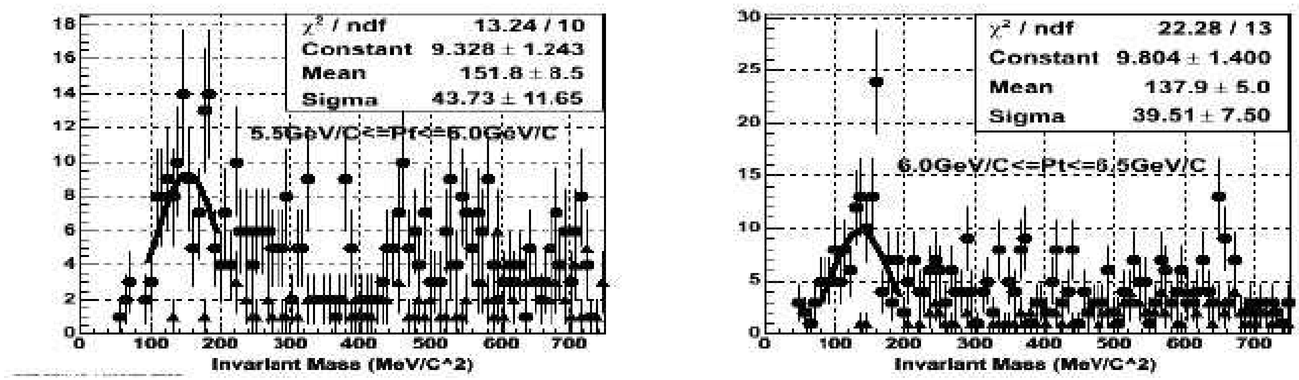

Figure 5.71: dAu at $\sqrt{s_{NN}}$=200 GeV,high tower2 data:$M_{\gamma\gamma}$

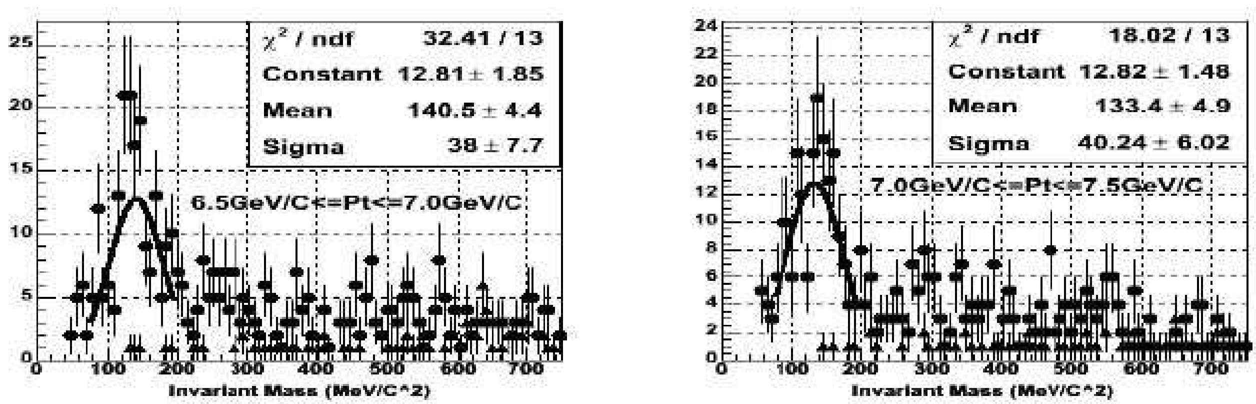

Figure 5.72: dAu at $\sqrt{s_{NN}}$=200 GeV,high tower2 data:$M_{\gamma\gamma}$

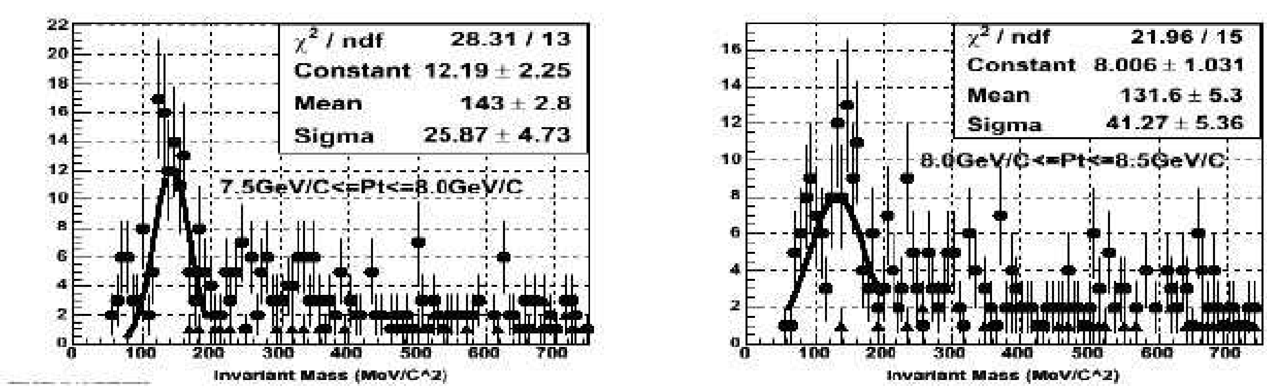

Figure 5.73: dAu at $\sqrt{s_{NN}}$=200 GeV,high tower2 data:$M_{\gamma\gamma}$

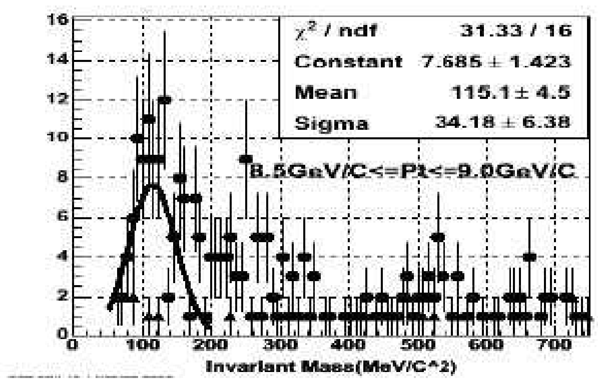

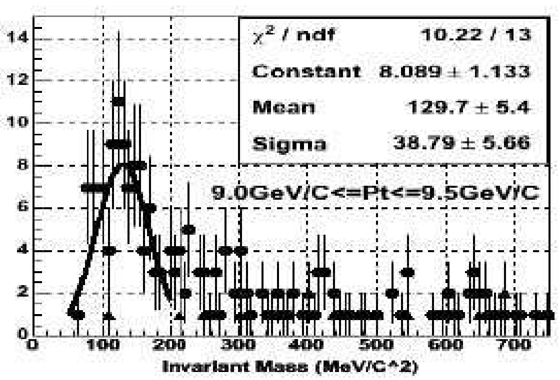

Figure 5.74: dAu at $\sqrt{s_{NN}}$=200 GeV,high tower2 data:$M_{\gamma\gamma}$

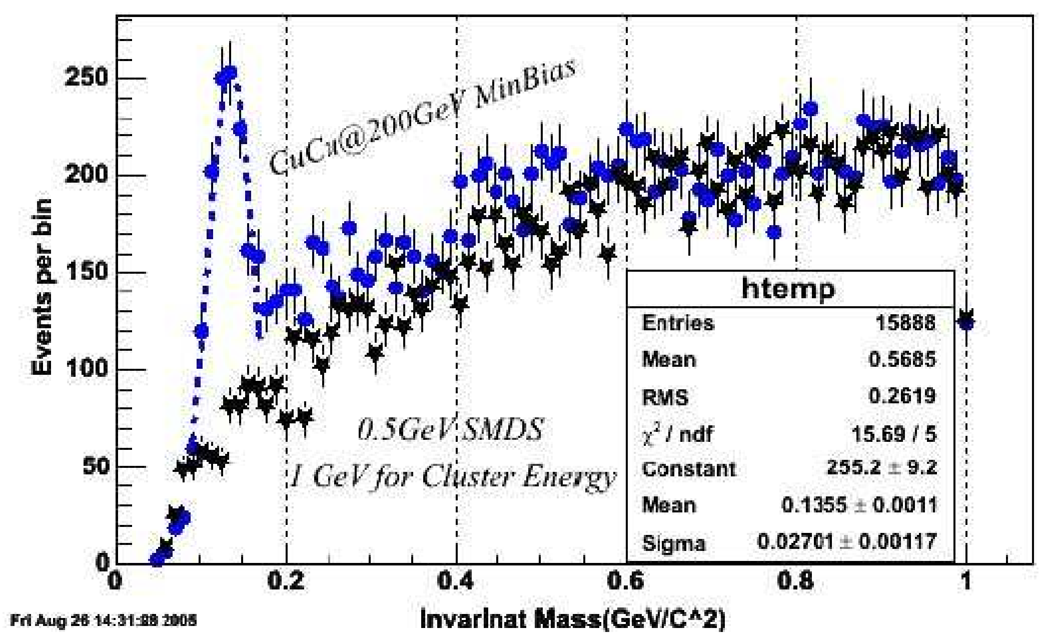

Figure 5.75: cucu at $\sqrt{s_{NN}}$=200 GeV, minimum bias data:$M_{\gamma\gamma}$

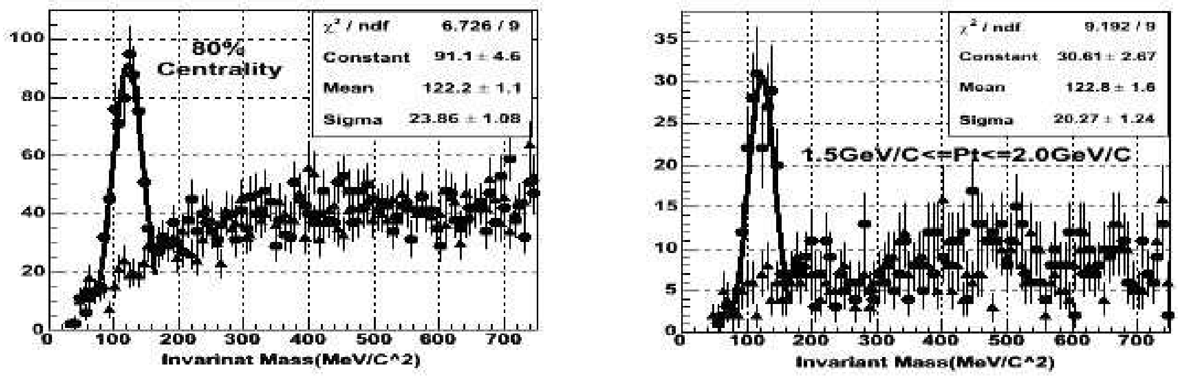

Figure 5.76: AuAu at $\sqrt{s_{NN}}$=62.4GeV,minimum bias data:$M_{\gamma\gamma}$

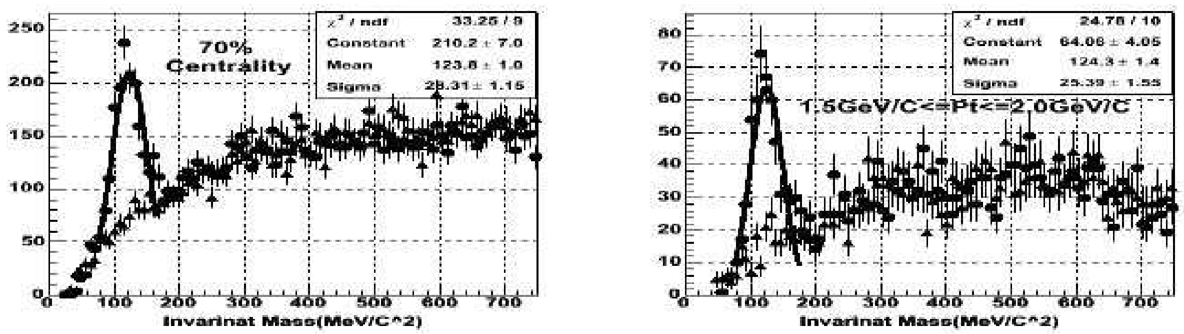

Figure 5.77: AuAu at $\sqrt{s_{NN}}$=62.4GeV,minimum bias data:$M_{\gamma\gamma}$

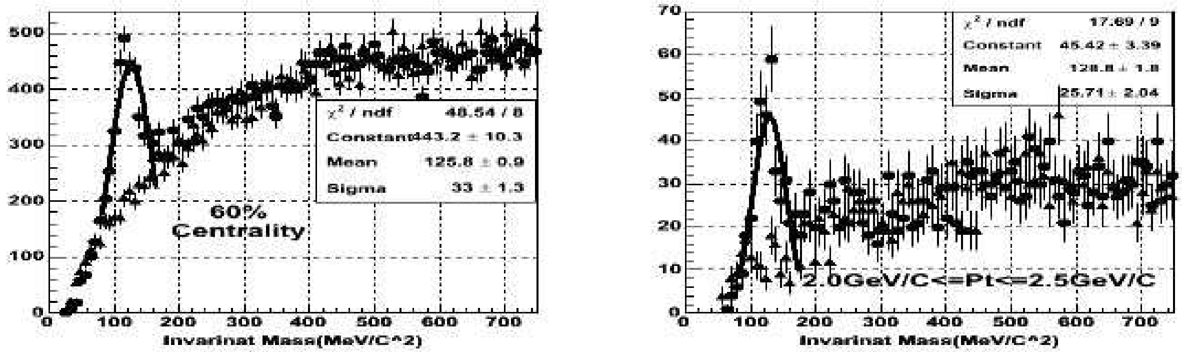

Figure 5.78: AuAu at $\sqrt{s_{NN}}$=62.4GeV,minimum bias data:$M_{\gamma\gamma}$

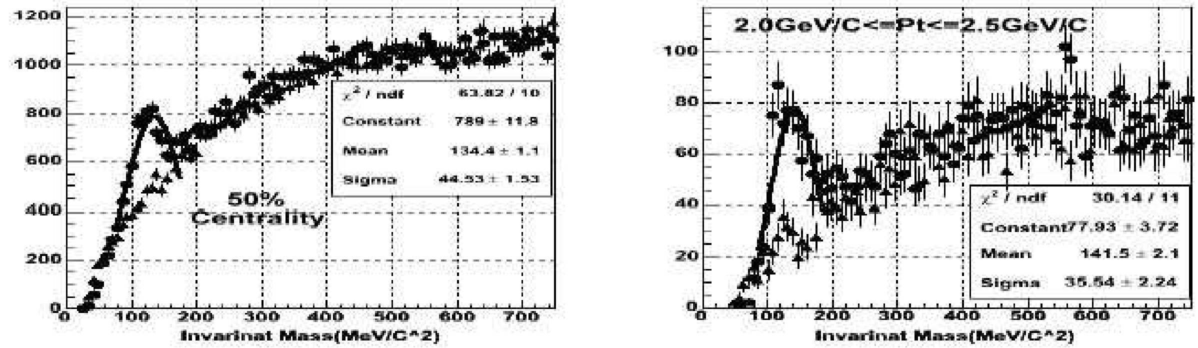

Figure 5.79: AuAu at $\sqrt{s_{NN}}$=62.4GeV,minimum bias data:$M_{\gamma\gamma}$

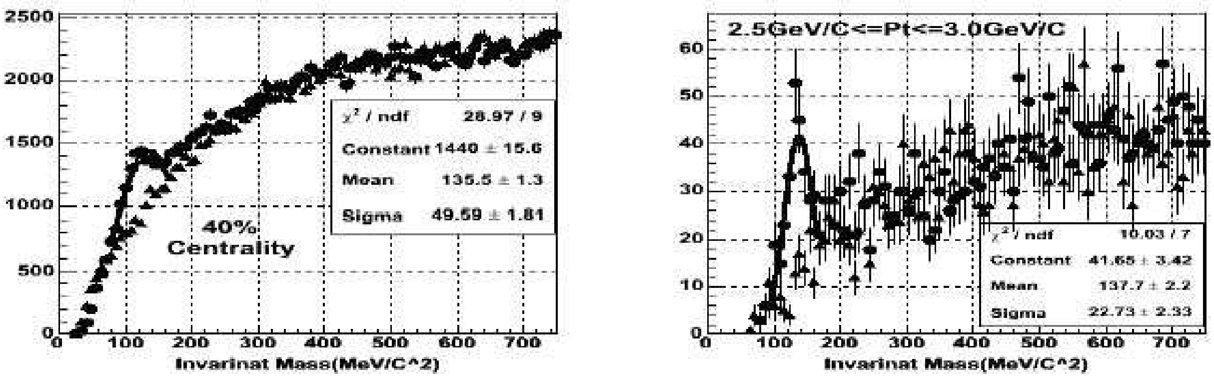

Figure 5.80: AuAu at $\sqrt{s_{NN}}$=62.4GeV,minimum bias data:$M_{\gamma\gamma}$

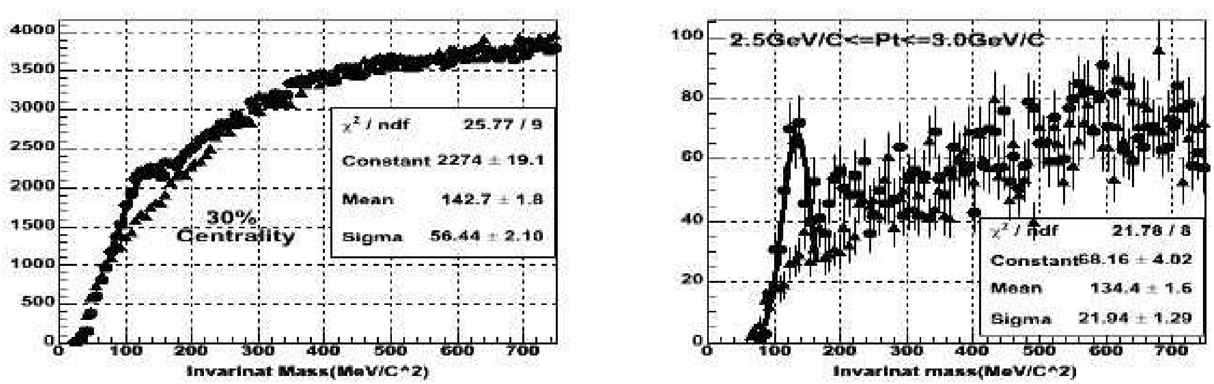

Figure 5.81: AuAu at $\sqrt{s_{NN}}$=62.4GeV,minimum bias data:$M_{\gamma\gamma}$

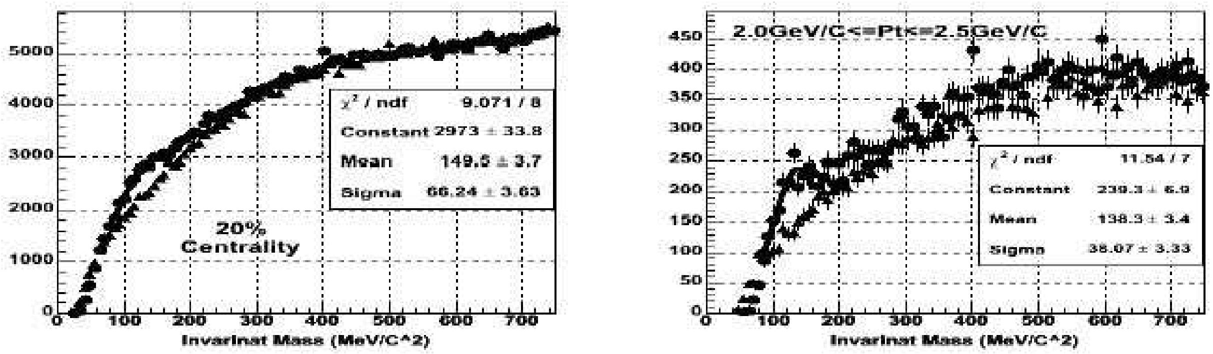

Figure 5.82: AuAu at $\sqrt{s_{NN}}$=62.4GeV,minimum bias data:$M_{\gamma\gamma}$

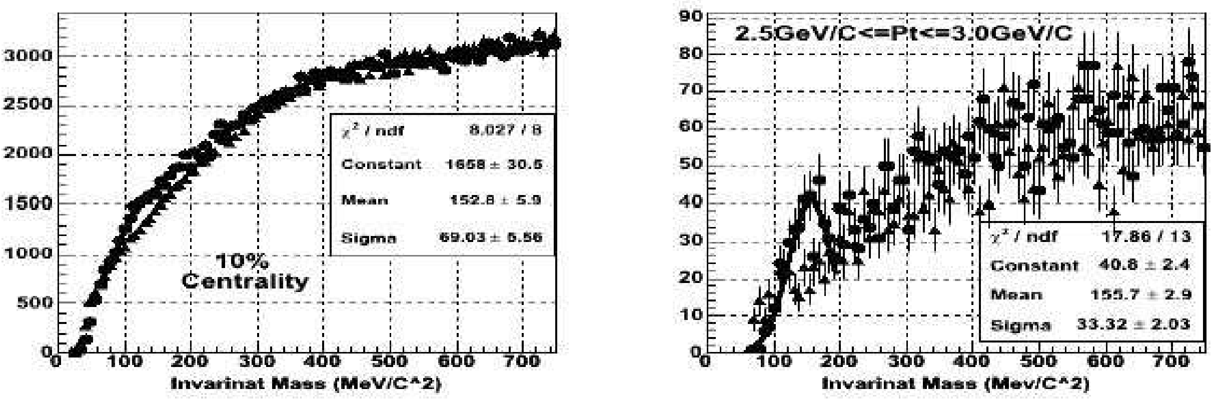

Figure 5.83: AuAu at $\sqrt{s_{NN}}$=62.4GeV,minimum bias data:$M_{\gamma\gamma}$

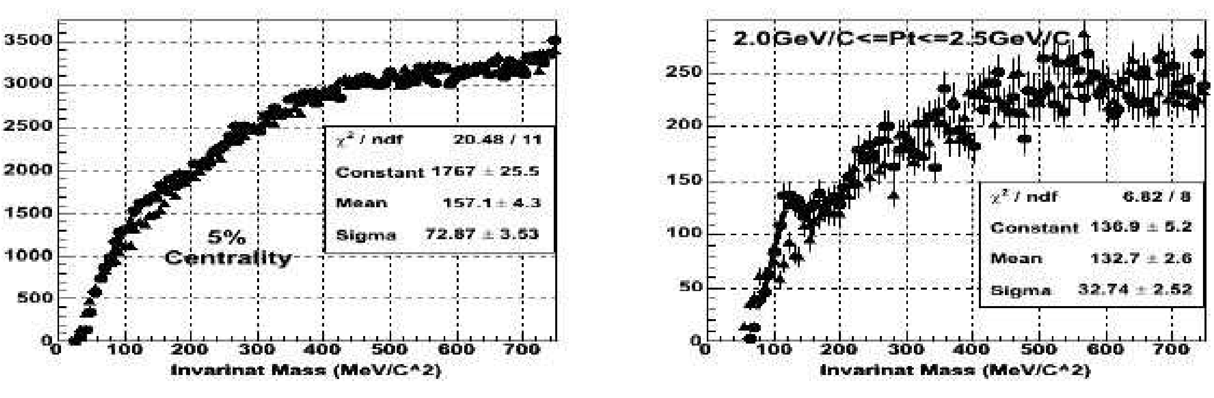

Figure 5.84: AuAu at $\sqrt{s_{NN}}$=62.4GeV,minimum bias data:$M_{\gamma\gamma}$

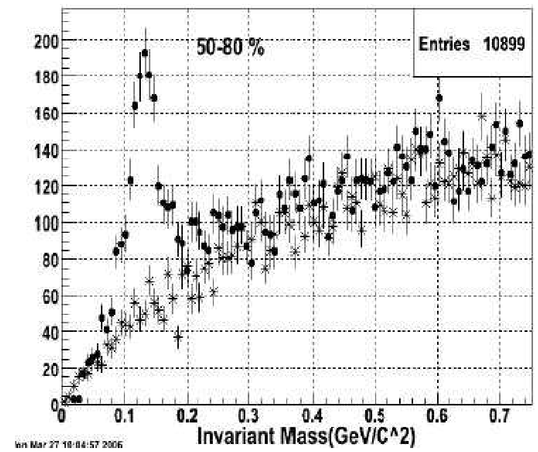

Figure 5.85: AuAu at $\sqrt{s_{NN}}$=200GeV:$M_{\gamma\gamma}$

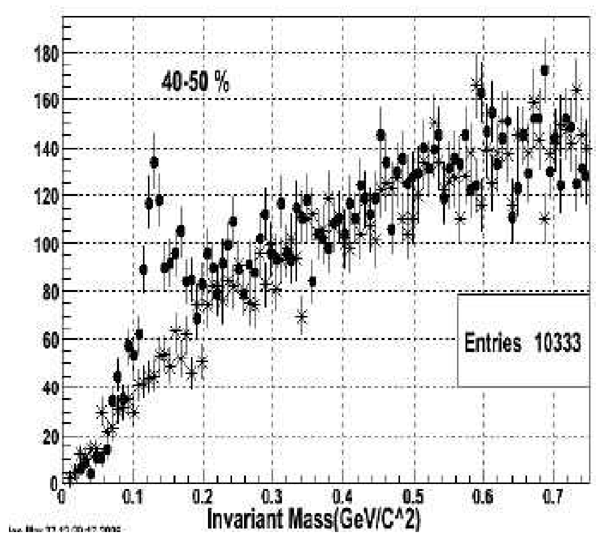

Figure 5.86: AuAu at $\sqrt{s_{NN}}$=200GeV:$M_{\gamma\gamma}$

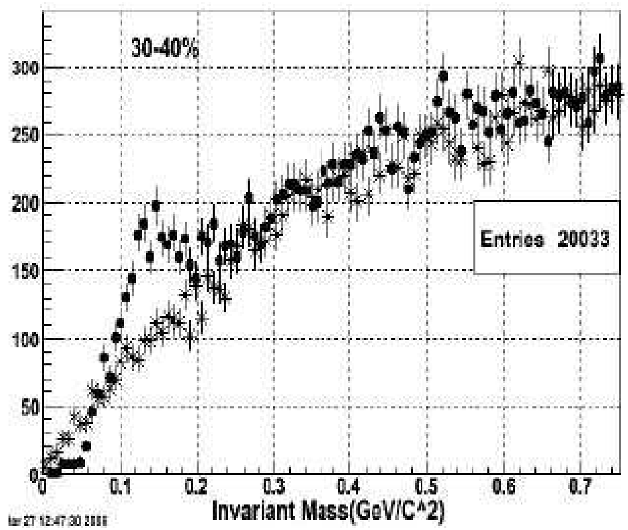

Figure 5.87: AuAu at $\sqrt{s_{NN}}$=200GeV:$M_{\gamma\gamma}$

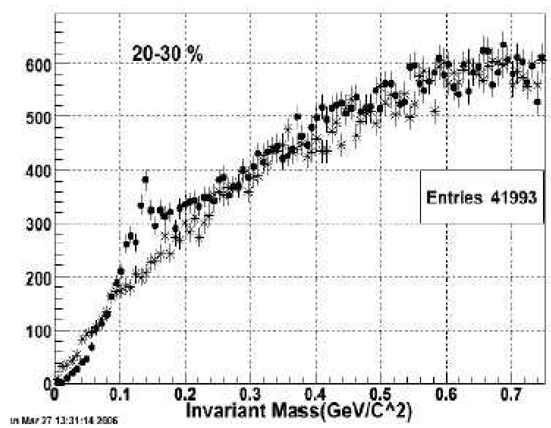

Figure 5.88: AuAu at $\sqrt{s_{NN}}$=200GeV:$M_{\gamma\gamma}$

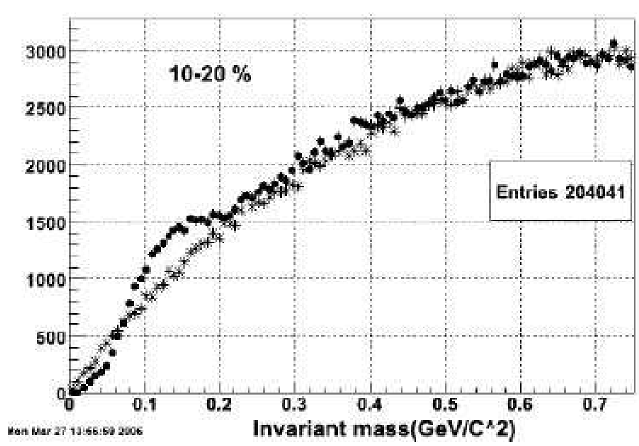

Figure 5.89: AuAu at $\sqrt{s_{NN}}$=200GeV:$M_{\gamma\gamma}$

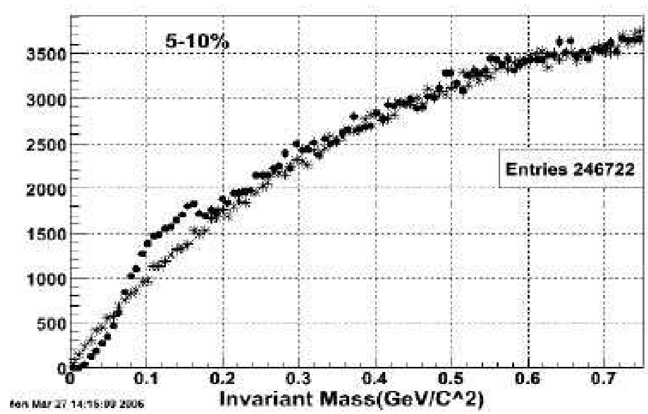

Figure 5.90: AuAu at $\sqrt{s_{NN}}$=200GeV:$M_{\gamma\gamma}$

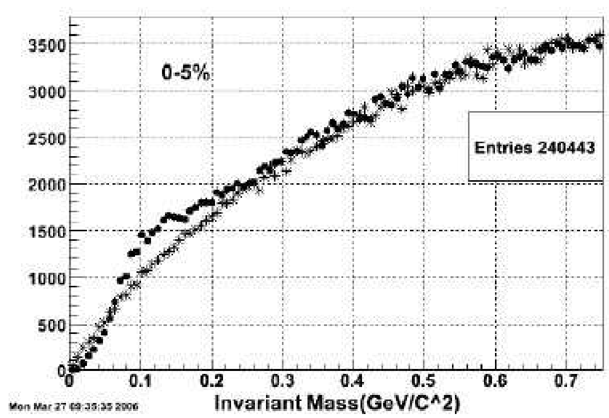

Figure 5.91: AuAu at $\sqrt{s_{NN}}$=200GeV:$M_{\gamma\gamma}$

Summary

One of the main goals of the STAR experiment is the detection of the quark-gluon plasma (QGP), which is a phase of strongly interacting matter where quarks and gluons are no longer confined in the nucleons, but instead can move freely over longer distances. Such a phase probably existed shortly after the Big Bang, and it is expected that it can be recreated for a short time in the laboratory by heavy ion collisions at a sufficiently large energy density. This new phase of matter is distinctively different from usual hadronic matter, and it is the experimental challenge to prove the fleeting existence of the QGP based on its characteristic signatures in the products of a heavy ion collision.

One of the main focus of this work is the measurement of elliptic flow of inclusive photons in $Au + Au$ collisions at a center of mass energy of $\sqrt{s_{NN}}$ = 200GeV in the STAR experiment at RHIC/BNL. In addition, the azimuthal correlations was analyzed in $p + p$ collisions at the same energy.

Two remarkable results have been established at RHIC energies by all different experiments. The first remarkable result at RHIC energy is the fit of the hydrodynamic model to elliptic flow measurements of the charged hadrons at low p_t. Hence, the hydrodynamic calculations assume local thermal equilibrium in the early stage t <1 fm/c to reproduce the magnitude of the observed v_2 at RHIC.

The suppression of the production of particles with large transverse momenta (p_t) in central $Au+Au$ collisions compared to the expectation from scaled $p+p$ reactions, is the second remarkable result. The production of these particles is dominated by so-called hard processes, parton-parton interactions with large momentum transfer, and the subsequent fragmentation of partons into observable particles. A confirmation of the jet quenching scenario directly from Au+Au collisions is provided by the measurement of direct photons. Direct photons with large p_t are likewise produced in hard parton-parton collisions. By contrast to the hard-scattered partons they are not

influenced by the strong interaction and can penetrate the hot and dense medium, which is created in central heavy ion collisions at RHIC.

These two remarkable results have motivated us for the performed work in this thesis. The elliptic flow measurements of non-strongly interacting particles is very important for confirming the observed collective motion of the hadronic particles in the formed matter at RHIC. The interaction of the fast propagating partons with the medium "jet quenching" in the heavy-ion collsions at RHIC energy must affect the inclusive photons production. One of the promising measurements to study such effect is the elliptic flow of inclusive photons, since, the different sources of the photon productions have different v_2 values.

One aspect of this work was the analysis of the elliptic flow of inclusive photons. The reaction plane was determined using two tracker detectors loacted at different pseudorapidity to sense the effect of the auto-correlation and non-flow on the measurements. The inclusive photons were detected via the BEMC. The similarity of the elliptic flow of inclusive photons with that of other mesons implements that the elliptic flow of direct photons is negligible. Also, it is observed the elliptic flow of inclusive photons decreases with transverse momentum at high p_t and its finite value at high p_t is dominated by the non-flow effect.

In order to extract the elliptic flow of direct photons, neutral pions are reconstructed via their two decay photons, which are detected by the electromagnetic calorimeter (BEMC) of the STAR experiment. The reconstructions of neutral pions was the second goal of this work. A new clustering algorithm is developed for neutral pions reconstruction. A clear neutral pion peak is seen in all different collision systems where the cluster splitting is suppressed. The lack of π^0 embedded data for AuAu at $\sqrt{s_{NN}}$=200GeV has stopped us from pushing the analysis toward the corrected contribution of neutral pions.

Bibliography

[1] F. Abe et al. Observation of Top Quark Production in $p\overline{p}$ Collisions with the Collider Detector at Fermilab. *Physical Review Letters*, Vol. 74, No. 14, pages 2626-2631; April 3, 1995.

[2] J. C. Collins and M. J. Perry Superdense Matter: Neutrons or Asymptotically Free Quarks?. *Physical Review Letters*, Vol. 34, No. 21, pages 1353-1356; May 26, 1975.

[3] J. D. Bjorken Asymptotic Sum Rules at Infinite Momentum. *Physical Review*, Vol. 179, No.5 March 25 1969.

[4] J. D. Bjorken and E. A. Paschos Inelastic Electron-Proton and γ-Proton Scattering and the Structure of the Nucleon. *Physical Review*, Vol. 185, No. 5, September 25, 1969.

[5] D. H. Perkins Introduction to High Energy Physics. 3^{rd} *edition*, 1987.

[6] F. Wilczek, Rev. Mod. Phys. 71, S85-S95 (1999)

[7] L. Landau, in Niels Bohr and the Development of Physics, ed. W. Pauli (McGraw-Hill, New York 1955).

[8] D. J. Gross and F. Wilczek. *Physics Review Letters*, 30 (1973) 1343.

[9] H. D. Politzer. *Physics Review Letters*, 30 (1973) 1346.

[10] Kolb E, Turner MS. The Early Universe. Redwood City, CA: Addison-Wesley (1990).

[11] Davis et al. *Physical Review Letters*, Volume 92, Number 2, 16 January 2004.

[12] M. Creutz. *Physical Review*, D15 (1977) 1128.

[13] K. G. Wilson. *Physical Review*, D10 (1974) 2445.

[14] E. Laermann, O. Philipsen. *Ann. Rev. Nucl. Part. Sci.*, 53 (2003) 163.

[15] F. Karsch. Lecture Notes in Physics 583 (2002) 209.

[16] M. G. Alford, K. Rajagopal and F. Wilczek. *Nucl. Phys.* B 537 (1999) 443.

[17] K. Rajagopal and F. Wilczek. *arXiv: hep-ph/0011333.*

[18] M. G. Alford. *Ann. Rev. Nucl. Part. Sci* 51 (2001) 131.

[19] T. Schafer. *arXiv: hep-ph/0304281.*

[20] D. H. Rischke. *arXiv: nucl-th/0305030.*

[21] D. K. Hong. *arXiv: hep-ph/0101025.*

[22] Z. Fodor, S. D. Katz, JHEP 0404 (2004) 050.

[23] S. Ejiri, et al. Prog. Theor. Phys. Suppl. 153 (2004) 118.

[24] W. Greiner, S. Schramm, E. Stein, Quantum Chromodynamics, 2nd Eddition, Springer-Verlag, 2002.

[25] V. V. Klimov, Sov. Phys. JETP 55 (1982) 199.

[26] H. A. Weldon, Phys. Rev. D26 (1982) 1394.

[27] S. Datta, F. Karsch, P. Petreczky, I. Wetzorke, Nucl. Phys. Proc. Suppl. 119 (2003) 487.

[28] M. Asakawa, T. Hatsuda, Phys. Rev. Lett. 92 (2004) 012001.

[29] S. Datta, F. Karsch, P. Petreczky, I. Wetzorke, Phys. Rev. D69 (2004) 094507.

[30] F. Karsch, et al. Nucl. Phys. A715 (2003) 701.

[31] E. V. Shuryak, I. Zahed, Phys. Rev. D70 (2004) 054507.

[32] K. Kajantie, M. Laine, K. Rummukainen, Y. Schroder, Phys. Rev. D67 (2003) 105008.

[33] A. D. Linde, Phys. Lett. B96 (1980) 289.

[34] D. J. Gross, R. D. Pisarski, L. G. Yaffe, Rev. Mod. Phys. 53 (1981) 43.

[35] J. Anderson, E. Braaten, and M. Strickland, hep-ph/9905337; J. P. Blaizot, E. Iancu and A. Rebjam, hep-ph/9906340.

[36] Shifman MA. Annu Rev. Nucl. Part. Sci. 33:199 (1983).

[37] Pochodzalla J, et. al. Phys. Rev. Lett. 175:1040 (1995).

[38] Polyakov AM. Phys. Lett. 72B:224 (1977).

[39] Polonyi J. hep-ph/ 9509334.

[40] Hwa RC, Kajantie K. Phys. Rev. Lett.56:696 (1986).

[41] Blaizot JP, Mueller AH, Nucl. Phys. B 289:847 (1987).

[42] Anishetty R, Koehler P, McLerran L.Phys. Rev. D 22:2793 (1980).

[43] Bialas A, Czyz W. Phys. Rev. D 31:198 (1985).

[44] Kajantie K, Matsui T. Phys. Lett.164B:373 (1985).

[45] Wang XN, Gyulassy M. Phys. Rev. D 44:3501 (1991); Phys. Rev. D 45:844 (1992); Comp. Phys. Comm. 83:307 (1994).

[46] Geiger K, Muller B. Nucl. Phys. B 369:600 (1992).

[47] Geiger K. Phys. Rep. 258:237 (1995).

[48] Eskola KJ, Wang XN. Phys. Rev. D 49:1284 (1994).

[49] Shuryak E. Phys. Rev. Lett. 68:3270 (1992).

[50] Biro TS, et al. Phys. Rev. C 48:1275 (1993).

[51] Geiger K, Kapusta JI. Phys. Rev. D 47:4905 (1993).

[52] Xiong L, Shuryak EV. Phys. Rev. C 49:2207 (1994).

[53] Bjorken JD. Phys. Rev. D 27:140 (1983).

[54] Blaizot JP, Ollitrault JY. Quark-Gluon Plasma, ed. RC Hwa. Singapore: World Sci. 393 pp. (1991).

[55] Hung CM, Shuryak EV. Phys. Rev. Lett. 75:4003 (1995).

[56] Rischke DH, Gyulassy M. Nucl. Phys A597:701 (1996).

[57] Pratt S. Phys. Rev. Lett. 53:1219 (1984);Phys. Rev. D 33:1314 (1986).

[58] Bertsch G, Gong M, Tohyama M. Phys.Rev. C 37:1896 (1988); Bertsch GF.Nucl. Phys. A 498:173c (1989).

[59] Gavin S. Nucl. Phys. A 544:459 (1992).

[60] Haglin K, Pratt S. Phys. Lett. B 328:255 (1994).

[61] L. D. Landau and E. M. Lifshitz, Statistical Physics, Pergamon Press, Oxford, third edition, (1980).

[62] Kajantie K, McLerran L. Annu. Rev.Nucl. Part. Sci. 37:293 (1987).

[63] Bernard V. Quark-Gluon Plasma Signatures. (1990).

[64] Singh CP. Phys. Rep. 236:147 (1993).

[65] Muller B. Rep. Prog. Phys. 58:611 (1995).

[66] Cleymans J, Redlich K, Satz H. Z. Phys.C 52:517 (1991).

[67] Gale C, Lichard P. Phys. Rev. D 49:3338 (1994); Song C, Ko CM, Gale C. Phys.Rev. D 50:R1827 (1994).

[68] Ruuskanen PV. Nucl. Phys. A 525:255c (1991); ibid. A544:169c (1992).

[69] C. Y. Wong. Introduction to Highe-Energy Heavy-Ion Collisions. World Scientific, Singapore, 1994.

[70] Heinz U, Lee KS. Phys. Lett. 259B:162 (1991).

[71] Heinz U. Nucl. Phys. A 566:205c (1994) .

[72] Letessier J, Tounsi A, Rafelski J. Phys.Lett. 292B:417 (1992) .

[73] Letessier J, Rafelski J, Tounsi A. Phys.Lett. 321B:394 (1994) .

[74] Cerny V, et al. Z. Phys. C 46:481 (1990) .

[75] Hufner J, Povh P, Gardner S. Phys. Lett.238B:103 (1990) .

[76] Cleymans J, Thews RL. Z. Phys. C 45:391 (1990) .

[77] Matsui T, Satz H. Phys. Lett. 178B:416 (1986) .

[78] Blaizot JP, Ollitrault JY. Phys. Lett.199B:499 (1987) .

[79] Karsch F, Petronzio R. Phys. Lett. 212B:255 (1988) .

[80] Gazdzicki M, Mrowczynski S. Z. Phys.C 49:546 (1991) .

[81] Lietava R. Z. Phys. C 50:107 (1991).

[82] Pisarski RD. Phys. Lett. 110B:155 (1982).

[83] Bochkarev AI, Shaposhnikov ME. Phys.Lett. 145B:276 (1984); Nucl. Phys. B 268:220 (1986); Z. Phys. C 36:267 (1987).

[84] Dosch HG, Narison S. Phys. Lett.203B:155 (1988).

[85] Furnstahl RJ, HatsudaT, Lee SH. Phys.Rev. D 42:1744 (1990).

[86] Gale C, Kapusta J. Nucl. Phys. B 357:65 (1991).

[87] Barz HW, et al. Phys. Lett. 265B:219 (1991).

[88] Aouissat Z, Chanfray G, Schuck P,Welke G. Z. Phys. A 340:347 (1991).

[89] Asakawa M, Ko CM, Levai P, Qiu XJ.Phys. Rev. C 46:1159 (1992).

[90] Herrmann M, Friman BL, NorenbergW.Z. Phys. A 343:119 (1992).

[91] Hatsuda T,KoikeY, Lee SH. Nucl. Phys.B 394:221 (1993).

[92] Bjorken JD. Fermilab publication 82/59.

[93] Svetitsky B. Phys. Rev. D 37:2484(1988).

[94] Thoma MH, Gyulassy M. Nucl. Phys. B 351:491 (1991); Braaten E, Thoma MH.Phys. Rev. D 44:R2625 (1991) .

[95] Mrowczynski S. Phys. Lett. 269B:383 (1991) .

[96] KoikeY, Matsui T. Phys. Rev.D45:3237 (1992) .

[97] Migdal AB. Sov. Phys. JETP 5:527 (1957) .

[98] Gyulassy M, Wang XN. Nucl. Phys. B 420:583 (1994) .

[99] Baier R, Dokshitser Yu L, Peigne S,Schiff D. Phys. Lett. 345B:277 (1995) .

[100] J. D. Bjorken, FERMILAB-PUB-82-59-THY and erratum(unpublished).

[101] Appel DA. Phys. Rev. D 33:717 (1986).

[102] Blaizot JP, McLerran L. Phys. Rev. D 34:2739 (1986) .

[103] Rammerstorfer M, Heinz U. Phys. Rev.D 41:306 (1990) .

[104] Pan J, Gale C. Phys. Rev. D 50:3235 (1994) .

[105] E. V. Shuryak, I. Zahed, Phys. Rev. D70 (2004) 054507 .

[106] F. Karsch, Lect. Notes Phys. 583 (2002) 209 .

[107] E. Laermann, O. Philipsen, Ann. Rev. Nucl. Part. Sci. 53 (2003) 163 .

[108] J.D. Bjorken, Phys. Rev. D27 (1983) 140.

[109] M. Gyulassy and M. Plumer. Phys. Lett. B243 (1990) 432.

[110] R. Baier, Y. L. Dokshitzer, S. Peigne, et al. Phys. Lett. B345 (1995) 277.

[111] C. Caso et al. Eur. Phys. J. C3 (1998) 1.

[112] C.-Y.Wong. Introduction to High-Energy Heavy-Ion Collisions. World Scientific,Singapore, 1994.

[113] M. Jacob and P. Landshoff. Sci. Am. 242 (1980) 46.

[114] J. C. Collins, D. E. Soper, and G. Sterman. Nucl. Phys. B261 (1985) 104 .

[115] S. Adler, et al., Phys. Rev. Lett. 91 (2003) 241803 .

[116] J. W. Cronin et al. Phys. Rev. D11 (1975) 3105 .

[117] B. P. Roe. Particle Physics at the New Millennium. Springer, New York, 1996 .

[118] D. H. Perkins. Introduction to High Energy Physics. Cambridge University Press, Cambridge, 2000 .

[119] J. J. Aubert et al. Phys. Lett. B123 (1983) 275 .

[120] G. Piller and W. Weise. Phys. Rept. 330 (2000) 1 .

[121] X.-N. Wang and M. Gyulassy. Phys. Rev. Lett. 68 (1992) 1480 .

[122] S. Chekanov et al. Phys. Rev. D67 (2003) 012007 .

[123] M. Froissart. Phys. Rev. 123 (1961) 1053 .

[124] D. Kharzeev, E. Levin, and L. McLerran. Phys. Lett. B561 (2003) 93 .

[125] X.-N. Wang and M. Gyulassy. Phys. Rev. Lett. 68 (1992) 1480 .

[126] M. Gyulassy and X.-n. Wang. Nucl. Phys. B420 (1994) 583 .

[127] A. B. Migdal. Phys. Rev. 103 6 (1956) 1811 .

[128] R. Baier, Y. L. Dokshitzer, A. H. Mueller, et al. Nucl. Phys. B483 (1997) 291 .

[129] M. Gyulassy, P. Levai, and I. Vitev. Phys. Rev. Lett. 85 (2000) 5535 .

[130] M. Gyulassy, I. Vitev, X.-N. Wang, et al. Jet Quenching and Radiative Energy Loss in Dense Nuclear Matter. nucl-th/0302077, 2003.

[131] E. Wang and X.-N. Wang. Phys. Rev. Lett. 89 (2002) 162301 .

[132] I. Vitev and M. Gyulassy. Phys. Rev. Lett. 89 (2002) 252301 .

[133] E. D. Bloom, et al., Phys. Rev. Lett. 23 (1969) 930.

[134] M. Breidenbach, et al., Phys. Rev. Lett. 23 (1969) 935.

[135] J. D. Bjorken, Phys. Rev. 179 (1969) 1547.

[136] M. May, et al., Phys. Rev. Lett. 35 (1975) 407.

[137] M. Arneodo, et al., Nucl. Phys. B481 (1996) 3.

[138] S. S. Adler, et al., Phys. Rev. Lett. 91 (2003) 072303.

[139] A. L. S. Angelis, et al., Phys. Lett. B185 (1987) 213.

[140] M. M. Aggarwal, et al., Eur. Phys. J. C23 (2002) 225.

[141] J. Slivova, Ph.D thesis, Charles University, Prague, 2003, from the CERES experiment. (2003).

[142] R. Albrecht, et al., Eur. Phys. J. C5 (1998) 255.

[143] D. dEnterria, Phys. Lett. B596 (2004) 32.

[144] H. Busching, J. Phys. G31 (2005) S473.

[145] I. Arsene et al. [BRAHMS Collaboration], Phys. Rev. Lett. 91 (2003) 072305.

[146] S.S. Adler et al. [PHENIX Collaboration], Phys. Rev. Lett. 91 (2003) 072303.

[147] B.B. Back et al. [PHOBOS Collaboration], Phys. Rev. Lett. 91 (2003) 072302.

[148] J. Adams et al. [STAR Collaboration], Phys. Rev. Lett. 91 (2003) 072304.

[149] C. Adler et al. [STAR Collaboration], Phys. Rev. Lett. 90 (2003) 082302.

[150] J. Adams et al. [STAR Collaboration], Phys. Rev. Lett. 93 (2004) 252301.

[151] C.-Y.Wong. Introduction to High-Energy Heavy-Ion Collisions. World Scientific, Singapore, 1994.

[152] T. Peitzmann and M. H. Thoma. Phys. Rept. 364 (2002) 175.

[153] F. Arleo et al. Photon Physics in Heavy Ion Collisions at the LHC. hepph/0311131, 2003.

[154] R. Rapp. Mod. Phys. Lett. A19 (2004) 1717.

[155] J. I. Kapusta, P. Lichard, and D. Seibert. Phys. Rev. D44 (1991) 2774.

[156] C. Gale and J. I. Kapusta. Nucl. Phys. B357 (1991) 65.

[157] E. Braaten and R. D. Pisarski. Nucl. Phys. B337 (1990) 569.

[158] M. H. Thoma. New Developments and Applications of Thermal Field Theory. hep-ph/0010164, 2000.

[159] P. Aurenche, F. Gelis, R. Kobes, et al. Phys. Rev. D58 (1998) 085003.

[160] F. D. Steffen and M. H. Thoma. Phys. Lett. B510 (2001) 98.

[161] P. Aurenche, F. Gelis, and H. Zaraket. Phys. Rev. D61 (2000) 116001.

[162] P. Arnold, G. D. Moore, and L. G. Yaffe. JHEP 12 (2001) 009.

[163] F. Karsch. Z. Phys. C38 (1988) 147.

[164] C. Song. Phys. Rev. C47 (1993) 2861.

[165] C.-S. Song and G. I. Fai. Phys. Rev. C58 (1998) 1689.

[166] A. Dumitru, L. Frankfurt, L. Gerland, et al. Phys. Rev. C64 (2001) 054909.

[167] D. K. Srivastava and K. Geiger. Phys. Rev. C58 (1998) 1734.

[168] S. A. Bass, B. Muller, and D. K. Srivastava. Phys. Rev. Lett. 90 (2003) 082301.

[169] R. J. Fries, B. Muller, and D. K. Srivastava. Phys. Rev. Lett. 90 (2003) 132301.

[170] J.-P. Blaizot and J.-Y. Ollitrault. In R. C. Hwa (Editor) Quark-Gluon Plasma, World Scientific, Singapore. 1990 .

[171] J.-P. Blaizot. Lect. Notes Phys. 583(2002)117.

[172] Z. Fodor and S. D. Katz. JHEP 03 (2002) 014.

[173] F. D. Steffen. Bremsstrahlung out of the Quark-Gluon Plasma, 1999.

[174] T. Hirano. J. Phys. G30 (2004) S845.

[175] M. M. Aggarwal et al. Phys. Rev. Lett. 85 (2000) 3595.

[176] D. Bucher.Ph.D. thesis, 1999.

[177] M. Shimomura (PHENIX Collaboration), these proceedings.

[178] S. S. Adler et al., Phys. Rev. Lett. 94 (2005) 232301.

[179] I. Vitev and M. Gyulassy, Phys. Rev. Lett. 89 (2002) 252301.

[180] Glassgold AE, Heckrotte W, Watson KM. Ann. Phys.(NY) 6:1(1959).

[181] Chapline GF, et al. Phys. Rev. D 8:4302(1973).

[182] Scheid W, Mller H, Greiner W. Phys. Rev. Lett. 32:741(1974).

[183] Wong CY, Welton TA. Phys. Lett. B 34: 243(1974).

[184] Abul-Magd AY. Phys. Rev. C 12:343(1975).

[185] Sobel MI, Siemens PJ, Bethe HA. Nucl. Phys. A251:502(1975).

[186] Kitazoe Y, Sano M. Prog. Theor. Phys.54:922(1975);

[187] Gustafsson H, et al. Phys. Rev. Lett. 52:1590(1984).

[188] Renfordt RE, et al. Phys. Rev. Lett. 53:763(1984).

[189] Strbele H, et al. Phys. Rev. C 27:1349(1983).

[190] Baden A, et al. Nucl. Instr. Meth. 203:189(1982).

[191] Buchwald G, et al. Phys. Rev. Lett. 52:1594(1984).

[192] Stcker H, Greiner W. Phys. Rep. 137:277(1986).

[193] E877 Collaboration, J. Barrette et al., Phys. Rev. Lett. 70, 2996 (1993).

[194] NA49 Collaboration, T. Wienold et al., Nucl. Phys. A610, 76c (1996).

[195] P. F. Kolb, J. Sollfrank, and U. W. Heinz. Trans- verse Flow and the Quark-Hadron Phase Transition." Phys. Rev., C62:054909, 2000.

[196] A.M. Poskanzer and S.A. Voloshin, Phys. Rev. C 58,1671 (1998).

[197] S. A. Voloshin and A. M. Poskanzer, The physics of the centrality dependence of elliptic flow. Phys. Lett. B 474, 27-32 2000

[198] H. Sorge, Highly Sensitive Centrality Dependence of Elliptic Flow: A Novel Signature of the Phase Transition in QCD. Phys. Rev. Lett. 82, 2048 (1999)

[199] H. Heiselberg and A. -M. Levy, Elliptic flow and Hanbury-Brown-Twiss correlations in noncentral nuclear collisions. Phys. Rev. C59, 2716 (1999).

[200] J. -Y. Ollitrault, Flow systematics from SIS to SPS energies. Nucl. Phys. A638, 195c (1998).

[201] J. -Y. Ollitrault, Anisotropy as a signature of transverse collective flow. Phys. Rev. D46, 229 (1992).

[202] J. Adams st al.arXiv:nucl-ex/0409033 v3 2 May 2005

[203] P.F. Kolb and U. Heinz, in Quark Gluon Plasma 3, editors: R.C. Hwa and X.N. Wang, World Scientific, Singapore; arXiv: nucl-th/0305084.

[204] J. Adams et al. [STAR Collaboration], Phys. Rev. Lett. 92 (2004) 052302.

[205] P. Huovinen, P.F. Kolb, U. Heinz, P.V. Ruuskanen and S.A. Voloshin, Phys. Lett. B503 (2001) 58.

[206] P. Huovinen, private communications (2003).

[207] P. F. Kolb and U. Heinz, in Quark Gluon Plasma 3, eds. R.C. Hwa and X.N. Wang (World Scientific, Singapore, 2003); nucl-th/0305084.

[208] C. Adler et al. [STAR Collaboration], Phys. Rev. Lett. 87 (2001) 182301.

[209] STAR Collaboration, J. Adams et al ., Phys. Rev. Lett. 93, 252301 (2004).

[210] J. I. Kapusta, P. Lichard and D. Seibert, Phys. Rev.D 44, 2774 (1991). P. Arnold, G. D. Moore and L. G. Yaffe, JHEP 0112, 009 (2001).

[211] R. J. Fries, B. Muller and D. K. Srivastava, Phys. Rev. Lett. 90, 132301 (2003).

[212] B. G. Zakharov, JETP Lett. 80, 1 (2004); R. J. Fries, B. Muller and D. K. Srivastava, Phys. Rev. C 72, 041902 (2005). C. Gale, T. C. Awes, R. J. Fries and D. K. Srivastava, J. Phys. G 30, S1013 (2004).

[213] S. Turbide, C. Gale, S. Jeon and G. D. Moore, Phys. Rev. C 72, 014906 (2005).

[214] L. Xiong, E. V. Shuryak and G. E. Brown, Phys. Rev. D 46, 3798 (1992); V. V. Goloviznin and K. Redlich, Phys. Lett. B 319, 520 (1993); C. Song, Phys. Rev. C 47, 2861 (1993).

[215] S. Turbide, R. Rapp, and C. Gale, Phys. Rev. C 69, 014903 (2004).

[216] J. F. Owens, Rev. Mod. Phys. 59, 465 (1987).

[217] B. G. Zakharov, JETP Lett. 80, 1 (2004).

[218] R. J. Fries, B. Muller and D. K. Srivastava, Phys. Rev. Lett. 90, 132301 (2003).

[219] E.L. Feinberg, Nuovo Cimento 34, 391 (1976); E.V. Shuryak, Phys. Lett. B78, 150 (1978); S. Turbide, R. Rapp, C. Gale, Phys. Rev. C69, 014903 (2004).

[220] S. Turbide, C. Gale, R. J. Fries, hep-ph/0508201.

[221] J. Ashman et al. Phys. Lett., B 206;364, 1988.

[222] M. Tanaka. FEB/SBE: Commissioning with Au Beam and Run for the FY1996 AtR Transfer Line Commissioning. Technical Report 453, BNL, November 1997.

[223] Lutz G, Schwarz AS. Annu. Rev. Nucl. Part. Sci. 45:295 (1995)

[224] Blum W, Rolandi L. Particle Detection with Drift Chambers, ed. Bonaudi F, Fabjan CW. Berlin: Springer-Verlag (1994)

[225] Fabjan C. Experimental Techniques in High Energy Physics, ed. T Ferbel. Menlo Park, CA: Addison-Wesley. 257 pp. (1987)

[226] Kierstaed JA, et al. Brookhaven Natl. Lab. Rep. BNL-52321. 215 pp. (1991)

[227] Conceptual Design Report for the Solenoidal Tracker At RHIC, The STAR Collaboration, PUB-5347 (1992); J.W. Harris et al, Nucl. Phys. A 566, 277c (1994).

[228] R.L. Brown et al., Proc. 1997 IEEE Particle Accelerator Conf., 3230 (1998) and F. Bergsma et al., The STAR Detector Magenet Subsystem.

[229] D. Lynn et al., Nucl. Instrum. Meth. A447, 264 (2000) and R. Bellwied et al., The STAR Silicon Vertex Tracker.

[230] H. Wieman et al., IEEE Trans. Nucl. Sci. 44, 671 (1997) and M. Anderson et al., The STAR Time Projection Chamber.

[231] S. Klein et al., IEEE Trans. Nucl. Sci. 43, 1768 (1996) and M. Anderson et al., A Readout System for the STAR Time Projection Chamber.

[232] A. Schuttauf et al., Nuc. Phys. A661, 677c (1999) and K.H. Ackerman et al., The Forward Time Projection Chamber in STAR.

[233] M. Beddo et al., The STAR Barrell Electromagnetic Calorimeter.

[234] C.E. Allgower et al., The STAR Endcap Electromagnetic Calorimeter.

[235] H.J. Crawford and Volker Lindenstruth, Apparatus and Method for Managing Digital Resources by Passing Digital Resource Tokens Between Queues, US Patent 5,918,055 (1999).

[236] A. Ljubicic Jr., M. Botlo, F. Heistermann, S. Jacobson, M. J. LeVine, J. M. Nelson, M. Nguyen, H. Roehrich, E. Schaefer, J. J. Schanback, R. Scheetz, D. Schmischke, M. W. Schulz and K. Sulimma, Design and implementation of the STAR experiments DAQ, IEEE Trans. Nuc. Sci., 45, No. 4, pp. 1907-1912 (1998).

[237] A. Ljubicic Jr., J. M. Landgraf, M. J. LeVine, J. M. Nelson, D. Roerich, J. J. Shamback, D. Schmische, M. W. Schulz, C. Struck, C. R. Consiglio, R. Scheetz and Y. Zhao, The STAR experiments data acquisition system, IEEE Trans. Nuc. Sci., 47, No. 2, pp. 99- 102 (2000).

[238] "The RHIC Zero Degree Calorimeter", C. Adler, A. Denisov, E. Garcia, M.

Murray, H. Strobele, and S. White, Nucl. Instrum. Meth. A470, 488 (2001).

[239] CERES, G. Agakishiev et al., First results from the CERES radial TPC, Nucl. Phys. A661, 673 (1999).

[240] H. Wieman et al., STAR TPC at RHIC, IEEE Trans. Nucl. Sci. 44 (1997) 671

[241] X. Bittl et al., Diffusion and Drift Studies of Ar-DME/CO2/CH4 Gas Mixtures for a radial TPC in the EB Field, Nucl. Instr. Meth. A 398 (1997) 249.

[242] F. Bieser et al., The Forward Time Projection Chamber for the STAR Detector, MPI PhE/98-3, 1998.

[243] K. H. Ackermann et al., The forward time projection chamber (FTPC) in STAR, Nucl. Instrum. Meth. A499, 713 (2003).

[244] J. Gonzalez. Calibration of the STAR Zero Degree Calorimeters. Technical report, 2001.

[245] R.J. Glauber. Lectures in Theoretical Physics, volume 1. Interscience, New York, 1959.

[246] J. Adams et al. Production of charged pions and hadrons in Au + Au collisions at center of mass energy 130-GeV. 2003.

[247] J. Dunlop. http://www.star.bnl.gov/protected/common/common2004/ trigger2004/200gev/200gevFaq.html., 2004.

[248] STAR. http://www.star.bnl.gov/STAR/comp/simu/newsite/geometry.html., 2005.

[249] A.M. Poskanzer and S.A. Voloshin, Phys. Rev. C 58,1671 (1998).

[250] E877 Collaboration, J. Barrette et al., Phys. Rev. C 56, 3254 (1997).

[251] E877 Collaboration, J. Barrette et al., Phys. Rev. C 55, 1420 (1997).

[252] Streamer Chamber Collaboration, P. Danielewicz et al., Phys. Rev. C 38, 120 (1988).

[253] STAR Collaboration, C. Adler et al ., Phys. Rev. C 66, 034904 (2002).

[254] S. Eidelman et al. Physics Letters B 592 (2004) 1+.

[255] R. Brun, R. Hagelberg, M. Hansroul, and J. C. Lassalle. GEANT: Simula- tion program for particle physics experiments. User guide and reference manual. CERN-DD-78-2-REV.

Abstract

ELLIPTIC FLOW MEASUREMENTS OF INCLUSIVE PHOTONS AND NEUTRAL PION RECONSTRUCTIONS

by

AHMED HAMED

August 2006

Advisor: Dr. Thomas M. Cormier.

Major: High Energy Nuclear Physics

Degree: Doctor of Philosophy

The discovery of asymptotic freedom in the theory of the strong interaction has initiated the high-energy heavy-ion collisions program. It is expected such collisions to produce a deconfined phase of quarks and gluons. The prediction of the phase transition to occur in the vicinity of non-pQCD regime increases the challenges at the theoretical and experimental levels. The Relativistic Heavy Ion collider (RHIC) at Brookhaven National Laboratory was constructed to explore the QGP-hadronic matter phase transition.

The elliptic flow, $(v2)$, is one of the important charactersitics of a thermally expanding fireball created in relativistic heavy ion collision. Typically, elliptic flow is measured for strongly interacting particles which decouple from the thermal medium at later times. Direct photons, which decouple from the medium upon creation, carry information for the entire fireball evolution, in particular the information about the early QGP stage. We measure the inclusive photons elliptic flow in Au+Au collisions using STAR BEMC. To reduce the effect of so-called "non-flow" we use the FTPC

to determine the event plane. It is observed that $v2(p_t)$ decreases at high transverse momentum similar to that of charged hadrons.

Neutral pions represent a significant background for the direct photon measurements. In oreder to reconstruct the neutral pions in the high multiplicity Au+Au collisions environment, we have developed a new cluster finder for STAR BEMC, which suppresses cluster splitting and allows to obtain clear neutral pion invariant mass peak at all centralities.

In this dissertation elliptic flow measurements of inclusive photons is presented and disscused in the sight of the theoretical predictions for such measurements. The algorithm and the results of a new cluster finder for the neutral pion reconstructions are also included in this work.

Autobiographical Statement

Author	AHMED HAMED
1985 – 1989	B.Sc. in Physics Garyounis University Libya, Benghazi
1995 – 1997	M.Sc. in Physics Suez Canal University Egypt, Ismallia
2001 – 2003	Graduate Teaching Assistant Physics Department Wayne State University Detroit, MI, USA
2003 – 2006	Graduate Research Assistant High Energy Nuclear Physics Group Wayne State University Detroit, MI, USA